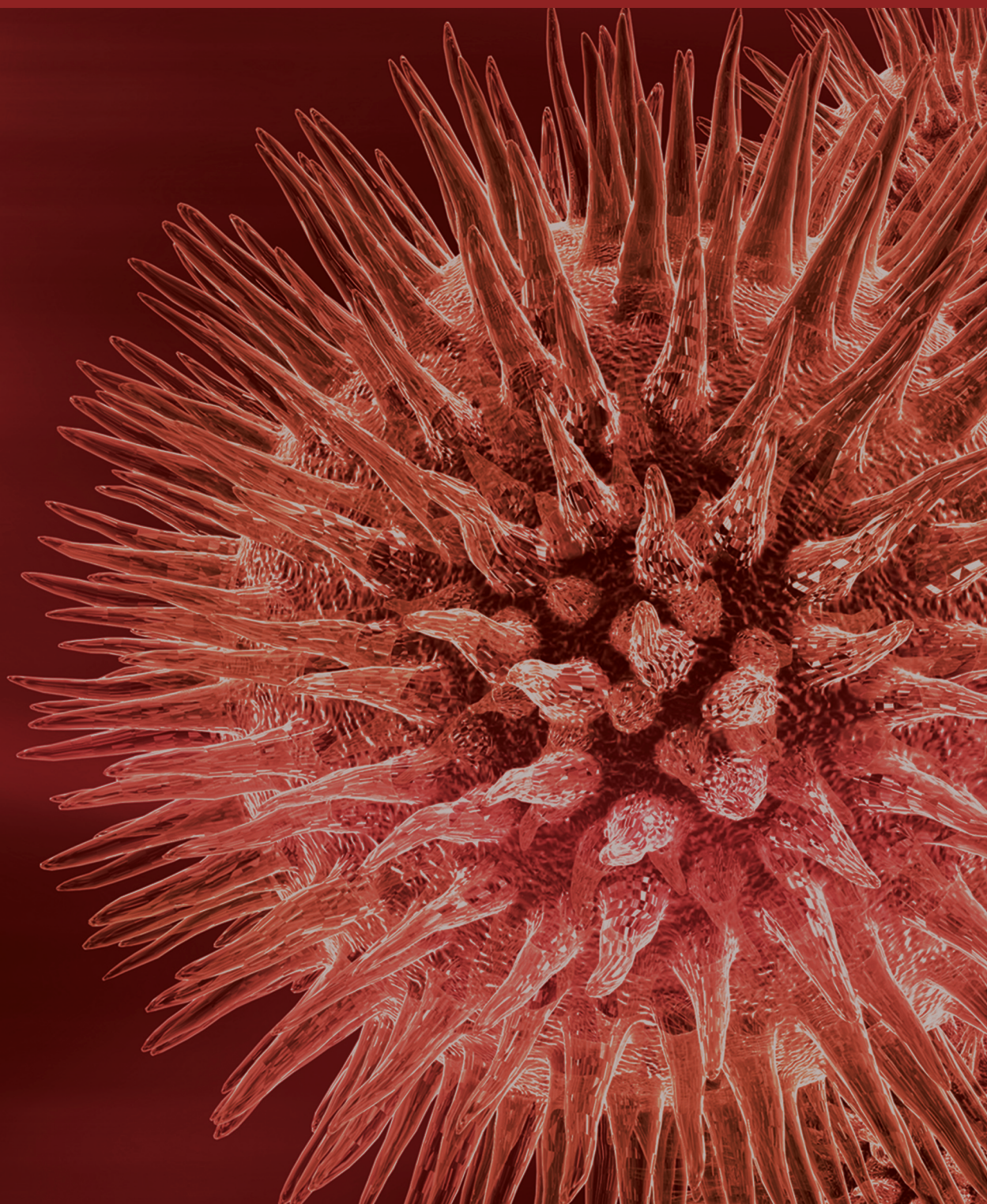


BioMed Research International

# **Nano-/Microfabrication of Biomaterials**

Guest Editors: Inn-Kyu Kang, Yoshihiro Ito, and Oh Hyeong Kwon





---

# **Nano-/Microfabrication of Biomaterials**

BioMed Research International

---

## **Nano-/Microfabrication of Biomaterials**

Guest Editors: Inn-Kyu Kang, Yoshihiro Ito,  
and Oh Hyeong Kwon



---

Copyright © 2014 Hindawi Publishing Corporation. All rights reserved.

This is a special issue published in “BioMed Research International.” All articles are open access articles distributed under the Creative Commons Attribution License, which permits unrestricted use, distribution, and reproduction in any medium, provided the original work is properly cited.

## Contents

**Nano-/Microfabrication of Biomaterials**, Inn-Kyu Kang, Yoshihiro Ito, and Oh Hyeong Kwon  
Volume 2014, Article ID 963972, 2 pages

**Biodegradable and Elastomeric Poly(glycerol sebacate) as a Coating Material for Nitinol Bare Stent**,  
Min Ji Kim, Moon Young Hwang, JiHeung Kim, and Dong June Chung  
Volume 2014, Article ID 956952, 7 pages

**Reduction-Triggered Breakable Micelles of Amphiphilic Polyamide Amine-g-Polyethylene Glycol for Methotrexate Delivery**, Yihang Huang, Jun Liu, Yani Cui, Huanan Li, Yong Sun, Yujiang Fan, and Xingdong Zhang  
Volume 2014, Article ID 904634, 11 pages

**The Morphology and Functions of Articular Chondrocytes on a Honeycomb-Patterned Surface**,  
Joshua O. Eniwumide, Masaru Tanaka, Nobuhiro Nagai, Yuka Morita, Joost de Bruijn, Sadaaki Yamamoto, Shin Onodera, Eiji Kondo, Kazunori Yasuda, and Masatsugu Shimomura  
Volume 2014, Article ID 710354, 10 pages

**Effects of Prepolymerized Particle Size and Polymerization Kinetics on Volumetric Shrinkage of Dental Modeling Resins**, Tae-Yub Kwon, Jung-Yun Ha, Ju-Na Chun, Jun Sik Son, and Kyo-Han Kim  
Volume 2014, Article ID 914739, 6 pages

**Preparation of Cylinder-Shaped Porous Sponges of Poly(L-lactic acid), Poly(DL-lactic-co-glycolic acid), and Poly( $\epsilon$ -caprolactone)**, Xiaoming He, Naoki Kawazoe, and Guoping Chen  
Volume 2014, Article ID 106082, 8 pages

**Collagen Scaffolds with Controlled Insulin Release and Controlled Pore Structure for Cartilage Tissue Engineering**, Himansu Sekhar Nanda, Shangwu Chen, Qin Zhang, Naoki Kawazoe, and Guoping Chen  
Volume 2014, Article ID 623805, 10 pages

**Impact of Core-Forming Segment Structure on Drug Loading in Biodegradable Polymeric Micelles Using PEG-*b*-Poly(lactide-co-depsipeptide) Block Copolymers**, Akihiro Takahashi, Yuta Ozaki, Akinori Kuzuya, and Yuichi Ohya  
Volume 2014, Article ID 579212, 10 pages

**Fabrication and Characterization of Thermoresponsive Polystyrene Nanofibrous Mats for Cultured Cell Recovery**, Hwan Hee Oh, Young-Gwang Ko, Hiroshi Uyama, Won Ho Park, Donghwan Cho, and Oh Hyeong Kwon  
Volume 2014, Article ID 480694, 9 pages

**Enhanced Neural Cell Adhesion and Neurite Outgrowth on Graphene-Based Biomimetic Substrates**, Suck Won Hong, Jong Ho Lee, Seok Hee Kang, Eun Young Hwang, Yu-Shik Hwang, Mi Hee Lee, Dong-Wook Han, and Jong-Chul Park  
Volume 2014, Article ID 212149, 8 pages

**Specific Intracellular Uptake of Herceptin-Conjugated CdSe/ZnS Quantum Dots into Breast Cancer Cells**, Seung-Jin Han, Pierson Rathinaraj, Soo-Young Park, Young Kyoo Kim, Joon Hyung Lee, Inn-Kyu Kang, Jong-Sik Moon, and Jeffrey G. Winiarz  
Volume 2014, Article ID 954307, 9 pages



---

**Immobilization of Bone Morphogenetic Protein on DOPA- or Dopamine-Treated Titanium Surfaces to Enhance Osseointegration**, Jeonghwa Kang, Seiichi Tada, Takashi Kitajima, Tae Il Son, Toshiro Aigaki, and Yoshihiro Ito

Volume 2013, Article ID 265980, 6 pages

**Fabrication of Microfibrous and Nano-/Microfibrous Scaffolds: Melt and Hybrid Electrospinning and Surface Modification of Poly(L-lactic acid) with Plasticizer**, Young Il Yoon, Ko Eun Park, Seung Jin Lee, and Won Ho Park

Volume 2013, Article ID 309048, 10 pages

## Editorial

# Nano-/Microfabrication of Biomaterials

Inn-Kyu Kang,<sup>1</sup> Yoshihiro Ito,<sup>2</sup> and Oh Hyeong Kwon<sup>3</sup>

<sup>1</sup> Department of Polymer Science and Engineering, Kyungpook National University, Daegu 702-701, Republic of Korea

<sup>2</sup> Nano Medical Engineering Laboratory, RIKEN, Saitama 351-0198, Japan

<sup>3</sup> Department of Polymer Science and Engineering, Kumoh National Institute of Technology, Gumi 730-701, Republic of Korea

Correspondence should be addressed to Inn-Kyu Kang; [ikkang@knu.ac.kr](mailto:ikkang@knu.ac.kr)

Received 15 May 2014; Accepted 15 May 2014; Published 27 May 2014

Copyright © 2014 Inn-Kyu Kang et al. This is an open access article distributed under the Creative Commons Attribution License, which permits unrestricted use, distribution, and reproduction in any medium, provided the original work is properly cited.

The surface composition and functionality of biomaterials and scaffolds are the most important factors for their applications in biomedical fields and tissue regeneration. Bulk and surface properties of biomaterials influence vital cell activities such as cell adhesion, proliferation, extracellular matrix secretion, and differentiation. Nano-/microstructural control is found to be another key factor in tailoring the bioactivity of material surfaces. The morphological/topographical designing of the grafts is also proved to be a strategic approach in improving the bioactivity and biological responses of the biomaterial. Furthermore, the nano-/microstructured grafts possess higher specific surface area, which will provide much more adsorption sites to adsorb bioactive molecules.

In view of these specialties of the biomaterials, several investigators are invited to contribute original research findings that can stimulate continuing efforts to understand the dimensions of the polymers and bioceramics as well as their composites essentially with bioactive compositions along with 2D/3D nano-/microlevel surface structures. The special issue is divided into three categories based on the key words of nanoparticles, surface control, and 3D scaffolds. The published works are briefly addressed as follows.

In the category of nanoparticles, S.-J. Han et al. prepared herceptin-immobilized CdSe/ZnS core-shell quantum dots (QDs). Mean size of the quantum dots (28 nm) as determined by dynamic light scattering was increased up to 86 nm after herceptin immobilization. It was found, from *in vitro* cell culture experiment, that keratin forming cancer cells (KB) were well proliferated in the presence of herceptin-conjugated QDs (QD-Her) while most of breast cancer cells (SK-BR3) were dead. The data from confocal laser scanning

microscope showed that the QD-Her specifically bound to the membrane of SK-BR3 and almost saturated after 6 hours of incubation. This result suggested that growth signal of the breast cancer cell is completely inhibited by specific binding of the herceptin to the Her-2 receptor of SK-BR3 membrane, resulting in cell death. A. Takahashi et al. reported impact of core-forming segment structure on drug loading in biodegradable polymeric micelles using PEG-*b*-poly(lactide-*co*-depsipeptide) block copolymers. As a result, the drug loading increased with increase in the mole fraction of depsipeptide unit in the hydrophobic segments. Y. Huang et al. prepared reduction-triggered breakable polymeric micelles incorporated with methotrexate (MTX) using amphiphilic PAA-*g*-PEG copolymers having S-S bonds in the backbone. The drug loading content and drug loading efficiency increased along with more hydrophobic segments in the copolymers. In reductive environments, the entire MTX payload could be quickly released due to the reduction-triggered breakage of the micelles.

In the category of surface control, J. Kang et al. immobilized bone morphogenetic protein (BMP) on DOPA- or dopamine-treated titanium surfaces to enhance osseointegration. The immobilized BMP induced specific signal transduction and alkali phosphatase, a differentiation marker. J. O. Eniwumide et al. investigated the potential of a novel micropatterned substrate for neocartilage formation. In the comparison of flat and honeycomb-patterned surface, accumulation of DNA and keratin sulphate was higher on the honeycomb surface, suggesting potential usefulness of honeycomb-based scaffolds during early cultures of neocartilage and engineered soft tissue. T.-Y. Kwon et

al. examined the polymerization shrinkage of five dental modeling resins as well as one temporary PMMA/MMA resin (control). They concluded, from the study of final volumetric shrinkage values for the modeling resins, that the optimal control of the polymerization kinetics seems to be more important for producing high-precision resin structures rather than using dental modeling resins. S. W. Hong et al. studied enhanced neural cell adhesion and neurite outgrowth on graphene-based biomimetic substrates. The result implied that graphene and CNTs, even though they were the same carbon-based nanomaterials, show differential influences on neural cells. Furthermore, graphene-coated or -patterned substrates were shown to substantially enhance the adhesion and neurite outgrowth of PC-12 cells. M. J. Kim et al. synthesized and evaluated biodegradable and elastomeric polyesters (poly(glycerol sebacate) (PGS)) using polycondensation between glycerol and sebacic acid to form a cross-linked network structure without using exogenous catalysts. They reported that synthesized materials possess good mechanical properties and elasticity and surface erosion biodegradation behavior and that the surface morphology and thickness of coating layer could be controlled by adjusting the electrospinning conditions and solution parameters.

In the category of 3D scaffolds, X. He et al. prepared cylinder-shaped porous sponges of poly(L-lactic acid), poly(DL-lactic-co-glycolic acid), and poly( $\epsilon$ -caprolactone). SEM observation showed that the cylinder-shaped sponges had evenly distributed bulk pore structures and the wall surfaces were less porous with a smaller pore size than the wall bulk pore structures. The porosity and pore size of the sponges could be controlled by the ratio and size of the porogen materials. They also studied collagen scaffolds with controlled insulin release and controlled pore structure for cartilage tissue engineering. Collagen-microbead hybrid scaffold was prepared by hybridization of insulin loaded PLGA microbeads with collagen using a freeze-drying technique. The pore structure of the hybrid scaffold was controlled by using preprepared ice particulates having a diameter range of 150–250  $\mu\text{m}$ . Hybrid scaffold had a controlled pore structure with pore size equivalent to ice particulates and good interconnection. Culture of bovine articular chondrocytes in the hybrid scaffold demonstrated high bioactivity of the released insulin. The hybrid scaffold facilitated cell seeding and spatial cell distribution and promoted cell proliferation. H. H. Oh et al. fabricated and characterized thermoresponsive polystyrene nanofibrous mats for cultured cell recovery. Cultured cells were easily detached from the PIPAAm-grafted surfaces by reducing culture temperature to 20°C, while negligible cells were detached from ungrafted surfaces. Moreover, cells on PIPAAm-grafted PS nanofibrous mats were detached more rapidly than those on PIPAAm-grafted PS dishes. Y. I. Yoon et al. fabricated nano-/microfibrous scaffolds using melt and hybrid electrospinning and surface modification of poly(L-lactic acid) with plasticizer. The silk fibroin (SF)/PLA (20/80) scaffolds consisted of a randomly oriented structure of PLA microfibers (average fiber diameter = 8.9  $\mu\text{m}$ ) and SF nanofibers (average fiber diameter = 820 nm). The PLA nano-/microfiber (20/80) scaffolds were found to have pore parameters similar to the PLA microfiber scaffolds. The PLA

scaffolds were treated with plasma in the presence of either oxygen or ammonia gas to modify the surface of the fibers. They claimed that the control of surface property and fiber diameter could be useful in the design and tailoring of novel scaffolds for tissue engineering.

*Inn-Kyu Kang  
Yoshihiro Ito  
Oh Hyeong Kwon*

## Research Article

# Biodegradable and Elastomeric Poly(glycerol sebacate) as a Coating Material for Nitinol Bare Stent

Min Ji Kim,<sup>1</sup> Moon Young Hwang,<sup>1</sup> JiHeung Kim,<sup>2</sup> and Dong June Chung<sup>1</sup>

<sup>1</sup> Department of Polymer Science and Engineering, Sungkyunkwan University, Suwon 440746, Republic of Korea

<sup>2</sup> School of Chemical Engineering, Sungkyunkwan University, Suwon 440746, Republic of Korea

Correspondence should be addressed to Dong June Chung; [djchung@skku.edu](mailto:djchung@skku.edu)

Received 10 January 2014; Revised 4 March 2014; Accepted 2 April 2014; Published 13 May 2014

Academic Editor: Yoshihiro Ito

Copyright © 2014 Min Ji Kim et al. This is an open access article distributed under the Creative Commons Attribution License, which permits unrestricted use, distribution, and reproduction in any medium, provided the original work is properly cited.

We synthesized and evaluated biodegradable and elastomeric polyesters (poly(glycerol sebacate) (PGS)) using polycondensation between glycerol and sebacic acid to form a cross-linked network structure without using exogenous catalysts. Synthesized materials possess good mechanical properties, elasticity, and surface erosion biodegradation behavior. The tensile strength of the PGS was as high as  $0.28 \pm 0.004$  MPa, and Young's modulus was  $0.122 \pm 0.0003$  MPa. Elongation was as high as  $237.8 \pm 0.64\%$ , and repeated elongation behavior was also observed to at least three times the original length without rupture. The water-in-air contact angles of the PGS surfaces were about  $60^\circ$ . We also analyzed the properties of an electrospray coating of biodegradable PGS on a nitinol stent for the purpose of enhancing long-term patency for the therapeutic treatment of varicose veins disease. The surface morphology and thickness of coating layer could be controlled by adjusting the electrospraying conditions and solution parameters.

## 1. Introduction

Biodegradable elastomers are important materials for a wide variety of medical applications. Elastomers have gained popularity because they can provide stability and structural integrity in mechanically dynamic environments without irritation to the host tissues [1, 2], and they exhibit mechanical properties similar to those of soft tissues [3–5]. For the special scaffold requiring strong mechanical properties, tough and biodegradable elastomers (poly( $\epsilon$ -caprolactone) (PCL) [6, 7], poly(glycerol sebacate) (PGS) [8], and their blended materials) were frequently adapted for *in vivo* tissue regeneration or substitution trials in many clinical fields [9–11]. But these attempts were mainly related to the improvement of tissue regeneration capability, drug sustainability, and cell adhesion properties through electrospinning process [12–14].

Stent surgery is widely used for therapeutic treatment of coronary artery and varicose veins disease, and several kinds of commercialized bare metal stents have been used in clinical settings in spite of their risks including inflammation, late thrombosis or restenosis, and fracture formation in long-term duration.

To reduce such complications, we selected PGS as biodegradable and elastic polymer for the enhancement of mechanical strength and durability of bare nitinol stent which is used for the interventional treatment of superficial femoral artery disease. PGS (one of the excellent, tough, and biodegradable polymers) was obtained as low molecular weight ( $<10,000$ ) prepolymer through polycondensation and often blended with PCL for satisfying electrospray condition because of its weak solution property (low viscosity in organic solvent). After electrospray coating, their own tough and elastic behaviors were exhibited through additional curing reaction.

In this study, we synthesized relatively high molecular weight (31,000 in  $M_w$ ) PGS prepolymer and examined the suitability for electrospray coating method (a useful technique to obtain uniform coating layer on three-dimensional structures [15–20]), and we also confirmed the biodegradable and elastomeric properties after postcuring. For the basic study of this purpose, we measured the surface morphology and thickness of the coated films to study the feasibility of PGS as a novel coating material for nitinol bare stent. By this method, we expect that stent durability, which is essential

factor for the therapeutic treatment of varicose veins disease, will enhance.

## 2. Experimental

**2.1. Materials and Synthesis of PGS [2, 8].** The PGS polymer was synthesized by polycondensation of 0.1 mol each of glycerol (glycerin, 99.0%, Samchun Pure Chemical Co., Seoul, Korea) and sebacic acid (Tokyo Chem. Indus. Co., Tokyo, Japan). Both reagents were mixed together in a three-necked flask at 130°C under an argon environment for 3 h, and the pressure of reaction flask was reduced from 1 Torr to 40 mTorr. After pressure reduction, the reaction was continued for 45 h at 120°C under a reduced atmosphere. Then partly cross-linked PGS prepolymer was obtained (yield for viscous liquid phase polymer, above 80%). Supplemental cross-linking (postcuring) reaction of PGS prepolymer was done in vacuum oven at 100°C for additional 48 hours.

**2.2. Polymer Characterization.** The resulting material after supplemental cross-linking was soaked in 100% ethanol for 24 h and was subsequently soaked in PBS for 24 h to remove unreacted reagents prior to instrumental analysis and mechanical testing.

Polymer synthesis was confirmed by GPC, <sup>1</sup>H-NMR, and FT-IR measurements. GPC (gel permeation chromatography, Waters 515, Styragel column, Milford, MA, USA) was used to measure the time-dependent molecular weight changes of PGS prepolymer. A PGS solution (1 wt%) was prepared in chloroform (as the mobile phase of GPC) for the measurements. The elution rate of the mobile phase was adjusted to 1 mL/min, and a styrene standard was used for molecular weight calibration. <sup>1</sup>H-NMR (nuclear magnetic resonance, Varian Unity Inova, 500 MHz, Germany) spectra for PGS prepolymer were obtained using CDCl<sub>3</sub> as a solvent. The chemical composition was determined by calculating the signal integrals of -COCH<sub>2</sub>CH<sub>2</sub>CH<sub>2</sub>- at 1.2, 1.5, and 2.2 ppm for sebacic acid and -CH<sub>2</sub>CH- at 3.7, 4.2, and 5.2 ppm for glycerol. Also, each functional group of the synthesized polymers was examined by FT-IR (Bruker IFS-66/S FT-IR, Bruker Optics, Germany).

Tensile tests after postcuring were conducted on 22 × 6 × 1.5 mm (according to ASTM standard D412-a) polymer strips cut from polymer sheets on a UTM LR30K Plus (Lyord Instrument Ltd., West Success, UK) equipped with a 250 N load cell.

The strain rate was 50 mm/min, and all samples were elongated to failure. Values were converted to stress-strain and Young's modulus was calculated from the initial slope using 4–6 samples. The cross-linking density ( $n$ ) was calculated according to the theory of rubber elasticity using the following equation [2, 21]:

$$n = \frac{E_0}{3RT} = \frac{\rho}{(M_w)_c}, \quad (1)$$

where  $n$  represents the number of active network chain segments per unit volume (mol/m<sup>3</sup>),  $(M_w)_c$  represents the molecular weight between cross-links (g/mol),  $E_0$  represents Young's modulus (Pa),  $R$  is the universal gas constant,  $T$  is the absolute temperature (K), and  $\rho$  is the measured elastomer density (g/cm).

Swelling by hydration of postcured PGS was conducted by the immersion of cross-linked PGS samples in PBS (phosphate buffered solution), deionized water, and ethanol. The swelling ratio was calculated using the following equation:

$$\text{Swelling ratio (\%)} = \frac{W_s - W_o}{W_o} \times 100, \quad (2)$$

where  $W_s$  represents the weight of swollen PGS and  $W_o$  represents the weight of dried PGS.

To calculate the surface energy of the polymers, we measured the contact angles in deionized water, dodecane, 1,1,2,2-tetrabromoethane, and glycerin using a contact angle meter (GBX DIGIDROP, Scientific Instrumentation, Romans, France) at room temperature. The surface energy was calculated by the following:

$$\begin{aligned} \gamma_s &= \gamma_s^a + \gamma_s^b + \gamma_s^c, \\ \gamma(1 + \cos \theta) &= 2\sqrt{\gamma_s^a \cdot \gamma_L^a} + 2\sqrt{\gamma_s^b \cdot \gamma_L^b} + 2\sqrt{\gamma_s^c \cdot \gamma_L^c}, \end{aligned} \quad (3)$$

where  $\gamma_s^a$ ,  $\gamma_s^b$ ,  $\gamma_s^c$  were collected from a previous report [22].

**2.3. In Vitro Degradation.** The degradation test was conducted using an enzyme solution (porcine liver esterase, 40 units/mL in PBS), an NaOH solution (0.1 mM), and PBS (pH 7.0). Disk-type postcured PGS specimens (10 mm in diameter, 2 mm in thickness) were degraded under *in vitro* conditions for predetermined time intervals. Degradation profiles were measured by incubating PGS in three kinds of solutions (20 mL) at 37°C with shaking. After the predetermined incubation time, the samples were removed, washed in deionized water, dried at 90°C for seven days, and weighed to determine the weight loss. The degradation ratio was calculated by comparing the initial weight ( $W_0$ ) with the weight measured at a given time point ( $W_t$ ).

**2.4. Electrospray Coating of PGS on Nitinol Stents.** Nitinol stents (10 × 75 mm, diameter × length) were kindly provided from S&G Bio Co. (Sungnam, Korea) and used as specimens in the PGS prepolymer coating experiments. They were cleaned before use in a water/ethanol (1:1 in volume ratio) solution using an ultrasonic cleaner. The experimental setup and processing conditions for the electrospray coating are shown in Figure 1. An acetone and ethanol mixture (3:7 in volume ratio) was used as a solvent for the PGS prepolymer ( $M_w = 31,000$  g/mol) solution. The electrospray coating process was done using eSpray electro-spraying system (NanoNC, Seoul, Korea) equipped with 20 mL syringe fitted with a needle (32 gauge, I.D., 0.1 mm and O.D., 0.23 mm) on KDS

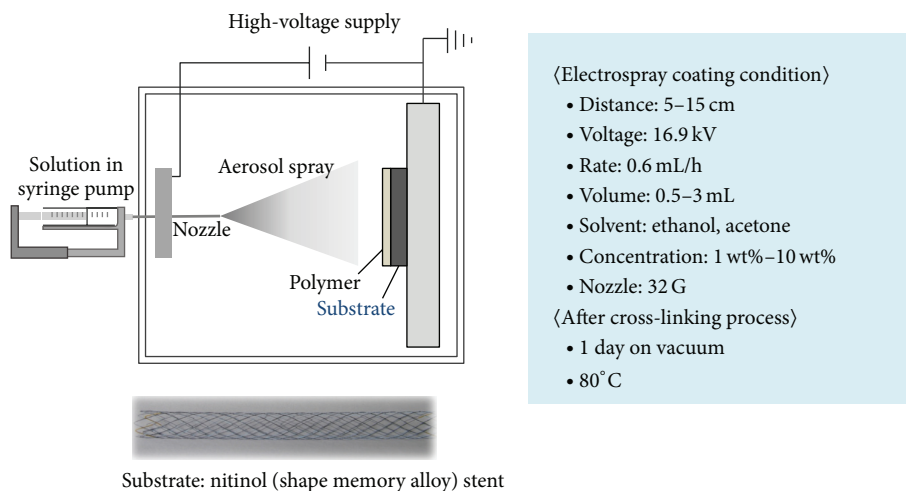


FIGURE 1: Schematic diagram of the electro spray coating process.

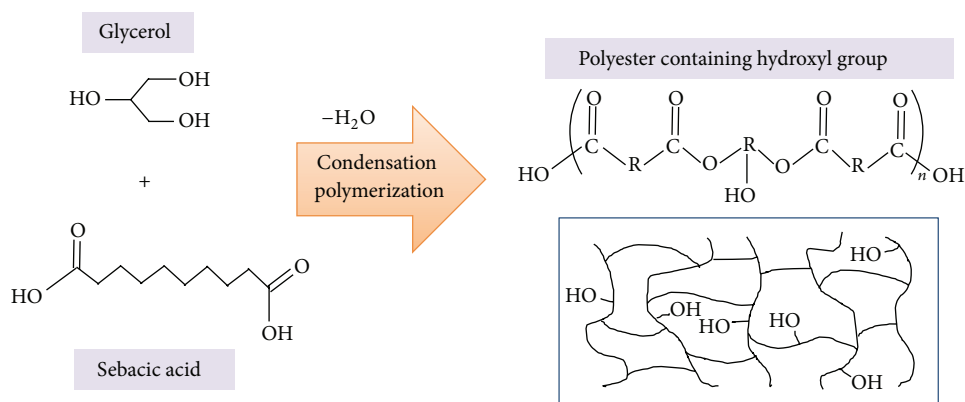


FIGURE 2: Polycondensation of glycerol and sebacic acid yielding the PGS polymer.

100 syringe pump (KD Science, Holliston, MA, USA). Nitinol stent was rotating on the collector side connected with electrode during electro spray coating process. After electro spray coating, for the supplemental cross-linking of coated PGS, the coated stents were placed in a vacuum oven at 100° C for 48 hrs additionally.

The morphologies of the coated surfaces were characterized by scanning electron microscopy (SEM; S-2400, Hitachi, Tokyo, Japan). The polymer-coated surfaces were sputter-coated with Au-Pd using a sputtering system before SEM observation. To evaluate the thickness of the coated polymer films on the stent strut, the morphology of the cross-sectionally cut surface in a liquid nitrogen environment was investigated with SEM.

### 3. Results and Discussion

**3.1. Polymer Characterization.** The PGS polymer was prepared by polycondensation of glycerol and sebacic acid (Figure 2) after 48 hours of reaction time. The resulting

polymer had a small number of cross-linking points and hydroxyl groups directly attached to the backbone, as were seen by spectroscopic analysis. After 48 hours of reaction time, the obtained partly cross-linked PGS prepolymer had a weight-average molecular weight ( $M_w$ ) of 31,000 and a number average molecular weight ( $M_n$ ) of 2,300 (as determined by GPC) with polydispersity index (PDI) of 13.0. The molar composition of the PGS prepolymer was approximately 1:1 glycerol/sebacic acid, as confirmed by  $^1H$  NMR analysis (proton peaks of  $-COCH_2CH_2CH_2-$  shown at 1.2, 1.5, and 2.2 ppm and proton peaks of  $-CH_2CH$  shown at 3.1, 4.2, and 5.2 ppm, data not shown). In addition, we observed FT-IR peaks at 1800–1600  $cm^{-1}$  (C=O), 3500–3200  $cm^{-1}$  (–OH), and 1375  $cm^{-1}$  (–CH) (data not shown), which confirms the existence of ester groups formed through polycondensation.

Such partly cross-linked PGS prepolymer (viscous liquid phase) can be solved in polar organic solvent owing to the remained –OH groups in PGS and applied for stent coating material. But fully cross-linked PGS polymer after postcuring

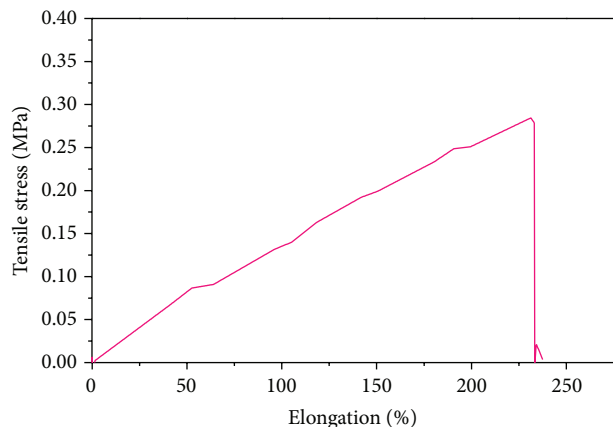


FIGURE 3: Stress-strain curves of PGS after postcuring for additional 48 h at 100°C.

could not dissolve in any kinds of organic solvent and shows elastic behaviors.

**3.2. Mechanical Tests and Swelling Ratio.** Tensile test results of thin strips of fully cross-linked PGS through supplemental cross-linking process revealed a stress-strain curve characteristic originating from elastomeric and tough materials (Figure 3). Permanent deformation was not observed during the tensile tests. Young's modulus and elongation at break of the PGS were  $0.122 \pm 0.0003$  MPa and  $237.8 \pm 0.64\%$  (those of PCL were  $225 \pm 11$  MPa and  $93 \pm 9\%$  in membrane type [23]). In another report, Young's modulus of PGS:PCL blended membrane is also increased according to the increase of PCL ratio in composite [11]. These data meant that PGS showed more elastic behavior than that of PCL, and the PGS could be elongated repeatedly to several times its original length without rupture. The ultimate tensile strength is greater than 0.3 MPa. The value of Young's modulus of PGS is located between that of ligaments (in KPa range) and tendons (in GPa range), and the strain to failure of PGS is similar to that of arteries and veins (over 260% elongation).

Also, the cross-linking density ( $n$ ) and relative molecular mass between cross-links ( $(M_w)_c$ ) were calculated using the density and Young's modulus of the samples as previously described (see (1)). The cross-linking density was  $16.4 \text{ mol/m}^3$ , and the relative molecular mass between cross-links was about 58,000 g/mol.

The degree of swelling of the elastomeric networks in ethanol was about 85% (Figure 4). However, the degree of swelling of PGS in deionized water and PBS was about 5%. Therefore, the synthesized polymer should not excessively swell in *in vivo* conditions.

**3.3. Contact Angle Measurements.** Interfacial characteristics of coating polymers are significantly important for films, coating, printing, and adhesives. Water-in-air contact angle of coated PGS surface is about  $60^\circ$  (that of PCL is  $120^\circ$  [9]), and such hydrophilicity of PGS is related to the remained -OH groups after postcuring as shown in Figure 2. This

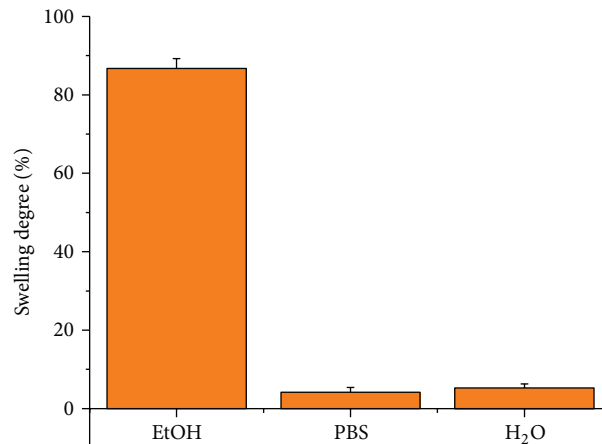


FIGURE 4: The solvent-dependent swelling behaviors of PGS.

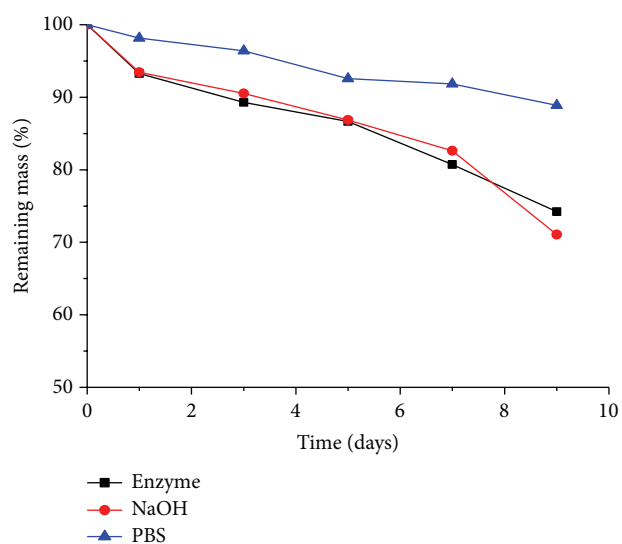


FIGURE 5: Degradation studies of PGS in solvents ( $\blacktriangle$ : PBS,  $\bullet$ : 0.1 mM NaOH,  $\blacksquare$ : enzyme solution) at 37°C.

is greatly related to the formation of H bonding between PGS and metal and also affected the adhesion property of PGS on metal stent. In addition, we calculated the surface energy using (3) of the three-component system for the surface tension method with dodecane (a nonpolar solvent), 1,1,2,2-tetrabromoethane (a polar solvent), and glycerin (a hydrogen-bonding solvent). The surface energy of the PGS polymer was 63.13 dyne/cm. This value is relatively high compared to those of polytetrafluoroethylene (19.1 dyne/cm) and polyethylene (33.1 dyne/cm).

**3.4. In Vitro Degradation Studies.** We examined the degradation characteristics of PGS under *in vitro* conditions (Figure 5). Agitation for nine days in NaOH solution at 37°C caused the polymer to degrade by 30%, as measured by change of a dry sample. In enzyme degradation, the PGS

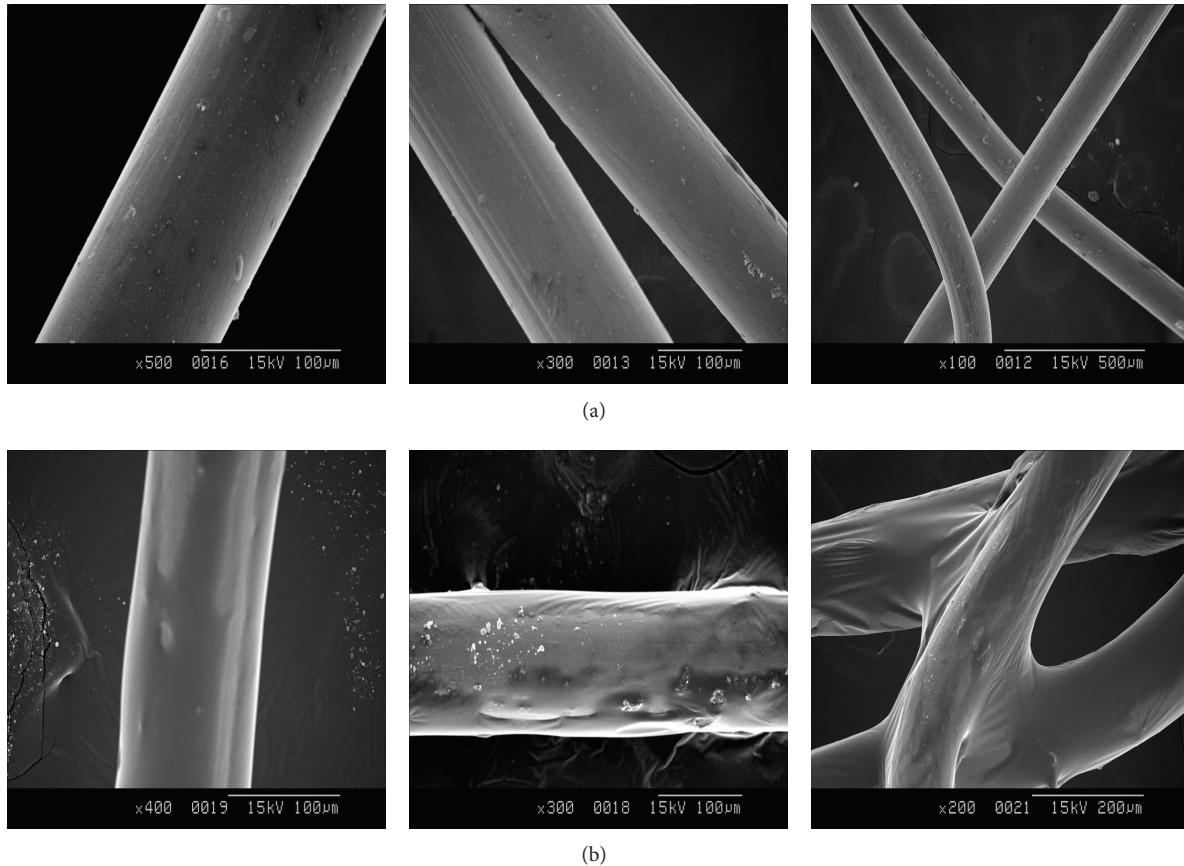


FIGURE 6: Surface morphology observation of PGS-coated stent by SEM: (a) an uncoated nitinol stent and (b) a PGS-coated stent under the electrospinning conditions of 10 wt% PGS solution in acetone and ethanol mixture (3:7 in volume ratio) at 0.6 mL/h flow rate.

polymer was degraded by 25% over nine days in esterase solutions, while it degraded by 10% in PBS solutions.

**3.5. Electro Spray Coating on a Nitinol Stent.** The surface morphologies of bare and coated stents were observed using SEM (Figure 6). Compared to bare stents, coated stents had smoother surfaces. Also, we observed the concentration effects of the coating materials on the resulting surface morphologies and thickness.

From the microscopic images of cross-sectional area of stent strut as shown in Figure 7, PGS polymer was well coated over the whole area of strut through electro spray method in spite of concentration difference of PGS solutions. When a 1 mL of PGS concentration (1 wt%) was sprayed, the surface was rough and the thickness of the polymer coating was about  $1.4 \mu\text{m}$ . However, the coated stent with same volume of a PGS concentration (10 wt%) showed a smooth surface and a thickness of about  $6.0 \mu\text{m}$ , likely caused by solvent evaporation during the electro spray coating. In high concentration polymer solutions, the solvent evaporates much less than in low concentration solutions, leaving thick and smooth surfaces. In addition, the coating thickness can be adjusted simply using the law of conservation of mass.

This shows that the polymeric droplets were continuously deposited on the polymer film during the electro spraying. Thus, the surface morphologies and thickness can be controlled by changing the concentration and amount of polymer solution.

#### 4. Conclusion

In this study, we synthesized biocompatible and elastomeric biomaterials (PGS, poly (glycerol sebacate)) through condensation polymerization. These polymers exhibit tunable mechanical properties and considerable flexibility. We also studied the degradation characteristics of the PGS polymers. For application to biomedical implants, we examined an electro spray coating of PGS on metal stents. By examining the solution parameters, we confirmed that the surface morphology of the coated film is related to the PGS solution concentration, and the thickness of the film is linearly proportional to the volume and concentration. It is expected that drug-eluting stents coated with a drug and PGS polymers can be applied practically in clinical applications.

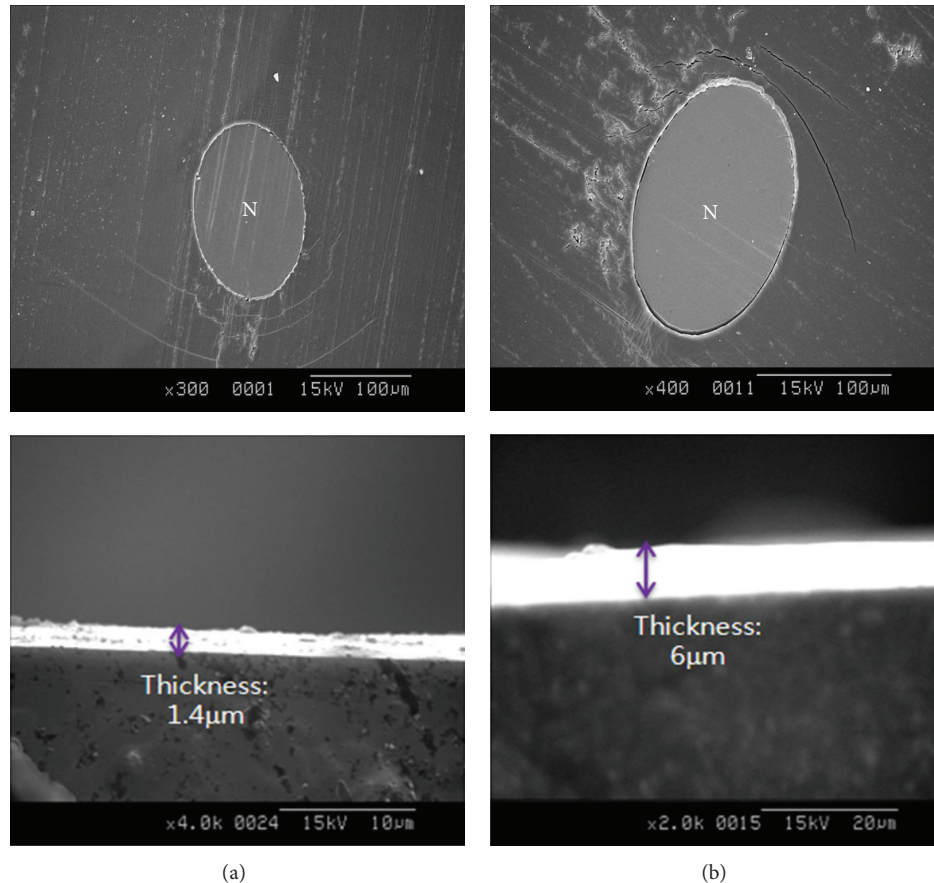


FIGURE 7: Cross-sectional SEM images of PGS coated on stent struts with volume differences: 1 mL of 1 wt% PGS solution (a) and 10 wt% PGS solution (b) in acetone and ethanol mixture (3 : 7 in volume ratio).

## Conflict of Interests

The authors declare that there is no conflict of interests regarding the publication of this paper.

## Acknowledgments

This work was supported by a grant from the Fundamental R&D Program for Core Technology of Materials funded by the Ministry of Knowledge and Economy (Grant No. M2009-10-0013) and also supported by the Fundamental Technology R&D Program for Society of the National Research Foundation (NRF) funded by the Ministry of Science, ICT & Future Planning (Grant No. 2013M3C8A3075845).

## References

- [1] R. Langer and J. P. Vacanti, "Tissue engineering," *Science*, vol. 260, no. 5110, pp. 920–926, 1993.
- [2] Y. Wang, G. A. Ameer, B. J. Sheppard, and R. Langer, "A tough biodegradable elastomer," *Nature Biotechnology*, vol. 20, no. 6, pp. 602–606, 2002.
- [3] A. P. Pêgo, A. A. Poot, D. W. Grijpma, and J. Feijen, "Biodegradable elastomeric scaffolds for soft tissue engineering," *Journal of Controlled Release*, vol. 87, no. 1–3, pp. 69–79, 2013.
- [4] J. Yang, A. R. Webb, and G. A. Ameer, "Novel citric acid-based biodegradable elastomers for tissue engineering," *Advanced Materials*, vol. 16, no. 6, pp. 511–516, 2004.
- [5] F. Gu, H. M. Younes, A. O. S. El-Kadi, R. J. Neufeld, and B. G. Amsden, "Sustained interferon- $\gamma$  delivery from a photocrosslinked biodegradable elastomer," *Journal of Controlled Release*, vol. 102, no. 3, pp. 607–617, 2005.
- [6] S. M. Mantila Roosa, J. M. Kemppainen, E. N. Moffitt, P. H. Krebsbach, and S. J. Hollister, "The pore size of polycaprolactone scaffolds has limited influence on bone regeneration in an in vivo model," *Journal of Biomedical Materials Research A*, vol. 92, no. 1, pp. 359–368, 2010.
- [7] K.-J. Wu, C.-S. Wu, and J.-S. Chang, "Biodegradability and mechanical properties of polycaprolactone composites encapsulating phosphate-solubilizing bacterium *Bacillus* sp. PG01," *Process Biochemistry*, vol. 42, no. 4, pp. 669–675, 2007.
- [8] Y. Wang, Y. M. Kim, and R. Langer, "In vivo degradation characteristics of poly(glycerol sebacate)," *Journal of Biomedical Materials Research A*, vol. 66, no. 1, pp. 192–197, 2003.
- [9] S. Salehi, M. Fathi, S. H. Javanmard et al., "Generation of PGS/PCL blend nanofibrous scaffolds mimicking corneal

- stroma structure," *Macromolecular Materials Engineering*, vol. 299, no. 4, pp. 455–469, 2014.
- [10] S. Sant, C. M. Hwang, S.-H. Lee, and A. Khademhosseini, "Hybrid PGS-PCL microfibrinous scaffolds with improved mechanical and biological properties," *Journal of Tissue Engineering and Regenerative Medicine*, vol. 5, no. 4, pp. 283–291, 2011.
- [11] N. Masoumi, B. L. Larson, N. Annabi et al., "Electrospun PGS:PCL microfibers align human valvular intestinal cells and provide tunable scaffold anisotropy," *Advanced Healthcare Materials*, 2014.
- [12] C. G. Park, M. H. Kim, M. Park et al., "Polymeric nanofiber coated esophageal stent for sustained delivery of an anticancer drug," *Macromolecular Research*, vol. 19, no. 11, pp. 1210–1216, 2011.
- [13] J. Choi, S. B. Cho, B. S. Lee, Y. K. Joung, K. Park, and D. G. Han, "Improvement of interfacial adhesion of biodegradable polymers coated on metal surface by nanocoupling," *Langmuir*, vol. 27, no. 23, pp. 14232–14239, 2011.
- [14] E. Lih, Q. V. Bash, B. J. Park, Y. K. Joung, and D. G. Han, "Surface modification of stainless steel by introduction of various hydroxyl groups for biodegradable PCL polymer coating," *Biomaterials Research*, vol. 17, no. 4, pp. 176–180, 2013.
- [15] S. B. Cho, C. H. Park, K. Park, D. J. Chung, and D. K. Han, "Biodegradable PLGA polymer coating on biomedical metal implants using electrospraying," *Polymer*, vol. 33, no. 6, pp. 620–624, 2009.
- [16] S. G. Kumbar, S. Bhattacharyya, S. Sethuraman, and C. T. Laurencin, "A preliminary report on a novel electrospray technique for nanoparticle based biomedical implants coating: precision electrospraying," *Journal of Biomedical Materials Research B*, vol. 81, no. 1, pp. 91–103, 2007.
- [17] D. H. Kim, Y. I. Jeong, C. W. Chung et al., "Preclinical evaluation of sorafenib-eluting stent for suppression of human cholangiocarcinoma cells," *International Journal of Nanomedicine*, vol. 8, pp. 1697–1711, 2013.
- [18] H. Xu, J. Su, J. Sun, and T. Ren, "Preparation and characterization of new nano-composite scaffolds loaded with vascular stents," *International Journal of Molecular Sciences*, vol. 13, no. 3, pp. 3366–3381, 2012.
- [19] C. Hu, S. Liu, B. Li, H. Yang, C. Fan, and W. Cui, "Micro-/nanometer rough structure of a superhydrophobic biodegradable coating by electrospraying for initial anti-bioadhesion," *Advanced Healthcare Materials*, vol. 2, no. 10, pp. 1314–1321, 2014.
- [20] R. Bakhshi, M. J. Edirisinghe, A. Darbyshire, Z. Ahmad, and A. M. Seifalian, "Electrohydrodynamic jetting behaviour of polyhedral oligomeric silsesquioxane nanocomposite," *Journal of Biomaterials Applications*, vol. 23, no. 4, pp. 293–309, 2009.
- [21] L. H. Sperling, *Introduction to Physical Polymer Science*, John Wiley & Sons, New York, NY, USA, 1992.
- [22] D. I. Ryu, J. H. Kim, and Y. S. Shin, *The Interfacial Science*, Chonnam National University Press, Kwangju, Korea, 1998.
- [23] L. P. K. Ang, Y. C. Zi, R. W. Beuerman, S. H. Teoh, X. Zhu, and D. T. H. Tan, "The development of a serum-free derived bioengineered conjunctival epithelial equivalent using an ultrathin poly( $\epsilon$ -caprolactone) membrane substrate," *Investigative Ophthalmology and Visual Science*, vol. 47, no. 1, pp. 105–112, 2006.

## Research Article

# Reduction-Triggered Breakable Micelles of Amphiphilic Polyamide Amine-g-Polyethylene Glycol for Methotrexate Delivery

**Yihang Huang, Jun Liu, Yani Cui, Huanan Li, Yong Sun, Yujiang Fan, and Xingdong Zhang**

National Engineering Research Center for Biomaterials, Sichuan University, 29 Wangjiang Road, Chengdu 610064, China

Correspondence should be addressed to Yong Sun; sunyong8702@scu.edu.cn and Yujiang Fan; fan\_yujiang@scu.edu.cn

Received 17 January 2014; Revised 20 March 2014; Accepted 21 March 2014; Published 13 April 2014

Academic Editor: Yoshihiro Ito

Copyright © 2014 Yihang Huang et al. This is an open access article distributed under the Creative Commons Attribution License, which permits unrestricted use, distribution, and reproduction in any medium, provided the original work is properly cited.

Reduction-triggered breakable polymeric micelles incorporated with MTX were prepared using amphiphilic PAA-g-PEG copolymers having S-S bonds in the backbone. The micelles were spherical with diameters less than 70 nm. The micelles could encapsulate the hydrophobic MTX in the hydrophobic core. The drug loading content and drug loading efficiency of the micelles were highly dependent on the copolymer chemical structure, ranging from 2.9 to 7.5% and 31.9 to 82.5%, respectively. Both the drug loading content and drug loading efficiency increased along with more hydrophobic segments in the copolymers. In normal circumstance, these micelles were capable of keeping stable and hold most of the MTX in the core, stabilizing the incorporated MTX through the  $\pi$ - $\pi$  stacking with the phenyl groups in the backbone of the copolymers. In reductive environments that mimicked the intracellular compartments, the entire MTX payload could be quickly released due to the reduction-triggered breakage of the micelles. These micelles showed good antiproliferative activity against several cancer cell lines, including KB, 4T-1 and HepG2, especially within the low drug concentration scope.

## 1. Introduction

Chemotherapy is one of the major approaches for cancer treatment. Methotrexate (MTX) is a folate antimetabolite that blocks the synthesis pathway of DNA by inhabiting the activity of dihydrofolate reductase (DHFR) [1, 2]. It shows a greater toxic effect on rapidly dividing cancerous cells, which replicate their DNA much faster, than on normal cells. Thus, it is widely used in treatment of a number of human cancers [3]. However, the therapeutic effect of MTX is hindered by its toxic dose-related side effects, as well as the drug resistance by target cells. These drawbacks of MTX are closely related to its poor water-solubility and very short circulation half-life, which results in an essentially uniform tissue distribution [4]. Therefore, there is an urgent demand for formulations that are capable of efficiently enhancing drug targeting and reducing side effects [5].

In the past decades, many studies have demonstrated that nanoscaled drug delivery systems could encapsulate

cytotoxic and poorly water soluble drugs for improving pharmacokinetic behavior, reducing toxicity, overcoming drug-resistance mechanisms, and enhancing tumor targeting through the enhanced permeation and retention (EPR) effect [6–8]. Polymeric micelles, formed from hydrophobic inner core and hydrophilic outer shell, have been demonstrated by many investigators to have potential usefulness in the process of tumor targeting drug delivery through intravenous injection [9–11]. The hydrophobic core functions as a nanoreservoir of hydrophobic drugs, whereas the hydrophilic outer shell improves solubility of hydrophobic drugs, provides a defense layer against attack of the reticuloendothelial system (RES), increases preservation of bioactive agents within the micellar core for long blood circulation, enhances targeting performance against tumor, and lessens the adverse effects of anticancer drugs [12, 13].

Advances in MTX delivery have been made by incorporating MTX with various nanoparticulate carrier systems, such as polymer-based particles [14], dendrimers [15–17],

liposomes [18], micelles [19, 20], and inorganic nanoparticles [21]. In these rationally designed delivery carriers, intracellular translocation across the plasma membrane could be critical, because the nanoparticulate carriers generally show low cellular membrane permeability and enter the cell mainly through the endocytotic pathway with the formation of endosome [22]. It was reported that anticancer drugs delivered by nanoparticles were trapped in the endocytic vesicles, suggesting quite slow intracellular drug release due to the intracellular barriers of cellular organelle membrane [23–27].

Because the physicochemical properties and biological functions of tumor are different from that of normal tissues, drug carriers could be designed to release the loaded drugs after reaching the cancer cells by introducing sensitive functional groups in response to certain stimuli of the cancer cells [28]. Higher concentration of reductive glutathione (GSH) inside the tumor cells over normal cells provides a reducing intracellular environment as the inbuilt mechanism for release of anticancer drugs [29]. Therefore, controlling the release of anticancer drugs from polymeric micelles using reduction-sensitivity as a trigger to enhance tumor-killing efficacy and to minimize harmful side effects has been considered a promising way for intracellular drug delivery. Many researchers demonstrated that polymeric micelles, polymersomes, and nanogels containing S–S linkage prevented the premature release of loaded cargos in extracellular media but quickly released the DNA, siRNA, or drug cargoes inside the cells or under a reductive condition mimicking that of the intracellular compartments [30–34].

In our previous research [35, 36], amphiphilic reduction-triggered breakable micelles from polyamide amine-*g*-polyethyleneglycol (PAA-*g*-PEG) were developed to encapsulate the anticancer drug doxorubicin (DOX). In these micelles, phenyl groups were interspersed in the hydrophobic segment to interact with the aromatic structure of DOX through the  $\pi$ - $\pi$  stacking, thus increasing the stability and drug loading ability. On the other hand, the hydrophilic segment of polyethyleneglycol (PEG) was oriented on the surface of the micelles, which determined the high biocompatibility of the micelles. In this work, 6 kinds of the PAA-*g*-PEG micelles with different hydrophobic/hydrophilic ratio were investigated as nanocarrier for MTX. MTX was encapsulated in PAA-*g*-PEG micelles using solvent dispersion/dialysis process. The size and morphology of drug-loaded micelles were characterized by DLS and TEM. Drug loading content, drug loading efficiency, and drug release behavior under reductive condition were studied using ultraviolet spectroscopy. The antiproliferative activity of MTX-incorporated micelles was measured against different tumor cells in comparison with those of free MTX.

## 2. Materials and Methods

**2.1. Materials.** Acryloyl chloride, phenethylamine, and ethanolamine were purchased from Sigma-Aldrich. Cystamine dihydrochloride, N,N'-dicyclohexyl carbodiimide (DCC), dimethylamine pyridine (DMAP), triethylamine (TEA),

and succinic anhydride were purchased from Asta Tech Pharmaceutical Co., Ltd. (Chengdu, China). Polyethyleneglycol monomethyl ether (MPEG, Mn 2000 and 5000) were obtained from Fluka and were dried by azeotropic distillation from dry toluene immediately before used. Methotrexate (MTX) was purchased from Aladdin Reagent Inc. (Shanghai, China). All other agents are of analytical grade. The chemicals were used as-received unless otherwise addressed.

**2.2. Synthesis of the Reduction-Degradable PAA-*g*-PEG Copolymers.** Preparation of reduction-degradable PAA-*g*-PEG copolymers was performed by the method reported previously [35]. Briefly, cystamine bisacrylamide was synthesized by reacting acryloyl chloride with cystamine dihydrochloride in dichloromethane/water. Then, the freshly obtained cystamine bisacrylamide (1.044 g, 4 mmol) was reacted with a mixture of phenethylamine and ethanolamine (total 4 mmol, mol ratio: phenethylamine/ethanolamine = 8/2, 7/3, and 6/4, resp.) at 125°C under Ar atmosphere to acquire PAA containing disulfide linkage. Finally, as an example, amphiphilic PAA-*g*-PEG (PAA(8:2)-PEG2000) copolymers were obtained by coupling  $\alpha$ -carboxy- $\omega$ -methoxy polyethyleneglycol (MPEGCOOH, 1.05 g, Mn = 2000, 0.5 mmol of carboxyl) on PAA (0.74 g, phenethylamine/ethanolamine = 8/2, 0.4 mmol of hydroxyl group) using DCC (0.124 g, 0.7 mmol) as coupling agent and DMAP (0.061 g, 0.05 mmol) as catalyst in dry DMSO at room temperature. Following this way, six kinds of amphiphilic reduction-degradable PAA-*g*-PEG copolymers were prepared. The structure and molecule weight of the copolymers were characterized by <sup>1</sup>H NMR (VarianUNITY INOVA400) and FT-IR (Perkin Elmer FT-IR spectrometer Frontier).

**2.3. Fabrication and Characterization of Micelles with/without Drug.** A DMSO (10 mL) solution of PAA-*g*-PEG graft copolymer (10 mg) was dropped into deionized water under vigorous ultrasonic agitation using a Type 60 Sonic Dismembrator (Fisher Scientific). The mixture was then dialyzed (Spectra/Por MWCO 8000–14000) against deionized water for 48 h to obtain the PAA-*g*-PEG micelle. For preparing MTX-incorporated micelle, PAA-*g*-PEG copolymer (10 mg) and MTX (1 mg) were dissolved in DMSO (5 mL) in a glass vial. The solution was then added dropwise to pure water (10 mL) under vigorous ultrasonic agitation. The resulting mixture was dialyzed against 1000 mL of deionized water for 24 h. The thus obtained micelle suspension was filtered through a 0.45  $\mu$ m membrane filter (Millipore) to remove the MTX aggregates. Subsequently, the mixture was ultrafiltered through a Millipore Centrifugal Filter Device (MWCO: 10,000) at 3500 r/min until the intraluminal fluid reached 3 mL to further remove unpacked free MTX and DMSO and concentrate the MTX-incorporated micelles suspension. The suspension was collected and freeze-dried to obtain MTX-incorporated micelles. The whole procedure was performed in dark.

Mean micelle diameters were measured on dynamic light scattering (DLS, Malvern Nano-ZS) using the micelle suspension (0.5 mg/mL) after filtered through a Durapore 0.22  $\mu\text{m}$  membrane (Millipore). The morphology of the micelles was analyzed using transmission electronic microscopy (TEM, Hitachi H-600). The micelle suspension sample (0.1 wt%) was dropped on a carbon-coated copper grid, followed by drying in air, and negatively staining with 3 wt% ammonium molybdate aqueous solution before observation. MTX dispersion in the micelles was analyzed by X-ray diffraction (XRD, Tongda TD-3500 diffractometer, Dandong, China) scanning from 5 to 40° with 0.06°/sec. The critical micelle concentration (CMC) was determined by fluorescence spectrophotometer (F-7000 fluorescence spectrophotometer, PerkinElmer) using pyrene as the fluorescence probe [35]. The drug loading content (DLC) and drug loading efficiency (DLE) was determined by ultraviolet spectroscopy measurement (PerkinElmer Lambda 650 S, excitation at 303 nm [37]) in DMSO using calibration curve obtained from MTX/DMSO solutions with different MTX concentrations and calculated as follows:

$$\text{DLC (wt\%)} = \left[ \frac{\text{weight of loaded drug}}{\text{weight of drug loaded micelle}} \right] \times 100\%,$$

$$\text{DLE (\%)} = \left[ \frac{\text{weight of loaded drug}}{\text{weight of drug in feed}} \right] \times 100\%.$$

(1)

**2.4. In Vitro Drug Release Behaviors.** *In vitro* drug release behavior of MTX-incorporated micelles was studied by a dialyzing method. Briefly, the suspensions of MTX-incorporated micelles in 2 mL of PBS buffer (10 mM, pH = 7.4) were dialyzed against 30 mL of PBS buffer (MWCO 8000–14,000) without DTT or containing 10 mM DTT to imitate the reducing environment. After predefined time intervals, 10 mL dialysate was replaced by equivalent fresh buffer. The amount of released MTX was calculated based on the absorbance intensity at 303 nm [37] using ultraviolet spectroscopy measurement using calibration curve obtained from MTX/PBS solutions with different MTX concentrations. Each batch sample was measured in triplicate.

**2.5. Biocompatibility of PAA-g-PEG Micelles.** Biocompatibility of the polymeric micelles was evaluated by coculturing the micelle suspensions with L929, HepG2, 4T1, and KB cells in 96-well plates (100  $\mu\text{L}$ ,  $4 \times 10^3$  cells/well). The cells were preincubated for 24 h in DMEM (L929 and HepG2) or RPMI 1640 (4T1 and KB) supplemented with 10% fetal bovine serum, 1% benzylpenicillin/streptomycin at 37°C in a humidified atmosphere with 5% CO<sub>2</sub>. Then the culture media were replaced by corresponding medium (200  $\mu\text{L}$ ) containing different concentration (0, 10, 40, 100, and 250  $\mu\text{g/mL}$ ) of polymeric micelles. After incubated for another 48 h, the cell viability was determined by MTT assay [35].

**2.6. Antiproliferative Activity of MTX-Loaded Micelles against Cancer Cell Lines.** 4T1, KB, and HepG2 cancer cell lines were seeded on 96-well plates (100  $\mu\text{L}$ ,  $4 \times 10^3$  cells/well)

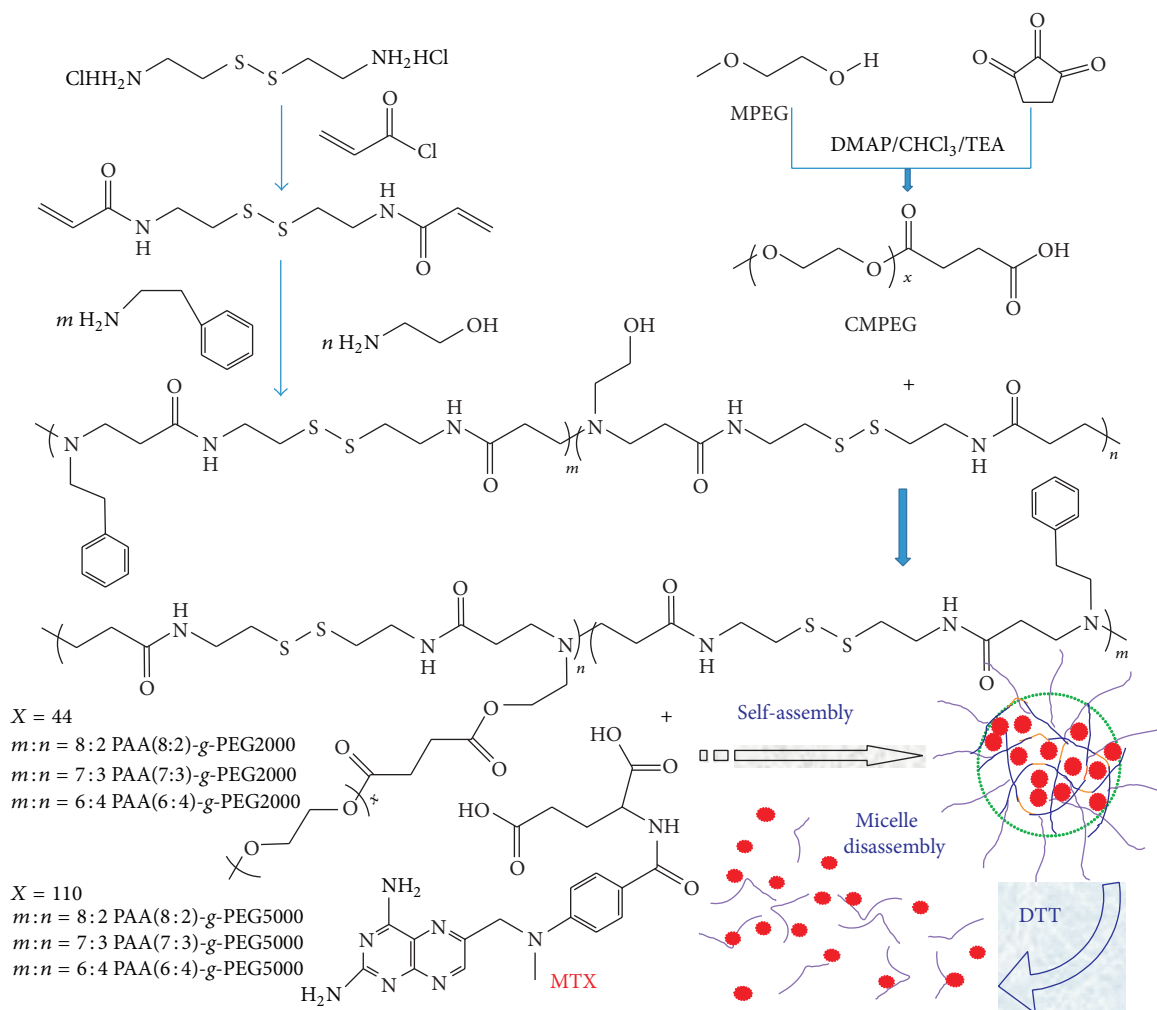
and incubated for 24 h in DMEM (HepG2) or RPMI 1640 (4T1 and KB) supplemented with 10% fetal bovine serum, 1% benzylpenicillin/streptomycin at 37°C in a humidified atmosphere with 5% CO<sub>2</sub>. Then the culture medium was replaced with 200  $\mu\text{L}$  of preprepared culture medium containing free MTX or MTX-incorporated micelles at different MTX concentration (0.01, 0.1, 0.5, 1.0, 5.0, 10.0, and 20.0  $\mu\text{g/mL}$ ). The cells were cultured for another 48 h for 4T1 cells and 72 h for KB and HepG2 cells. Then, the cell viability was measured by MTT assay as described above.

### 3. Result and Discussion

**3.1. Synthesis of the Reduction-Degradable PAA-g-PEG Copolymers.** 6 kinds of reduction-degradable amphiphilic PAA-g-PEG copolymers were synthesized according to Scheme 1 as described in previous reports [35, 36]. At first, cystamine bisacrylamide was synthesized through a classical reaction involving the N-acylation of cystamine dihydrochloride by acryloyl chloride in a water/dichloromethane two-phase system. Next, the obtained cystamine bisacrylamide was reacted with primary amines by way of the Michael addition to form the polyamide amine (PAA). Finally, PAA-g-PEG copolymers were obtained by grafting MPEG-COOH onto the hydroxyl of PAA main chain using DCC as the condensing agent.

A mixture of phenylethylamine and ethanolamine were adopted as the amine compounds. The use of ethanolamine introduced hydroxyl into the polymer backbone for the condensation reaction in the next step. Phenylethylamine made the polymer backbone hydrophobic. Since interactions among the hydrophobic segments were the driving force in the formation of micelles, the interaction should strengthen the stability of micelles. The aromatic structure in phenylethylamine further provided potential benefit for stabilizing the drug-loaded micelles through the  $\pi$ - $\pi$  stacking interaction with MTX. Changing the proportion of two amine compounds, three PAA(PAA(8:2), PAA(7:3), and PAA(6:4)) with different hydrophobic properties were obtained. These PAA copolymers were grafted with two kinds of MPEG-COOH (Mn = 2000/5000), respectively, to form 6 PAA-g-PEG graft copolymers (Table 1). As shown in Scheme 1, many disulfide (S–S) bonds were equably distributed throughout the backbone of the copolymers structure. These S–S bonds that came from cystamine were stable in normal condition and quickly fractured in reductive condition. Therefore, the micelles based on these amphiphilic copolymers were capable of keeping high stability in the absence of reductive agents, whereas quickly degrading under the reductive condition.

The final structure of PEG-g-PAA was confirmed by <sup>1</sup>H NMR (Figure 1(a)). The signals at 3.5 ppm (–CH<sub>2</sub>CH<sub>2</sub>–) indicated the presence of methylene group of the poly ethyleneglycol methyl ether methacrylate, and 4.15 ppm (–CH<sub>2</sub>CH<sub>2</sub>–O–CH<sub>3</sub>) indicated the presence of methyl group of the poly ethyleneglycol methyl ether methacrylate. Peak at 7.25 ppm (–C<sub>6</sub>H<sub>5</sub>–) indicated the presence of benzene of the phenylethylamine [38]. These <sup>1</sup>H NMR results indicated that



SCHEME 1: Chemical structure of reduction-degradable PAA-g-PEG amphiphilic copolymers and micelles.

TABLE 1: Synthesis of amphiphilic polyamide amine-g-polyethylene glycol graft copolymers.

| Entry            | PAA   |                 | PAA-g-MPEG<br>Graft efficiency* |
|------------------|---|-----------------|---------------------------------|
|                  | BAC/phenylethylamine/<br>ethanolamine<br>Feed ratio | Measured ratio* |                                 |
| PAA(8:2)-PEG2000 | 9/8/2   | 9/8/2           | 93%                             |
| PAA(7:3)-PEG2000 | 9/7/3   | 9/7/3           | 84%                             |
| PAA(6:4)-PEG2000 | 9/6/4   | 9/6/4           | 71%                             |
| PAA(8:2)-PEG5000 | 9/8/2   | 9/8/2           | 79%                             |
| PAA(7:3)-PEG5000 | 9/7/3   | 9/7/3           | 67%                             |
| PAA(6:4)-PEG5000 | 9/6/4   | 9/6/4           | 58%                             |

\* Calculated from peak areas of respective protons in  $^1\text{H}$  NMR.

the structure of the copolymers was in agreement with the predicted structures as shown in Scheme 1.

In the FT-IR spectrum of PAA (Figure 1(b)-(B)), a new absorption at about  $3010\text{--}3100\text{ cm}^{-1}$  typically for benzene

appeared compared with cystamine bisacrylamide (Figure 1(b)-(A)). Meanwhile, in Figure 1(b)-(D), the ester peak at  $1720\text{ cm}^{-1}$  almost completely disappeared, indicating the decrease of ester proportion in the copolymer in contrast with that in MPEGCOOH (Figure 1(b)-(C)). In addition, the PEG-g-PAA conjugate showed the intense stretching bands at  $2863\text{ cm}^{-1}$  and  $1098\text{ cm}^{-1}$  for PEG block, and a broad band  $\text{--OC--NH--}$  at about  $3226\text{ cm}^{-1}$  and  $3037, 1450\text{ to }1640\text{ cm}^{-1}$ . FT-IR spectra results indicated that the characteristic functional groups of the copolymers were in agreement with the predicted functional groups.

**3.2. Fabrication and Characterization of the Micelles with/without MTX.** MTX-incorporated micelles were fabricated by dialyzing PAA-g-PEG copolymer with MTX. After the incorporation of MTX, amide bond between  $1450$  and  $1640\text{ cm}^{-1}$  merged to form a broad peak because of the  $\text{C=N}$  double bond in MTX (Figure 1(b)-(E)). The size, size distributions, and morphology of the micelles were analyzed by DLS and TEM. The representative DLS profiles and TEM images for MTX-incorporated micelles of copolymer

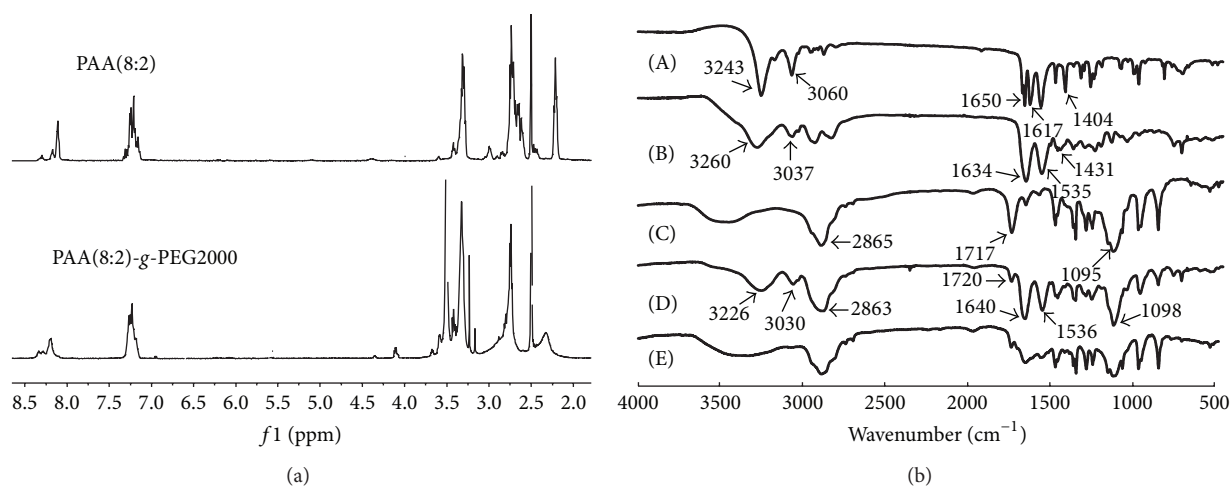


FIGURE 1:  $^1\text{H}$  NMR spectra (a) of PAA(8:2) and PAA(8:2)-g-MPEG2000 and FTIR spectra (b) of cystamine bisacrylamide (A), PAA (b), MPEGCOOH (C), PAA(8:2)-g-MPEG2000 (D), and MTX-incorporated PAA(8:2)-g-MPEG2000 micelles (E).

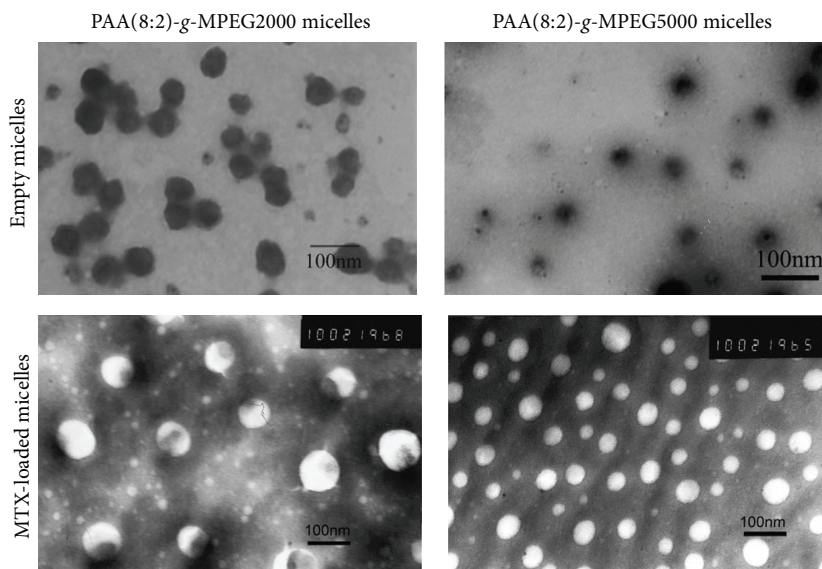


FIGURE 2: TEM images of PAA(8:2)-g-MPEG2000 micelle, PAA(8:2)-g-MPEG5000 micelle, MTX-incorporated PAA(8:2)-g-MPEG2000 micelle, and MTX-incorporated PAA(8:2)-g-MPEG5000 micelles.

PAA(8:2)-PEG2000 and PAA(8:2)-PEG5000 were shown in Figure 2, and results for all the 6 kinds of micelles were summarized in Table 2. Since TEM results were obtained under the condition of dehydration, which were a little different from the results obtained from DLS measurement in the aqueous solution. But these copolymers formed spherical blank micelles with diameter less than 70 nm. Generally, nanoparticles smaller than 100 nm were favorable for extravasation of the nanoparticles into tumors through EPR effect, because the discontinuous endothelium of tumor blood vessels form many pores ranging in size from 200 nm to 2  $\mu\text{m}$  with the average pore size approximately 400 nm on the vessel walls [39]. The micelles have relatively low CMCs, which was suitable for encapsulating hydrophobic drugs.

The theoretical drug loading content (DLC) was set at 9.09 wt%. The highest drug loading content and drug loading efficiency (DLE) were obtained in PAA(8:2)-PEG2000 micelles at 7.5% and 82%, respectively. With more hydrophobic segments, the DLC and DLE obviously increased, because more hydrophobic segments could increase the hydrophobic interaction of the copolymer hydrophobic segment and the hydrophobic interaction with the drug. Further, the introduction of phenyl group in the hydrophobic segment of the copolymer could provide  $\pi$ - $\pi$  stacking between the drug and the copolymer, which could further increase the stability of the micelles. In our previous study, DLC of DOX-incorporated micelles with similar structure could reach 20% [36]. Compared to DOX, due to less aromatic structure

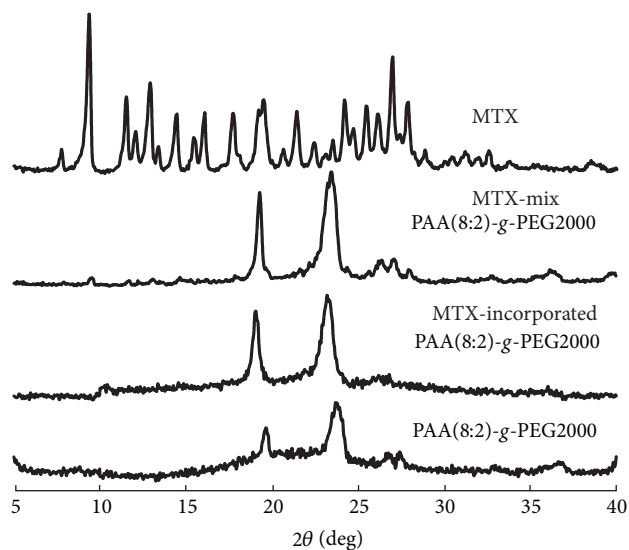


FIGURE 3: XRD diffractograms of MTX, MTX/PAA(8:2)-g-PEG2000 mixture, MTX-incorporated PAA(8:2)-g-PEG2000 micelles, and PAA(8:2)-g-PEG2000 micelles.

and more amino and carboxyl in MTX, the maximum DLC for MTX was less than that for DOX. Both DLC and DLE decreased when increasing the density of PEG. The reason might be the decrease of the hydrophobic PAA in the core of the micelles. Considering the micelle size, DLC and DLE, PAA(8:2)-g-PEG2000 and PAA(8:2)-g-PEG5000 micelles were selected as typical examples for the further investigation.

X-ray diffraction indicated that MTX dispersed uniformly inside the micelles. Free MTX was a crystalline compound as shown in Figure 3 for its characteristic diffraction pattern. PAA(8:2)-g-PEG2000 micelles without drug had two peaks at  $2\theta$  values of 19 and 23 in its diffractograms, probably due to the crystalline nature of the PEG segments. In the diffractograms of MTX and PAA(8:2)-g-PEG2000 mixture, MTX crystalline peaks at  $2\theta$  values of 10 and 27 could be detected. However, in the diffractograms of MTX-incorporated PAA(8:2)-g-PEG2000 micelles, nearly no other peak was found compared with that of the micelles without drug. The peaks at  $2\theta$  values of 19 and 23 did not change after the drug was incorporated, indicating that the crystalline structure of PEG layer was not disturbed. These results revealed that the MTX dispersed at the molecular level within the hydrophobic core of micelles.

**3.3. Reduction-Triggered Drug Release In Vitro.** The *in vitro* drug release behaviors of PAA-g-PEG micelles were carried out by dialysis against PBS buffered solution (pH 7.4, 10 mM) without DTT or containing 10 mM DTT, which was used as reductant to imitate the reducing environment in cancer cells. The MTX-release profiles of PAA(8:2)-g-PEG2000 and PAA(8:2)-g-PEG5000 in the absence and presence of DTT were shown in Figure 4. For an ideal nanoparticle drug delivery system, the drug release should be as less as possible before the nanoparticles arrived at the targeting cancer cells.

TABLE 2: Properties of the reduction-triggered breakable micelles.

| Series           | Micelle size (nm) <sup>a</sup> |             | CMC (mg/L) <sup>b</sup> | DLC (%) <sup>c</sup> | DLE (%) <sup>c</sup> |
|------------------|--------------------------------|-------------|-------------------------|----------------------|----------------------|
|                  | Without drug                   | Drug loaded |                         |                      |                      |
| PAA(8:2)-PEG2000 | 55                             | 73          | 4.5                     | 7.5                  | 82.5                 |
| PAA(7:3)-PEG2000 | 37                             | 56          | 20.1                    | 6.3                  | 69.3                 |
| PAA(6:4)-PEG2000 | 18                             | 38          | 52.3                    | 5.5                  | 60.5                 |
| PAA(8:2)-PEG5000 | 34                             | 42          | 9.4                     | 6.9                  | 75.9                 |
| PAA(7:3)-PEG5000 | 38                             | 61          | 27.2                    | 5.1                  | 56.1                 |
| PAA(6:4)-PEG5000 | 70                             | 98          | 44.0                    | 2.9                  | 31.9                 |

<sup>a</sup>Micelle sizes were measured by DLS.

<sup>b</sup>Measured using pyrene as a fluorescence probe.

<sup>c</sup>Measured by fluorescence measurement.

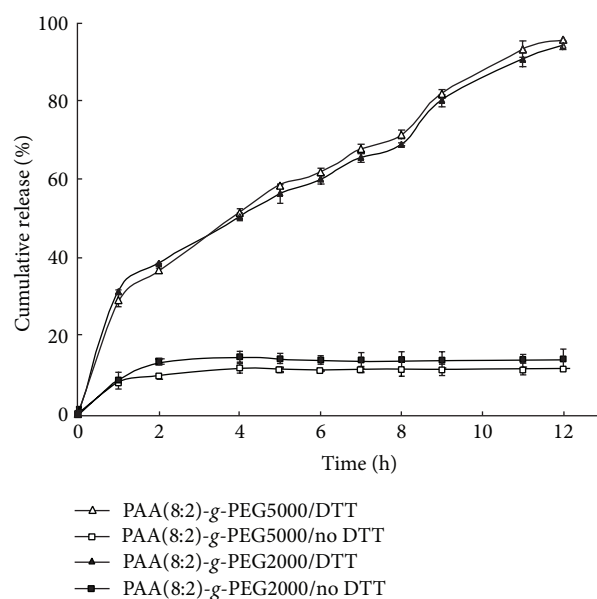


FIGURE 4: *In vitro* MTX release profiles of MTX-incorporated PAA(8:2)-g-PEG2000 and PAA(8:2)-g-PEG5000 micelles in PBS buffer solution (pH 7.4, 10 mM) at 37°C without DTT or containing 10 mM DTT.

However, small amount of drugs were unavoidably released in the neutral pH without the addition of reductive agent, which mimetic the physiological condition during the transfer process of micelles to the cancer cells. In the pH 7.4 PBS buffer solution without the existence of DTT, small amount of drug (about 10%) was released within the first 2 h. Thereafter, no tendency of further release was observed until 12 h. In a research of doxorubicin (DOX) encapsulated PEG-SS-PCL micelles, Zhong and coworkers reported that less than 20% of drug was released at neutral pH in 24 h [40]. The similar phenomenon was found in our prior reported work about DOX encapsulated PEG-g-PAA micelles [35]. Since MTX was an aromatic compound that was almost water insoluble, its hydrophobic nature and aromatic structure benefited its tight incorporation with the hydrophobic segment of the polymeric micelles and  $\pi$ - $\pi$  stacking with the phenyl of PAA in the micelle core. Therefore, the initial fast release within

2 h was ascribed to small amount of drugs adhered on micelle PEG shell. After these loosely adhered drugs were washed off, the tightly encapsulated MTX in the micelle core was hardly released in PBS buffer without reductant. This property was in favor of keeping most of the drug in the micelles and delivering to the tumor site.

Remarkably, the PAA-g-PEG micelles released MTX rapidly in the presence of 10 mM DTT, a reductive environment analogous to that of the intracellular compartments such as cytosol in the cancer cells. As it can be found in Figure 4, there was a relatively faster release at the first 1 hour. Then, the accumulative release of MTX raised gradually to near 100% in 12 h. Obviously, the acceleration of MTX release in the presence of DTT was resulted from the breakage of the micelle core due to the reduction-triggered cleavage of S-S bonds of the copolymer backbone [38]. It implied that the hydrophobic MTX was mainly entrapped in the hydrophobic cores of the micelles. As described above, the S-S bonds in the copolymer structure could be quickly reductively cleaved. Since the cleavage of the S-S bond in the hydrophobic segment would result in the lack of enough hydrophobic interaction of the core, the micelles could subsequently disassemble. The MTX incorporated in the core of the micelles then released along with the breakage of the micelle carriers.

This reduction-triggered breakage of micelles provided a useful releasing mechanism in cancer therapy in reducing side effect and enhancing tumor targeting. Because most MTX was incorporated in micelles core, the PEG shells might serve as a protective biological layer to improve micelle stability at normal physiological conditions (pH 7.4, without reductant) in preventing protein adsorption, elongating the circulation half-life in the blood stream, thus increasing the probability for tumor targeting through EPR effect. Once the micelles reached the tumor site, they might be internalized by cancer cells. The reductive intracellular environment might quickly break the S-S bond, resulting in the breakage of micelles and the fast release of the drug. This could be crucial for realizing the full therapeutic effect of MTX. Because the micelles were generally internalized by cells through the endocytotic pathway, MTX delivered by these nanoparticulate carriers were restricted within the endosome or lysosome [41–43]. The quick release of the MTX from the carriers thus provided the possibility for efficient endosome escape and enhanced its therapeutic effect. Therefore, this reduction-sensitive micelle might provide a promising approach for tumor targeting delivery of MTX.

**3.4. Antiproliferative Activity of MTX-Incorporated Micelles on Cancer Cell Lines.** The cytotoxicity of PEG-g-PAA micelles (without incorporation of MTX) was evaluated by coculturing different concentration of PAA(8:2)-g-PEG2000 micelles with L929 normal cells and HepG2, KB, 4T1 cancer cells. As shown in Figure 5, at low concentration (10  $\mu\text{g}/\text{mL}$ ), all the cells proliferated well, with exceeded 100% cell viability compared with the control group which was cultured without the addition of micelles. Increasing the micelle concentration resulted in little decrease of the cell viability. But the cells

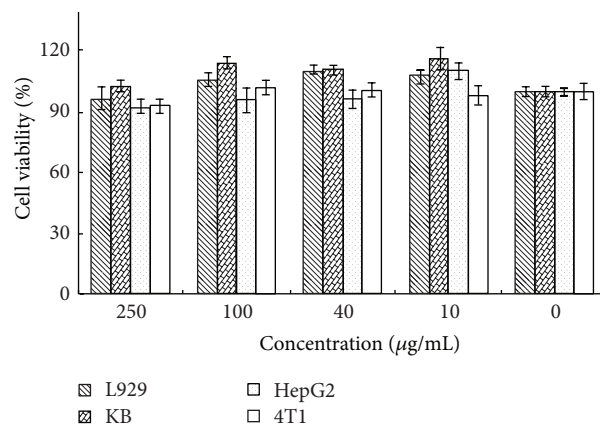


FIGURE 5: Biocompatibility assay of PAA(8:2)-g-PEG2000 micelles against L929, KB, HepG2, and 4T1 cells after incubation for 2 days. The standard deviation for each data point was averaged over five samples ( $n = 5$ ).

still proliferated well. Even at very high micelle concentration (250  $\mu\text{g}/\text{mL}$ ), all the cell viability could keep higher than 90%. These results indicated that the micelles did not show cytotoxicity against L929 normal cells and HepG2, KB, 4T1 cancer cells. Therefore, the copolymers were considered to have good biocompatibility.

The antiproliferative activities of the MTX-incorporated micelles on different cancer cell lines were evaluated by examining the cell viability using MTT assay after being cocultured with MTX-incorporated micelles or free MTX. In order to investigate the effects of micelles on different tumor cells, 4T1, KB, and HepG2 cancer cell lines were chosen for the cellular growth inhibition test. Because the life cycle of 4T1 cell is different from that of KB and HepG2 cancer cells, studies on HepG2 and KB cancer cells were over 72 h and on 4T1 cancer cell was over 48 h. The final MTX concentrations in the culture medium were adjusted varying from 0.01 to 20  $\mu\text{g}/\text{mL}$ , and the results of MTT assay were shown in Figure 6. Both MTX-incorporated micelles and free MTX were observed dose-dependent antiproliferative activities against the three cancer cell lines. Since the MTX was a cytotoxic anticancer drug, these antiproliferative activities obviously came from the cytotoxicity of MTX, because the micelles without the incorporation of MTX did not affect the growth of cells. The MTX-incorporated micelles and free MTX showed similar inhabitation effect on these cancer cells, with a little slightly higher cytotoxicity of the PAA(8:2)-g-PEG2000 MTX-incorporated micelles than that of MTX itself, and a little slightly lower cytotoxicity of the PAA(8:2)-g-PEG5000 MTX-incorporated micelles.

Interestingly, at low MTX concentration (<0.1  $\mu\text{g}/\text{mL}$ ), drug-loaded PAA(8:2)-g-PEG2000 micelles showed obviously stronger effect on killing cancer cells than pure MTX. But, with the increase of MTX concentration, the cytotoxicity of both the MTX-incorporated micelles and free MTX became nearly the same. The reason of these results might be due to the fact that, in the case of low MTX concentration, the internalization by the cancer cells of free MTX

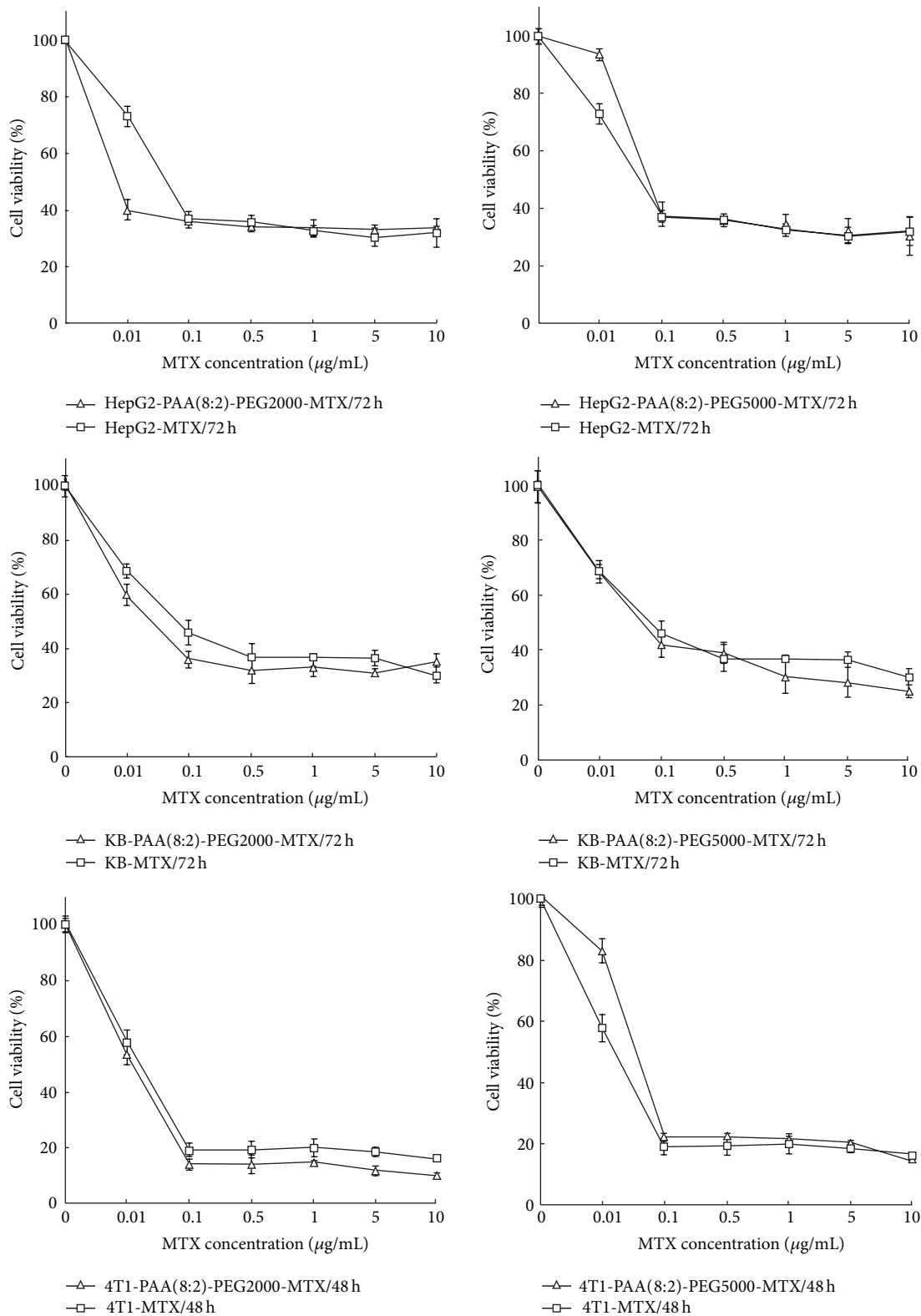


FIGURE 6: Antiproliferative activity of MTX-incorporated PAA(8:2)-g-PEG2000 micelles, PAA(8:2)-g-PEG5000 micelles, and free MTX on 4T1 after incubation for 2 days and KB and HepG2 cells after incubation for 3 days. The standard deviation for each data point was averaged over five samples ( $n = 5$ ).

through diffusion mechanism might not be efficient because of the lack of driving force; namely, the difference of MTX concentration with intracellular and extracellular was low. When the MTX-incorporated PAA(8:2)-*g*-PEG2000 micelles were applied on cancer cells, the increase of concentration of the total formulation might enhance the intracellular uptake of MTX and improve proliferation inhibition efficiency at low MTX concentration. In contrast, for the PAA(8:2)-*g*-PEG5000 micelles, since MPEG was exposed on the micelle surface in aqueous solution, the thick hydrophilic PEG layer might delay the uptake of micelles into the cells and more micelles might remain in the media. This fact might be one of the reasons for the slightly lower cytotoxicity of PAA(8:2)-*g*-PEG5000 MTX-incorporated micelles [44].

When the MTX concentration exceeded 0.5  $\mu\text{g}/\text{mL}$ , the cytotoxicity of both micelles and the free MTX became very close, indicating that the MTX-incorporated micelles possessed comparable antiproliferative activities. It is a common phenomenon that the anticancer drugs delivery by nanoparticulate systems showed lower cytotoxicity than the drugs themselves, due to the entrapment of the nanoparticles within the endosome or lysosome and the delayed liberation of drugs from the carriers. Therefore, many stimuli-sensitive carrier systems were investigated to improving the delivery performance by accelerating the drug release after the carriers reached the cancer cells. The reduction-triggered breakable micelles in this present research could enter the cells through an endocytic mechanism, release the drug quickly inside the cells, and deliver the drug to the acting site in cytosol or inside membrane-bound cellular organelles. Therefore, these MTX-incorporated micelles that were able to realize rapid intracellular drug release might provide an effective tool for promoting the growth inhibition effect on cancer cells, especially within the low drug concentration scope.

#### 4. Conclusion

Reduction-triggered breakable polymeric micelles incorporated with MTX were prepared using reductively breakable amphiphilic PAA-*g*-PEG copolymers. The micelles are spherical with diameters less than 70 nm. The shell-core structure of the micelles provided the properties to encapsulate the hydrophobic anticancer drug MTX in the hydrophobic core with DLC ranging from 2.9 to 7.5% and DLE 31.9 to 82.5%, which were highly dependent on the copolymer chemical structure. These micelles were capable of keeping stable and hold most MTX in the core in normal circumstance, whereas, in reductive environments that mimicked the intracellular compartments in the cancer cells, the entire drug payloads could be quickly released due to the reduction-triggered breakage of the micelles. Their antiproliferative activities on cancer cells were similar or slightly higher comparing with free MTX, especially within the low drug concentration scope.

#### Conflict of Interests

The authors declare that there is no conflict of interests regarding the publication of this paper.

#### Acknowledgment

This study was financially supported by the National Natural Science Foundation of China (Grant nos. 50973071 and 21174090).

#### References

- [1] S. Vezmar, A. Becker, U. Bode, and U. Jaehde, "Biochemical and clinical aspects of methotrexate neurotoxicity," *Chemotherapy*, vol. 49, no. 1-2, pp. 92–104, 2003.
- [2] F. M. Huennekens, "The methotrexate story: a paradigm for development of cancer chemotherapeutic agents," *Advances in Enzyme Regulation*, vol. 34, pp. 397–402, 1994.
- [3] D. Banerjee, P. Mayer-Kuckuk, G. Capioux, T. Budak-Alpdogan, R. Gorlick, and J. R. Bertino, "Novel aspects of resistance to drugs targeted to dihydrofolate reductase and thymidylate synthase," *Biochimica et Biophysica Acta, Molecular Basis of Disease*, vol. 1587, no. 2-3, pp. 164–173, 2002.
- [4] E. J. Estlin, "Continuing therapy for childhood acute lymphoblastic leukaemia: clinical and cellular pharmacology of methotrexate, 6-mercaptopurine and 6-thioguanine," *Cancer Treatment Reviews*, vol. 27, no. 6, pp. 351–363, 2001.
- [5] Y. Li and G. S. Kwon, "Micelle-like structures of poly(ethylene oxide)-block-poly(2-hydroxyethyl aspartamide)-methotrexate conjugates," *Colloids and Surfaces B: Biointerfaces*, vol. 16, no. 1-4, pp. 217–226, 1999.
- [6] J. A. Hubbell and A. Chilkoti, "Nanomaterials for drug delivery," *Science*, vol. 337, no. 6092, pp. 303–305, 2012.
- [7] N. Tang, G. Du, N. Wang, C. Liu, H. Hang, and W. Liang, "Improving penetration in tumors with nanoassemblies of phospholipids and doxorubicin," *Journal of the National Cancer Institute*, vol. 99, no. 13, pp. 1004–1015, 2007.
- [8] H. Cabral, Y. Matsumoto, K. Mizuno et al., "Accumulation of sub-100 nm polymeric micelles in poorly permeable tumours depends on size," *Nature Nanotechnology*, vol. 6, no. 12, pp. 815–823, 2011.
- [9] M. Sivasubramanian, Y. J. Kim, S. Y. Chae et al., "Thiolated glycol chitosan bearing- $\alpha$ -cyclodextrin for sustained delivery of PEGylated human growth hormone," *Journal of Biomaterials Science-Polymer Edition*, vol. 23, no. 15, pp. 1995–2005, 2013.
- [10] Y. Y. Wang, G. L. Wu, X. M. Li, Y. N. Wang, H. Gao, and J. B. Ma, "Synthesis, characterization and controlled drug release from temperatureresponsive poly(ether-urethane) particles based on PEG-diisocyanates and aliphatic diols," *Journal of Biomaterials Science-Polymer Edition*, vol. 24, no. 14, pp. 1676–1691, 2013.
- [11] C. L. Li, B. L. Wang, Y. J. Liu et al., "Synthesis and evaluation of star-shaped poly( $\epsilon$ -caprolactone)-poly(2-hydroxyethyl methacrylate) as potential anticancer drug delivery carriers," *Journal of Biomaterials Science-Polymer Edition*, vol. 24, pp. 741–757, 2013.
- [12] J. Fang, H. Nakamura, and H. Maeda, "The EPR effect: unique features of tumor blood vessels for drug delivery, factors involved, and limitations and augmentation of the effect," *Advanced Drug Delivery Reviews*, vol. 63, no. 3, pp. 136–151, 2011.

- [13] A. S. Mikhail and C. Allen, "Block copolymer micelles for delivery of cancer therapy: transport at the whole body, tissue and cellular levels," *Journal of Controlled Release*, vol. 138, no. 3, pp. 214–223, 2009.
- [14] J. Jingou, H. Shilei, L. Weiqi, W. Danjun, W. Tengfei, and X. Yi, "Preparation, characterization of hydrophilic and hydrophobic drug in combine loaded chitosan/cyclodextrin nanoparticles and *in vitro* release study," *Colloids and Surfaces B: Biointerfaces*, vol. 83, no. 1, pp. 103–107, 2011.
- [15] R. S. Dhanikula and P. Hildgen, "Influence of molecular architecture of polyether-co-polyester dendrimers on the encapsulation and release of methotrexate," *Biomaterials*, vol. 28, no. 20, pp. 3140–3152, 2007.
- [16] S. Natali and J. Mijovic, "Dendrimers as drug carriers: dynamics of PEGylated and methotrexate-loaded dendrimers in aqueous solution," *Macromolecules*, vol. 43, no. 6, pp. 3011–3017, 2010.
- [17] S. Gurdag, J. Khandare, S. Stapels, L. H. Matherly, and R. M. Kannan, "Activity of dendrimer-methotrexate conjugates on methotrexate-sensitive and -resistant cell lines," *Bioconjugate Chemistry*, vol. 17, no. 2, pp. 275–283, 2006.
- [18] L. Battaglia, L. Serpe, E. Muntoni, G. Zara, M. Trotta, and M. Gallarate, "Methotrexate-loaded SLNs prepared by coacervation technique: *in vitro* cytotoxicity and *in vivo* pharmacokinetics and biodistribution," *Nanomedicine*, vol. 6, no. 9, pp. 1561–1573, 2011.
- [19] B. Hoang, R. M. Reilly, and C. Allen, "Block copolymer micelles target auger electron radiotherapy to the nucleus of HER2-positive breast cancer cells," *Biomacromolecules*, vol. 13, no. 2, pp. 455–465, 2012.
- [20] H. Wei, X.-Z. Zhang, W.-Q. Chen, S.-X. Cheng, and R.-X. Zhuo, "Self-assembled thermosensitive micelles based on poly(L-lactide-star block-N-isopropylacrylamide) for drug delivery," *Journal of Biomedical Materials Research A*, vol. 83, no. 4, pp. 980–989, 2007.
- [21] N. Kohler, C. Sun, A. Fichtenholtz, J. Gunn, C. Fang, and M. Zhang, "Methotrexate-immobilized poly(ethylene glycol) magnetic nanoparticles for MR imaging and drug delivery," *Small*, vol. 2, no. 6, pp. 785–792, 2006.
- [22] J. M. Rosenholm, E. Peuhu, L. T. Bate-Eya, J. E. Eriksson, C. Sahlgren, and M. Lindén, "Cancer-cell-specific induction of apoptosis using mesoporous silica nanoparticles as drug-delivery vectors," *Small*, vol. 6, no. 11, pp. 1234–1241, 2010.
- [23] M. Nakayama, T. Okano, T. Miyazaki, F. Kohori, K. Sakai, and M. Yokoyama, "Molecular design of biodegradable polymeric micelles for temperature-responsive drug release," *Journal of Controlled Release*, vol. 115, no. 1, pp. 46–56, 2006.
- [24] H. J. Song, C. Su, W. Y. Cui et al., "Folic acid-chitosan conjugated nanoparticles for improving tumor-targeted drug delivery," *BioMed Research International*, vol. 2013, Article ID 723158, 6 pages, 2013.
- [25] J. Varshosaz, H. Sadeghi-aliabadi, S. Ghasemi, and B. Behdadfar, "Use of magnetic folate-dextran-retinoic acid micelles for dual targeting of doxorubicin in breast cancer," *BioMed Research International*, vol. 2013, 16 pages, 2013.
- [26] D. Schmaljohann, "Thermo- and pH-responsive polymers in drug delivery," *Advanced Drug Delivery Reviews*, vol. 58, no. 15, pp. 1655–1670, 2006.
- [27] N. Y. Hernández-Pedro, E. Rangel-López, R. Magaña-Maldonado et al., "Application of nanoparticles on diagnosis and therapy in gliomas," *BioMed Research International*, vol. 2013, Article ID 351031, 20 pages, 2013.
- [28] A. N. Koo, K. H. Min, H. J. Lee et al., "Tumor accumulation and antitumor efficacy of docetaxel-loaded core-shell-corona micelles with shell-specific redox-responsive cross-links," *Biomaterials*, vol. 33, no. 5, pp. 1489–1499, 2012.
- [29] K. Xiao, Y. Li, J. Luo et al., "The effect of surface charge on *in vivo* biodistribution of PEG-oligocholeic acid based micellar nanoparticles," *Biomaterials*, vol. 32, no. 13, pp. 3435–3446, 2011.
- [30] J.-H. Ryu, R. Roy, J. Ventura, and S. Thayumanavan, "Redox-sensitive disassembly of amphiphilic copolymer based micelles," *Langmuir*, vol. 26, no. 10, pp. 7086–7092, 2010.
- [31] B. Goldenbogen, N. Brodersen, A. Gramatica et al., "Reduction-sensitive liposomes from a multifunctional lipid conjugate and natural phospholipids: reduction and release kinetics and cellular uptake," *Langmuir*, vol. 27, no. 17, pp. 10820–10829, 2011.
- [32] S. Cerritelli, D. Velluto, and J. A. Hubbell, "PEG-SS-PPS: Reduction-sensitive disulfide block copolymer vesicles for intracellular drug delivery," *Biomacromolecules*, vol. 8, no. 6, pp. 1966–1972, 2007.
- [33] S. Matsumoto, R. J. Christie, N. Nishiyama et al., "Environment-responsive block copolymer micelles with a disulfide cross-linked core for enhanced siRNA delivery," *Biomacromolecules*, vol. 10, no. 1, pp. 119–127, 2009.
- [34] H. Li, J. Yang, X. Hu, J. Liang, Y. Fan, and X. Zhang, "Super-absorbent polysaccharide hydrogels based on pullulan derivate as antibacterial release wound dressing," *Journal of Biomedical Materials Research A*, vol. 98, no. 1, pp. 31–39, 2011.
- [35] Y. Sun, X. Yan, T. Yuan et al., "Disassemblable micelles based on reduction-degradable amphiphilic graft copolymers for intracellular delivery of doxorubicin," *Biomaterials*, vol. 31, no. 27, pp. 7124–7131, 2010.
- [36] Y. Sun, W. Zou, S. Q. Bian et al., "Bioreducible PAA-g-PEG graft micelles with high doxorubicin loading for targeted antitumor effect against mouse breast carcinoma," *Biomaterials*, vol. 34, no. 28, pp. 6818–6828, 2013.
- [37] J. Ji, D. Wu, L. Liu, J. Chen, and Y. Xu, "Preparation, evaluation, and *in vitro* release of folic acid conjugated O-carboxymethyl chitosan nanoparticles loaded with methotrexate," *Journal of Applied Polymer Science*, vol. 125, no. 2, pp. E208–E215, 2012.
- [38] Y. Sun, Y. H. Huang, S. Q. Bian, J. Liang, Y. J. Fan, and X. D. Zhang, "Reduction-degradable PEG-b-PAA-b-PEG triblock copolymer micelles incorporated with MTX for cancer chemotherapy," *Colloids and Surfaces B: Biointerfaces*, vol. 112, pp. 197–203, 2013.
- [39] S. K. Hobbs, W. L. Monsky, F. Yuan et al., "Regulation of transport pathways in tumor vessels: role of tumor type and microenvironment," *Proceedings of the National Academy of Sciences of the United States of America*, vol. 95, no. 8, pp. 4607–4612, 1998.
- [40] H. Sun, B. Guo, R. Cheng, F. Meng, H. Liu, and Z. Zhong, "Biodegradable micelles with sheddable poly(ethylene glycol) shells for triggered intracellular release of doxorubicin," *Biomaterials*, vol. 30, no. 31, pp. 6358–6366, 2009.
- [41] M. L. Adams, A. Lavasanifar, and G. S. Kwon, "Amphiphilic block copolymers for drug delivery," *Journal of Pharmaceutical Sciences*, vol. 92, no. 7, pp. 1343–1355, 2003.
- [42] R. Savić, A. Eisenberg, and D. Maysinger, "Block copolymer micelles as delivery vehicles of hydrophobic drugs: micelle-cell interactions," *Journal of Drug Targeting*, vol. 14, no. 6, pp. 343–355, 2006.

- [43] K. Kataoka, A. Harada, and Y. Nagasaki, "Block copolymer micelles for drug delivery: design, characterization and biological significance," *Advanced Drug Delivery Reviews*, vol. 47, no. 1, pp. 113–131, 2001.
- [44] Y. Hu, J. Xie, Y. W. Tong, and C.-H. Wang, "Effect of PEG conformation and particle size on the cellular uptake efficiency of nanoparticles with the HepG2 cells," *Journal of Controlled Release*, vol. 118, no. 1, pp. 7–17, 2007.

## Research Article

# The Morphology and Functions of Articular Chondrocytes on a Honeycomb-Patterned Surface

Joshua O. Eniwumide,<sup>1</sup> Masaru Tanaka,<sup>2,3</sup> Nobuhiro Nagai,<sup>2</sup>  
Yuka Morita,<sup>2</sup> Joost de Bruijn,<sup>4</sup> Sadaaki Yamamoto,<sup>2</sup> Shin Onodera,<sup>5</sup> Eiji Kondo,<sup>5</sup>  
Kazunori Yasuda,<sup>5</sup> and Masatsugu Shimomura<sup>2,6</sup>

<sup>1</sup> Institute of Multidisciplinary Research for Advanced Materials, Tohoku University, 2-1-1. Katahira, Aoba-ku, Sendai 980-8577, Japan

<sup>2</sup> Creative Research Initiative "Sousei" (CRIS), Hokkaido University, N21 W10 Kita-ku, Sapporo 001-0021, Japan

<sup>3</sup> Department of Biochemical Engineering, Graduate School of Science and Engineering, Yamagata University, 4-3-16 Jonan, Yonezawa 992-8510, Japan

<sup>4</sup> School of Engineering and Materials Sciences, Queen Mary University of London, London E1 4NS, UK

<sup>5</sup> Department of Sports Medicine and Joint Reconstruction Surgery, Hokkaido University School of Medicine, Kita-15 Nishi-7 Kita-ku, Sapporo 060-8638, Japan

<sup>6</sup> World Premier International Research Center Advanced Institute for Materials Research (WPI-AIMR), Tohoku University, Katahira 2-1-1, Sendai 980-8577, Japan

Correspondence should be addressed to Joshua O. Eniwumide; [joshuaeniwumide@hotmail.com](mailto:joshuaeniwumide@hotmail.com) and Masaru Tanaka; [tanaka@yz.yamagata-u.ac.jp](mailto:tanaka@yz.yamagata-u.ac.jp)

Received 13 January 2014; Accepted 7 March 2014; Published 6 April 2014

Academic Editor: Inn-Kyu Kang

Copyright © 2014 Joshua O. Eniwumide et al. This is an open access article distributed under the Creative Commons Attribution License, which permits unrestricted use, distribution, and reproduction in any medium, provided the original work is properly cited.

The present study investigated the potential of a novel micropatterned substrate for neocartilage formation. Articular chondrocytes were cultured on poly( $\epsilon$ -caprolactone) materials whose surfaces were either flat or honeycomb-patterned. The latter was prepared using a novel self-organization technique, while the former, was prepared by spin-coating. The chondrocytes attached and proliferated on both surfaces. On the honeycomb films, chondrocytes were found at the top surface and encased within the 10  $\mu\text{m}$  pores. Meanwhile, chondrocytes on the spin-coated surface flattened out. Accumulation of DNA and keratin sulphate was comparatively higher on the honeycomb films within the first 7 days. At their respective peaks, DNA concentration increased on the honeycomb and flat surfaces by approximately 210% and 400% of their day 1 values, respectively. However, cultures on the flat surface took longer to peak. Extracellular Matrix (ECM) concentrations peaked at 900% and 320% increases for the honeycomb and flat cultures. Type II collagen was upregulated on the honeycomb and flat surfaces by as much as 28% and 25% of their day 1 values, while aggrecan was downregulated with time, by 3.4% and 7.4%. These initial results demonstrate the potential usefulness of honeycomb-based scaffolds during early cultures neocartilage and soft tissue engineering.

## 1. Introduction

A topical approach to addressing diseased or damaged joint tissues combines cells, often autologous, with either biological or artificial scaffold [1]. The scaffolds function as carriers of the cells [2–5], retaining them at the defect site. In addition to giving structural support and some mechanical integrity, the scaffolds are required to encourage the cells to multiply and produce new ECM. Therefore, the cells must interact with

the scaffold, usually by attaching, multiplying, and possibly forming neotissue. In the case of articular cartilage, the cell-material interactions are complicated by the necessity to maintain their rounded morphology [6]. Failure to achieve this may result in their dedifferentiation, changing their pattern of gene expression from chondrocyte-specific to one resembling fibroblastic or chondroprogenitor-like cells. These are associated with the production of type I collagen and nonaggregating glycosaminoglycan (GAG) [7–9]. This

morphology and, indeed, the phenotype are successfully maintained by seeding the cells within hydrogels such as agarose and alginate [10, 11]. However, the pore sizes inside these hydrogels may be as little as 2–500 nm for alginate, and up to 500 nm for agarose, depending on their concentrations [12, 13]. In both cases, this results in nutrient deprivation and death of cells at the centre of constructs, thicker than 1 mm [14]. Therefore, there is an ongoing search for ideal scaffold materials, which support chondrocyte proliferation, allow sufficient transport of oxygen and nutrients to cells at all regions and efficient waste removal, maintain their phenotypic functions, and degrade at a rate synchronised with neotissue formation. On this topic, we have reported that honeycomb-patterned porous polymer films (honeycomb films) can be prepared by casting polymers, dissolved in a water-immiscible solvent under high humidity [15, 16]. This technology was adapted for biological applications. Specifically, the morphology and hence the functionality of hepatocytes [17, 18], cardiac myocytes [19], neural progenitor cells [20, 21], and endothelial cells [22] were all manipulated by altering the size and shape of the micropores of the honeycomb films. More recently, bone formation has been found to be enhanced on honeycombed surfaces [23], as well as sustaining the adiponectin secretion by mesenteric-visceral adipocytes over extended culture periods [24]. Chondrocytes have been cultured on several micropatterned surfaces, for an enhanced proliferation compared with nonpatterned surfaces of the same materials [25, 26]. However, maintaining the chondrocytes phenotypes on such surfaces is still a challenge.

In the present study, we observe the behaviour of articular chondrocytes on honeycomb-patterned films. The purposely designed surfaces had highly regular pores, interconnected and 10  $\mu\text{m}$  in diameter. The attachment and changes to their morphology over time were monitored. In addition, the organisation of their cytoskeleton on the honeycomb films was visualised. Their survival and proliferation on the honeycomb films were compared with those on flat nonpatterned substrate derived from the same polymeric materials. Additionally, the accumulation of ECM proteins on the two surfaces was quantified. Finally, we assess the ability of the honeycomb films to maintain the cells phenotype over a prolonged culture period.

## 2. Materials and Methods

**2.1. Film Preparation.** Honeycomb (HC) films were prepared from biodegradable polymers poly( $\epsilon$ -caprolactone) (PCL; MW = 70,000–100,000) and a copolymer of N-dodecylacrylamide and  $\omega$ -carboxyethyl acrylamide (Cap; MW = 22,000). Cap served as an emulsifier as described in a previous study [15]. Briefly, PCL and Cap (10:1 wt%) were dissolved in chloroform at a concentration of 5 g/L. The polymer solution was poured into a round glass dish (9.3 cm in diameter), containing polyethylene terephthalate (PET) discs. The discs, which were 14 mm in diameter, were completely immersed in the polymer solution, while humid air (23%  $\pm$  2%) was blown on their surface, at 1.0 L/min. This resulted in films with a 10  $\mu\text{m}$  pore diameter. Alternatively,

0.5 mL of the polymer solution was transferred onto the PET discs dropwise using a pipette. The discs, with the polymer layer, were spun at 1000 rpm for 30 seconds using a spin coater (IH-7D, Mikasa). The resulting specimens contained a flat geometry and hence were termed as *flat films*. These were used as the control groups in comparative studies. Prior to cell culture, both groups of films were immersed in 1-propanol for 12 min to remove the Cap on the surface of the honeycomb films and subsequently sterilised by washing 3 times in pure ethanol and 3 times in sterile, deionised water. This washing procedure was followed by 2–3 hours of exposure to ultraviolet light.

**2.2. Cell Isolation and Culture.** Articular chondrocytes were obtained from 8–10-week Japanese white rabbits. The rabbits, purchased from a local abattoir, were sacrificed using 10 mL injection of 2.5 g/100 mL of Phenobarbiturate (Dainippon, Sumitomo Pharma, Japan). Slices of full thickness cartilage were removed from the rabbits articulating joints, namely, the humeral and femoral heads, and the femoral condyles, using a sterile scalpel, immediately after sacrifice. The explants were kept immersed in a Petri dish containing PBS (Takara Bio, Tokyo, Japan) to maintain hydration. Once all the explants had been removed, the EBSS was aspirated, and the cartilage explants were finely diced using a sterile scalpel. The diced explants were transferred into a 50 mL conical tube, to which 50  $\mu\text{g}$  trypsin dissolved in 10 mL of DMEM supplemented with 10% FCS (Thermo Trace, Australia) solution was added. The falcon tube, containing the explants in trypsin, was incubated in a shaking water-bath at 37°C for 30 minutes. After this time, the trypsin was aspirated and replaced with a solution containing 50  $\mu\text{g}$  of collagenase, dissolved in 50 mL of DMEM (10% FCS). These were incubated in the water-bath at 37°C for 5 hours. The resulting suspension was filtered through a 70  $\mu\text{m}$  sterile cell sieve (BD Biosciences, MA, USA) and centrifuged at 720 g for 5 minutes. The supernatant was aspirated and the cells were washed with DMEM (Invitrogen, Tokyo, Japan) supplemented with 10% FCS (Thermo Trace, Australia) three times. Following this, the cells were expanded in monolayer, by incubation in DMEM, supplemented with 10% FBS at 37°C and 5% CO<sub>2</sub> for 7 days. The cells were subsequently trypsinised and washed 3 times in serum-supplemented DMEM. After the third wash, the cells were resuspended in 10 mL of DMEM supplemented with 10% FBS (Thermo Trace, Australia) and loaded onto either the flat or honeycomb-patterned films at a concentration of  $10 \times 10^4$  cells per disc.

The cell-seeded PCL films were transferred to individual wells of 24-well plates (IWAKI, Tokyo, Japan) and cultured in DMEM (supplemented with 10% FCS) for up to 14 days, while samples were obtained at 1, 3, and 7 days.

**2.3. Scanning Electron Microscopy.** Following their culture, samples were dehydrated at 6, 24, and 72 hours by washing in increasing concentrations of ethanol and subsequently dried using a critical point dryer (HCP-2, Hitachi). The dried samples were mounted on aluminium stages, with a double-sided adhesive tape, and coated with a 5 nm layer of palladium

TABLE 1: List of primers used in real-time PCR.

| Primer ID     | Primers (5'-3')                   | Expect size (bp) | Accession number |
|---------------|-----------------------------------|------------------|------------------|
| Collagen II-F | GAC CATC AAT GGC GGC TTC          | 139              | D83228.1         |
| Collagen II-R | CAC GCT GTT CTT GCA GTG GTAG      |                  |                  |
| Aggrecan-F    | GCT ACG ACG CCA TCT GCT AC        | 94               | L38480.1         |
| Aggrecan-R    | GTC TGG ACC GTG ATG TCC TC        |                  |                  |
| Collagen I-F  | GTT CTC AGG GTA GCC AAG GTC       | 105              | D49399.1         |
| Collagen I-R  | AGT CTC CAT CAT AAC CAA AGT CGT A |                  |                  |
| GAPDH-F       | CCC TCA ATG ACC ACT TTG TGA A     | 93               | L23961.1         |
| GAPDH-R       | AGG CCA TGT GGA CCA TGAG          |                  |                  |

gold, using an ion sputter coater (E-1030, Hitachi). These samples were observed using a scanning electron microscope (SEM; S-3500N, Hitachi).

**2.4. Cytoskeletal Staining and Confocal Laser Scanning Microscopy.** Alternatively, samples were transferred to separate multiwell plates. These were then fixed with 3.7% (v/v) formaldehyde for 10 minutes at room temperature and then washed 3 times with PBS. The samples were permeabilised for 15 min with 0.1% Triton X-100 (MP Biomedicals, Eschwege, Germany) and 1.0% bovine serum albumin (Sigma) in PBS. After rinsing twice with PBS, the cells were stained by incubating for 60 minutes with 0.03% (v/v) rhodamine-phalloidin (Molecular Probes, Eugene, OR) in PBS and 6.7% (v/v) of 4',6-diamidino-2-phenylindole (Dapi; Molecular Probes, Carlsbad, CA) at room temperature. The stained cells were then rinsed and analyzed using the confocal laser scanning microscope (FV-300, Olympus, Tokyo, Japan). The cell nucleus was observed at the excitation and emission wavelengths of 355 nm and 460 nm, respectively, while their actin fibres were observed at the excitation and emission wavelengths of 554 nm and 573 nm, respectively.

**2.5. DNA.** Cultured samples were obtained at predetermined time points. The cells were lysed by vortexing the individual discs in a falcon tube containing 1 mL of a lysate solution, containing 0.5% (v/v) Triton X-100, 150 mM NaCl, and 10 mM HEPES. DNA concentrations within the digested samples were measured using the Quant-Ti, PicoGreen kit (Invitrogen, Tokyo Japan). The commercially available assay, designed to measure double-stranded DNA, was used as directed by the manufacturer's instructions. However briefly, 0.5% (v/v) of the PicoGreen solution was dissolved in the accompanying buffer solution (10 nM Tris-HCL, 1 mM EDTA, pH 7.5). Standard DNA solutions were prepared by mixing Lambda double-stranded DNA in the buffer solution to achieve concentrations of 2000, 200, 20, 2, and 0.2 ng/mL. One hundred microlitres of the standard solutions and the extracted samples were transferred into separate wells of a 96-well plate (Costar, NY, USA) using a pipette. To each well, 100  $\mu$ L of the PicoGreen solution was added. Fluorescence emission was measured using a commercially available fluorimetry apparatus (TECAN, Tokyo, Japan) at the excitation and emission wavelengths of 485 nm and 535 nm, respectively.

**2.6. ECM.** The samples that were obtained and lysed for DNA measurements were also analyzed for ECM components using the commercially available Keratan Sulphate (KS) [27] ELISA kit (Seikagaku Corporation, Tokyo, Japan). The immunoassay method, which is based on a sandwich of enzymes and a monoclonal antibody specific to KS, was carried out as directed by the manufacturers. However, briefly standard solutions of KS were prepared by diluting the 80 ng/mL of KS with the provided sample diluent to make 40, 20, 10, 5, and 2.5 ng/mL. The sample diluents functioned as blank solution (0 ng/mL). The standard solutions and all reagents and samples were brought to  $21 \pm 1^\circ\text{C}$  prior to experimentation.

Each well of a 96-well plate (provided) was washed 4 times with 200  $\mu$ L of the washing solution (provided). Fifty microlitres of the KS standard solutions (and blank) and the experimental samples were transferred into individual wells of the 96-well plate, sealed (with provided cover film), and incubated for 60 minutes at  $37^\circ\text{C}$ . The reactants were removed, and each well was washed 4 times with 200  $\mu$ L of the wash solution. Twenty-five microlitres of Horseradish peroxidase-conjugated streptavidin solution and biotinylated antibody solution were added and mixed gently inside each well. This solution was sealed and incubated for 60 minutes at  $37^\circ\text{C}$ . After the incubation period, the reaction solution was removed and each well was washed 4 times with 200  $\mu$ L of the washing solution. Fifty microlitres of the substrate solution (supplied assay kit) was pipetted into each well, sealed, and incubated in the dark, at  $21 \pm 1^\circ\text{C}$ . After 10 minutes of incubation, 50  $\mu$ L of stop solution was added into each well and mixed gently. The absorbance was measured at 450 nm using a microplate reader (Bio-Rad, Tokyo, Japan).

**2.7. Gene Expression.** Total RNA of cultured chondrocytes at each time point was extracted using TRI reagent (Invitrogen, Tokyo, Japan) to evaluate the changes in their gene expression during cell culture. Total RNA was extracted according to the manufacturer's instructions. Yield and purity of the extracted RNA were determined using the spectrophotometer (Smart-spec Plus; Bio-Rad, Hercules, CA, USA).

All oligonucleotide primer sets were designed based upon the published mRNA sequence. The expected amplicon lengths ranged from 93 bp to 139 bp. Oligonucleotide primers used in this study are listed in Table 1. Real-time PCR was performed in Thermal Cycler Dice TP800 (Takara, Japan), using SYBR Premix Ex Taq (Takara, Japan). One microliter

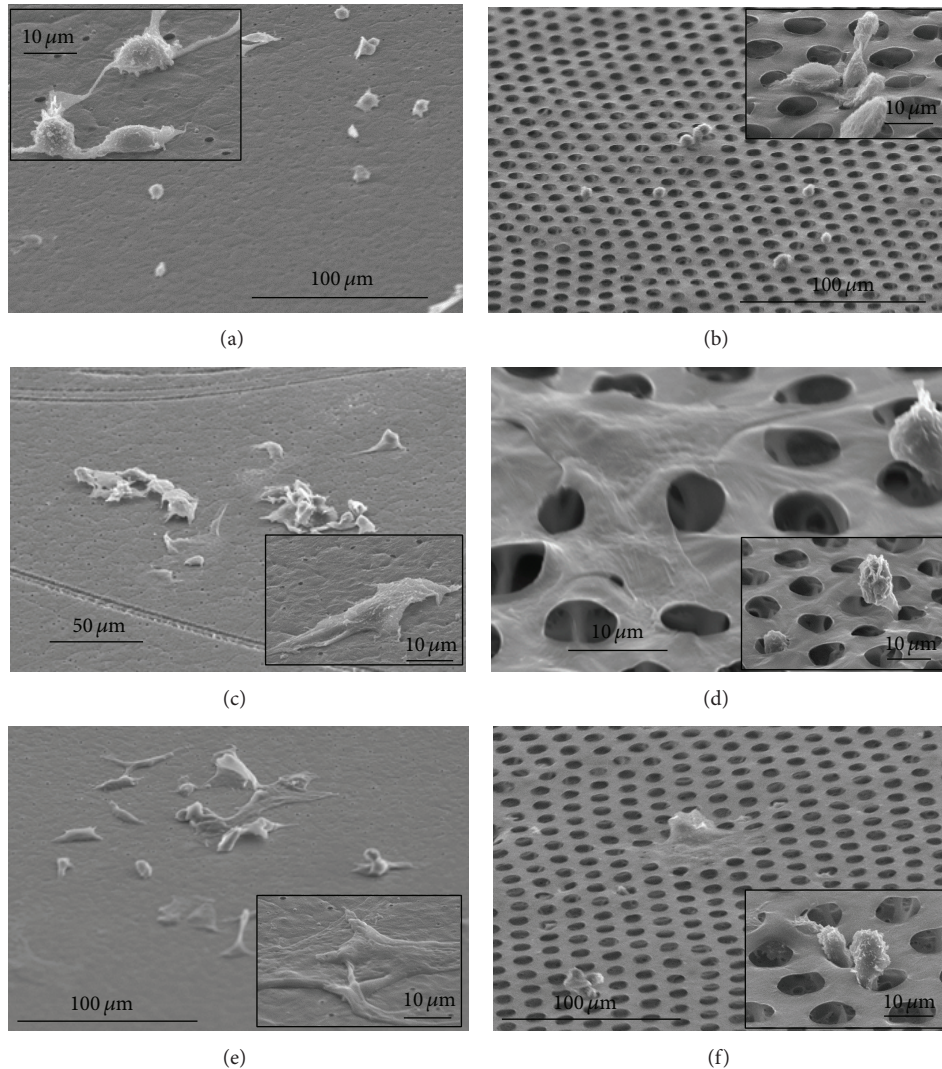


FIGURE 1: Representative scanning electron micrographs of articular chondrocytes, cultured on flat ((a), (c), and (e)) and honeycomb films ((b), (d), and (f)) for 6 ((a), (b)), 24 ((c), (d)), and 72 ((e), (f)) hours.

of cDNA template was used for real-time PCR in a final volume of  $25\ \mu\text{L}$ . cDNA was amplified according to the following condition:  $95^\circ\text{C}$  for 5 s and  $60^\circ\text{C}$  for 30 s at 40 amplification cycles. Changes to their fluorescence were monitored with SYBR Green after every cycle. A dissociation curve analysis was performed ( $0.5^\circ\text{C}/\text{s}$  increase from 60 to  $95^\circ\text{C}$  with continuous fluorescence readings) at the end of cycles to ensure that single PCR products were obtained. The amplicon size and reaction specificity were confirmed by 2.5% agarose gel electrophoresis. All reactions were repeated in 4 separate PCR runs, using RNA isolated from 12 samples per time point, for both the honeycomb and flat films. The results were evaluated using the Thermal Cycler Dice Real Time System software program. Glyceraldehyde-3-phosphate dehydrogenase (GAPDH) primers were used to normalize the samples.

**2.8. Data Analysis.** Numerical data were evaluated by analysis of variance using a commercially available statistical

software package. A statistical significance was deduced when the  $P$  value is less than 0.05.

### 3. Results

**3.1. Cell Attachment.** Early morphological changes to the chondrocytes on both the flat and honeycomb films were observed using scanning electron microscopy. The micrographs in Figures 1(a) and 1(b) show the distribution and morphology of chondrocytes after 6 hours of culture on both the flat and HC films. Observably, the cells on both films were morphologically rounded. While the cells demonstrated very little spreading, some cell-cell interactions were observed by those within close proximity on the flat film. Cells on the HC, however, either had processes which extended inside or were physically encapsulated within the pores. By 24 hours, more cells may be observed on the films. Although not completely flattened, some of the cells on the flat film had begun adopting a different morphology (Figure 1(c)), taking

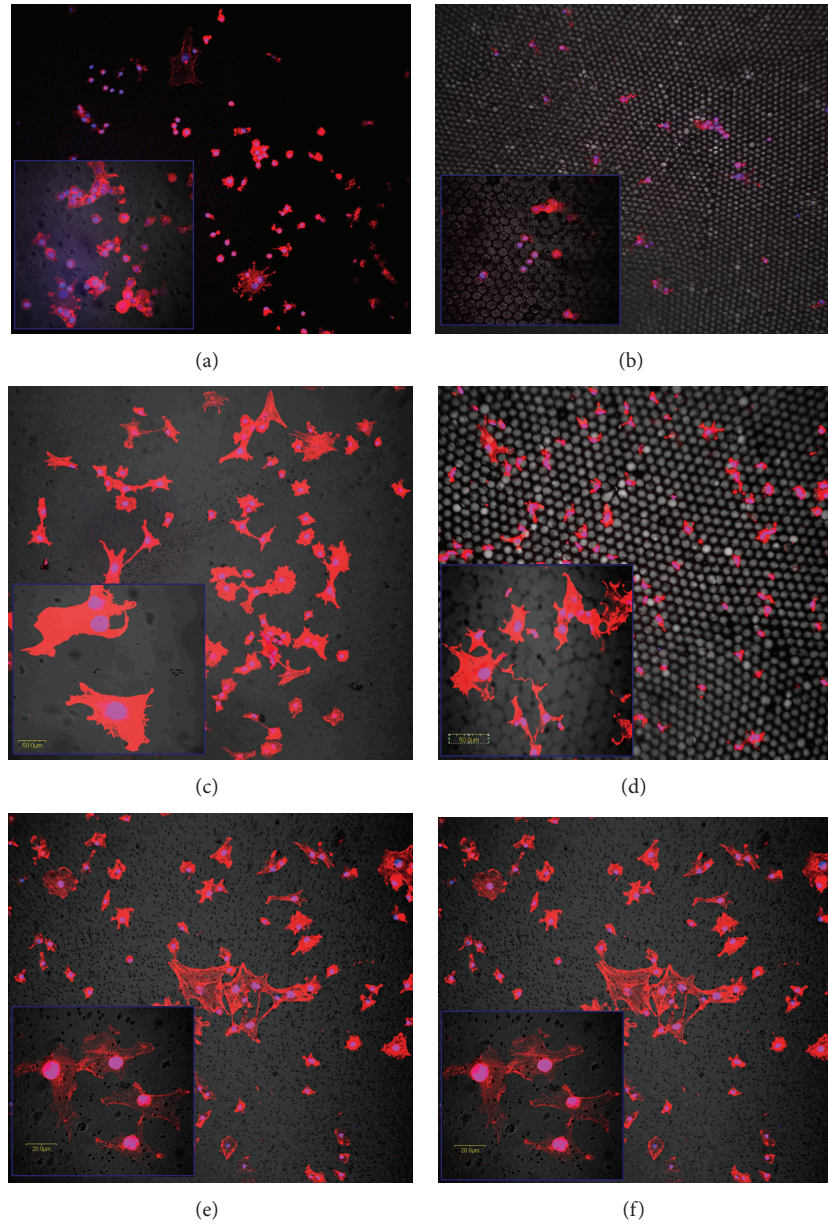


FIGURE 2: Low and high magnification confocal images of chondrocytes whose nuclei and cytoskeletal fibres were stained following 6 ((a), (b)), 24 ((c), (d)), and 72 ((e), (f)) hours of culture on either flat ((a), (c), and (e)) or honeycomb ((b), (d), and (f)) films.

over a larger area on the films. At the same time, chondrocytes on the honeycomb films were either completely flattened, covering areas of several pore sizes, or still rounded, with processes inside the pores (Figure 1(d)). At 72 hours, cells cultured on the flat films (Figure 1(c)) appeared relatively flatter than earlier time points observed. However, some cells, particularly on the honeycomb films, maintained their rounded morphology. Despite this, chondrocytes had begun to spread over the honeycomb films, covering several adjacent micropores (Figure 1(f)).

**3.2. Cytoskeletal Organisation.** The dual confocal images in Figure 2 show the cell nucleus (blue) and their cytoskeletal

actin fibres (red) following 6, 24, and 72 hours of culture. Collectively, these confocal images suggest an increased cell number over the 72-hour period. Additionally, the increasing surface area taken up by the cells actin network is indicative of their spreading. At 6 hours, the area covered by the actin fibres on either the flat or patterned films was not much bigger than that of the cell nucleus (Figures 2(a) and 2(b)). There were some exceptions, whereby, individual cells had produced and organised a relatively high amount of actin fibres. However, these were only associated with cells on the flat films. The micrographs corresponding to 24 hours showed that most of the cells were beginning to develop their cytoskeleton. However, greater extent of actin formation was

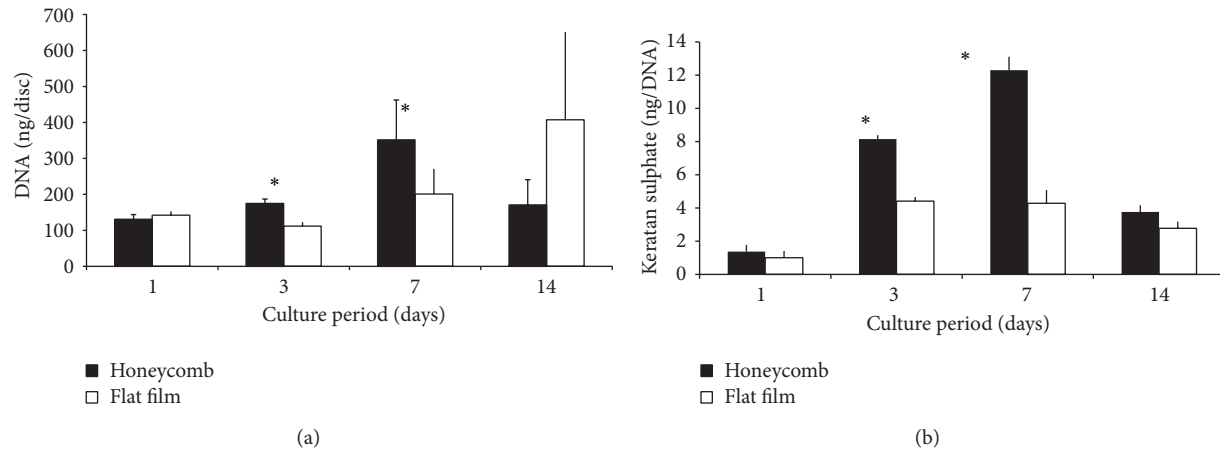


FIGURE 3: Graphs show (a) DNA and (b) keratin sulphate concentrations measured on honeycomb and flat films over the 14-day culture period. Data represents mean and standard deviations of 3–6 discs per sampled time point \* $P < 0.05$ .

observed by cells on the flat film (Figure 2(c)), compared with those on the honeycomb films (Figure 2(d)). In addition, the cells on the flat films had begun to form small clusters, consisting of 4–6 cells. This trend continued till 72 hours, where most cells on the flat films (Figure 2(e)) exhibited a relatively well-organised cytoskeleton compared to those on the honeycomb films (Figure 2(f)). Despite cell spreading being highest at 72 hours, a large proportion of cells still had less pronounced actin fibres. Moreover, the size differences between their nuclei and their network of actin fibres were not significantly different from those of cells imaged after 6 hours of culture. These cells were more prevalent on the honeycomb films.

**3.3. DNA and GAG Concentrations.** The concentrations of DNA and keratan sulphate retained on the films are summarised in Figure 3. For both the flat and HC films, the DNA concentration increased steadily over the 14 days. The peak DNA increase on the HC films occurred on day 7. The value was 200% of the day 1 value. Thereafter, DNA was reduced at day 14. By contrast, DNA concentration on the flat films peaked on day 14, with a 400% increase from the day 1 value.

Figure 3(b) shows keratan sulphate retained on the films, normalised to DNA concentration, over the 14-day culture period. The graph demonstrated steady increases with culture time. Evidently, keratin sulphate concentrations were higher on the honeycomb films at every time point than on those associated with the flat films. Accordingly, the biggest and most significant differences were at days 3 and 7. Keratin sulphate values for the HC and flat films peaked on day 7, after which they reduced from 12 and 6 ng/disk, respectively, to 4 and 3 ng/disk, which represents approximately 400% and 300% of their respective day 1 values.

**3.4. Gene Expression.** The expression of mRNA for aggrecan and type II collagen, relative to GAPDH, are presented in Figure 4. It is clearly demonstrated that the relative expressions of neither the type II collagen nor the aggrecan differed between the flat and honeycomb films. Accordingly,

aggrecan expression was always lower than that of type II collagen, irrespective of surface topography. Furthermore, the expression of type II collagen increased over the 14 days, while that of aggrecan appeared to have decreased slightly (ns). Figure 4(b) describes the temporal changes to these relative expressions at 3, 7, and 14 days. These were obtained by normalizing the corresponding time points to day 1 values to obtain the percentage differences. It may be observed that there was approximately 10% upregulation of type II collagen on both films, at days 3 and 7. By 14 days, this rose to approximately 25% of the day 1 values, with insignificant differences between cells on the honeycomb films and the flat films. By contrast, expression for aggrecan by cells on flat film was downregulated over the culture period. A peak downregulation of 7.4% was observed at day 3. However, by day 14, the reduction had reduced to approximately 2.9% of their day 1 values. With regard to cells on honeycomb films, there was an initial upregulation of 3.4%. However, by 14 days, aggrecan expression had reduced only by a mere 0.6% of its day 1 value.

The graphs in Figure 5 show the relative expression of type I collagen and the temporal changes to its expression on both films. A significant level of type I collagen, relative to GAPDH, was achieved on both films, from as early as day 1. Although not surpassing GAPDH, the expression for type I collagen increased steadily over the remaining culture period. The up-regulation of type I collagen increased from approximately 2.5% at day 3 on both film, to 14% and 17% on the flat and honeycomb films, respectively, at day 14. Interestingly, the upregulation type I collagen was higher on flat films than honeycomb at day 7, with their normalised values being 8.4% and 3.6%, respectively.

## 4. Discussion

The present study examined the behaviour of articular chondrocytes on HC films prepared using a novel self-organization method. At first, it was useful to determine whether the micropatterned surface was suitable for the

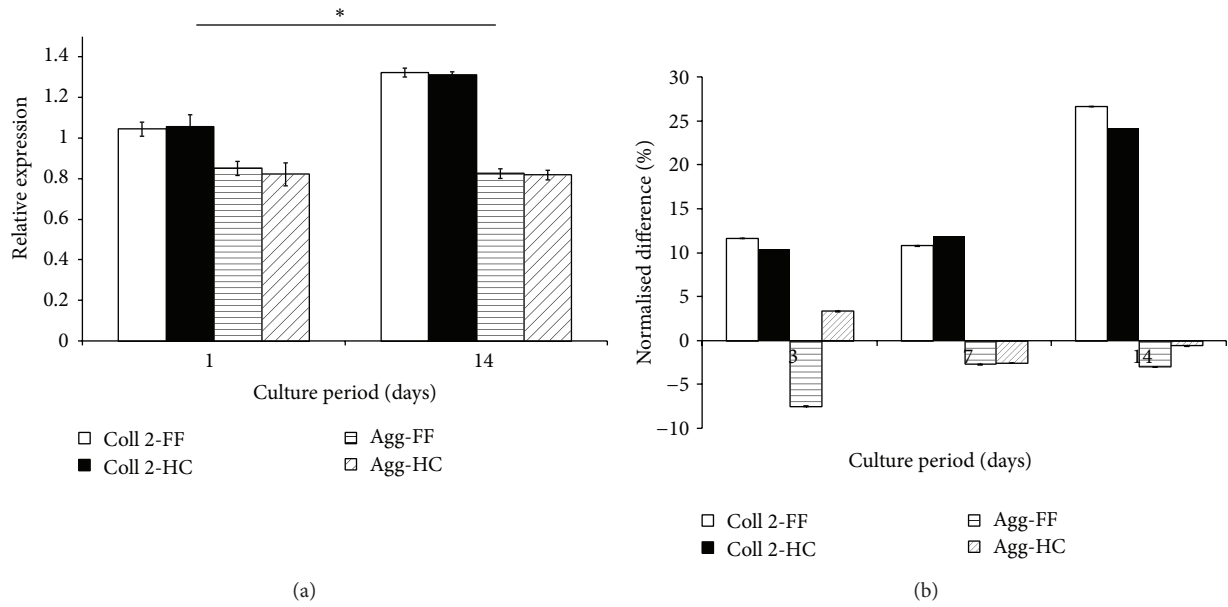


FIGURE 4: Graphs show (a) the expressions (relative to that of GAPDH) of collagen type 2 (Coll 2) and Aggrecan (Agg) after 1 and 14 days of culture on either the honeycomb (CH) or the flat (FF) films. Normalised to their day 1 values, (b) shows the temporal changes to their expression levels at days 3, 7, and 14, in terms of percentage difference. Data represents mean and standard deviations of 12 discs per sampled time point.

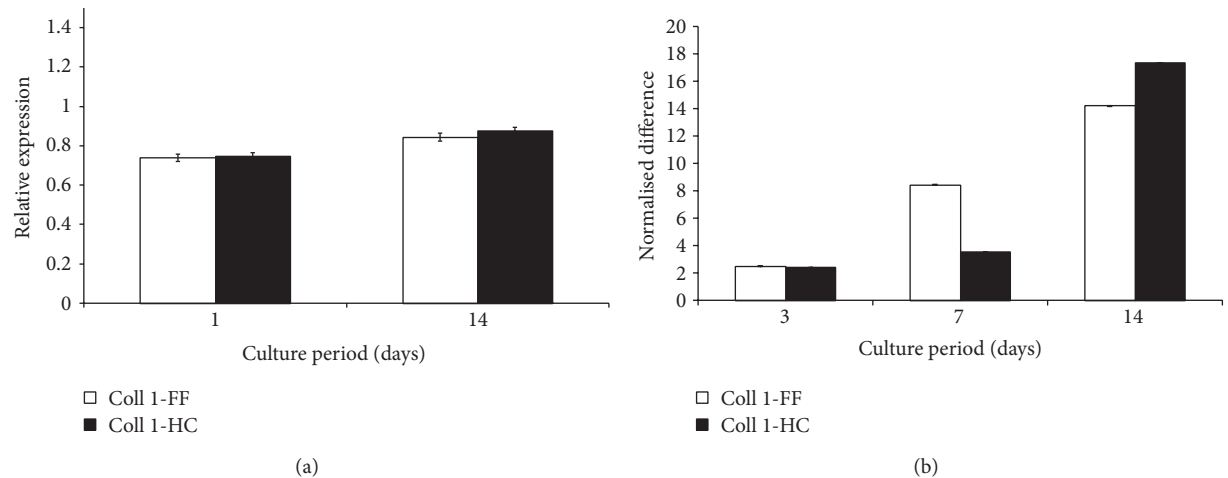


FIGURE 5: Graphs show (a) the expression (relative to that of GAPDH) of collagen type 1 (Coll 1) after 1 and 14 days of culture on either the honeycomb (CH) or the flat (FF) films. Normalised to its day 1 values, (b) shows the temporal changes to the expression levels at days 3, 7, and 14, in terms of percentage difference. Data represents mean and standard deviations of 12 discs per sampled time point.

chondrocytes, since their morphology is important and is governed *in vitro* by their spatial environment. Cytotoxicity on PCL surfaces was not a major concern, since porcine articular chondrocytes have been successfully cultured on PCL for up to 14 days by Tsai and colleagues [28]. Moreover, Cap, which served as an emulsifier has been used to make honeycomb-patterned films, and hepatocytes were successfully cultured [18].

The chondrocytes attached to both the flat and HC films PCL films used in the present study, the articular chondrocytes attached to both the flat and the honeycombed PCL surfaces. At the earliest observed time point, the cells

on both surfaces were typically round, sparse, and heterogeneously distributed. Although not quantitatively compared, the honeycomb films retained more cells at 6 hours than the flat films. SEM micrographs showed some cells within the pores. These cells were morphologically rounded, suggesting that they were physically entrapped.

The 24-hour samples had significantly higher cell number and were more homogeneously distributed on both films. It is, however, unlikely that proliferation is responsible for this. Rather, it is more plausible that the chondrocytes adhesion to the films at 6 hours were not strong enough to survive the preparation process required for SEM imaging, resulting in a

significant amount of the cell detachment. Between 6 and 24 hours more cells had attached to the surfaces, and stronger interactions had been formed. Presumably, this reduced cell detachment during the SEM sample preparation.

The organisation of chondrocytes actin cytoskeleton has been shown to correlate with their differentiation and gene expression [29]. Therefore, monitoring its developments on the microporous films was potentially useful for predicting their midterm survival and long-term functionality. The flattened appearance of the articular chondrocytes at 72 hours, combined with the larger surface area covered by their actin fibres, at the same time point, suggests that the majority of the cells had begun to spread on the films. Prior to this, their cytoskeletal organisation exhibited a ring-like distribution. This ring-like distribution was also observed in native cartilage by Ciolfi and coworkers [30], who suggested this to be their preferred actin organisation. By contrast, the actin filaments observed at 72 hours were extensive and appeared randomly organised, with respect to the honeycomb films.

The temporal changes to DNA concentration described the cells proliferation over the 14 days. For cells cultured on flat films, the biggest difference in DNA values occurring between days 7 and 14 suggests that cellular proliferation on the flat films was highest then. On the other hand, cell proliferation on the HC films peaked between days 3 and 7. The reduced DNA concentration may either be an indication of a pending viability issue or an incomplete digestion of the day 14 HC samples. Due to the heterogeneity of the HC-cellular constructs, it is likely that, during the course of time, the cells at the top flatten out and produce ECM. The ECM inevitably hinders access to the internal regions of the HC pores. A natural consequence is that the cells within may suffer from reduced nutrient supply. Indeed, cases of nutrient deficiency leading to reduced cellular activities and viabilities within 3D-cultures are all too common in the literatures. A further consequence is that only the cells (flattened) at the top of the HC surfaces, along with their ECM, were digested sufficiently to allow detection by the biochemical reagents. This is a probable explanation for the lower values of ECM, GAG and gene expression molecules measured from HC cultures.

Cellular viability was monitored regularly during the study using Calcein-AM-Ethidium Homodimer method. There was no viability issue observed with either of the culture setups. Therefore, it is fair to assume that the lower experimental parameters observed with the HC-cultures are most likely due to the incomplete digestion of the 3D-samples, caused by lack of access to the internal regions of the micropores, as opposed to a cellular viability challenge.

Interestingly, the amount of DNA associated with the flat films at day 14 is not significantly different to that on honeycomb at day 7. This implies either that cell proliferation on flat film has a longer lag phase than when cultured on the honeycomb films, or that this DNA value represents a maximum number of cells sustainable by the 14 mm diameter discs. The latter explanation is however unlikely, since cells are capable of forming multiple layers on flat and microporous surfaces [31]. By extending the culture period, it may be possible to determine the true maximum DNA value,

that is to say, the maximum number of cells sustainable by both films and how long it takes for the films to achieve their respective values.

The increased keratin sulphate concentration over the 14 days suggested that the cells on both films were producing ECM. Observably, ECM concentration on both types of surfaces peaked at day 7 and fell significantly thereafter, while the decline on the flat surface during the same time point was not significant. Matrix production by human chondrocytes, cultured on both flat and porous PCL scaffolds were previously observed to increase till 14 days, and decline henceforth [32].

While the keratin sulphate concentration on the films provides good indication of its production by the cells, it is worth noting that the higher concentration associated with HC films may result also from a higher retention on the microporous surface. Indeed, it is well reported that surface topography influences protein adsorption [33]. Moreover, adsorption of fibronectin and vitronectin to honeycomb films was found to be significantly higher than that on the corresponding flat surface [34]. This is conceivable, since the surface area of honeycomb films is higher than that of flat films [35]. Keratin sulphate is a small glycosaminoglycan (GAG) unit, essential to the formation of the larger, aggregating proteoglycan, aggrecan. As GAGs build up, aggrecan molecules are formed. These bind noncovalently to hyaluronan chains, to form an aggrecan-hyaluronan complex. This aggregating GAG molecule, whose chain length and molecular weight may reach 10,000 nm and 50,000 kDa, respectively, is involved in tissue hydration, load distribution, and the immobilisation and storage of growth factors [36]. Therefore, the comparatively high retention of keratin sulphate on the HC films may indicate a superior ability to induce neocartilage with functional ECM.

In a similar study, [26], chondrocytes were found to survive on polymeric surfaces with 5  $\mu\text{m}$  pore. Their proliferation and matrix synthesis were validated for up to 3 weeks. However, the cells were observed to spread on the films, adopting a flat morphology. Moreover, it was not determined whether the surfaces had maintained the cells phenotype. Notably, the 5  $\mu\text{m}$  pores are insufficient to accommodate the chondrocytes, therefore, excluding them from the internal surfaces. The present study assessed the possibility of maintaining the viability and morphology of articular chondrocytes on HC-patterned surfaces with 10  $\mu\text{m}$  pore diameter. Quantifying RT-PCR helped determine the gene expression levels of type II collagen and aggrecan. These genes had been identified as the major phenotypic markers for chondrogenic tissues [37–40]. Their levels of expression were compared to that of the protein, glyceraldehyde-3-phosphate dehydrogenase (GAPDH). The upregulation of type II collagen expression at days 3 and 7 (Figure 4(b)) correlates with the increased matrix synthesis (Figure 3(b)) observed at these time points. Furthermore, as the accumulation of matrix molecules on the cultured discs fell at day 14, the expression of collagen II, the major component of chondrocytes ECM, increased. This response may be associated with matrix turnover, during which anabolic and catabolic gene expression compete to balance matrix homeostasis [41].

On the other hand, the temporal downregulation of aggrecan (Figure 4(b)) may suggest that the chondrocytes were undergoing some sort of phenotypic change. The heterogeneity of chondrocytes within cartilage is such that the superficial zone of articular cartilage characteristically has one to several layers of flattened, disc-shaped cells. As well as having densely packed bundles of collagen fibres orientated parallel to the articulating surface, these cells are associated with relatively low proteoglycan content [36, 42]. Bearing in mind the fact that the chondrocytes had begun to spread over the films, adopting a flattened morphology by 72 hours (Figures 1(e) and 1(f)), it is therefore plausible that the cells were developing characteristics associated with cells at the superficial zones of articular cartilage. The chondrocytes situated inside the 10  $\mu\text{m}$  pores typically maintained their rounded morphology (Figures 1(d) and 1(f)). This may explain why the downregulation of aggrecan was less pronounced by cells on the HC films, compared to those cultured on the flat films, which had completely flattened out.

The expression level for type I collagen was measured to detect dedifferentiation of the chondrocytes back into their more fibroblastic progenitors. At 24 hours expression of type I collagen, relative to GAPDH, was approximately 0.74, compared to 1.04 and 0.85 of type II collagen and aggrecan, respectively. Nonetheless, expression of type I collagen was unexpected. It is worth noting that prior to their culture on the flat and honeycomb films, the cells were expanded in monolayer for 7 days. Such culture has been reported to induce chondrocytes dedifferentiation and the production of type I collagen [10, 36]. It is therefore likely that the expression of type I collagen by the cells from as early as 24 hours may have resulted from their expansion in monolayer. Moreover, the temporal upregulation of the gene for type I collagen suggests a continual trend by some cells to dedifferentiate, despite the simultaneous upregulation of the type II collagen gene.

## 5. Conclusions

In light of the observations made in this study, it is concluded that articular chondrocytes attach to honeycomb surfaces. This was manifested by increased concentration of DNA and accumulation of extracellular matrix molecules. The extent of these was either similar to or, at times, greater than the flat surfaces, within the first 7 days. However, by 14 days, the honeycomb fell short of the flat films.

Chondrocytes, being naturally round, may have been adversely affected by their adoption of a flat morphology when attached to and spread on the flat and honeycomb films. The extent of this was difficult to determine, since the onset of phenotypic change may have begun during the preculture phase.

Extending the culture period may be useful to observe the long-term fate of cells on the honeycomb surfaces. It may be possible that the formation of multilayer of cells, albeit heterogeneous in morphology, with the rounded cells within the pores, while the flattened ones are at the top, may produce neocartilage, which is structurally and functionally similar

to articular cartilage. Furthermore, by manipulating the pore geometry of the honeycomb films, the advantage achieved, in the first 7 days, with respect to both proliferation and matrix synthesis, may be prolonged.

## Conflict of Interests

The authors declare that there is no conflict of interests regarding the publication of this paper.

## References

- [1] R. Langer and J. P. Vacanti, "Tissue engineering," *Science*, vol. 260, no. 5110, pp. 920–926, 1993.
- [2] E. B. Hunziker, "Biologic repair of articular cartilage: defect models in experimental animals and matrix requirements," *Clinical Orthopaedics and Related Research*, no. 367, pp. S135–S146, 1999.
- [3] D. A. Grande, C. Halberstadt, G. Naughton, R. Schwartz, and R. Manji, "Evaluation of matrix scaffolds for tissue engineering of articular cartilage grafts," *Journal of Biomedical Materials Research*, vol. 34, no. 2, pp. 211–220, 1997.
- [4] L. E. Freed, D. A. Grande, Z. Lingbin, J. Emmanuel, J. C. Marquis, and R. Langer, "Joint resurfacing using allograft chondrocytes and synthetic biodegradable polymer scaffolds," *Journal of Biomedical Materials Research*, vol. 28, no. 8, pp. 891–899, 1994.
- [5] D. W. Huttmacher, "Scaffolds in tissue engineering bone and cartilage," *Biomaterials*, vol. 21, no. 24, pp. 2529–2543, 2000.
- [6] M. Shakibaei, P. De Souza, and H.-J. Merker, "Integrin expression and collagen type II implicated in maintenance of chondrocyte shape in monolayer culture: an immunomorphological study," *Cell Biology International*, vol. 21, no. 2, pp. 115–125, 1997.
- [7] J. H. Kimura, T. E. Hardingham, V. C. Hascall, and M. Solursh, "Biosynthesis of proteoglycans and their assembly into aggregates in cultures of chondrocytes from the Swarm rat chondrosarcoma," *Journal of Biological Chemistry*, vol. 254, no. 8, pp. 2600–2609, 1979.
- [8] R. A. Stockwell and G. Meachim, "The chondrocyte," in *Adult Articular Cartilage*, pp. 600–610, Pitman Medical Publishing, 1979.
- [9] D. G. Stokes, G. Liu, I. B. Coimbra, S. Piera-Velazquez, R. M. Crowl, and S. A. Jiménez, "Assessment of the gene expression profile of differentiated and dedifferentiated human fetal chondrocytes by microarray analysis," *Arthritis and Rheumatism*, vol. 46, no. 2, pp. 404–419, 2002.
- [10] M. D. Buschmann, Y. A. Gluzband, A. J. Grodzinsky, J. H. Kimura, and E. B. Hunziker, "Chondrocytes in agarose culture synthesize a mechanically functional extracellular matrix," *Journal of Orthopaedic Research*, vol. 10, no. 6, pp. 745–758, 1992.
- [11] H. J. Hauselmann, M. B. Aydelotte, B. L. Schumacher, K. E. Kuettner, S. H. Gitelis, and E. J.-M. A. Thonar, "Synthesis and turnover of proteoglycans by human and bovine adult articular chondrocytes cultured in alginate beads," *Matrix*, vol. 12, no. 2, pp. 116–129, 1992.
- [12] N. Pernodet, M. Maaloum, and B. Tinland, "Pore size of agarose gels by atomic force microscopy," *Electrophoresis*, vol. 18, no. 1, pp. 55–58, 1997.
- [13] M. George and T. E. Abraham, "Polyionic hydrocolloids for the intestinal delivery of protein drugs: alginate and chitosan—a

- review," *Journal of Controlled Release*, vol. 114, no. 1, pp. 1–14, 2006.
- [14] R. Sutherland, J. Freyer, and W. Mueller-Klieser, "Cellular growth and metabolic adaptations to nutrient stress environments in tumor microregions," *International Journal of Radiation Oncology Biology Physics*, vol. 12, no. 4, pp. 611–615, 1986.
- [15] N. Maruyama, T. Koito, J. Nishida et al., "Mesoscopic patterns of molecular aggregates on solid substrates," *Thin Solid Films*, vol. 327–329, no. 1–2, pp. 854–856, 1998.
- [16] M. Tanaka, M. Takebayashi, M. Miyama, J. Nishida, and M. Shimomura, "Design of novel biointerfaces (II). Fabrication of self-organized porous polymer film with highly uniform pores," *Bio-Medical Materials and Engineering*, vol. 14, no. 4, pp. 439–446, 2004.
- [17] K. Sato, K. Hasebe, M. Tanaka et al., "Preparation of the honeycomb patterned porous film of biodegradable polymer for tissue engineering scaffolds," *International Journal of Nanoscience*, vol. 1, no. 5–6, pp. 689–693, 2002.
- [18] M. Tanaka, K. Nishikawa, H. Okubo et al., "Control of hepatocyte adhesion and function on self-organized honeycomb-patterned polymer film," *Colloids and Surfaces A: Physicochemical and Engineering Aspects*, vol. 284–285, pp. 464–469, 2006.
- [19] T. Nishikawa, M. Nonomura, K. Arai et al., "Micropatterns based on deformation of a viscoelastic honeycomb mesh," *Langmuir*, vol. 19, no. 15, pp. 6193–6201, 2003.
- [20] A. Tsuruma, M. Tanaka, N. Fukushima, and M. Shimomura, "Morphological changes in neurons by self-organized patterned films," *e-Journal of Surface Science and Nanotechnology*, vol. 3, pp. 159–164, 2005.
- [21] A. D. Woolf and B. Pfleger, "Burden of major musculoskeletal conditions," *Bulletin of the World Health Organization*, vol. 81, no. 9, pp. 646–656, 2003.
- [22] M. Tanaka, A. Takayama, E. Ito, H. Sunami, S. Yamamoto, and M. Shimomura, "Effect of pore size of self-organized honeycomb-patterned polymer films on spreading, focal adhesion, proliferation, and function of endothelial cells," *Journal of Nanoscience and Nanotechnology*, vol. 7, no. 3, pp. 763–772, 2007.
- [23] M. A. Birch, M. Tanaka, G. Kirmizidis, S. Yamamoto, and M. Shimomura, "Microporous "honeycomb" films support enhanced bone formation in vitro," *Tissue Engineering A*, vol. 19, no. 17–18, pp. 2087–2096, 2013.
- [24] T. Sato, M. Tanaka, S. Yamamoto et al., "Effect of honeycomb-patterned surface topography on the function of mesenteric adipocytes," *Journal of Biomaterials Science*, vol. 21, no. 14, pp. 1947–1956, 2010.
- [25] D. W. Hamilton, M. O. Riehle, R. Rappuoli, W. Monaghan, R. Barbucci, and A. S. G. Curtis, "The response of primary articular chondrocytes to micrometric surface topography and sulphated hyaluronic acid-based matrices," *Cell Biology International*, vol. 29, no. 8, pp. 605–615, 2005.
- [26] Y. Fukuhira, H. Kaneko, M. Yamaga, M. Tanaka, S. Yamamoto, and M. Shimomura, "Effect of honeycomb-patterned structure on chondrocyte behavior in vitro," *Colloids and Surfaces A: Physicochemical and Engineering Aspects*, vol. 313–314, pp. 520–525, 2008.
- [27] M. Brittberg, A. Lindahl, A. Nilsson, C. Ohlsson, O. Isaksson, and L. Peterson, "Treatment of deep cartilage defects in the knee with autologous chondrocyte transplantation," *The New England Journal of Medicine*, vol. 331, no. 14, pp. 889–895, 1994.
- [28] W.-B. Tsai, C.-H. Chen, J.-F. Chen, and K.-Y. Chang, "The effects of types of degradable polymers on porcine chondrocyte adhesion, proliferation and gene expression," *Journal of Materials Science: Materials in Medicine*, vol. 17, no. 4, pp. 337–343, 2006.
- [29] P. D. Benya, P. D. Brown, and S. R. Padilla, "Microfilament modification by dihydrocytochalasin B causes retinoic acid-modulated chondrocytes to reexpress the differentiated collagen phenotype without a change in shape," *Journal of Cell Biology*, vol. 106, no. 1, pp. 161–170, 1988.
- [30] V. J. D. Ciolfi, R. Pilliar, C. McCulloch, S. X. Wang, M. D. Grynepas, and R. A. Kandel, "Chondrocyte interactions with porous titanium alloy and calcium polyphosphate substrates," *Biomaterials*, vol. 24, no. 26, pp. 4761–4770, 2003.
- [31] B. Annaz, K. A. Hing, M. Kayser, T. Buckland, and L. Di Silvio, "Porosity variation in hydroxyapatite and osteoblast morphology: a scanning electron microscopy study," *Journal of Microscopy*, vol. 215, no. 1, pp. 100–110, 2004.
- [32] R. Izquierdo, N. Garcia-Giralt, M. T. Rodriguez et al., "Biodegradable PCL scaffolds with an interconnected spherical pore network for tissue engineering," *Journal of Biomedical Materials Research A*, vol. 85, no. 1, pp. 25–35, 2008.
- [33] A. F. von Recum and T. G. van Kooten, "The influence of micro-topography on cellular response and the implications for silicone implants," *Journal of Biomaterials Science*, vol. 7, no. 2, pp. 181–198, 1995.
- [34] H. Sunami, E. Ito, M. Tanaka, S. Yamamoto, and M. Shimomura, "Effect of honeycomb film on protein adsorption, cell adhesion and proliferation," *Colloids and Surfaces A: Physicochemical and Engineering Aspects*, vol. 284–285, pp. 548–551, 2006.
- [35] S. Yamamoto, M. Tanaka, H. Sunami et al., "Relationship between adsorbed fibronectin and cell adhesion on a honeycomb-patterned film," *Surface Science*, vol. 600, no. 18, pp. 3785–3791, 2006.
- [36] G. Meachim and R. A. Stockwell, "The matrix," in *Adult Articular Cartilage*, pp. 600–610, Pitman Medical Publishing, 1979.
- [37] K. E. Kuettner, M. B. Aydelotte, and E. J.-M. A. Thonar, "Articular cartilage matrix and structure: a minireview," *Journal of Rheumatology*, vol. 18, no. 27, pp. 46–48, 1991.
- [38] K. E. Kuettner, V. A. Memoli, and B. U. Pauli, "Synthesis of cartilage matrix by mammalian chondrocytes in vitro. II. Maintenance of collagen and proteoglycan phenotype," *Journal of Cell Biology*, vol. 93, no. 3, pp. 751–757, 1982.
- [39] K. E. Kuettner, B. U. Pauli, and G. Gall, "Synthesis of cartilage matrix by mammalian chondrocytes in vitro. I. Isolation, culture characteristics, and morphology," *Journal of Cell Biology*, vol. 93, no. 3, pp. 743–750, 1982.
- [40] V. C. Mow, A. Ratcliffe, and A. R. Poole, "Cartilage and diarthrodial joints as paradigms for hierarchical materials and structures," *Biomaterials*, vol. 13, no. 2, pp. 67–97, 1992.
- [41] T. Aigner, S. Soeder, and J. Haag, "IL-1 $\beta$  and BMPs—interactive players of cartilage matrix degradation and regeneration," *European Cells and Materials*, vol. 12, pp. 49–56, 2006.
- [42] B. L. Schumacher, J.-L. Su, K. M. Lindley, K. E. Kuettner, and A. A. Cole, "Horizontally oriented clusters of multiple chondrons in the superficial zone of ankle, but not knee articular cartilage," *Anatomical Record*, vol. 266, no. 4, pp. 241–248, 2002.

## Research Article

# Effects of Prepolymerized Particle Size and Polymerization Kinetics on Volumetric Shrinkage of Dental Modeling Resins

Tae-Yub Kwon,<sup>1,2</sup> Jung-Yun Ha,<sup>2</sup> Ju-Na Chun,<sup>2</sup> Jun Sik Son,<sup>3</sup> and Kyo-Han Kim<sup>1,2</sup>

<sup>1</sup> Department of Dental Biomaterials, School of Dentistry, Kyungpook National University, 2-188-1 Samduk-dong, Jung-gu, Daegu 700-412, Republic of Korea

<sup>2</sup> Department of Medical & Biological Engineering, Graduate School, Kyungpook National University, 2-188-1 Samduk-dong, Jung-gu, Daegu 700-412, Republic of Korea

<sup>3</sup> Korea Textile Development Institute, 1083 Jungri-dong, Seo-gu, Daegu 703-712, Republic of Korea

Correspondence should be addressed to Kyo-Han Kim; [kyohan@knu.ac.kr](mailto:kyohan@knu.ac.kr)

Received 11 December 2013; Revised 17 February 2014; Accepted 17 February 2014; Published 17 March 2014

Academic Editor: Oh Hyeong Kwon

Copyright © 2014 Tae-Yub Kwon et al. This is an open access article distributed under the Creative Commons Attribution License, which permits unrestricted use, distribution, and reproduction in any medium, provided the original work is properly cited.

Dental modeling resins have been developed for use in areas where highly precise resin structures are needed. The manufacturers claim that these polymethyl methacrylate/methyl methacrylate (PMMA/MMA) resins show little or no shrinkage after polymerization. This study examined the polymerization shrinkage of five dental modeling resins as well as one temporary PMMA/MMA resin (control). The morphology and the particle size of the prepolymerized PMMA powders were investigated by scanning electron microscopy and laser diffraction particle size analysis, respectively. Linear polymerization shrinkage strains of the resins were monitored for 20 minutes using a custom-made linometer, and the final values (at 20 minutes) were converted into volumetric shrinkages. The final volumetric shrinkage values for the modeling resins were statistically similar ( $P > 0.05$ ) or significantly larger ( $P < 0.05$ ) than that of the control resin and were related to the polymerization kinetics ( $P < 0.05$ ) rather than the PMMA bead size ( $P = 0.335$ ). Therefore, the optimal control of the polymerization kinetics seems to be more important for producing high-precision resin structures rather than the use of dental modeling resins.

## 1. Introduction

The acrylic family of polymers includes polymers and copolymers of acrylic and methacrylic acids and esters, acrylonitrile, and acrylamide [1]. However, most of the acrylic family products are acrylic and methacrylic esters. Acrylates are highly reactive due to the absence of the protecting methyl group at the vicinity of the double bond and may pose biocompatibility and shelf-life problems [2]. Moreover, polyacrylates are very soft because the polymer chains are not rigid [1]. Thus, methacrylate and its polymer, polymethacrylate, tend to be used in medical and dental applications to prepare shaped objects. Methyl methacrylate (MMA) is the most commonly used monomer in dentistry. Polymethyl methacrylate (PMMA) resin was originally introduced as a denture base material and was also formerly used as dental restorative materials [3]. They are now widely used for provisional crowns, fixed partial dentures, or orthodontic

appliances and also for orthopedic surgery as bone cements [3].

Because of the very large (21 vol%) polymerization shrinkage, the polymerization of various PMMA products is carried out in stages to control the product dimensions for use in industrial applications [1, 4]. To prepare dental PMMA resins, a mixture of powdered polymer (prepolymerized PMMA particle) and monomer is used, and dissolution of the polymer in the monomer results in the formation of a plastic dough [5]. Along with this physical interaction, the resin is cured by the application of heat (heat-curing type) or chemicals (self-curing type). This mixed form enables ease of handling and minimizes shrinkage strain upon polymerization via the progressive substitution of the liquid monomer by the prepolymerized powder [3–5].

Dental modeling resins, which are also based on the PMMA/MMA system, have been developed for use in applications where highly precise resin structures are needed.

As osseointegrated implants show little mobility relative to the surrounding bone, a misfit of implant-supported fixed partial dentures can allow the transmission of stress via the implants to the surrounding bone [6]. Therefore, dental laboratories use modeling or pattern resins for the construction of implant-retained suprastructures that require a precise fit. Although the manufacturers claim that these resins show little or no shrinkage, the actual data appears limited. Moreover, the mechanism of how the resins control or reduce polymerization shrinkage is unknown.

This study examined the effects of the prepolymerized PMMA particle size and polymerization kinetics on the volumetric shrinkage of five dental modeling resins and one temporary resin (control). The “linometer” method was used for determining the linear polymerization shrinkage, which was finally converted into a volumetric shrinkage. We hypothesized that (1) PMMA particles of the modeling resin are larger than that of the temporary resin and (2) the modeling resins yield lower final volumetric shrinkage values than the temporary resin.

## 2. Materials and Methods

**2.1. Resin Materials Tested.** In this study, Pi-Ku-Plast (PK; bredent GmbH & Co. KG, Germany), DuraLay (DL; Reliance Dental Mfg. Co., USA), Fino Resin PR (FR; Fino GmbH, Germany), GC Pattern Resin (GP; GC Corp., Japan), GC Pattern Resin LS (GL; GC America Inc., USA), and the control Jet Tooth Shade (JT; Lang Dental Mfg. Co. Inc., USA) were used. They all had similar chemical compositions: PMMA powder containing benzoyl peroxide (BPO) initiator, MMA liquid containing a cross-linking monomer, a tertiary amine coinitiator, and an inhibitor [3, 4].

**2.2. Characterization of PMMA Particles.** The morphology of the PMMA powders was observed by field-emission scanning electron microscopy (FE-SEM, JSM-6700F, Jeol, Japan) after platinum sputtering. The PMMA particle size was analyzed using a laser diffraction particle size analyzer (LA-950, Horiba, Japan) with a run length of 30 seconds [7]. Prior to the analysis, the powders were dispersed in ethanol and ultrasonicated for 3 minutes to ensure good particle dispersion [7].

**2.3. Shrinkage Measurements.** Linear polymerization shrinkage measurements were performed using a custom-made linometer (R&B Inc., Korea) [8, 9]. A schematic illustration of the linometer is shown in Figure 1. All the resins were mixed at a powder/liquid ( $P/L$ ) ratio of 3:1 by volume [4]. Freshly mixed materials were transferred to a Teflon mold to ensure that the same amount ( $\sim 50 \text{ mm}^3$ ) of resin was used for each linometer sample. Then, the materials were transferred to the aluminum disc in the linometer that had been previously coated with separating grease (Dow Corning, USA) then covered with a glass slide and loaded under constant pressure. The surface of the glass slide facing the specimen was also coated with the separating grease. As the resin under the slide glass was self-cured, the aluminum disc under the resin

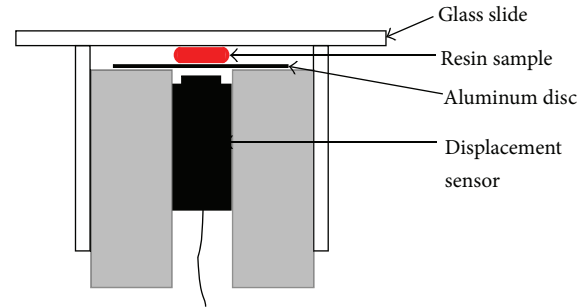


FIGURE 1: Schematic illustration of the linometer with a resin sample placed between the glass slide and aluminum disc.

moved upward. The amount of disc displacement was measured using a sensor every 0.5 seconds for 20 minutes. The displacements were related to the true linear polymerization shrinkage because the surfaces to which the materials were attached were greased to allow a free shrinking movement in the radial sense along these surfaces [8]. Ten measurements were made for each resin.

The linear polymerization shrinkage was calculated using [8]:

$$\text{lin \%} = \left[ \frac{\Delta L}{L + \Delta L} \right] \times 100, \quad (1)$$

where  $\Delta L$  is the recorded displacement and  $L$  is the thickness of the specimen after polymerization. Finally, volumetric shrinkage was calculated using [8]:

$$\text{vol\%} = 3 \text{ lin \%} - 0.03(\text{lin \%})^2 + 0.0001(\text{lin \%})^3. \quad (2)$$

Two principal parameters were derived to express the polymerization shrinkage kinetics [10]: (1) the initial shrinkage, which is characterized as the percentage change in shrinkage in the first 10 seconds after a positive increase in shrinkage strain and (2) the overall time constant, the time for the shrinkage to achieve a fraction of 0.632 (or  $1 - e^{-1}$ , which is derived from the Kohlrausch-Williams-Watts (KWW) stretched-exponential growth curve) of its final magnitude.

**2.4. Statistical Analysis.** For statistical analysis of the shrinkage data, one-way ANOVA and Tukey's post hoc test were used at  $\alpha = 0.05$ . Polynomial regression was performed to determine the correlations between the final shrinkage strain and the two kinetics parameters (initial shrinkage and overall time constant) as well as the prepolymerized particle size.

## 3. Results and Discussion

The curing shrinkage of resin-based dental materials is measured using a variety of methods. These include dilatometric methods [11], the bonded disc method [4, 10, 12], the linometer method [8], and the strain-gauge method [4]. Although it is commonly used, dilatometry is very sensitive to the ambient temperature during the experiment because the

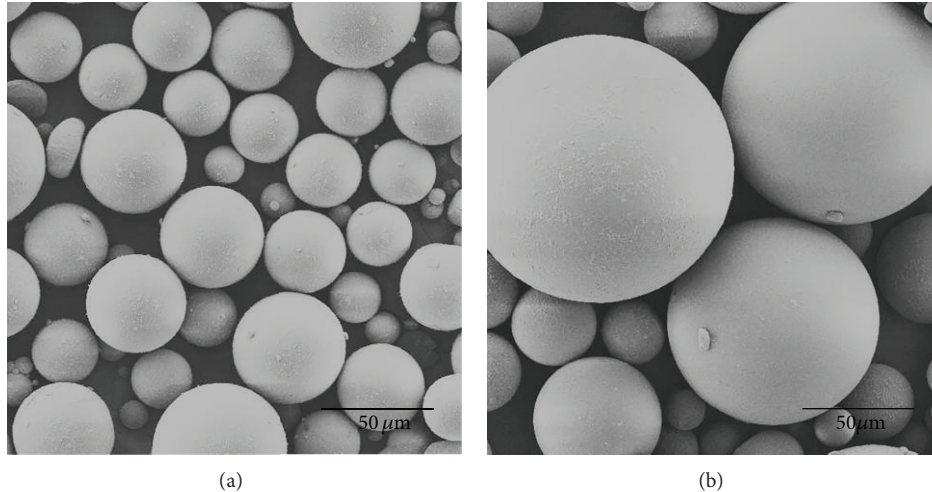


FIGURE 2: SEM images of the PMMA particles of the control (a) and GL (b) (original magnification 3000x). All particles tested in this study were spherical-shaped with different sizes.

volume of a medium in the dilatometer can increase as the temperature of the medium increases [12, 13]. On the other hand, the bonded disc method is relatively easy to use and does not require extensive and expensive instrumentation [11]. The linometer method is a modification of the bonded disc method and tracks the linear vertical displacement of a free floating aluminum disc fixed to the surface of a resinous material applied to a horizontal glass plate (Figure 1) [11, 13]. Like the bonded disc method, dimensional changes are confined to the thickness of the sample disc so that the fractional linear shrinkage approximates the volumetric shrinkage [8, 10]. Since the polymerization shrinkage strain can be reduced by the substitution of liquid monomer in a PMMA/MMA system by the prepolymerized powder [3–5], we hypothesize that the particle size is the main factor in decreasing the final volumetric shrinkage values in the dental modeling resins.

Figure 2 shows the representative SEM images of the PMMA particles of the temporary resin (control) and GL. In most dental acrylic resins, PMMA beads in the powder have diameters up to  $100\ \mu\text{m}$  [14]. These are produced via suspension polymerization in which the MMA monomer, containing the initiator, is suspended as droplets in water [14]. In this study, all PMMA particles showed a spherical morphology (bead-shaped) with various sizes. The PMMA particle size distribution of each resin is shown in Figure 3. Table 1 summarizes the median, mean, standard deviation, and mode of the particle sizes. Some differences between the median, mean, and mode indicate that the distributions are not completely symmetrical. Such trends were significant in FR, as indicated by the greater difference between the median and the mean than in the other resins. For GP and GL, large differences between the mode and the median or mean size indicate a bimodal distribution. The particle size of the modeling resins was similar to that of the control except for GP and GL, whose particle sizes were considerably larger. When powder and liquid are mixed, the MMA diffuses around and into the PMMA particles, releasing the prepolymerized

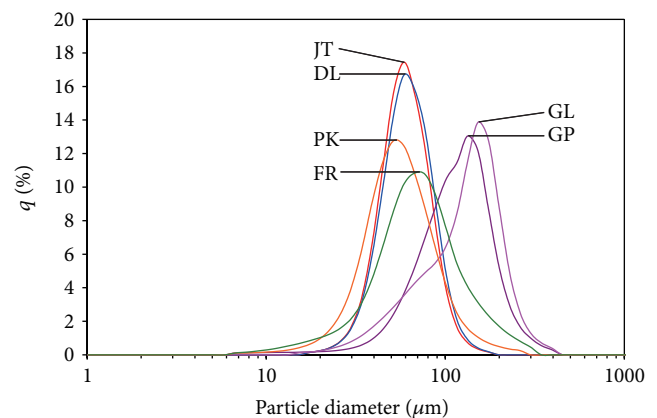


FIGURE 3: PMMA particle size distribution.

polymer chains from the surface of the particles [3, 7]. A small particle size may improve the wetting of the beads and reduces the doughing time by forming a smoother mix and a greater dissolution of the particles [5]. However, this is only a physical interaction between the powder and liquid [3]. The tertiary amines (in the liquid) carry out the redox initiation together with BPO (in the powder) in a short period of time at room temperature [3, 15].

Figure 4 shows the representative polymerization shrinkage strain of the materials. Once initiated, the initial rigid polymerization shrinkage proceeded rapidly, as a nearly linear function of time [10]. Nonetheless, the normalized overall shrinkage response was approximately represented by the KWW stretched-exponential growth curve [10, 16]. This is particularly appropriate for the situation following the initial linear shrinkage [10]. Thus, the kinetic behavior was characterized by an overall time constant associated with the curve [10]. In addition, the initial shrinkage, indicating the

TABLE 1: Volume-based PMMA particle size distribution.

| Material                      | Median size* | Mean size <sup>†</sup> | SD <sup>‡</sup> | Mode size <sup>§</sup> |
|-------------------------------|--------------|------------------------|-----------------|------------------------|
| JT (Jet Tooth Shade, control) | 55.41        | 58.28                  | 19.51           | 55.06                  |
| PK (Pi-Ku-Plast)              | 51.00        | 57.41                  | 30.35           | 48.32                  |
| DL (DuraLay)                  | 57.27        | 60.17                  | 20.37           | 55.42                  |
| FR (Fino Resin PR)            | 64.89        | 74.80                  | 44.57           | 63.31                  |
| GP (GC Pattern Resin)         | 110.15       | 116.27                 | 53.74           | 124.80                 |
| GL (GC Pattern Resin LS)      | 125.71       | 127.12                 | 59.70           | 143.32                 |

All values are in  $\mu\text{m}$ . \*The size that splits the volume distribution with half above and half below this diameter; <sup>†</sup>the volume mean diameter; <sup>‡</sup>standard deviation for the frequency distribution; <sup>§</sup>the peak of the frequency distribution.

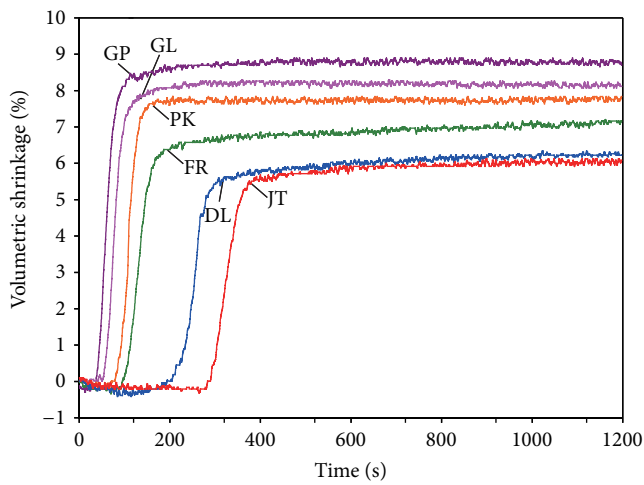


FIGURE 4: Representative volumetric shrinkage/time graphs (recorded 1 minute after starting the mix).

TABLE 2: Shrinkage data determined using a linometer.

| Material | Volumetric shrinkage (%) | Shrinkage in 10 seconds (%) | Overall time constant (s) |
|----------|--------------------------|-----------------------------|---------------------------|
| JT       | 6.15 $\pm$ 0.64 A        | 0.53 $\pm$ 0.09 A           | 316.82 $\pm$ 23.36 A      |
| PK       | 7.83 $\pm$ 1.57 AB       | 0.77 $\pm$ 0.18 A           | 120.56 $\pm$ 19.39 B      |
| DL       | 6.22 $\pm$ 1.24 A        | 0.52 $\pm$ 0.10 A           | 283.01 $\pm$ 28.91 C      |
| FR       | 7.11 $\pm$ 0.86 AB       | 0.74 $\pm$ 0.12 A           | 136.79 $\pm$ 19.41 B      |
| GP       | 8.70 $\pm$ 1.78 B        | 1.57 $\pm$ 0.27 B           | 78.43 $\pm$ 14.03 D       |
| GL       | 8.09 $\pm$ 1.91 B        | 1.59 $\pm$ 0.29 B           | 85.27 $\pm$ 6.85 D        |

Values are expressed as mean  $\pm$  standard deviation. Within a row, values followed by different uppercase letters are statistically different ( $P < 0.05$ ).

initial reaction speed, was used to characterize the kinetic behavior [17].

Table 2 lists the statistical analysis results of the final volumetric shrinkage, initial shrinkage, and overall time constant. The mean final volumetric shrinkage-strain values ranged from 6.15% to 8.70%. The values for the modeling resins were similar (PK, DL, and FR;  $P > 0.05$ ) or significantly greater (GP, GL;  $P < 0.05$ ) than that of the control resin. This suggests that the modeling resins did not necessarily produce less

polymerization shrinkage, but sometimes more shrinkage than the conventional PMMA/MMA resin when they were all mixed at the same  $P/L$  ratio. Both the initial shrinkage and the overall time constant also showed significant differences between the materials based on the one-way ANOVA ( $P < 0.001$ ).

Volumetric shrinkage strain of a resin can be used to represent the extent of polymerization [18] because there is a direct relationship between the volumetric shrinkage and the monomer conversion [17]. In the PMMA/MMA resins tested in this study, the amounts of BPO initiator in the powder and amine coinitiator in the liquid are different between the materials. Thus, the different final shrinkage strains for the resins may have been mainly due to the different concentrations of the chemical initiation system (BPO/amine) in the resins [4, 18]. As shown in Figure 4, the onsets of polymerization shrinkage also differed significantly from each other, possibly because of the different types and concentrations of inhibitors present in the resins. During the induction or inhibition period, polymerization is halted by the chemical inhibitors. At the end of this period, when the inhibitor is consumed, polymerization proceeds at the same rate as in the absence of inhibitor [1]. However, higher inhibitor levels can compromise the final degree of conversion [19].

Figure 5 shows the polynomial regression curves of volumetric shrinkage versus the median particle size, initial shrinkage, and overall time constant. In these statistical analyses, the median size was used because it is more commonly used and gives more meaningful information than the mean or mode size when using the laser diffraction technique. No statistical correlation was observed between the median PMMA particle size and the polymerization shrinkage in the present study ( $P = 0.335$ ) (Figure 5(a)). Thus, although the use of prepolymerized powder in PMMA resins can reduce shrinkage strain upon polymerization [3–5], the particle size did not significantly influence the final shrinkage value. In contrast, the regression curves between the shrinkage and initial shrinkage (Figure 5(b)) and overall time constant (Figure 5(c)) fitted well with a second-order polynomial. In a study by Silikas et al. [4], when PMMA/MMA resin specimens were prepared with different  $P/L$  ratios by volume, the final shrinkage-strain values correlated positively with the  $P/L$  ratios. On the contrary, when an additional 1.0% BPO was added in the powder, the final shrinkage-strain values correlated negatively with the  $P/L$  ratio [4]. Based on these findings, the volumetric shrinkage strain seems to be more dependent on the extent of polymerization or degree of conversion rather than on the size or amount of PMMA beads in the PMMA/MMA mixture [18].

In general, polymerization shrinkage proceeds in two stages: pregelation and postgelation (or rigid) shrinkage [10, 20]. Shrinkage magnitudes obtained in this study are equal to or close to the postgelation volumetric shrinkage values [10, 13]. Some of the shrinkage occurs prior to the development of elastic properties in the resin, and some after the elastic behavior dominates [11]. During pregel polymerization, the resin may flow, allowing internal stresses to be relieved [20]. After gelation, flow discontinues and cannot compensate for

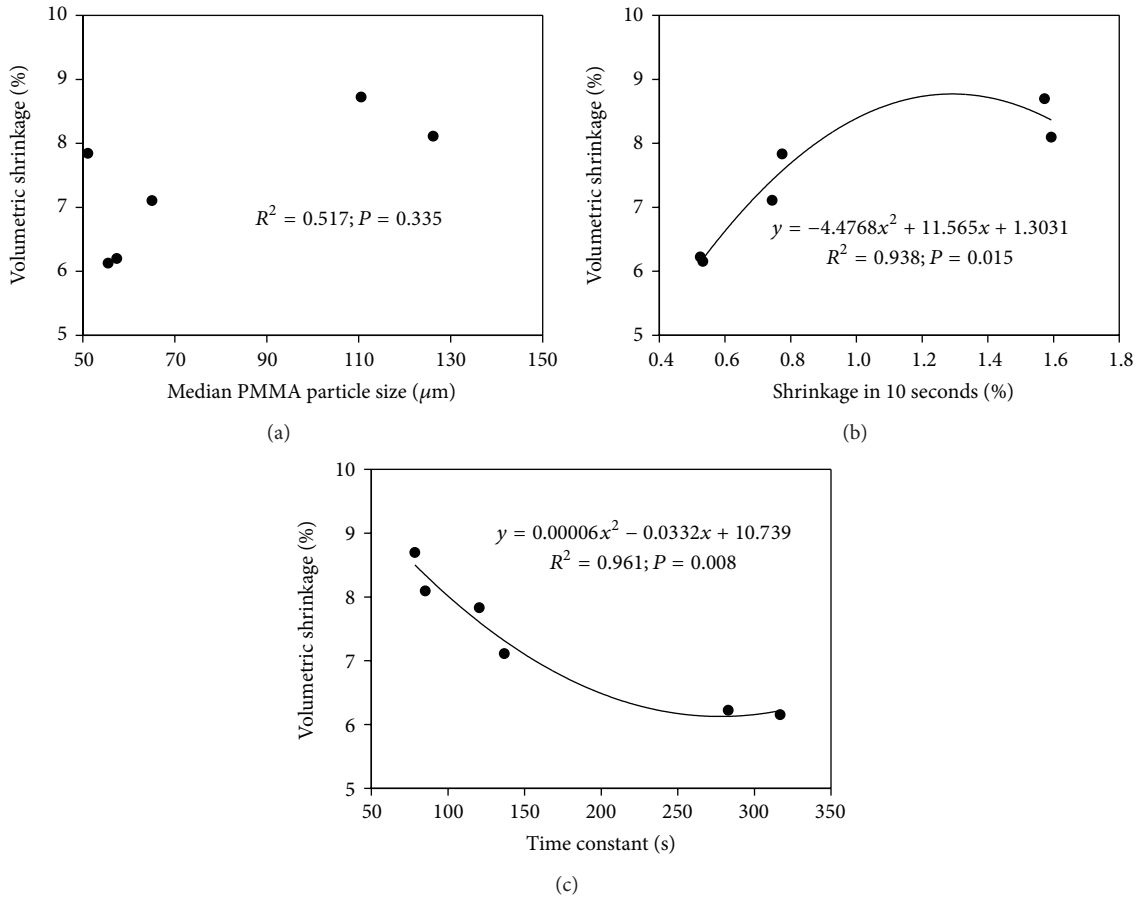


FIGURE 5: Polynomial regression curves of volumetric shrinkage versus the median particle size (a), initial shrinkage (b), and overall time constant (c).

the polymerization shrinkage stresses [13]. Although postgel polymerization shrinkage strain and stress are more clinically relevant [20], the measurement of only postgel shrinkage strain could provide lower values than that of total shrinkage strain [13]. Although the dilatometry method is often believed to measure total contraction (pregel and postgel), adhesion of the specimen to a plate introduces constraint, which limits the collection of shrinkage [11]. A relatively new video-controlled technique may provide values close to the total shrinkage-strains values [13], and the data obtained in this study can be verified using such a technique.

The findings of this study require rejection of both the null hypotheses and suggest that dental modeling resins may not necessarily provide lower volumetric polymerization shrinkage than conventional PMMA/MMA resins. The manufacturers of modeling resins do not specify the *P/L* mixing ratios because the products are generally used in the brush-dip technique. When using the technique, the *P/L* ratio can be altered by the skillfulness of the dental laboratory technicians or dental clinicians. In such a case, changes in the amounts of the BPO initiator in the powder and amine cointiator in the liquid can lead to changes in the rate of polymerization and, therefore, the final shrinkage-strain values [21]. In cases where resin samples are imperfectly cured, the measured shrinkage strain will be correspondingly

reduced [10]. Also, the low degree of conversion can affect the mechanical properties of a resin material [19]. In the case of dental modeling resins, however, reducing the volumetric shrinkage by controlling the degree of conversion at the cost of the mechanical properties might be permissible to some extent. Nonetheless, possible adverse effects of changing *P/L* ratio, producing either excessive shrinkage strain or underpolymerization, should be understood and where possible controlled [4]. These findings may also be helpful in determining the optimal formulation of “true” low or nonshrinkage dental acrylic resins.

#### 4. Conclusions

Within the limitations of this study, the following conclusions can be drawn.

- (1) The final volumetric shrinkage of dental PMMA/MMA resins, including modeling resins, was related to the polymerization kinetics rather than the prepolymerized PMMA particle sizes.
- (2) Dental modeling resins did not necessarily provide low volumetric shrinkage upon polymerization compared to the conventional PMMA/MMA resin when they were mixed at the same *P/L* ratio.

## Conflict of Interests

The authors declare that there is no conflict of interests regarding the publication of this paper.

## Acknowledgments

This work was supported by the National Research Foundation of Korea (NRF) Grant funded by the Korea Government (MSIP) (2008-0062282). The authors are also grateful to Dr. Myung-Hyun Lee, Korea Institute of Ceramic Engineering and Technology, Seoul, Republic of Korea, for his technical assistance with particle size analysis.

## References

- [1] G. Odian, *Principles of Polymerization*, John Wiley & Sons, Hoboken, NJ, USA, 2004.
- [2] K. L. van Landuyt, J. Snauwaert, J. de Munck et al., "Systematic review of the chemical composition of contemporary dental adhesives," *Biomaterials*, vol. 28, no. 26, pp. 3757–3785, 2007.
- [3] T. Y. Kwon, R. Bagheri, Y. K. Kim, K. H. Kim, and M. F. Burrow, "Cure mechanisms in materials for use in esthetic dentistry," *Journal of Investigative and Clinical Dentistry*, vol. 3, no. 1, pp. 3–16, 2012.
- [4] N. Silikas, A. Al-Kheraif, and D. C. Watts, "Influence of P/L ratio and peroxide/amine concentrations on shrinkage-strain kinetics during setting of PMMA/MMA biomaterial formulations," *Biomaterials*, vol. 26, no. 2, pp. 197–204, 2005.
- [5] D. Williams, R. W. Cahn, and M. B. Bever, *Concise Encyclopedia of Medical & Dental Materials*, Pergamon, Oxford, UK, 1990.
- [6] J. Fischer, A. Thoma, A. Suter, H. Lüthy, H.-U. Luder, and C. H.-F. Hämmerle, "Misfit of suprastructures on implants processed by electrical discharge machining or the Cresco method," *Quintessence International*, vol. 40, no. 6, pp. 515–522, 2009.
- [7] Y.-J. Kim, K.-H. Kim, and T.-Y. Kwon, "The influence of PMMA in 4-META/MMA-TBB resin on the degree of conversion and bonding durability to titanium," *Materials Science and Engineering C*, vol. 30, no. 1, pp. 219–223, 2010.
- [8] A. J. de Gee, A. J. Feilzer, and C. L. Davidson, "True linear polymerization shrinkage of unfilled resins and composites determined with a linometer," *Dental Materials*, vol. 9, no. 1, pp. 11–14, 1993.
- [9] S.-Y. Lee and S.-H. Park, "Correlation between the amount of linear polymerization shrinkage and cuspal deflection," *Operative Dentistry*, vol. 31, no. 3, pp. 364–370, 2006.
- [10] D. C. Watts and A. J. Cash, "Determination of polymerization shrinkage kinetics in visible-light-cured materials: methods development," *Dental Materials*, vol. 7, no. 4, pp. 281–287, 1991.
- [11] R. L. Sakaguchi, B. D. Wiltbank, and N. C. Shah, "Critical configuration analysis of four methods for measuring polymerization shrinkage strain of composites," *Dental Materials*, vol. 20, no. 4, pp. 388–396, 2004.
- [12] S. H. Kim and D. C. Watts, "Polymerization shrinkage-strain kinetics of temporary crown and bridge materials," *Dental Materials*, vol. 20, no. 1, pp. 88–95, 2004.
- [13] Y. Simon, E. Mortier, A. Dahoun, and D. Gerdolle, "Video-controlled characterization of polymerization shrinkage in light-cured dental composites," *Polymer Testing*, vol. 27, no. 6, pp. 717–721, 2008.
- [14] J. F. McCabe and A. W. G. Walls, *Applied Dental Materials*, Blackwell Publishing, Oxford, UK, 2008.
- [15] D. S. Achilias and I. Sideridou, "Study of the effect of two BPO/amine initiation systems on the free-radical polymerization of MMA used in dental resins and bone cements," *Journal of Macromolecular Science A: Pure and Applied Chemistry*, vol. 39, no. 12, pp. 1435–1450, 2002.
- [16] G. Williams and D. C. Watts, "Non-symmetrical dielectric relaxation behaviour arising from a simple empirical decay function," *Transactions of the Faraday Society*, vol. 66, pp. 80–85, 1970.
- [17] R. R. Braga and J. L. Ferracane, "Contraction stress related to degree of conversion and reaction kinetics," *Journal of Dental Research*, vol. 81, no. 2, pp. 114–118, 2002.
- [18] L. Feng and B. I. Suh, "The effect of curing modes on polymerization contraction stress of a dual cured composite," *Journal of Biomedical Materials Research B: Applied Biomaterials*, vol. 76, no. 1, pp. 196–202, 2006.
- [19] J. W. Stansbury, M. Trujillo-Lemon, H. Lu, X. Ding, Y. Lin, and J. Ge, "Conversion-dependent shrinkage stress and strain in dental resins and composites," *Dental Materials*, vol. 21, no. 1, pp. 56–67, 2005.
- [20] D. I. El-Korashy, "Post-gel shrinkage strain and degree of conversion of preheated resin composite cured using different regimens," *Operative Dentistry*, vol. 35, no. 2, pp. 172–179, 2010.
- [21] E. E. Rose, J. Lal, and R. Green, "Effects of peroxide, amine and hydroquinone in varying concentrations on the polymerization rate of polymethyl methacrylate slurries," *Journal of the American Dental Association*, vol. 56, no. 3, pp. 375–381, 1958.

## Research Article

# Preparation of Cylinder-Shaped Porous Sponges of Poly(L-lactic acid), Poly(DL-lactic-co-glycolic acid), and Poly( $\epsilon$ -caprolactone)

Xiaoming He, Naoki Kawazoe, and Guoping Chen

*Tissue Regeneration Materials Unit, International Center for Materials Nanoarchitectonics, National Institute for Materials Science, 1-1 Namiki, Tsukuba, Ibaraki 305-0044, Japan*

Correspondence should be addressed to Guoping Chen; [guoping.chen@nims.go.jp](mailto:guoping.chen@nims.go.jp)

Received 13 December 2013; Accepted 17 January 2014; Published 27 February 2014

Academic Editor: Yoshihiro Ito

Copyright © 2014 Xiaoming He et al. This is an open access article distributed under the Creative Commons Attribution License, which permits unrestricted use, distribution, and reproduction in any medium, provided the original work is properly cited.

Design of mechanical skeletons of biodegradable synthetic polymers such as poly(L-lactic acid) (PLLA), poly(DL-lactic-co-glycolic acid) (PLGA), and poly( $\epsilon$ -caprolactone) (PCL) is important in the construction of the hybrid scaffolds of biodegradable synthetic polymers and naturally derived polymers such as collagen. In this study, cylinder-shaped PLLA, PLGA, and PCL sponges were prepared by the porogen leaching method using a cylinder model. The effects of polymer type, polymer fraction, cylinder height, pore size, and porosity on the mechanical properties of the cylinder-shape sponges were investigated. SEM observation showed that these cylinder-shaped sponges had evenly distributed bulk pore structures and the wall surfaces were less porous with a smaller pore size than the wall bulk pore structures. The porosity and pore size of the sponges could be controlled by the ratio and size of the porogen materials. The PLGA sponges showed superior mechanical properties than those of the PLLA and PCL sponges. Higher porosity resulted in an inferior mechanical strength. The pore size and sponge height also affected the mechanical properties. The results indicate that cylinder-shaped sponges can be tethered by choosing the appropriate polymers, size and ratio of porogen materials and dimension of sponges based on the purpose of the application.

## 1. Introduction

Porous scaffolds have been used for three-dimensional cell cultures to construct functional tissues and organs for transplantation [1–4]. The porous scaffolds provide a temporary microenvironment for the seeded cells to control cell functions, provide sufficient space for new tissue formation, and protect cells from suppression by surrounding tissues. Various porous scaffolds have been developed from both synthetic and naturally derived polymers for tissue engineering and regeneration [5–12].

In addition to the ability to allow cell adhesion, promote cell proliferation and differentiation, assemble the cells and extracellular matrices, and guide the formation of functional tissues and organs, porous scaffolds should have high mechanical strength and high porosity [13, 14]. However,

porosity and mechanical strength are contradictory properties of porous scaffolds. Generally, high porosity results in low mechanical strength and vice versa. To solve the problem, biodegradable synthetic polymers such as poly(L-lactic acid) (PLLA), poly(glycolic acid) (PGA), poly(DL-lactic-co-glycolic acid) (PLGA), and poly( $\epsilon$ -caprolactone) (PCL) have been hybridized with naturally derived polymers such as collagen [15–19]. The mechanically strong synthetic polymers serve as a mechanical skeleton to support the hybrid porous scaffolds, whereas collagen sponges provide high porosity and a favorable microenvironment for cell proliferation and new tissue formation. We have used the hybridization method to prepare a new type of hybrid porous scaffolds by introducing collagen sponges into a cylinder-shaped PLLA sponge skeleton [20]. The cylinder-shaped PLLA-collagen hybrid sponges showed high mechanical strength and high

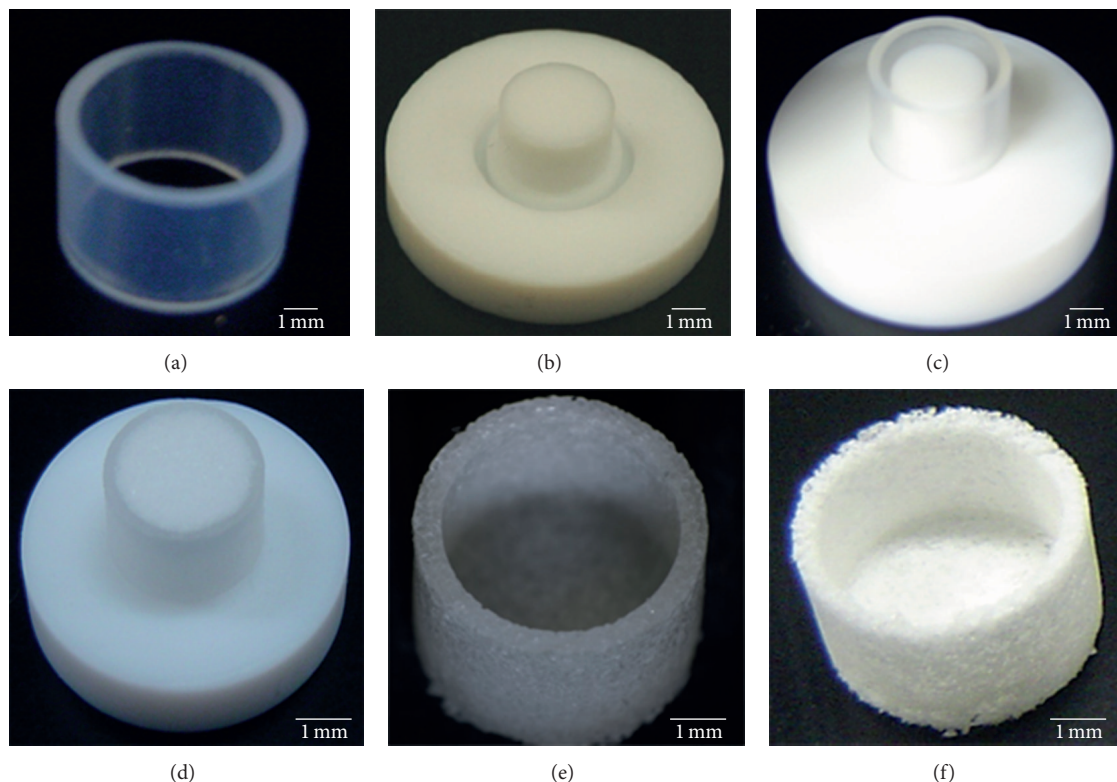


FIGURE 1: Photographs of the PFA tube (a), Teflon base (b), assembled Teflon mold (c), mixture of NaCl and PLLA filled within Teflon model (d), PLLA/NaCl cylinder (e), and cylinder-shaped PLLA sponge (f).

porosity. Compared to block-type hybrid sponges, cylinder-shaped PLLA-collagen hybrid sponges had a higher porosity [10, 20]. The key technique in the construction of such cylinder-shaped hybrid sponges is to assemble the cylinder-shaped porous skeletons from mechanically strong synthetic polymers. Therefore, in this study, we compared three types of biodegradable polymers, PLGA, PLLA, and PCL, for the creation of a mechanically strong and stable cylinder-shaped porous skeleton. The effects of synthetic polymer type, cylinder size, and preparation conditions on the mechanical strength of the cylinder-shaped skeletons were investigated to provide important information for polymer selection and the construction of optimal porous scaffolds for tissue engineering.

## 2. Experimental and Methods

Cylinder-shaped sponges were prepared by the method of porogen leaching using a Teflon mold. The Teflon mold consisted of a perfluoroalkoxy (PFA) tube having an inner diameter of 12 mm and a height of 9 mm (Figure 1(a)) and a Teflon base having a pillar with a diameter of 10 mm and a height of 6 mm (Figure 1(b)). The PFA tube was plugged into the groove to construct the Teflon mold (Figure 1(c)). By using the Teflon mold, cylinder-shaped sponges having an inner diameter of 10 mm, an outer diameter of 12 mm, and a height of 7 mm can be prepared. Poly(L-lactic acid) (PLLA, weight-average molecular weight:  $116,000 \pm 4700$ ,

Sigma-Aldrich, Inc., St. Louis, MO) was used to prepare the cylinder-shaped PLLA sponges. The  $T_g$  of PLLA is  $47^\circ\text{C}$  [21]. PLLA (1 g) was dissolved in chloroform (5 mL) in a glass tube, to which sieved sodium chloride (NaCl) particulates (9 g) were added and mixed well. Sieved NaCl particulates ranging between 90–150, 150–250, and 250–355  $\mu\text{m}$  were used to prepare the cylinder-shaped PLLA sponges with different pore sizes. The space between the PFA tube and the Teflon base of the Teflon mold was filled with the polymer solution/NaCl mixture by pressing the mixture into the space. The pressed mixture above the PFA tube was removed by trimming the top surface (Figure 1(d)). The filled Teflon mold was dried in an air draft for 1 day and vacuum-dried for another 3 days to allow the chloroform to evaporate completely. After drying, the Teflon mold was disassembled to remove the cylinder of the polymer/NaCl mixture from the Teflon mold (Figure 1(e)). The polymer/NaCl cylinder was immersed in deionized water to leach out the NaCl particulates. The deionized water was changed every hour. The washing was continued until the complete removal of NaCl. The cylinder-shaped PLLA sponges were dried in air after washing (Figure 1(f)).

The weight ratio of PLLA to NaCl particulates was adjusted at 1:4, 1:5, 1:6, 1:7, 1:8, and 1:9 to prepare cylinder-shaped PLLA sponges of different porosity. Either 4, 5, 6, 7, 8, or 9 grams of the sieved sodium chloride (NaCl) particulates, with a diameter ranging from 150 to 255  $\mu\text{m}$ , was added to the PLLA solution in chloroform (1 g/5 mL) and mixed well. The following steps were the same as those described above.

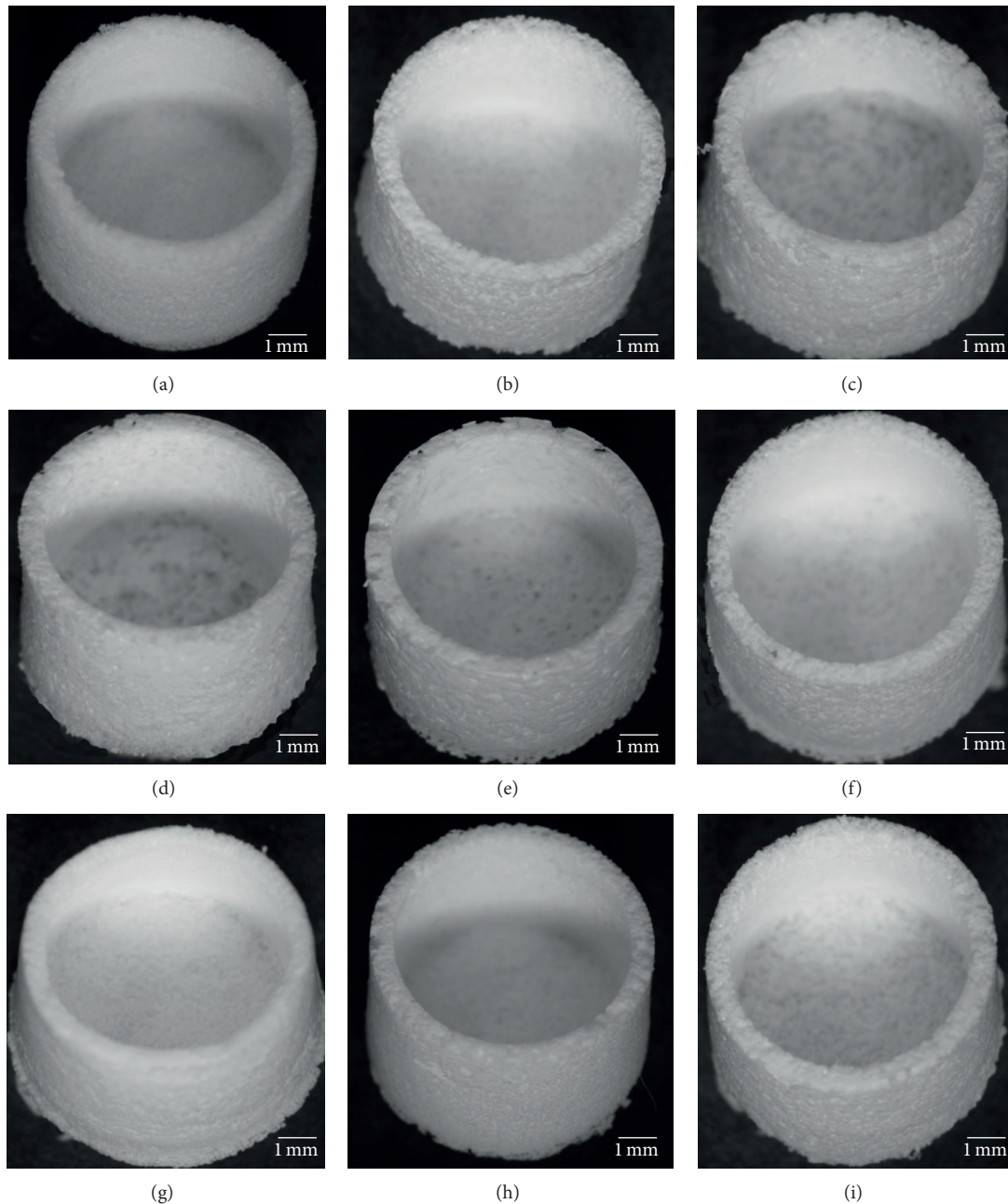


FIGURE 2: Photographs of cylinder-shaped PLLA (a–c), PLGA (d–f), and PCL (g–i) sponges prepared with NaCl particulates having a diameter range of 90–150  $\mu\text{m}$  (a, d, g), 150–250  $\mu\text{m}$  (b, e, h), and 250–355  $\mu\text{m}$  (c, f, i). The ratio of polymer to NaCl was 1 : 9.

Cylinder-shaped PLLA sponges of different heights were prepared by cutting the cylinder of the polymer/NaCl mixture to a specific height during the above described preparation using 150–255  $\mu\text{m}$  NaCl particulates and a polymer/NaCl ratio of 1 : 9. Five heights (2, 3, 4, 5, 6, and 7 mm) of cylinder-shaped PLLA sponges were prepared to compare the effect of height on the mechanical properties.

Cylinder-shaped PLGA and PCL sponges were prepared by the same method as the cylinder-shaped PLLA sponges described above. Poly(DL-lactic-co-glycolic acid) with a copolymer ratio of 75/25 (D,L-lactic acid/glycolic acid)

(PLGA, weight-average molecular weight:  $109,520 \pm 1,670$ , Sigma-Aldrich, Inc., St. Louis, MO) and poly( $\epsilon$ -caprolactone) (PCL, weight-average molecular weight:  $261,000 \pm 2800$ , Sigma-Aldrich, Inc., St. Louis, MO) were used to prepare the respective cylinder-shaped PLGA and PCL sponges. The Tg of PLGA and PCL is 41 and  $-56^\circ\text{C}$ , respectively [21]. Sieved NaCl particulates with diameter ranges of 90–150, 150–250, and 250–355  $\mu\text{m}$  were used. The ratio of polymer to NaCl particulates was 1 : 9. The sponge height was 7 mm.

Cross-sections of the cylinder-shaped PLLA, PLGA, and PCL sponges were made by sectioning the sponges with

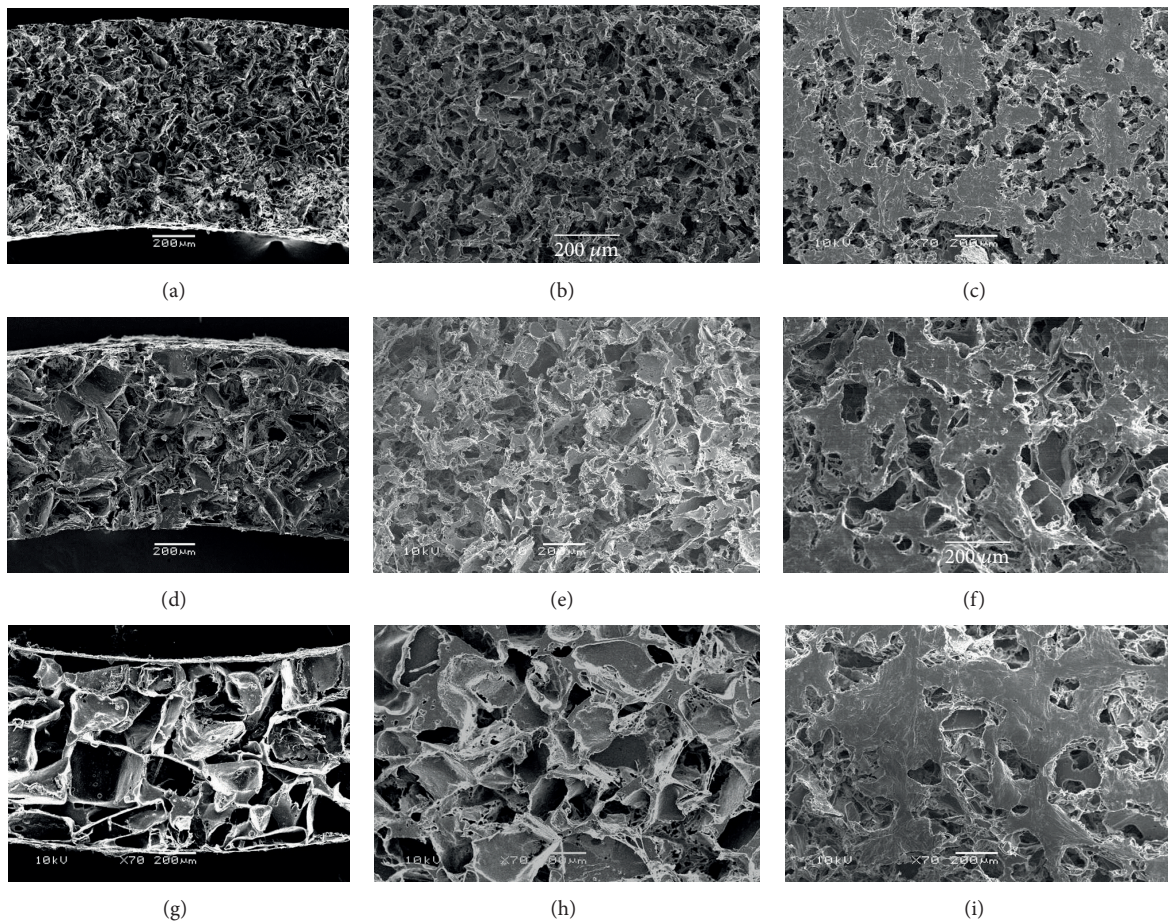


FIGURE 3: SEM microphotographs of vertical cross-sections (a, d, g), horizontal cross-sections (b, e, h), and the inner surfaces (c, f, i) of the cylinder-shaped PLLA sponges prepared with NaCl particulates having a diameter range of 90–150  $\mu\text{m}$  (a–c), 150–250  $\mu\text{m}$  (d–f), and 250–355  $\mu\text{m}$  (g–i). The ratio of polymer to NaCl was 1:9.

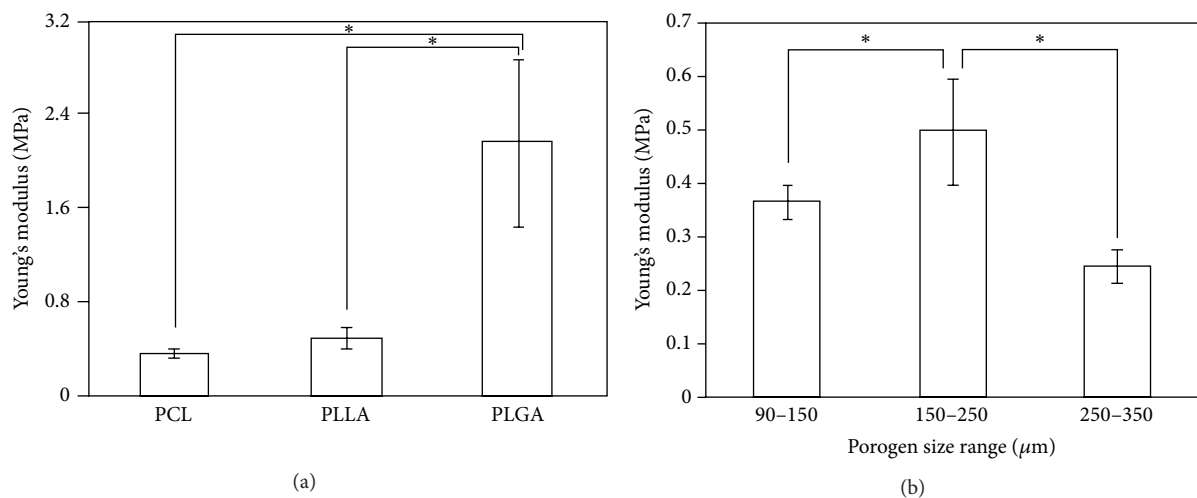


FIGURE 4: Young's modulus of cylinder-shaped PLLA, PLGA, and PCL sponges prepared with 150–250  $\mu\text{m}$  NaCl particulates (a) and cylinder-shaped PLLA sponges prepared with 90–150  $\mu\text{m}$ , 150–250  $\mu\text{m}$ , and 250–355  $\mu\text{m}$  NaCl particulates (b). The ratio of polymer to NaCl was 1:9. The data represent the mean  $\pm$  SD of six samples.

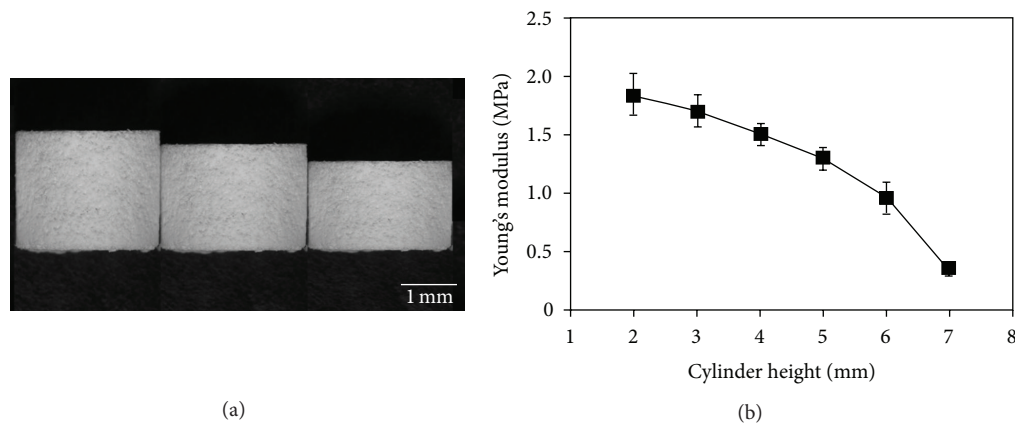


FIGURE 5: Photographs of cylinder-shaped PLLA sponges having a height of 7, 6, and 5 mm (a) and the change in Young's modulus with the sponge height (b). The data represent the mean  $\pm$  SD of six samples.

a razor blade. The cross-section samples were coated with platinum using a sputter coater (Sanyu Denshi, Tokyo, Japan). The wall surfaces and cross-sections of the sponges were observed by scanning electron microscopy (SEM) (JSM-6400Fs; JEOL, Tokyo, Japan).

A mercury porosimeter (Autopore IV, Shimadzu, Kyoto, Japan) was used to measure the porosity of the cylinder-shaped sponges. The sponges were cut into small pieces for the measurement.

A mechanical testing machine (TA.XTplus, Stable Micro System, UK) was used to measure the mechanical properties of the cylinder-shaped PLLA, PLGA, and PCL sponges. The dimension of each sample was measured. The dry sponges were compressed at a speed of 0.1 mm/min at room temperature. The load-deformation curves were recorded and used to calculate the elastic modulus. The calculation was done by using the software Texture Analyzer 32 provided by the same company. A total of six samples were used for the measurements of each sponge. Data were reported as mean  $\pm$  standard deviation. One-way analysis of variance (ANOVA) was performed to reveal difference in Young's modulus among groups using the *t*-test. All statistical analyses were executed using StatFlex Ver. 4.2;  $P < 0.05$  was considered statistically significant.

### 3. Results and Discussion

Porous cylinder-shaped sponges of PLLA, PLGA, and PCL were prepared using a porogen leaching method. NaCl particulates ranging between 90–150  $\mu\text{m}$ , 150–250  $\mu\text{m}$ , and 250–355  $\mu\text{m}$  were used as the porogen materials and the ratio of polymer to NaCl particulates was 1:9. Figure 2 shows the gross appearance of cylinder-shaped PLLA, PLGA, and PCL sponges. The height of these cylinder-like sponges was 7 mm. All of the sponges showed cylinder-like shape and were physically stable. The polymer type and the size of the NaCl particulates did not affect the gross appearance of the cylinder-shaped sponges. This method could be used to prepare cylinder-shaped sponges of different synthetic polymers by choosing the appropriate polymers.

The porous structures of the cylinder-shaped sponges were investigated by SEM observation. The SEM images of a horizontal cross-section, a vertical cross-section, and the wall surface of cylinder-shaped PLLA sponges are shown in Figure 3. All of these cylinder-shaped sponges were highly porous with evenly distributed and interconnected pore structures in the cross-sections (bulk pore structure). The pore shapes shown in the cross-sections were similar to those of NaCl particulates. The pore size of the cylinder-shaped PLLA sponges prepared with 90–150  $\mu\text{m}$ , 150–250  $\mu\text{m}$ , and 250–355  $\mu\text{m}$  NaCl particulates increased with the size increase of the NaCl particulates. However, pores on the wall surfaces were fewer and smaller than those in the cross-sections. The inner wall surface and outer wall surface of the cylinder-shaped PLLA sponge showed the same pore structures. The less dense and smaller pore structure on the wall surfaces might be due to the contact effect between the NaCl particulates and the Teflon mold when the mixture of polymer solution and NaCl particulates was pressed into the Teflon mold. The angles of the cuboidal-like NaCl particulates might contact the Teflon mold and give more space for the polymer solution to fill the spaces among the angles in contact with the Teflon mold. The structures of the inner wall and the outer wall surfaces of the cylinder-shaped sponges are expected to partially protect from cell leakage during the cell seeding and cell culture. The cylinder-shaped PLGA and PCL sponges showed similar pore structures compared to that of the cylinder-shaped PLLA sponges.

The mechanical properties of the cylinder-shaped PLLA, PCL, and PLGA sponges were measured by a compression test. The Young's modulus of cylinder-shaped PLLA, PCL, and PLGA sponges prepared with 150–250  $\mu\text{m}$  NaCl particulates and a ratio of polymer to NaCl of 1:9 changed depending on the polymers used for the sponge preparation (Figure 4(a)). The cylinder-shaped PLGA sponge showed the highest Young's modulus, and the PCL sponge showed the lowest. PLLA is a crystalline polymer with high rigidity, while PLGA is an amorphous polymer [21]. PCL is a semicrystalline polymer and is in a rubbery state at room temperature

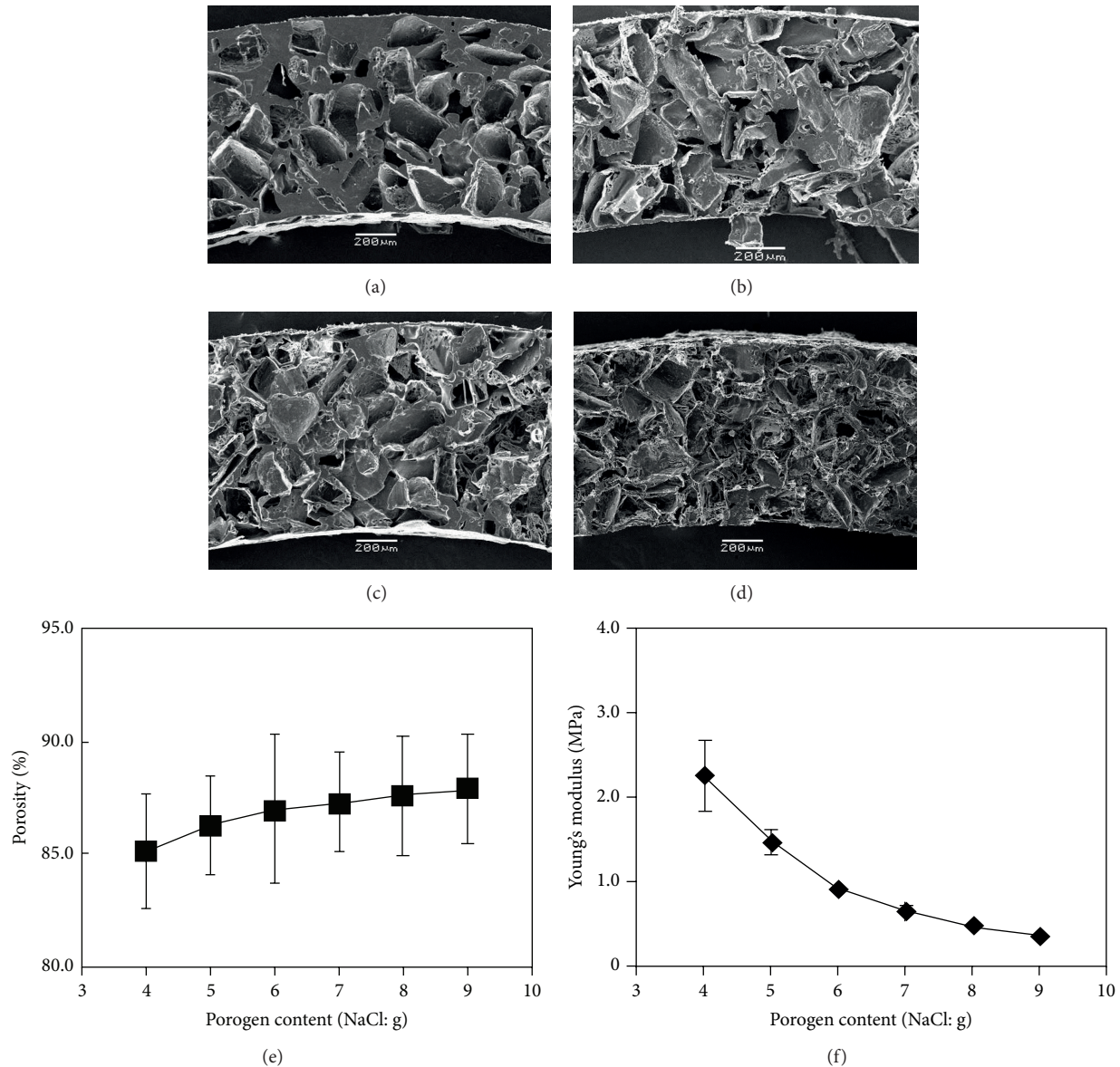


FIGURE 6: SEM microphotographs of vertical cross-sections (a–d) of the cylinder-shaped PLLA sponges prepared with 150–250 μm NaCl particulates at the polymer/NaCl ratio of 1: 4 (a), 1: 5 (b), 1: 6 (c) and 1: 9 (d) and the change of porosity (e) and Young's modulus (f) with the polymer/NaCl ratio. The porosity data represent the average ± SD of three samples and the Young's modulus data represent the mean ± SD of six samples.

because of its low glass transition temperature [22]. The viscoelastic property of PCL resulted in a low Young's modulus. The rigid crystalline PLLA also showed a low Young's modulus. The amorphous PLGA showed the highest Young's modulus. The low Young's modulus of cylinder-shaped PLGA sponge might be due to the difficulty in homogenous filling of PLLA/NaCl mixture in the space of Teflon mold because of the high viscosity of PLLA solution.

The size of the NaCl particulates also showed some effect on the Young's modulus. The cylinder-shaped PLLA sponges prepared with a ratio of polymer to NaCl of 1:9 and NaCl particles of different sizes ranging between 90–150 μm, 150–250 μm, and 250–355 μm were compared (Figure 4(b)). The

cylinder-shaped PLLA sponge prepared with 150–250 μm NaCl particulates showed the highest mechanical strength, suggesting that a cylinder-like PLLA sponge with pores ranging between 150 and 250 μm in size was architecturally stronger and more appropriate for applications in tissue engineering when high mechanical strength is necessary than the other tested configurations. The NaCl particles with sizes ranging between 150 and 250 μm might be appropriately packed and polymer matrix could appropriately fill the spaces among the NaCl particles.

The effect of the height of the cylinder-shaped PLLA sponge on the mechanical properties was investigated. Cylinder-shaped PLLA sponges with different heights of 2,

3, 4, 5, 6, and 7 mm were prepared and their mechanical strengths were compared (Figure 5). The mechanical strength decreased when the height of the cylinder-like PLLA sponge increased.

The mechanical property and porosity of cylinder-shaped PLLA sponges prepared with different ratio of PLLA to NaCl particulates were compared. Six types of cylinder-shaped PLLA sponges were prepared with a weight ratio of PLLA to NaCl particulates of 1:4, 1:5, 1:6, 1:7, 1:8, and 1:9. SEM microphotographs of the cross-sections of these PLLA sponges showed that more pores were observed in the cylinder-shaped PLLA sponge prepared with a higher weight fraction of NaCl particulates (Figures 6(a)–6(d)). The porosity increased when the NaCl ratio increased (Figure 6(e)). Young's modulus decreased with the increase in NaCl fraction (Figure 6(f)). A high ratio of NaCl particulates resulted in high porosity and low mechanical strength.

Mechanically strong biodegradable synthetic polymers have been hybridized with naturally derived biodegradable polymers to construct hybrid porous scaffolds [15–19]. The hybrid porous scaffolds combine the advantages of both polymers and have been used for the tissue engineering of various tissues, such as skin [23], cartilage [24, 25], bone [26], ligament [27], bladder [19], and osteochondral tissue [28]. Use of a cylinder-shaped skeleton can improve the mechanical property and simultaneously increase the porosity to provide more space for cell accommodation [20, 29]. The preparation of such cylinder-shaped skeleton is important for the formation of the hybrid structure. In this study, the effect of polymer type, pore size, and porosity on the property of the cylinder-shaped skeleton was discussed. PLLA, PLGA, and PCL can all be used to construct the cylinder-shaped sponges, while their mechanical property was dependent on the polymer type. Polymers should be selected based on the requirements of the tissue engineering application. The pore size, porosity, and cylinder height also affected the mechanical properties. The mechanical properties can be tethered by choosing the appropriate pore size and porosity and designing the dimension of the cylinder-shaped skeletons.

#### 4. Conclusions

Three biodegradable synthetic polymers, PLLA, PLGA, and PCL, were used to prepare cylinder-shaped sponges using a porogen leaching method and their properties were compared. The cylinder-shaped sponges showed a porous and interconnected structure in their bulk parts, while they were less porous with smaller pores on their surfaces. The pore size and porosity could be controlled by the size and ratio of the porogen materials. The pore size, porosity, and sponge height showed some effect on the mechanical property of the sponges. The mechanical property of the cylinder-shaped sponges was also dependent on the polymer type. The PLGA sponge showed the highest mechanical strength. Therefore, the pore structure and mechanical property of the cylinder-shaped sponges could be controlled by choosing the appropriate polymers and designing the preparation conditions according to the specific application in tissue engineering.

#### Conflict of Interests

The authors declare that there is no conflict of interests regarding the publication of this paper.

#### Acknowledgments

This work was supported by the World Premier International Research Center Initiative on Materials Nanoarchitectonics from the Ministry of Education, Culture, Sports, Science and Technology, Japan.

#### References

- [1] S. J. Hollister, "Porous scaffold design for tissue engineering," *Nature Materials*, vol. 4, pp. 518–524, 2005.
- [2] F. T. Moutos, L. E. Freed, and F. Guilak, "A biomimetic three-dimensional woven composite scaffold for functional tissue engineering of cartilage," *Nature Materials*, vol. 6, no. 2, pp. 162–167, 2007.
- [3] Y. Huang, X. Jin, X. Zhang et al., "In vitro and in vivo evaluation of akermanite bioceramics for bone regeneration," *Biomaterials*, vol. 30, no. 28, pp. 5041–5048, 2009.
- [4] Q. Fu, Y. Hong, X. Liu, H. Fan, and X. Zhang, "A hierarchically graded bioactive scaffold bonded to titanium substrates for attachment to bone," *Biomaterials*, vol. 32, no. 30, pp. 7333–7346, 2011.
- [5] H. Lu, T. Hoshiba, N. Kawazoe, and G. Chen, "Autologous extracellular matrix scaffolds for tissue engineering," *Biomaterials*, vol. 32, no. 10, pp. 2489–2499, 2011.
- [6] T. Hoshiba, N. Kawazoe, T. Tateishi, and G. Chen, "Development of extracellular matrices mimicking stepwise adipogenesis of mesenchymal stem cells," *Advanced Materials*, vol. 22, no. 28, pp. 3042–3047, 2010.
- [7] L. D. Wright, R. T. Young, T. Andric, and J. W. Freeman, "Fabrication and mechanical characterization of 3D electrospun scaffolds for tissue engineering," *Biomedical Materials*, vol. 5, no. 5, Article ID 055006, 2010.
- [8] Y.-G. Ko, N. Kawazoe, T. Tateishi, and G. Chen, "Preparation of novel collagen sponges using an ice particulate template," *Journal of Bioactive and Compatible Polymers*, vol. 25, no. 4, pp. 360–373, 2010.
- [9] S. C. Owen and M. S. Shoichet, "Design of three-dimensional biomimetic scaffolds," *Journal of Biomedical Materials Research A*, vol. 94, pp. 1321–1331, 2010.
- [10] Y.-G. Ko, S. Grice, N. Kawazoe, T. Tateishi, and G. Chen, "Preparation of collagen-glycosaminoglycan sponges with open surface porous structures using ice particulate template method," *Macromolecular Bioscience*, vol. 10, no. 8, pp. 860–871, 2010.
- [11] H. Lu, Y.-G. Ko, N. Kawazoe, and G. Chen, "Cartilage tissue engineering using funnel-like collagen sponges prepared with embossing ice particulate templates," *Biomaterials*, vol. 31, no. 22, pp. 5825–5835, 2010.
- [12] G. Chen, T. Ushida, and T. Tateishi, "Poly(DL-lactic-co-glycolic acid) sponge hybridized with collagen microsponges and deposited apatite particulates," *Journal of Biomedical Materials Research*, vol. 57, no. 1, pp. 8–14, 2001.
- [13] G. C. Engelmayr Jr., M. Cheng, C. J. Bettinger, J. T. Borenstein, R. Langer, and L. E. Freed, "Accordion-like honeycombs for tissue engineering of cardiac anisotropy," *Nature Materials*, vol. 7, no. 12, pp. 1003–1010, 2008.

- [14] I. S. Muhammad, X. Xu, and L. Li, "A review on biodegradable polymeric materials for bone tissue engineering applications," *Journal of Materials Science*, vol. 44, no. 21, pp. 5713–5724, 2009.
- [15] W. Dai, N. Kawazoe, X. Lin, J. Dong, and G. Chen, "The influence of structural design of PLGA/collagen hybrid scaffolds in cartilage tissue engineering," *Biomaterials*, vol. 31, no. 8, pp. 2141–2152, 2010.
- [16] M. Ananta, C. E. Aulin, J. Hilborn et al., "A poly(lactic acid-co-caprolactone)-collagen hybrid for tissue engineering applications," *Tissue Engineering A*, vol. 15, no. 7, pp. 1667–1675, 2009.
- [17] Y. Hiraoka, Y. Kimura, H. Ueda, and Y. Tabata, "Fabrication and biocompatibility of collagen sponge reinforced with poly(glycolic acid) fiber," *Tissue Engineering*, vol. 9, no. 6, pp. 1101–1112, 2003.
- [18] Y. Takahashi, M. Yamamoto, and Y. Tabata, "Enhanced osteoinduction by controlled release of bone morphogenetic protein-2 from biodegradable sponge composed of gelatin and  $\beta$ -tricalcium phosphate," *Biomaterials*, vol. 26, no. 23, pp. 4856–4865, 2005.
- [19] E.-M. Engelhardt, L. A. Micol, S. Houis et al., "A collagen-poly(lactic acid-co-caprolactone) hybrid scaffold for bladder tissue regeneration," *Biomaterials*, vol. 32, no. 16, pp. 3969–3976, 2011.
- [20] X. He, H. Lu, N. Kawazoe, T. Tateishi, and G. Chen, "A novel cylinder-type poly(L-Lactic Acid)-collagen hybrid sponge for cartilage tissue engineering," *Tissue Engineering C*, vol. 16, no. 3, pp. 329–338, 2010.
- [21] T. Yoshioka, F. Kamada, N. Kawazoe, T. Tateishi, and G. Chen, "Structural changes and biodegradation of PLLA, PCL, and PLGA sponges during in vitro incubation," *Polymer Engineering and Science*, vol. 50, no. 10, pp. 1895–1903, 2010.
- [22] M. A. Woodruff and D. W. Hutmacher, "The return of a forgotten polymer: polycaprolactone in the 21st century," *Progress in Polymer Science*, vol. 35, no. 10, pp. 1217–1256, 2010.
- [23] G. Chen, T. Sato, H. Ohgushi, T. Ushida, T. Tateishi, and J. Tanaka, "Culturing of skin fibroblasts in a thin PLGA-collagen hybrid mesh," *Biomaterials*, vol. 26, no. 15, pp. 2559–2566, 2005.
- [24] G. Chen, T. Sato, T. Ushida, N. Ochiai, and T. Tateishi, "Tissue engineering of cartilage using a hybrid scaffold of synthetic polymer and collagen," *Tissue Engineering*, vol. 10, no. 3-4, pp. 323–330, 2004.
- [25] G. Chen, T. Sato, T. Ushida et al., "The use of a novel PLGA fiber/collagen composite web as a scaffold for engineering of articular cartilage tissue with adjustable thickness," *Journal of Biomedical Materials Research A*, vol. 67, no. 4, pp. 1170–1180, 2003.
- [26] K. Tsuchiya, T. Mori, G. Chen et al., "Custom-shaping system for bone regeneration by seeding marrow stromal cells onto a web-like biodegradable hybrid sheet," *Cell and Tissue Research*, vol. 316, no. 2, pp. 141–153, 2004.
- [27] G. Chen, T. Sato, M. Sakane et al., "Application of PLGA-collagen hybrid mesh for three-dimensional culture of canine anterior cruciate ligament cells," *Materials Science and Engineering C*, vol. 24, no. 6–8, pp. 861–866, 2004.
- [28] G. Chen and J. Tanaka, "Osteochondral tissue engineering using a PLGA-collagen hybrid mesh," *Materials Science and Engineering C*, vol. 26, no. 1, pp. 124–129, 2006.
- [29] N. Kawazoe, C. Inoue, T. Tateishi, and G. Chen, "A cell leakproof PLGA-collagen hybrid scaffold for cartilage tissue engineering," *Biotechnology Progress*, vol. 26, no. 3, pp. 819–826, 2010.

## Research Article

# Collagen Scaffolds with Controlled Insulin Release and Controlled Pore Structure for Cartilage Tissue Engineering

Himansu Sekhar Nanda,<sup>1,2</sup> Shangwu Chen,<sup>1,2</sup> Qin Zhang,<sup>1,2</sup>  
Naoki Kawazoe,<sup>1</sup> and Guoping Chen<sup>1,2</sup>

<sup>1</sup> Tissue Regeneration Materials Unit, International Centre for Materials Nanoarchitectonics, National Institute for Materials Science, 1-1 Namiki, Tsukuba, Ibaraki 305-0044, Japan

<sup>2</sup> Department of Materials Science and Engineering, Graduate School of Pure and Applied Sciences, University of Tsukuba, 1-1-1 Tennodai, Tsukuba, Ibaraki 305-8571, Japan

Correspondence should be addressed to Guoping Chen; [guoping.chen@nims.go.jp](mailto:guoping.chen@nims.go.jp)

Received 13 December 2013; Accepted 20 January 2014; Published 25 February 2014

Academic Editor: Oh Hyeong Kwon

Copyright © 2014 Himansu Sekhar Nanda et al. This is an open access article distributed under the Creative Commons Attribution License, which permits unrestricted use, distribution, and reproduction in any medium, provided the original work is properly cited.

Controlled and local release of growth factors and nutrients from porous scaffolds is important for maintenance of cell survival, proliferation, and promotion of tissue regeneration. The purpose of the present research was to design a controlled release porous collagen-microbead hybrid scaffold with controlled pore structure capable of releasing insulin for application to cartilage tissue regeneration. Collagen-microbead hybrid scaffold was prepared by hybridization of insulin loaded PLGA microbeads with collagen using a freeze-drying technique. The pore structure of the hybrid scaffold was controlled by using preprepared ice particulates having a diameter range of 150–250  $\mu\text{m}$ . Hybrid scaffold had a controlled pore structure with pore size equivalent to ice particulates and good interconnection. The microbeads showed an even spatial distribution throughout the pore walls. *In vitro* insulin release profile from the hybrid scaffold exhibited a zero order release kinetics up to a period of 4 weeks without initial burst release. Culture of bovine articular chondrocytes in the hybrid scaffold demonstrated high bioactivity of the released insulin. The hybrid scaffold facilitated cell seeding and spatial cell distribution and promoted cell proliferation.

## 1. Introduction

Hyaline articular cartilage is composed of abundant chondrocytes and limited progenitor cells sparsely embedded in nonvascular extracellular matrix (ECM). Articular cartilage defects are very difficult to heal due to its limited ability of self-repair and regeneration [1–3]. Such defects if untreated may lead to the serious problem of osteoarthritis, a major clinical problem around the world [4, 5]. Current treatment methods for articular cartilage defects include abrasion arthroplasty, subchondral drilling, osteochondral allografting, and periosteal or perichondral tissue grafting [6, 7]. However none of the treatment methods can reproduce the exact characteristics of a hyaline cartilage for optimal healing of the tissue defects. Therefore, cartilage tissue engineering using porous scaffolds, chondrocytes or human mesenchymal stem cells (hMSCs), and bioactive instructive cues has been

evolved as an alternative and promising approach to treat cartilage defects [1–3, 6, 8].

Porous scaffolds prepared from biodegradable polymers have been well studied for their ability to regenerate various types of tissues such as skin, cartilage, and bone [9–14]. Collagen as a natural biomaterial and a component of native extracellular matrix (ECM) is extensively investigated for preparation of porous scaffolds for cartilage tissue engineering [10, 13, 15]. However weak mechanical strength of the scaffolds prepared from collagen remains a major hurdle behind the clinical application. Recently, we have developed collagen porous scaffolds with controlled pore structures as an ideal platform for cartilage tissue regeneration because of its high porosity with good pore interconnection, excellent control over the pore structure, and impressive biomechanical properties [15]. Large scaffolds are often needed for major cartilage defects. Formation of necrotic cores due to nutrient

depletion is another problem during *in vitro* cell culture over these three-dimensional (3D) scaffolds. It is difficult for nutrients and essential growth factors to diffuse inside the complex porous network of the 3D construct for proper nourishment of the inner cell mass leading to the formation of necrotic cores [16, 17]. Growth factor and therapeutics are widely employed for maintenance of cell viability, proliferation, and promotion of tissue regeneration [18, 19]. Controlled and localized delivery of these factors has been addressed to improve on site access to the cells in 3D microenvironment [18–22]. Insulin administration has demonstrated its ability to prolong the survival of chondrocytes and prevent the formation of necrotic cores inside the 3D collagen hydrogel construct [4, 17]. Furthermore insulin has its structural similarity to IGF-1 and may bind to the IGF-1 receptor to elicit similar effect on cartilage. This suggests that insulin can be an appropriate and inexpensive alternative growth factor to improve cartilage regeneration in 3D porous scaffolds [22]. Therefore development of suitable porous scaffold having good mechanical strength and controlled release of bioactive insulin for a prolonged duration is desirable for cartilage tissue engineering. Controlled and prolonged delivery of the insulin using PLGA microbeads prepared by water-in-oil-in-water (w-o-w) double emulsification technique has been demonstrated to be useful in cartilage tissue engineering [22]. Entrapment of these biodegradable microbeads carrying insulin within porous scaffolds of high mechanical strength may generate appropriate scaffolds for cartilage tissue regeneration.

In this research, we have made an attempt to prepare porous scaffolds with a controlled pore structure and controlled release of insulin as a bioactive 3D culture system for cartilage tissue engineering. The porous scaffold was prepared by spatial localization of insulin loaded PLGA microbeads in a 3D collagen porous scaffold by using a freeze-drying technique. Preprepared ice particulates having a diameter range of 150–250  $\mu\text{m}$  were used to control the pore structure of the scaffold. *In vitro* insulin release and degradation were studied over 4-week period at 37°C under shaking condition. Bovine articular chondrocytes were cultured in the hybrid scaffold to investigate the effect of released insulin on cell viability and proliferation.

## 2. Materials and Methods

**2.1. Materials.** PLGA (copolymer composition ratio of 50:50, weight average molecular weight of 20 kDa, and inherent viscosity of 0.187 to 0.229 dL/g), methylene chloride ( $\text{CH}_2\text{Cl}_2$ ), polyvinyl alcohol (86–90 mol% hydrolysis), recombinant human insulin, hydrochloric acid (HCl), sodium hydroxide (NaOH), absolute ethanol (99.5%), N-hydroxysuccinimide esters (NHS), 25% glutaraldehyde solution, and sodium dihydrogen phosphate ( $\text{NaH}_2\text{PO}_4$ ) were obtained from Wako Pure Chemicals Ltd., Japan. L-cysteine hydrochloride monohydrate (minimum 98%), ethylene diamine tetra acetic acid (EDTA), papain, DNA quantification kit, Dulbecco's Modified Eagle's Medium (DMEM), growth supplements, and antibiotics were

obtained from Sigma-Aldrich, USA. Phosphate buffer saline (10x, pH = 7.4) was obtained from Nacali Tesque Inc., Japan. Porcine collagen type-1 was obtained from Nitta Gelatin, Japan. 1-Ethyl-3-[3-dimethylaminopropyl] carbodiimide hydrochloride (EDC/EDAC) was obtained from Peptide Institute Inc., Japan. Cellstain Double Staining Kit was obtained from Dojindo Laboratories, Japan. Micro BCA protein assay Kit was obtained from Pierce Biotechnology, USA. All the materials in this study were used as received without further purification. Molecular biology grade milli-Q water from millipore water system (Millipore Corporation, USA) was used for preparation of all the solutions and reagents.

### 2.2. Methods

**2.2.1. Insulin Microencapsulation.** Insulin was microencapsulated in PLGA microbeads using w-o-w double emulsion technique [22–24]. PLGA solution at concentration of 0.5  $\text{g mL}^{-1}$  was prepared by dissolving PLGA in methylene chloride. 50  $\mu\text{L}$  of insulin solution (insulin in 0.01 M HCl) at a concentration of 20  $\text{mg mL}^{-1}$  ( $w_1$ ) was dispersed in 1 mL of PLGA (o) by homogenization at 8000 rpm for 1 minute. The resulted emulsion was further reemulsified in 2 mL saturated PVA ( $w_2$ ) prepared by mixing 1:1 (v/v) of 3% aqueous PVA and methylene chloride. The reemulsification process was carried out under high speed homogenization at 2000 rpm for 10 minutes. The double emulsion was added dropwise to 200 mL of 0.5% (w/v) PVA and stirred magnetically at 300 rpm in a hood for overnight to allow adequate solvent evaporation. The hardened microbeads were recovered after centrifugation (3500 rpm for 5 minutes). The microbeads were washed with milli-Q water and freeze-dried for 48 hours in a freeze drier (Vir Tis AdVantage Benchtop Freeze Dryer, S P Industries Inc., Japan) below 5 kPa to obtain dried insulin loaded PLGA microbeads.

**2.2.2. Preparation of Collagen-Microbead Hybrid Porous Scaffold.** The collagen-microbead hybrid porous scaffolds were prepared by a freeze-drying method using preprepared ice particulates of a diameter range of 150–250  $\mu\text{m}$  as porogen material [15]. Ice particulates were prepared by spraying pure water droplets into liquid  $\text{N}_2$  and stabilized at  $-15^\circ\text{C}$  in a low temperature chamber (WT-201, ESPEC Corp., Osaka, Japan). The ice particulates of 150–250  $\mu\text{m}$  were selectively sieved using two testing sieves having mesh pores of 150 and 250  $\mu\text{m}$  (Tokyo screen co. ltd., Japan). Hybrid scaffold was prepared from 2.0% (w/v) collagen aqueous solution with a ratio of ice particulate to collagen as 50:50 (w/v). The collagen aqueous solution (2.2% (w/v)) was prepared by dissolving freeze-dried collagen in a mixture solution of acetic acid (0.1 M, pH 3.0) and 10% ethanol. Dried insulin loaded PLGA microbeads were dispersed in 10% ethanol to prepare a suspension. The microbead suspension was sonicated for 1 minute in an ultrasonic water bath (Branson Ultrasonic Corporation, USA) in order to ensure free dispersion of microbeads. 2.2% (w/v) collagen aqueous solution was mixed with the prepared microbead suspension at a ratio of 9:1 to

prepare microbead dispersed collagen aqueous solution. The manipulation was carried out at 4°C and the mixture solution was stirred under magnetic stirring for 1-2 hour. The mixture solution was transferred to a low temperature chamber maintained at -5°C and stirred magnetically for 2 hours for temperature balance. Ice particulates were added to the collagen-microbead mixture solution and mixed thoroughly to prepare a homogeneous ternary mixture of ice particulates, collagen, and microbeads. The final mixture was molded in a 5 mm thick silicone frame template. The mold was freeze-dried for 72 hours in a freeze drier. The freeze-dried scaffolds were cross-linked in 50 mM EDC and 20 mM NHS in 90% (v/v) ethanol for 24 hours at room temperature (RT). The cross-linked scaffolds were washed with milli-Q water and subjected to second freeze drying to prepare the final hybrid scaffolds. Control collagen porous scaffold was also prepared by using the similar procedure without the use of microbeads.

**2.2.3. Scanning Electron Microscopy (SEM).** The morphology of insulin loaded microbeads and scaffold microstructure was examined using a scanning electron microscope (SEM, JSM-5610, JEOL Ltd., Tokyo, Japan). Freeze-dried microbeads were dispersed over a carbon adhesive mounted over a copper stub and were sputtered with a thin layer of platinum by a sputter-coater (ESC-101, Elionix, Tokyo, Japan) for 500 seconds. The freeze-dried collagen scaffolds were cut into cross-sections and mounted on a carbon adhesive over the SEM stub. The cross-sections were sputter-coated with platinum for 300 seconds. The microbeads and scaffold cross-sections were observed at an acceleration potential of 5 kV and 10 kV, respectively.

**2.2.4. Microbead Size Analysis.** 10 mg of freeze-dried microbeads was suspended in 1 mL of milli-Q water and sonicated for 30 seconds using an ultrasonic water bath. The samples were analyzed for their average size as well as size distribution profile using a laser diffraction particle size analyzer (SALD 7000, Shimadzu Corporation, Japan). The microbead size was measured for three batches of formulation and the mean average was calculated as mean  $\pm$  standard deviation ( $n = 3$ ).

**2.2.5. Insulin Loading Efficiency (LE).** The confirmation of insulin loading as well as insulin quantification in microbeads was carried out using Micro-BCA Protein Assay Kit. 10 mg of dried insulin incorporated microbeads was dissolved in 1 mL of methylene chloride at RT. Insulin was extracted into 0.01 M HCl under vigorous shaking for 2 minutes in a high speed vortex device (Vortex Genie, Fischer, Pittsburgh, PA) at a setting of 10. The suspension was allowed to settle for 5 minutes at RT and supernatant aqueous phase containing insulin was extracted. 150  $\mu$ L of the supernatant solution was used for the insulin quantification. Briefly 150  $\mu$ L of albumin (BSA) standard in duplicate, and individual samples in triplicate, was added to individual wells of a 96-well plate. 150  $\mu$ L of assay working agent was added to each of the wells containing standards as well as samples. The plate was covered with a sealing tape and the mixing of the solutions in the wells was

ensured by shaking the plate in a microplate shaker for 30 seconds. The microplate was incubated at 37°C for 2 hours. Following the incubation period, the plate was cooled at RT and the absorbance was measured at 562 nm by a microplate reader (Bio-Rad Laboratories, USA). The blank absorbance was subtracted and the insulin concentration ( $\mu$ g/mL) of the unknown samples was measured by comparing with a standard curve ( $R^2 = 0.998$ ) obtained from BSA standards. Total quantity of the incorporated insulin was calculated. The LE was calculated using following equation [23]:

$$\begin{aligned} \text{LE (\%)} &= \left[ \frac{\text{Weight of the incorporated insulin}}{\text{weight of total insulin used for incorporation}} \right] \\ &\times 100. \end{aligned} \quad (1)$$

**2.2.6. Mechanical Strength: Compression Test.** Compression test was performed for evaluation of mechanical strength of the prepared scaffolds. The control collagen scaffold and collagen-microbead hybrid scaffold were cut into discs of a dimension of  $\varnothing$  6 mm  $\times$  H 4 mm and compressed with a texture analyzer (TA.XTPlus, Texture Technologies Corp., USA) at a rate of 0.1 mm/s. Young's modulus was calculated from the initial linear region of stress-strain relationship. The data was expressed as mean  $\pm$  SD ( $n = 4$ ).

**2.2.7. In Vitro Insulin Release and Microbead Degradation.** *In vitro* insulin release from microbeads and hybrid scaffold was studied in PBS (pH = 7.4) at 37°C. 30 mg of microbeads was added in 2 mL tubes. Control collagen and collagen-microbead hybrid scaffolds were cut into discs of dimension of  $\varnothing$  10 mm  $\times$  H 5 mm and placed in 50 mL tubes. 1.2 mL of sterile PBS was added to the tubes containing microbead and 1 mL PBS was added to the tubes containing scaffolds. The tubes were tightly capped and incubated in a shaking water bath incubator (Taitec Corporation, Japan) at 37°C with a shaking speed of 50 rpm. The scaffolds were degassed before incubation to ensure the entry of PBS into the scaffold pores. After predetermined time points of 1, 2, 4, 8, 12, 16, 20, 24, and 28 days, the required volume of release medium (1 mL from microbeads and 0.5 mL from scaffolds) was collected and replaced with equivalent volume of fresh PBS. The insulin amount in released medium was quantified by Micro BCA protein assay and the cumulative release (%) was plotted against time to obtain the release curve. The experiments were performed in triplicate and data points in the curve were presented as mean  $\pm$  standard deviation. The microbeads and scaffolds after 1-, 2-, and 4-week release period were collected and washed with milli-Q. The microbeads and scaffolds were freeze-dried. The freeze-dried samples were weighed for determination of dry weight of remaining microbeads. The remaining microbead weight (%) was plotted against the time to obtain the weight loss profile. The freeze-dried microbeads and cross-sections of scaffolds were observed under SEM.

**2.2.8. In Vitro Chondrocyte Culture.** The control collagen scaffolds and collagen-microbead hybrid scaffolds were used for culture of bovine articular chondrocytes (BAC). The scaffolds were cut into discs of a dimension of  $\text{Ø } 6 \text{ mm} \times \text{H } 3 \text{ mm}$  and sterilized with 70% ethanol. The sterile scaffolds were transferred to a clean bench, washed with PBS and incubated with cell culture medium for 3 hours in a  $\text{CO}_2$  incubator (Sanyo Corporation, Japan) equilibrated with 5%  $\text{CO}_2$  at  $37^\circ\text{C}$ . Bovine articular chondrocytes isolated from articular cartilage from the knees of a 9-week-old female calf were cultured in  $75 \text{ cm}^2$  tissue culture flasks in Dulbecco's Modified Eagle's Medium (DMEM) containing 10% fetal bovine serum, 4500 mg/L glucose, 4 mM glutamine, 100 U/mL penicillin, 100  $\mu\text{g}/\text{mL}$  streptomycin, 0.1 mM nonessential amino acids, 0.4 mM proline, 1 mM sodium pyruvate, and 50  $\mu\text{g}/\text{mL}$  ascorbic acid. The cells were harvested by treatment with trypsin/EDTA solution after 80% confluence. Cells were seeded in the scaffolds by dispensing 80  $\mu\text{L}$  of cell suspension with  $7.5 \times 10^5$  cells/scaffold. The cell-scaffold constructs were incubated for 3 hours in a  $\text{CO}_2$  incubator to allow cell adhesion. Following cell adhesion, the cell-scaffold constructs were transferred to new tissue culture plates and 10 mL cell culture medium was added. The cells were cultured for 1 week. Cell culture medium supplemented with 100 nM insulin was added to the wells containing control collagen scaffold as a positive control. Culture medium was changed twice a week. Cell seeding efficiency in the scaffolds was evaluated by counting the nonadhered cells using a hemocytometer as following equation:

$$\begin{aligned} & \text{Cell seeding efficiency (\%)} \\ &= \left[ (\text{number of seeded cells} \right. \\ & \quad \left. - \text{number of nonadhered cells to the scaffold}) \right. \\ & \quad \left. \times (\text{number of seeded cells})^{-1} \right] \times 100. \end{aligned} \quad (2)$$

The cell-scaffold constructs after 3 hours and 1 week of cell culture were fixed with 0.01% glutaraldehyde at RT. The fixed constructs were washed with milli-Q, freeze-dried and observed for cell adhesion and distribution using SEM.

Cell viability was evaluated by performing live-dead staining assay using Cellstain Double Staining Kit. After 1 week of cell culture, cell-scaffold constructs were washed with PBS and incubated in 2  $\mu\text{M}$  calcein-AM and 4  $\mu\text{M}$  propidium iodide solution in cell culture medium for 10 minutes. The cell seeding surface layer was cut and removed. The inner cross-section of specimen at approximate depth of 1 mm below the seeding surface was observed for live and dead cells using a fluorescence microscope (Olympus Corp., Japan).

The cell proliferation in the scaffolds was evaluated by quantifying the DNA amount in cell-scaffold constructs after 1-, 3-, and 7-day culture period. At each time point, the cell-scaffold constructs were collected, washed, and freeze-dried. The freeze-dried cell-scaffold constructs were digested with papain solution. Papain was dissolved at 400  $\mu\text{g mL}^{-1}$  in 0.1 M phosphate buffer (pH = 6.0) prepared with sodium dihydrogen phosphate, L-cysteine hydrochloride monohydrate,

and ethylene diamine tetra acetic acid (EDTA). 500  $\mu\text{L}$  of papain solution was added to each aliquot containing freeze-dried cell-scaffold construct. The aliquots were incubated in a shaking incubator at  $60^\circ\text{C}$  with shaking speed of 150 rpm (24 hours) for complete digestion. The digested samples were used to measure the DNA content by using a standard curve ( $R^2 = 0.999$ ) prepared using calf thymus DNA standard and fluorescence dye (Hoechst 33258). The fluorescence emission was measured using FP-6500 spectrofluorometer (JASCO, Japan) at an excitation wavelength of 360 nm and emission wavelength of 460 nm. Four samples were used to calculate the average and SD ( $n = 4$ ).

**2.2.9. Statistical Analysis.** All data were expressed as the mean  $\pm$  standard deviation (SD). One-way analysis of variance was performed to reveal significant differences, followed by Tukey's post hoc test for pairwise comparison. Statistical analysis was executed using Kyplot 2.0 beta 15. The difference was considered significant when the  $P$  value was less than 0.05.

### 3. Results and Discussion

**3.1. Morphology, Size Distribution, and LE of Insulin Loaded PLGA Microbeads.** Human recombinant insulin was microencapsulated in PLGA microbeads using a w-o-w double emulsion technique. Figure 1 shows the morphology and size distribution of the prepared microbeads. The microbeads were of spherical morphology with smooth surface without visible surface pores (Figure 1(a)). The microbeads showed narrow particle size distribution (Figure 1(b)). The mean diameter of the microbeads was  $11.2 \pm 0.9 \mu\text{m}$  as determined using a laser particle size analyzer. The insulin LE of the microbeads was  $67.3 \pm 3.9\%$ .

**3.2. Scaffold Microstructure and Mechanical Strength.** Porous scaffolds with controlled pore structures were prepared by using preprepared ice particulates as a porogen material. Figure 2 represents SEM microstructure of the control collagen scaffolds and collagen-microbead hybrid porous scaffolds. Figures 2(a) and 2(c) show the microstructure of control collagen scaffolds and Figures 2(b) and 2(d) show the microstructure of collagen-microbead hybrid scaffolds. All the scaffolds prepared with ice particulates had controlled pore structure and the large pores were replica of the ice particulates used during fabrication process. The large pores were connected to each other with interconnected small holes. The interconnected pores could facilitate cell migration, nutrient diffusion, and metabolic waste removal. The hybrid scaffolds exhibited a homogeneous spatial distribution of microbeads throughout the pore walls of the scaffold. The homogeneous and even distribution of microbeads could be useful for maintaining a uniform spatial release of insulin throughout the 3D microenvironment of hybrid scaffolds to meet the onsite insulin demand for the cultured chondrocytes.

The mechanical strength of the scaffolds was determined using a compression test. Figure 3 represents Young's

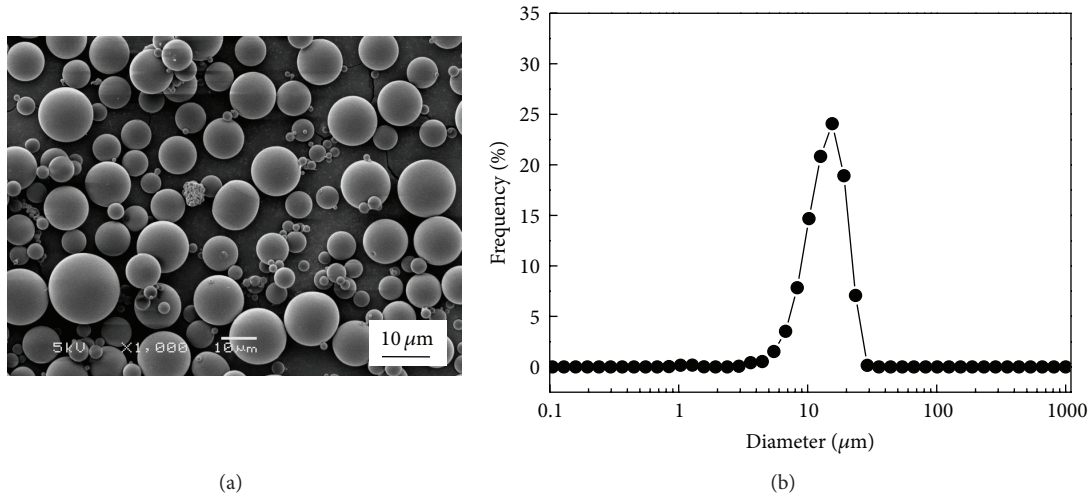


FIGURE 1: SEM photomicrographs of insulin loaded PLGA microbeads (a) size distribution of PLGA microbeads (b).

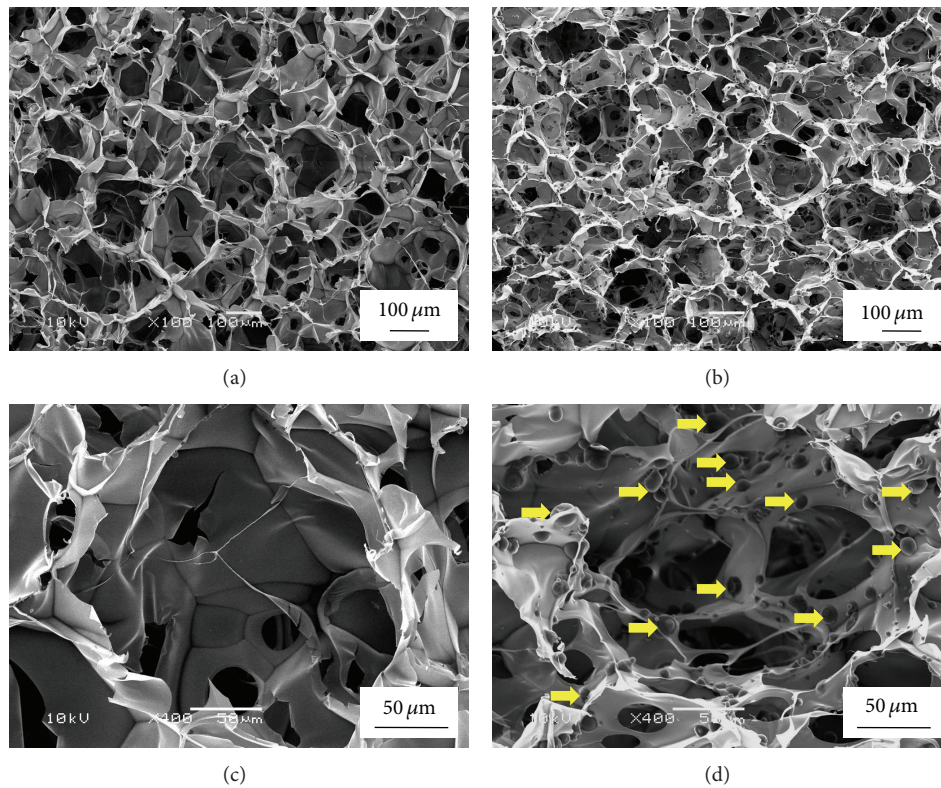


FIGURE 2: SEM photomicrographs of control collagen scaffolds (a), (c) and collagen-microbead hybrid porous scaffolds (b), (d) at low (a), (b) and high (c), (d) magnifications. Yellow arrows represent the integrated insulin loaded PLGA microbeads in porous collagen matrix.

modulus of the different scaffolds. The results indicated the control and collagen-microbead hybrid scaffolds had high mechanical strength, which was much higher than previously reported collagen scaffolds prepared without ice particulates [15]. Furthermore mechanical strength of hybrid scaffold was not compromised after the introduction of PLGA microbeads.

**3.3. In Vitro Insulin Release and Microbead Degradation.** *In vitro* insulin release from microbeads and hybrid scaffold was studied for 4 weeks and the release profiles are shown in Figure 4. Figure 4(a) represents the cumulative release profile for entire 4 weeks and Figure 4(b) represents the release profile for a short time scale of 4 days. The release profile from microbeads showed a usual trend of initial burst release

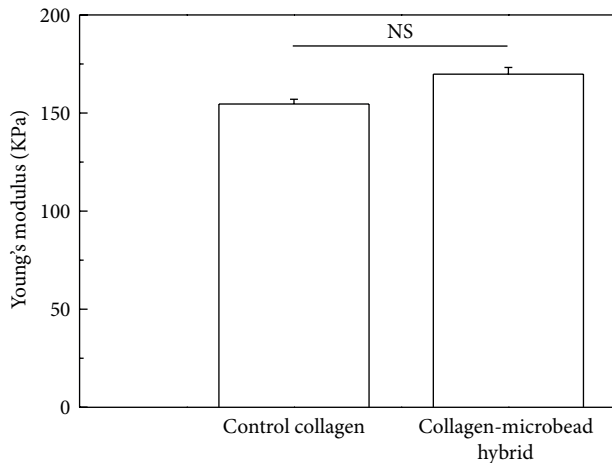


FIGURE 3: Compressive Young's modulus of control collagen and collagen-microbead hybrid scaffold. Data represent mean  $\pm$  SD ( $n = 4$ ), NS: no significant difference.

of 33% in the first day. The initial burst release was followed by a rise in cumulative insulin up to 3 weeks and a very slow release phase during the 4th week. However the hybridization of the microbeads in porous collagen scaffold avoided the initial burst release and a zero order release kinetics was achieved up to a period of 4 weeks. The suppression of insulin release from hybrid scaffold could be due to delayed induction of initial protein release from the microbeads inside the porous scaffolds [25, 26]. The result indicated entrapment of biodegradable microbeads containing insulin inside porous collagen matrix should be an effective strategy for long-term delivery of the insulin without initial burst release.

Degradation of microbeads was studied using weight loss profile (Figure 4(c)). The weight loss profile demonstrated a quicker weight loss of microbeads in their free state compared to scaffold integrated state. This indicated degradation of microbeads was controlled after introduction to porous collagen matrix and showed their presence till the end of 4 weeks (Figure 5). Therefore a more controlled degradation of microbeads in collagen-microbead hybrid scaffolds could lead to a better control over the release of insulin and should sustain the release for a prolonged period.

**3.4. Cell Adhesion, Viability, and Proliferation in Hybrid Scaffold.** Control collagen and collagen-microbead hybrid scaffolds were cultured with bovine articular chondrocytes. All the scaffolds were seeded with the cell suspension containing the same number of chondrocytes. The seeding efficiencies of control collagen and collagen-microbead hybrid scaffolds were  $87.1 \pm 1.1\%$  and  $87.0 \pm 1.4\%$ . Both control and hybrid scaffolds showed high cell seeding efficiencies. No significant difference in the seeding efficiency was observed among the scaffold groups indicating that microbead incorporation did not cause any difference in seeding efficiency. Figures 6(a)–6(d) present the SEM photomicrographs of cell adhesion and distribution at the inner cross sections of the scaffolds after 3 hours of culture. The cells adhered to the surface of the pore

walls. Homogeneous cell distribution was observed at the entire inner cross-sections of the scaffolds, which indicated that the interconnected pore structure facilitated the cells to reach the inner pores in the scaffolds. Cells from the seeding surface could migrate into the inner bulk pores via interconnected pore structures and distributed in the entire scaffold. Figures 6(e)–6(h) show the SEM photomicrographs of inner cross-sections of the porous scaffolds after 1 week of cell culture. More cells were observed indicating cell proliferation in the scaffolds.

Figure 7 represents cell viability at the inner cross-sections of different scaffolds after 1 week of cell culture. Fluorescence from the migrated cells was observed at an approximate depth of 1 mm below the seeding surface. Green fluorescence represents the live cells and red fluorescence dots indicate the dead cells. More dead cells were detected in control collagen scaffold without insulin supplement compared to collagen scaffolds supplemented with 100 nM external insulin and collagen-microbead hybrid scaffolds. This indicated insulin had some effect on maintenance of chondrocyte viability. Furthermore very few or no dead cells were detected from the collagen-microbead hybrid scaffolds. This might be due to the sustainable local concentration of released insulin from the hybrid scaffolds.

Figure 8 shows the cell proliferation of different scaffolds. All the scaffolds showed an increased DNA amount during 7-day culture period. A significant difference in the cell number among the scaffold groups was noticed after 3 and 7 days of culture. Cell proliferation in the scaffolds showed an increase order of collagen control scaffold without insulin < control collagen scaffold with 100 nM external insulin supplement < hybrid scaffold. This result suggested that insulin promoted chondrocyte proliferation. The insulin released from the spatially located microbeads in the hybrid scaffolds might have met the local insulin demand for the chondrocytes for their survival and usual proliferation. However due to extensive cell proliferation with time, the diffusion of bioactive insulin from cell culture medium might not be sufficient to nourish the interior cells of the scaffold supplemented with external insulin. This suggested the unavailability or limited availability of insulin to the cells inside the control scaffolds might be the reason for low cell viability and proliferation.

The study depicted a controlled release approach to promote cell proliferation in 3D porous collagen for cartilage tissue engineering. Owing to the importance of collagen porous scaffolds of controlled pore structure and improved mechanical strength in cartilage tissue regeneration, controlled release function via biodegradable microbeads was additionally introduced in order to improve the regeneration potential of the prepared scaffold. The present approach suggested the possibility to use other bioactive growth factors as nutrients for cell survival in large and thick 3D porous scaffolds for tissue engineering and regenerative medicine.

## 4. Conclusion

A controlled release porous collagen-microbead hybrid scaffold having a controlled pore structure was prepared by

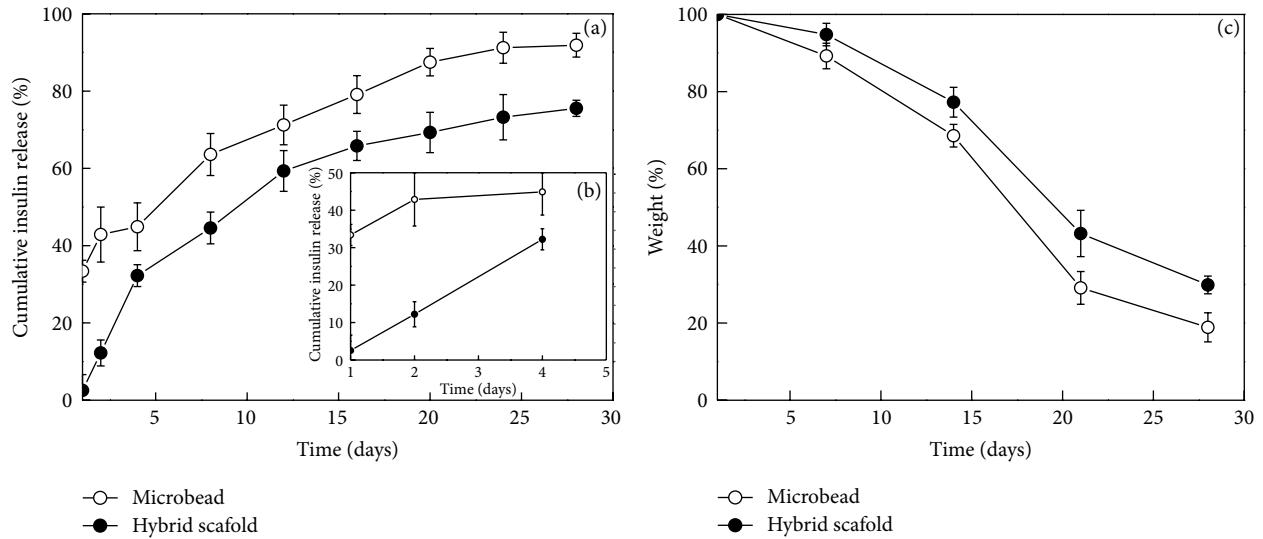


FIGURE 4: Cumulative insulin releases profile (a), (b) and weight loss profile (c) from free microbeads and hybrid scaffold for 4 weeks.

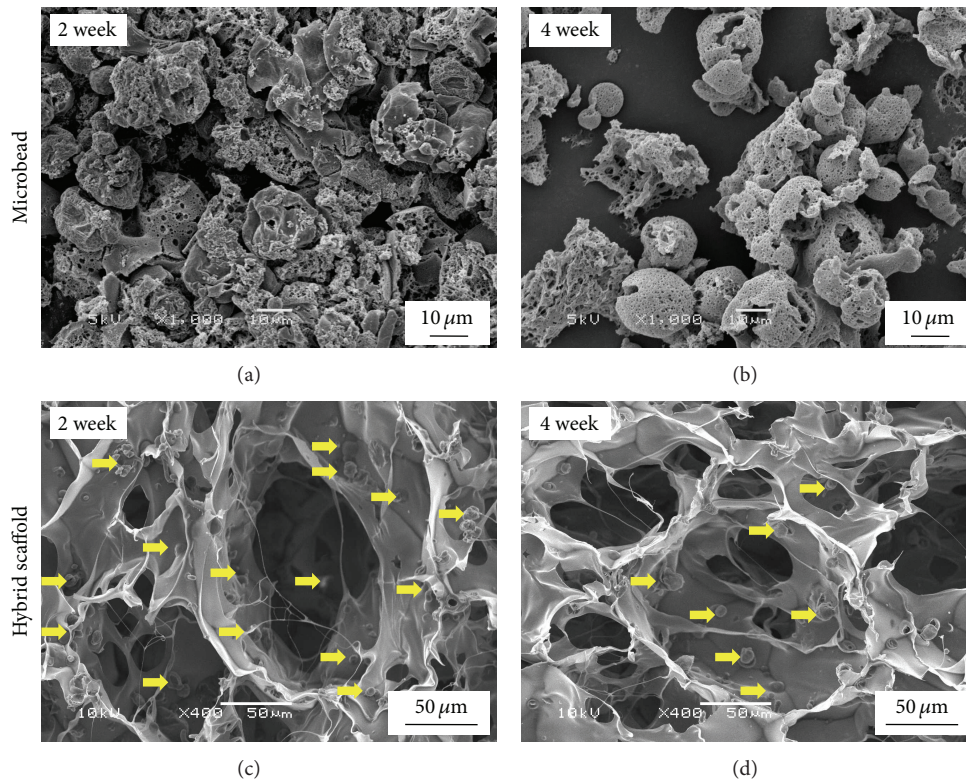


FIGURE 5: SEM photomicrographs of free microbeads and collagen-microbead hybrid scaffold after incubation for 2 and 4 weeks. Yellow arrows represent the degraded insulin loaded PLGA microbeads in porous collagen matrix.

introduction of insulin loaded PLGA microbeads into porous collagen sponge formed with prepared ice particulates. The collagen-microbead hybrid scaffold demonstrated a high mechanical strength and a stable release of insulin for 4 weeks. The released insulin demonstrated its effect on cultured chondrocytes for their survival and proliferation. The bioactive hybrid scaffold should be useful for maintenance

of prolonged survival and proliferation of cultured chondrocytes for application to cartilage tissue engineering.

**Conflict of Interests**

The authors declare that there is no conflict of interests regarding the publication of this paper.

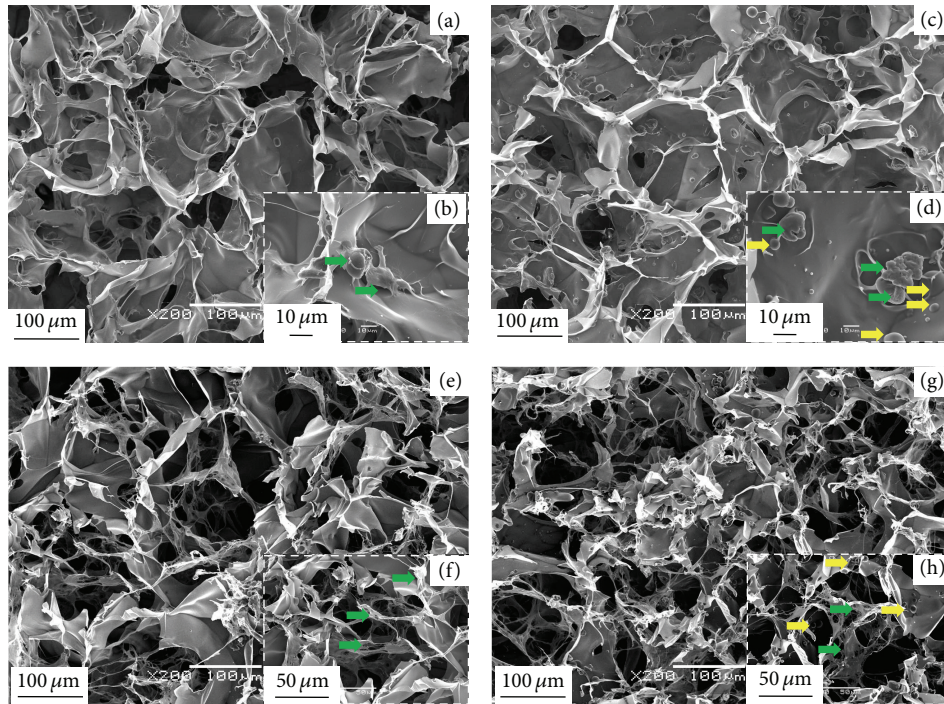


FIGURE 6: SEM photomicrographs of the cross-sections of control collagen (a), (b), (e), and (f) and collagen-microbead hybrid (c), (d), (g), and (h) scaffolds after 3 hours ((a)–(d)) and 1 week ((e)–(h)) of chondrocyte culture. Yellow arrows represent the integrated insulin loaded PLGA microbeads in porous collagen matrix and green arrows represent adhered chondrocytes.

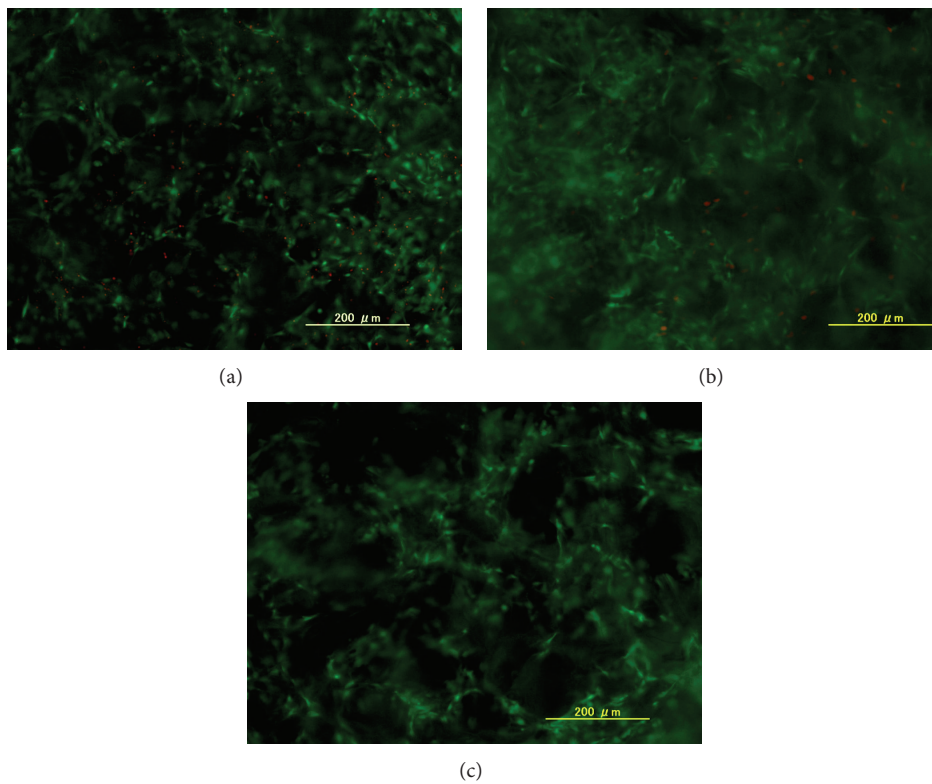


FIGURE 7: Live and dead staining of internal cross-sections of control collagen scaffold without insulin (a), control collagen scaffold with 100 nM insulin supplemented in medium (b), and collagen-microbead hybrid scaffold (c) after 1 week of chondrocyte culture. Green fluorescence indicates live cells and red fluorescence dots indicate dead cells.

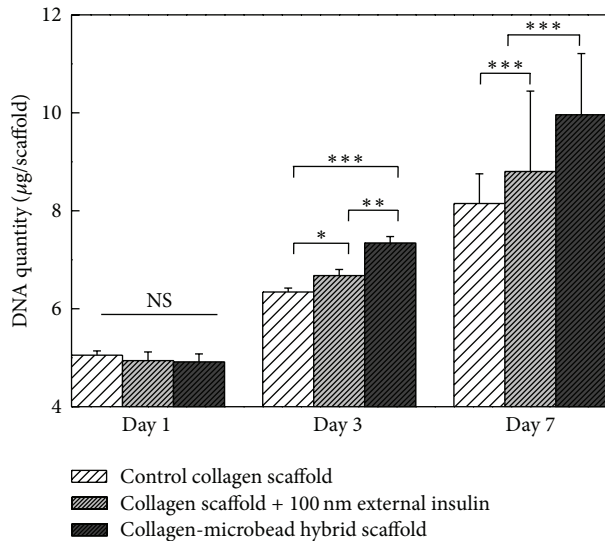


FIGURE 8: DNA amount in the cell/scaffold constructs of control collagen scaffold, control collagen scaffold supplemented with 100 nM insulin, and collagen-microbead hybrid scaffold after 1, 3, and 7 days of chondrocyte culture. Data represent mean  $\pm$  SD ( $n = 4$ ), \*significant ( $P < 0.05$ ), \*\* significant ( $P < 0.01$ ), \*\*\* significant ( $P < 0.001$ ), NS: no significant difference.

## Acknowledgment

The authors would like to acknowledge the financial support from World Premier International (WPI) Research Centre Initiative, Ministry of Education, Culture, Sports, Science and Technology, Japan.

## References

- J. S. Temenoff and A. G. Mikos, "Review: tissue engineering for regeneration of articular cartilage," *Biomaterials*, vol. 21, no. 5, pp. 431–440, 2000.
- W. Kafienah, M. Jakob, O. Démartheau et al., "Three-dimensional tissue engineering of hyaline cartilage: comparison of adult nasal and articular chondrocytes," *Tissue Engineering*, vol. 8, no. 5, pp. 817–826, 2002.
- D. W. Huttmacher, "Scaffolds in tissue engineering bone and cartilage," *Biomaterials*, vol. 21, no. 24, pp. 2529–2543, 2000.
- R. F. Loeser, C. A. Pacione, and S. Chubinskaya, "The combination of insulin-like growth factor 1 and osteogenic protein 1 promotes increased survival of and matrix synthesis by normal and osteoarthritic human articular chondrocytes," *Arthritis and Rheumatism*, vol. 48, no. 8, pp. 2188–2196, 2003.
- D. Nestic, R. Whiteside, M. Brittberg, D. Wendt, I. Martin, and P. Mainil-Varlet, "Cartilage tissue engineering for degenerative joint disease," *Advanced Drug Delivery Reviews*, vol. 58, no. 2, pp. 300–322, 2006.
- T. Minas and S. Nehrer, "Current concepts in the treatment of articular cartilage defects," *Orthopedics*, vol. 20, no. 6, pp. 525–538, 1997.
- E. B. Hunziker, "Articular cartilage repair: basic science and clinical progress. A review of the current status and prospects," *Osteoarthritis and Cartilage*, vol. 10, no. 6, pp. 432–463, 2002.
- W.-J. Li, R. Tuli, C. Okafor et al., "A three-dimensional nanofibrous scaffold for cartilage tissue engineering using human mesenchymal stem cells," *Biomaterials*, vol. 26, no. 6, pp. 599–609, 2005.
- H. Lu, H. H. Oh, N. Kawazoe, K. Yamagishi, and G. Chen, "PLLA-collagen and PLLA-gelatin hybrid scaffolds with funnel-like porous structure for skin tissue engineering," *Science and Technology of Advanced Materials*, vol. 13, no. 6, Article ID 064210, 2012.
- W. Dai, Z. Yao, J. Dong, N. Kawazoe, C. Zhang, and G. Chen, "Cartilage tissue engineering with controllable shape using a poly (lactic-co-glycolic acid)/collagen hybrid scaffold," *Journal of Bioactive and Compatible Polymers*, vol. 28, no. 3, pp. 247–257, 2013.
- S. J. Hollister, "Porous scaffold design for tissue engineering," *Nature Materials*, vol. 4, no. 7, pp. 518–524, 2005.
- A. Borzacchiello, A. Gloria, L. Mayol et al., "Natural/synthetic porous scaffold designs and properties for fibro-cartilaginous tissue engineering," *Journal of Bioactive and Compatible Polymers*, vol. 26, no. 5, pp. 437–451, 2011.
- H. Lu, Y.-G. Ko, N. Kawazoe, and G. Chen, "Cartilage tissue engineering using funnel-like collagen sponges prepared with embossing ice particulate templates," *Biomaterials*, vol. 31, no. 22, pp. 5825–5835, 2010.
- Y.-G. Ko, N. Kawazoe, T. Tateishi, and G. Chen, "Preparation of chitosan scaffolds with a hierarchical porous structure," *Journal of Biomedical Materials Research B*, vol. 93, no. 2, pp. 341–350, 2010.
- Q. Zhang, H. Lu, N. Kawazoe, and G. Chen, "Preparation of collagen scaffolds with controlled pore structures and improved mechanical property for cartilage tissue engineering," *Journal of Bioactive and Compatible Polymers*, vol. 28, no. 5, pp. 426–438, 2013.
- K. Song, Y. Liu, H. M. Macedo et al., "Fabrication and evaluation of a sustained-release chitosan-based scaffold embedded with PLGA microspheres," *Materials Science and Engineering C*, vol. 33, no. 3, pp. 1506–1513, 2013.
- E. C. Ko, Y. Fujihara, T. Ogasawara et al., "Administration of the insulin into the scaffold atelocollagen for tissue-engineered cartilage," *Journal of Biomedical Materials Research A*, vol. 97, no. 2, pp. 186–192, 2011.
- K. Lee, E. A. Silva, and D. J. Mooney, "Growth factor delivery-based tissue engineering: general approaches and a review of recent developments," *Journal of the Royal Society Interface*, vol. 8, no. 55, pp. 153–170, 2011.
- F.-M. Chen, M. Zhang, and Z.-F. Wu, "Toward delivery of multiple growth factors in tissue engineering," *Biomaterials*, vol. 31, no. 24, pp. 6279–6308, 2010.
- P. Tayalia and D. J. Mooney, "Controlled growth factor delivery for tissue engineering," *Advanced Materials*, vol. 21, no. 32–33, pp. 3269–3285, 2009.
- K. Lee, E. A. Silva, and D. J. Mooney, "Growth factor delivery-based tissue engineering: general approaches and a review of recent developments," *Journal of the Royal Society Interface*, vol. 8, no. 55, pp. 153–170, 2011.
- K. Andreas, R. Zehbe, M. Kazubek et al., "Biodegradable insulin-loaded PLGA microspheres fabricated by three different emulsification techniques: investigation for cartilage tissue engineering," *Acta Biomaterialia*, vol. 7, no. 4, pp. 1485–1495, 2011.

- [23] M. Ye, S. Kim, and K. Park, "Issues in long-term protein delivery using biodegradable microparticles," *Journal of Controlled Release*, vol. 146, no. 2, pp. 241–260, 2010.
- [24] C. Manoharan and J. Singh, "Insulin loaded PLGA microspheres: effect of zinc salts on encapsulation, release, and stability," *Journal of Pharmaceutical Sciences*, vol. 98, no. 2, pp. 529–542, 2009.
- [25] M. Lee, T. T. Chen, M. L. Iruela-Arispe, B. M. Wu, and J. C. Y. Dunn, "Modulation of protein delivery from modular polymer scaffolds," *Biomaterials*, vol. 28, no. 10, pp. 1862–1870, 2007.
- [26] F. Ungaro, M. Biondi, I. d'Angelo et al., "Microsphere-integrated collagen scaffolds for tissue engineering: effect of microsphere formulation and scaffold properties on protein release kinetics," *Journal of Controlled Release*, vol. 113, no. 2, pp. 128–136, 2006.

## Research Article

# Impact of Core-Forming Segment Structure on Drug Loading in Biodegradable Polymeric Micelles Using PEG-*b*-Poly(lactide-*co*-depsipeptide) Block Copolymers

Akihiro Takahashi,<sup>1</sup> Yuta Ozaki,<sup>2</sup> Akinori Kuzuya,<sup>1,2</sup> and Yuichi Ohya<sup>1,2</sup>

<sup>1</sup> Organization for Research and Development of Innovative Science and Technology (ORDIST), Kansai University, 3-3-35 Yamate, Suita, Osaka 564-8680, Japan

<sup>2</sup> Department of Chemistry and Materials Engineering, Faculty of Chemistry, Materials and Bioengineering, Kansai University, 3-3-35 Yamate, Suita, Osaka 564-8680, Japan

Correspondence should be addressed to Yuichi Ohya; [yohya@kansai-u.ac.jp](mailto:yohya@kansai-u.ac.jp)

Received 13 December 2013; Accepted 30 December 2013; Published 20 February 2014

Academic Editor: Inn-Kyu Kang

Copyright © 2014 Akihiro Takahashi et al. This is an open access article distributed under the Creative Commons Attribution License, which permits unrestricted use, distribution, and reproduction in any medium, provided the original work is properly cited.

We synthesized series of amphiphilic AB-type block copolymers having systematic variation in the core-forming segments using poly(lactide-*co*-depsipeptide)s as a hydrophobic segment and prepared polymeric micelles using the block copolymers, PEG-*b*-poly(lactide-*co*-depsipeptide). We then discussed the relationship between the core-forming segment structure and drug loading efficiency for the polymeric micelles. PEG-*b*-poly(lactide-*co*-depsipeptide)s, PEG-*b*-PLGL containing L-leucine (Leu), and PEG-*b*-PLGF containing L-phenylalanine (Phe), with similar molecular weights and various mole fractions of depsipeptide units, were synthesized. Polymeric micelles entrapping model drug (fluorescein, FL) were prepared using these copolymers. As a result, PEG-*b*-poly(lactide-*co*-depsipeptide) micelles showed higher drug loading compared with PEG-*b*-PLLA and PEG-*b*-PDLLA as controls. The drug loading increased with increase in the mole fraction of depsipeptide unit in the hydrophobic segments. The introduction of aliphatic and aromatic depsipeptide units was effective to achieve higher FL loading into the micelles. PEG-*b*-PLGL micelle showed higher drug loading than PEG-*b*-PLGF micelle when the amount of FL in feed was high. These results obtained in this study should be useful for strategic design of polymeric micelle-type drug delivery carrier with high drug loading efficiency.

## 1. Introduction

Polymeric micelles have attracted much attention in the last two decades as multifunctional nanotechnology-based drug delivery vehicles especially for poorly water-soluble drugs [1–5]. Typically, polymeric micelles are formed by self-aggregation of amphiphilic AB-type diblock copolymers with hydrophobic and hydrophilic segments consisting of inside core and outside shell, respectively. The inner hydrophobic core of a polymeric micelle has a large capacity to accommodate hydrophobic drugs [6], while the hydrophilic shell allows retaining colloidal stability of the polymeric micelle in an aqueous environment [7]. The polymeric micelles are less prone to dissociate even at low concentrations and thus can maintain their micellar structures

that facilitate prolonged circulation in the bloodstream by escaping from renal clearance and reticuloendothelial system [8]. The hydrophobic core generally consists of a biodegradable polymer such as poly( $\beta$ -benzyl-L-aspartate) (PBLA) [9], poly(DL-lactide) (PDLLA) [10], and poly( $\epsilon$ -caprolactone) (PCL) [11]. A water-soluble polymer may also be used as core-forming segment to render hydrophobicity by the chemical conjugation of a hydrophobic drug [12–14] or polyion complex formation through the association of two oppositely charged polyelectrolytes (polyion complex micelles) [15–17]. Polymeric micelle having hydrophobic core can physically entrap hydrophobic drugs such as doxorubicin (DOX), an anticancer drug, and be used as a carrier to deliver the drugs to a desired site. However, it is not easy to achieve high drug loading and/or entrapment efficiency

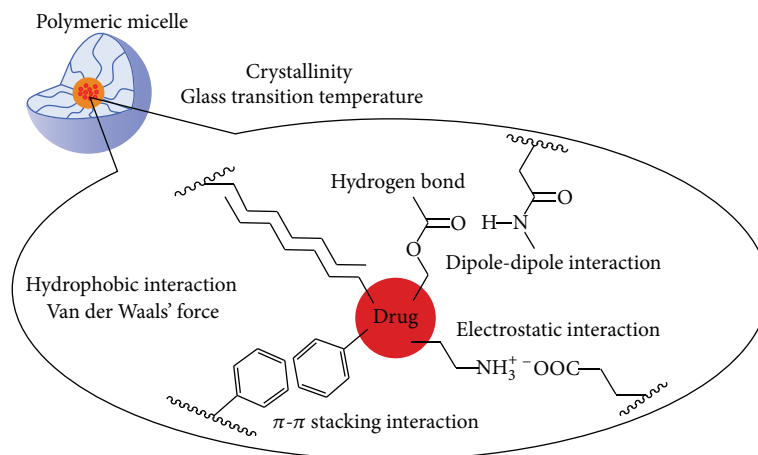


FIGURE 1: The factors which influence the drug loading efficiency for the polymeric micelle physically entrapping drugs.

when the combination of drug and core-forming polymer is not ideal. In fact, some researchers reported the difficulty of physical entrapment of DOX into polymeric micelles [18–22]. To achieve efficient drug delivery to a desired site and to reduce the dose, side effects, and total cost of the formulation, drug loading efficiency is desired to be high enough. The drug loading efficiency strongly depends on solubility of the drug in water (hydrophilicity/hydrophobicity), the preparation method as well as the interaction between the drug and micelle core-forming segment (e.g., hydrogen bonding, hydrophobic interaction,  $\pi$ - $\pi$  stacking interaction, dipole-dipole interaction, electrostatic interaction, etc.), and the physical properties of core-forming segment (crystallinity, glass transition temperature, etc.) (Figure 1). However, no systematic study on the relationship between drug loading efficiency and core-forming polymer structure has been carried out.

Polydepsipeptides are copolymers of amino acids and hydroxyl acids and possess degradability of polyesters and functionality of polypeptides. Previously, we reported the synthesis of biodegradable copolymers of lactide and depsipeptide, poly(lactide-*co*-depsipeptide), with reactive side-chain groups such as COOH, NH<sub>2</sub>, OH, and SH by ring-opening copolymerization of lactide with cyclodepsipeptides consisting of the corresponding amino acids and glycolic acid (Glc) [23–26]. Using poly(lactide-*co*-depsipeptide)s we can easily prepare biodegradable copolymers having various properties (hydrophilicity, hydrophobicity, crystallinity, reactivity, electronegativity or -positivity, etc.). So, polydepsipeptide copolymer is one of the most convenient materials for the studies in which systematic variation of the biodegradable polymer properties is needed.

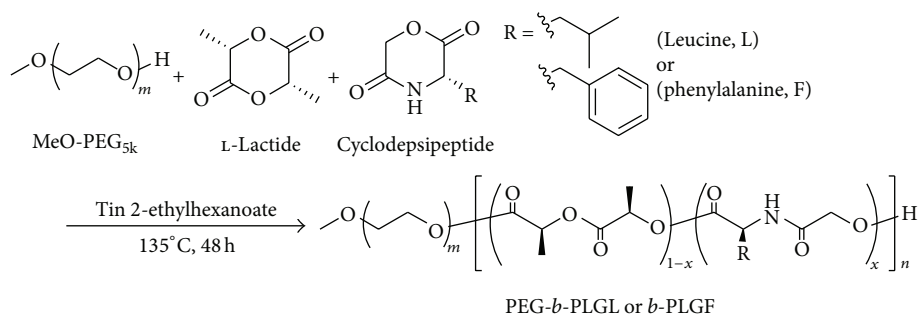
In this study, we synthesized various biodegradable amphiphilic AB-type diblock copolymers of poly(ethylene glycol) (PEG) and poly(lactide-*co*-depsipeptide) containing different amino acids as a hydrophilic segment and a hydrophobic segment, respectively, for preparation of polymeric micelles. We investigated the relationship between the polymer structure and the entrapment behavior of model drugs into the polymeric micelles to optimize the structures

of hydrophobic core of the polymeric micelles as drug carriers. We chose L-leucine (Leu) and L-phenylalanine (Phe) as hydrophobic amino acids. PEG-*b*-poly(lactide-*co*-depsipeptide)s were synthesized by ring-opening copolymerization of lactide (LA) with cyclodepsipeptides, cyclo(Glc-Leu), or cyclo(Glc-Phe) using MeO-PEG as a macroinitiator to give PEG-*b*-poly[LA-*co*-(Glc-Leu)] (PEG-*b*-PLGL) and PEG-*b*-poly[LA-*co*-(Glc-Phe)] (PEG-*b*-PLGF). AB-type diblock copolymers of PEG with poly(L-lactide) or poly(DL-lactide), PEG-*b*-PLLA or PEG-*b*-PDLLA, were also synthesized and used as controls. Fluorescein (FL), 4-aminofluorescein (AF), pyrene (PY), and DOX were chosen as model drugs. The structures of these drug model compounds are shown in Supporting Information (see Figure S1 in Supplementary Material available online at <http://dx.doi.org/10.1155/2014/579212>). Using these copolymers and model drugs, polymeric micelles entrapping the model drugs were prepared by solvent evaporation method. The relationship between the polymer structure, the drug loading, and entrapment efficiency of drugs were then investigated.

## 2. Experimental Section

**2.1. Materials.** Monomethoxy-poly(ethylene glycol) (Mn = 5,000 Da) (MeO-PEG) was purchased from Fluka. Tin 2-ethylhexanoate, PY, and DOX were purchased from Wako Pure Chemical Ind., Ltd. FL and AF were purchased from Tokyo Chemical Industry Co., LTD. Lactides (L- and D,L-isomers) were purchased from Musashino Chemical Laboratory, Ltd. (Tokyo, Japan) and used without further treatment. Organic solvents were purified by usual distillation. Other reagents were of commercial grades and used without further purification.

**2.2. Measurements.** <sup>1</sup>H NMR spectra were recorded on a JNM-GSX-400 (JEOL, 400 MHz) nuclear magnetic resonance instrument using deuterated chloroform (CDCl<sub>3</sub>) as solvent. The chemical shifts were calibrated against TMS



SCHEME 1: Synthetic route of PEG-*b*-poly(LA-*co*-depsipeptide) copolymers.

and solvent signal of  $\text{CDCl}_3$ . The degree of polymerization of lactide and depsipeptide units in hydrophobic segment of the copolymers was calculated based on integral ratios in the  $^1\text{H}$  NMR spectra of PEG-*b*-PLGL and PEG-*b*-PLGF. The number average molecular weight ( $M_n$ ) and polydispersity index ( $M_w/M_n$ ) for PEG-*b*-PLGL and PEG-*b*-PLGF were determined by size exclusion chromatography (SEC) (column: TSKgel Multipore HXLM  $\times$  2; detector: refractive index) using DMF as an eluent at a flow rate of 1.0 mL/min at  $40^\circ\text{C}$  and a series of PEG as standards. Calorimetric analysis was carried out by differential scanning calorimetry (DSC) (Shimadzu DSC-60). The hydrodynamic diameter of micelles was measured by dynamic light scattering (DLS) (Malvern Instruments Ltd. Zetasizer nano Z ZEN 2600). The amounts of encapsulated drug molecules in the micelles were determined by UV-vis absorption spectra in KCl/NaOH solution (for FL and AF) or DMSO (for PY and DOX) using a spectrophotometer (Shimadzu UV-2400PC).

### 2.3. Synthesis of PEG-*b*-Poly(LA-*co*-depsipeptide) Copolymers.

A series of PEG-*b*-poly(LA-*co*-depsipeptide) copolymers was synthesized through bulk ring-opening copolymerization of L-LA with cyclo(Glc-Leu) or cyclo(Glc-Phe) using tin 2-ethylhexanoate as a catalyst according to the same method reported previously [23] as shown in Scheme 1. Typical example for PEG-*b*-PLGL is as follows. Under a nitrogen atmosphere, MeO-PEG (400 mg,  $80.0\ \mu\text{mol}$ ), L-LA (277 mg,  $1.90\ \text{mmol}$ ), and cyclo(Glc-Leu) ( $329\ \text{mg}$ ,  $1.90\ \text{mmol}$ ) were placed into a glass tube, followed by the addition of a freshly prepared solution of tin 2-ethylhexanoate ( $1.60\ \text{mg}$ ,  $3.80\ \mu\text{mol}$ ) in anhydrous THF in a glove box. The solvent was removed under vacuum overnight. The tube was then purged with argon and sealed in vacuo. The sealed tube was placed in an oil bath at  $160^\circ\text{C}$  for 2 min and then at  $135^\circ\text{C}$  for 24 h. The purification of the reaction mixture was performed by the reprecipitation three times using chloroform as a solvent and diethyl ether as a nonsolvent. The obtained precipitate was dried under vacuum overnight to give PEG-*b*-PLGL copolymer with 49% mole fraction of Glc-Leu unit in the PLGL segments (code: **b-PLGL<sub>49</sub>**) (yield: 86%).  $^1\text{H}$  NMR (400 MHz,  $\text{CDCl}_3$ ):  $\delta = 0.75\text{--}1.06$

(br,  $\text{CH}_2\text{CH}(\text{CH}_3)_2$ ), 1.45–1.63 (m,  $\text{COCH}(\text{O})\text{CH}_3$ ), 1.63–1.83 (br,  $\text{CHCH}_2\text{CH}$  and  $\text{CH}_2\text{CH}(\text{CH}_3)_2$ ), 3.38 (s,  $\text{CH}_3\text{O}$ ), 3.52–3.80 (m,  $\text{CH}_3\text{O}(\text{CH}_2\text{CH}_2\text{O})_m\text{CH}_2\text{CH}_2$ ), 4.06–4.91 (br,  $\text{OCH}_2\text{CH}_2\text{OCO}$ ,  $\text{COCH}(\text{CH}_2)\text{NH}$  and  $\text{NHCOCH}_2\text{O}$ ), 5.01–5.26 (m,  $\text{OCOCH}(\text{CH}_3)\text{O}$ ).

PEG-*b*-PLGF with 49% mole fraction of Glc-Phe unit in the PLGF segments (code: **b-PLGF<sub>49</sub>**) was synthesized by the same method described above using cyclo(Glc-Phe) instead of cyclo(Glc-Leu) (yield = 76%).  $^1\text{H}$  NMR (400 MHz,  $\text{CDCl}_3$ ):  $\delta = 1.41\text{--}1.66$  (m,  $\text{COCH}(\text{O})\text{CH}_3$ ), 3.00–3.35 (m,  $\text{CHCH}_2\text{C}$ ), 3.38 (s,  $\text{CH}_3\text{O}$ ), 3.43–3.75 (m,  $\text{CH}_3\text{O}(\text{CH}_2\text{CH}_2\text{O})_m\text{CH}_2\text{CH}_2$ ), 4.16–4.97 (br,  $\text{OCH}_2\text{CH}_2\text{OCO}$ ,  $\text{COCH}(\text{CH}_2)\text{NH}$  and  $\text{NHCOCH}_2\text{O}$ ), 4.98–5.28 (m,  $\text{OCOCH}(\text{CH}_3)\text{O}$ ), 7.05–7.40 (br,  $\text{C}_6\text{H}_5$ ).

Other PEG-*b*-PLGL and PEG-*b*-PLGF copolymers (code: **b-PLGL<sub>x</sub>** and **b-PLGF<sub>x</sub>**) with various mole fraction of depsipeptide unit ( $x$ ) were also synthesized by changing feed ratio of cyclodepsipeptide, cyclo(Glc-Leu), or cyclo(Glc-Phe) to L-LA. The feeding amounts and the results of the synthesis were described in supporting information.

### 2.4. Preparation of Drug-Loaded Micelles.

Drug-loaded micelles were prepared by a solvent evaporation method. Briefly, a given amount of the copolymer and model drug was dissolved in THF (2 mL) in a glass vial at room temperature. Then, the polymer/drug mixture solution was added dropwise into 10 mL of deionized water under vigorous stirring. After stirring, THF was completely removed under reduced pressure with a rotary evaporator at room temperature to give aqueous micelle solution. To remove insoluble part of drugs, centrifugation (14,000 rpm, 15 min, 2 times) and filtration were carried out. Then, the solution was lyophilized to give powdery drug-loaded micelle.

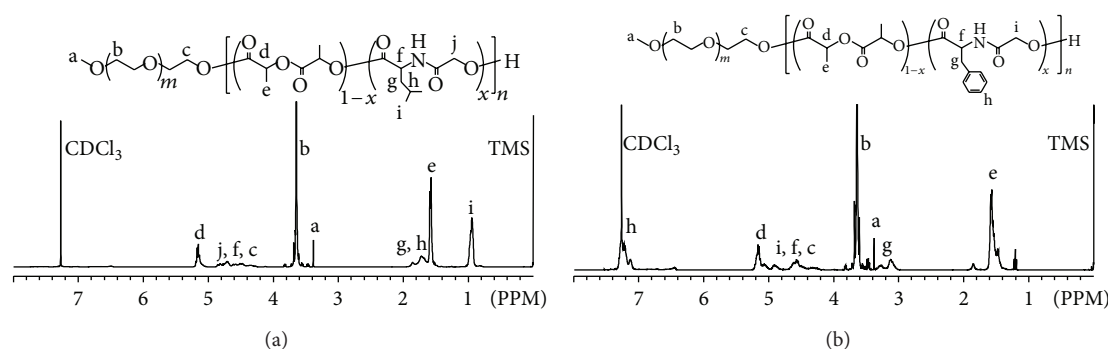
### 2.5. Characterization of Micelles.

Hydrodynamic diameters of micelles were measured by DLS before lyophilization. The amount of drugs was calculated by measurement of the absorbance of drugs using Shimadzu UV-2400PC spectrophotometer.  $\lambda_{\text{max}}$  for FL, AF, PY, and DOX were 491, 488, 338 and 485 nm, respectively. Polymer recovery (PR), drug

TABLE 1: Results of characterization of copolymers.

| Code                              | $w^a$ [mol%] | $Mn^b (\times 10^{-4})$ | $Mn^c (\times 10^{-4})$ | $Mw/Mn^c$ | $DP^{b,d}$ | $x^{b,e}$ [mol%] | $X_c^f$ [%] |
|-----------------------------------|--------------|-------------------------|-------------------------|-----------|------------|------------------|-------------|
| <b><i>b</i>-PLLA</b>              | —            | 1.15                    | 0.90                    | 1.27      | 45         | —                | 35          |
| <b><i>b</i>-PDLLA</b>             | —            | 1.15                    | 0.81                    | 1.29      | 45         | —                | —           |
| <b><i>b</i>-PLGL<sub>20</sub></b> | 20           | 1.09                    | 0.92                    | 1.35      | 40         | 20               | 0           |
| <b><i>b</i>-PLGL<sub>37</sub></b> | 40           | 1.13                    | 1.03                    | 1.35      | 40         | 37               | 0           |
| <b><i>b</i>-PLGL<sub>49</sub></b> | 50           | 1.11                    | 0.90                    | 1.38      | 39         | 49               | 0           |
| <b><i>b</i>-PLGL<sub>59</sub></b> | 60           | 1.24                    | 1.11                    | 1.42      | 46         | 59               | 0           |
| <b><i>b</i>-PLGL<sub>75</sub></b> | 75           | 1.17                    | 1.02                    | 1.39      | 41         | 75               | 0           |
| <b><i>b</i>-PLGF<sub>24</sub></b> | 24           | 1.06                    | 0.91                    | 1.38      | 34         | 24               | 0           |
| <b><i>b</i>-PLGF<sub>49</sub></b> | 50           | 1.11                    | 0.91                    | 1.38      | 35         | 49               | 0           |
| <b><i>b</i>-PLGF<sub>73</sub></b> | 68           | 1.10                    | 0.89                    | 1.42      | 32         | 73               | 0           |

<sup>a</sup>Mole fraction of depsipeptide units in feed. <sup>b</sup>Estimated by <sup>1</sup>H NMR (solvent: CDCl<sub>3</sub>). <sup>c</sup>Estimated by SEC (eluent: DMF; standard: PEG). <sup>d</sup>Degree of polymerization of sum of lactide and depsipeptide units. <sup>e</sup> $x$ : mole fraction of depsipeptide units in a hydrophobic segment of diblock copolymers. <sup>f</sup> $X_c$ : crystallinity determined by differential scanning calorimetry (DSC).  $X_c = (\Delta H_m + \Delta H_c) / \Delta H_{m, \text{theory}}$  ( $\Delta H_{m, \text{theory}} = -93.7$  J/g).

FIGURE 2: <sup>1</sup>H NMR spectra of (a) PEG-*b*-PLGL (***b*-PLGL<sub>49</sub>**) and (b) PEG-*b*-PLGF (***b*-PLGF<sub>49</sub>**) in CDCl<sub>3</sub>.

loading (DL), entrapment efficiency (EE), and drug recovery (DR) were calculated by the following equations:

$$PR (\%) = \frac{(\text{polymer found})}{(\text{polymer in feed})} (w/w) \times 100,$$

$$DL (\%) = \frac{(\text{drug found})}{(\text{micelle found})} (w/w) \times 100,$$

$$EE (\%) = \frac{[(\text{drug found}) / (\text{micelle found})] (w/w)}{[(\text{drug in feed}) / (\text{micelle in feed})] (w/w)} \times 100,$$

$$DR (\%) = \frac{(\text{drug found})}{(\text{drug in feed})} (w/w) \times 100.$$

(1)

### 3. Results and Discussion

**3.1. Synthesis of PEG-*b*-Poly(LA-co-depsipeptide) Copolymers.** PEG-*b*-poly(LA-co-depsipeptide) copolymers with various mole fraction of depsipeptide units and similar molecular weights were successfully synthesized. The structures of the copolymers were characterized by <sup>1</sup>H NMR spectroscopy in CDCl<sub>3</sub> (Figure 2). The spectrum was given as a simple

integration of MeO-PEG and PLGL or PLGF. Figure 3 shows the results of SEC for PEG-*b*-PLLA, PEG-*b*-PDLLA, PEG-*b*-PLGL, and PEG-*b*-PLGF, and all of the obtained block copolymers showed unimodal molecular weight distribution. The number average molecular weight ( $M_n$ ) estimated from <sup>1</sup>H NMR spectra and SEC, degree of polymerization of each hydrophobic segment, mole fraction of depsipeptide unit in each poly (LA-co-depsipeptide) segment, and crystallinity estimated by DSC were summarized in Table 1. We use sample codes ***b*-PLLA**, ***b*-PDLLA**, ***b*-PLGL<sub>x</sub>**, and ***b*-PLGF<sub>x</sub>** for PEG-*b*-PLLA, PEG-*b*-PDLLA, PEG-*b*-PLGL, and PEG-*b*-PLGF, respectively, and the subscript numbers ( $x$ ) in the codes for ***b*-PLGL<sub>x</sub>** and ***b*-PLGF<sub>x</sub>** mean the mole fraction of depsipeptide units.  $M_n$  values for all copolymers estimated from <sup>1</sup>H NMR spectra were around  $1.1 \times 10^4$  Da, and these values showed relatively good consistency with the results obtained from SEC measurements. The mole fraction of depsipeptide units in each hydrophobic segment ( $x$ ) was calculated from integration ratio of methine groups of L-LA to methyl groups of Leu or methylene groups of Phe. The crystallinity of hydrophobic segment of copolymers was estimated from a fusion enthalpy measured by DSC. All of PEG-*b*-PLGL and PEG-*b*-PLGF copolymers did not show fusion enthalpy, indicating that the hydrophobic segments in

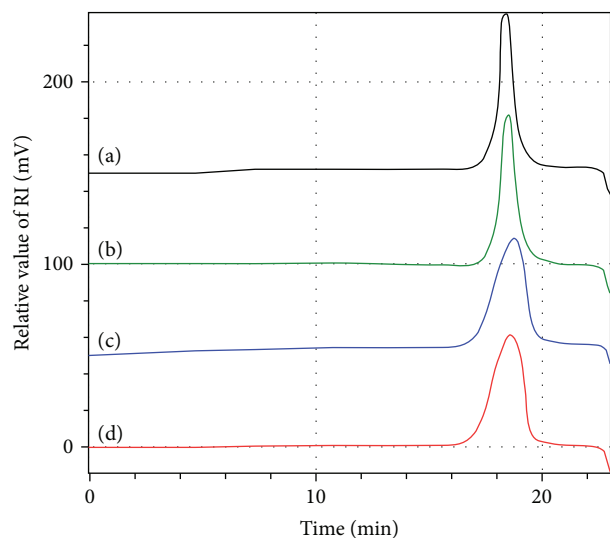


FIGURE 3: Size exclusion chromatograms of (a) PEG-*b*-PLLA, (b) PEG-*b*-PDLLA, (c) PEG-*b*-PLGL (*b*-PLGL<sub>49</sub>), and (d) PEG-*b*-PLGF<sub>49</sub> (*b*-PLGF<sub>49</sub>).

these copolymers were amorphous. On the other hand, PEG-*b*-PLLA showed a fusion enthalpy peak, and the crystallinity of PLLA segment was calculated to be ca. 35%.

### 3.2. Effects of Copolymer Structures on Drug Loading into Micelles.

To discuss the relationship between copolymer structures and drug loading behavior, we selected FL, non-ionic aromatic fluorophore having hydroxyl groups and cyclic ester group, as a model drug and prepared FL-loaded micelles using various block copolymers with various amount of FL in feed. The results are summarized in Table 2. In Table 2, each polymeric micelle was expressed by code such as *b*-PLGL<sub>x</sub>(Y), where Y means the amount of model drug in feed (wt% to polymer). As a trend, yields of micelles, drug recovery (DR), and polymer recovery (PR) were decreased with increase in FL in feed. Presumably, much amount of FL inhibits the formation of micelle and the copolymers precipitated together with unloaded FL: coprecipitation of the copolymer and FL occurred. Before discussing the influence of polymer structures on the drug loading behavior, to estimate the effect of crystallinity of hydrophobic segment, the results for semicrystalline *b*-PLLA and amorphous *b*-PDLLA were discussed. Figure 4 shows the relationship of DL, DR, and hydrodynamic diameter with FL in feed for *b*-PLLA and *b*-PDLLA micelles. When the amount of FL in feed was below 25 wt%, DL for *b*-PLLA and *b*-PDLLA micelles was almost the same and increased with increase in the amounts of FL in feed. However, the DL for *b*-PLLA micelle was slightly decreased with increase in the amounts of FL in feed where the amounts of FL in feed were more than 30 wt%. In this condition, *b*-PDLLA micelles showed higher DL than *b*-PLLA micelle. These results suggest that amorphous state of hydrophobic segments in the core of polymeric micelle is suitable to entrap FL molecules at the high range of feed amount. But the crystallinity does not

have significant influence on the drug loading when the feed amount of FL is below 25%. In addition, increase in hydrodynamic diameter of micelles was observed with the increase in feed amount of FL.

The results for *b*-PLGL and *b*-PLGF micelles were then compared to discuss the effect of side-chain structures of the core-forming segment. Figure 5 shows the results for *b*-PLGL<sub>49</sub> and *b*-PLGF<sub>49</sub> micelles as typical examples. Both of *b*-PLGL and *b*-PLGF micelles showed similar tendency and higher DL values compared with *b*-PLLA and *b*-PDLLA micelles. DL increased with increase in the amount of FL in feed until the feed amount was 35 wt%, but decreased at the high feed amount of FL (40%). *b*-PLGL micelle showed slightly higher DL value compared with *b*-PLGF micelle.

To discuss the effect of side-chain structure of core-forming segment in detail, the dependence of DL and hydrodynamic diameter on the mole fraction of depsipeptide units for *b*-PLGL and *b*-PLGF micelles was summarized in Figure 6. In Figures 6(a), 6(b), and 6(c), the plots at which mole ratio for depsipeptide units is 0% mean the results of *b*-PLLA micelles, and the results of *b*-PDLLA micelles were shown as open triangles. *b*-PLGL and *b*-PLGF micelles showed higher DL compared with *b*-PLLA and *b*-PDLLA micelles at the ranges of the amount of FL feed (30–40 wt%). In addition to the decrease in crystallinity of the hydrophobic segments, the introductions of aliphatic (Leu) and aromatic (Phe) side chains had positive influence on DL of the micelles. Additionally, the presence of amino bonds might have some positive influence on the drug loading behavior for these micelles. In Figure 6(a) (the amount of FL in feed = 25 wt%), the DL for *b*-PLGL micelles increased with increase in the mole fraction of depsipeptide units until they reached 49%, but plateaued where the mole fraction of depsipeptide units was over 50%. In Figures 6(b) and 6(c) (the amounts of FL in feed = 30 and 35 wt%) showed similar trend for DL versus mole fraction of depsipeptide units. *b*-PLGF micelles showed a similar tendency in the relationship of DL and mole fraction of depsipeptide units as *b*-PLGL micelles showed. Interestingly, the maximum DL values in each figure for *b*-PLGL micelles were higher than those for *b*-PLGF micelles. Before the experiments, we presumed that *b*-PLGF with aromatic side chains would show higher DL value than aliphatic *b*-PLGL because of  $\pi$ - $\pi$  stacking interaction of benzyl groups of PLGF segment and aromatic FL molecules. But the results were reverse. The reason has not been explained. Based on these results, the miscibility of FL with PLGL segments is higher than PLGF. Flexibility and segmental dynamics of PLGL in the micelle core can presumably be favorable to uptake larger amounts of FL molecules compared with PLGF having aromatic side chains.

Finally, we discussed the combination of core-forming segment and drugs (Table 3). AF was chosen to discuss the effect of polar (amino) group on DL for the micelles. As a result, DL values of AF for all polymeric micelles tested were significantly smaller than those of FL. But the DL values of AF for *b*-PLGL and *b*-PLGF micelles were larger than those for *b*-PLLA and *b*-PDLLA micelles, showing similar trends as the cases of FL. These results mean that small difference in drug molecule structure has great influence

TABLE 2: Results of preparation of fluorescein-loaded polymeric micelles.

| Code                              | Fluorescein in feed [wt%] | Yield mg (%) | PR [%] | DL [%] | EE [%] | DR [%] |
|-----------------------------------|---------------------------|--------------|--------|--------|--------|--------|
| <i>b</i> -PLLA(0)                 | 0                         | 21.0 (84)    | 84     | 0.0    | —      | —      |
| <i>b</i> -PLLA(10)                | 10                        | 16.7 (60)    | 60     | 10.4   | 104    | 63     |
| <i>b</i> -PLLA(15)                | 15                        | 16.0 (54)    | 55     | 13.5   | 90     | 49     |
| <i>b</i> -PLLA(20)                | 20                        | 14.4 (46)    | 48     | 16.9   | 85     | 39     |
| <i>b</i> -PLLA(25)                | 25                        | 12.1 (36)    | 40     | 17.9   | 72     | 26     |
| <i>b</i> -PLLA(30)                | 30                        | 7.0 (20)     | 23     | 16.6   | 60     | 11     |
| <i>b</i> -PLLA(35)                | 35                        | 1.6 (4)      | 5      | 14.5   | 41     | 1.7    |
| <i>b</i> -PDLLA(0)                | 0                         | 22.3 (89)    | 89     | 0.0    | —      | —      |
| <i>b</i> -PDLLA(10)               | 10                        | 22.3 (80)    | 79     | 11.6   | 116    | 93     |
| <i>b</i> -PDLLA(15)               | 15                        | 20.0 (68)    | 69     | 13.9   | 92     | 63     |
| <i>b</i> -PDLLA(20)               | 20                        | 21.2 (68)    | 71     | 16.3   | 82     | 55     |
| <i>b</i> -PDLLA(25)               | 25                        | 16.9 (51)    | 56     | 17.8   | 71     | 36     |
| <i>b</i> -PDLLA(30)               | 30                        | 13.8 (39)    | 44     | 20.0   | 67     | 26     |
| <i>b</i> -PDLLA(35)               | 35                        | 2.7 (7)      | 9      | 19.9   | 57     | 4.0    |
| <i>b</i> -PLGL <sub>20</sub> (0)  | 0                         | 22.0 (89)    | 89     | 0.0    | —      | —      |
| <i>b</i> -PLGL <sub>20</sub> (25) | 25                        | 24.9 (75)    | 78     | 21.7   | 87     | 65     |
| <i>b</i> -PLGL <sub>20</sub> (30) | 30                        | 23.1 (65)    | 72     | 21.7   | 72     | 47     |
| <i>b</i> -PLGL <sub>20</sub> (35) | 35                        | 12.9 (34)    | 41     | 20.2   | 58     | 19     |
| <i>b</i> -PLGL <sub>20</sub> (40) | 40                        | 5.2 (12)     | 16     | 22.0   | 55     | 6.9    |
| <i>b</i> -PLGL <sub>37</sub> (0)  | 0                         | 20.4 (82)    | 82     | 0.0    | —      | —      |
| <i>b</i> -PLGL <sub>37</sub> (25) | 25                        | 26.8 (80)    | 83     | 22.4   | 90     | 72     |
| <i>b</i> -PLGL <sub>37</sub> (30) | 30                        | 29.7 (83)    | 86     | 27.8   | 93     | 77     |
| <i>b</i> -PLGL <sub>37</sub> (35) | 35                        | 18.9 (49)    | 56     | 25.3   | 72     | 36     |
| <i>b</i> -PLGL <sub>37</sub> (40) | 40                        | 6.6 (16)     | 20     | 25.6   | 64     | 10     |
| <i>b</i> -PLGL <sub>49</sub> (0)  | 0                         | 20.7 (83)    | 83     | 0.0    | —      | —      |
| <i>b</i> -PLGL <sub>49</sub> (25) | 25                        | 27.6 (83)    | 82     | 25.5   | 102    | 85     |
| <i>b</i> -PLGL <sub>49</sub> (30) | 30                        | 25.8 (72)    | 73     | 29.0   | 97     | 70     |
| <i>b</i> -PLGL <sub>49</sub> (35) | 35                        | 19.5 (51)    | 55     | 29.2   | 83     | 42     |
| <i>b</i> -PLGL <sub>49</sub> (40) | 40                        | 9.0 (22)     | 27     | 24.1   | 60     | 13     |
| <i>b</i> -PLGL <sub>59</sub> (0)  | 0                         | 22.6 (90)    | 90     | 0.0    | —      | —      |
| <i>b</i> -PLGL <sub>59</sub> (25) | 25                        | 26.5 (80)    | 81     | 24.0   | 96     | 76     |
| <i>b</i> -PLGL <sub>59</sub> (30) | 30                        | 28.1 (79)    | 81     | 27.7   | 92     | 73     |
| <i>b</i> -PLGL <sub>59</sub> (35) | 35                        | 19.8 (51)    | 56     | 29.0   | 83     | 43     |
| <i>b</i> -PLGL <sub>59</sub> (40) | 40                        | 7.1 (17)     | 20     | 29.6   | 74     | 12.6   |
| <i>b</i> -PLGL <sub>75</sub> (0)  | 0                         | 22.8 (91)    | 91     | 0.0    | —      | —      |
| <i>b</i> -PLGL <sub>75</sub> (25) | 25                        | 26.9 (81)    | 81     | 24.8   | 99     | 80     |
| <i>b</i> -PLGL <sub>75</sub> (30) | 30                        | 25.7 (72)    | 72     | 29.6   | 99     | 71     |
| <i>b</i> -PLGL <sub>75</sub> (35) | 35                        | 19.2 (50)    | 55     | 28.9   | 83     | 41     |
| <i>b</i> -PLGL <sub>75</sub> (40) | 40                        | 11.1 (27)    | 32     | 28.5   | 71     | 19     |
| <i>b</i> -PLGF <sub>24</sub> (0)  | 0                         | 23.0 (92)    | 92     | 0.0    | —      | —      |
| <i>b</i> -PLGF <sub>24</sub> (24) | 25                        | 22.9 (69)    | 73     | 20.6   | 82     | 57     |
| <i>b</i> -PLGF <sub>24</sub> (30) | 30                        | 22.3 (62)    | 68     | 23.7   | 79     | 49     |
| <i>b</i> -PLGF <sub>24</sub> (35) | 35                        | 12.7 (33)    | 39     | 24.1   | 68     | 23     |
| <i>b</i> -PLGF <sub>24</sub> (40) | 40                        | 8.8 (21)     | 27     | 22.0   | 55     | 12     |

TABLE 2: Continued.

| Code                              | Fluorescein in feed [wt%] | Yield mg (%) | PR [%] | DL [%] | EE [%] | DR [%] |
|-----------------------------------|---------------------------|--------------|--------|--------|--------|--------|
| <i>b</i> -PLGF <sub>49</sub> (0)  | 0                         | 20.8 (83)    | 83     | 0.0    | —      | —      |
| <i>b</i> -PLGF <sub>49</sub> (25) | 25                        | 26.4 (79)    | 82     | 22.8   | 91     | 72     |
| <i>b</i> -PLGF <sub>49</sub> (30) | 30                        | 22.8 (64)    | 69     | 24.6   | 82     | 52     |
| <i>b</i> -PLGF <sub>49</sub> (35) | 35                        | 11.0 (29)    | 32     | 26.2   | 75     | 21     |
| <i>b</i> -PLGF <sub>49</sub> (40) | 40                        | 4.6 (11)     | 14     | 22.4   | 56     | 6.2    |
| <i>b</i> -PLGF <sub>73</sub> (0)  | 0                         | 22.3 (89)    | 89     | 0.0    | —      | —      |
| <i>b</i> -PLGF <sub>73</sub> (25) | 25                        | 23.4 (70)    | 71     | 23.6   | 95     | 66     |
| <i>b</i> -PLGF <sub>73</sub> (30) | 30                        | 18.6 (52)    | 56     | 24.1   | 80     | 42     |
| <i>b</i> -PLGF <sub>73</sub> (35) | 35                        | 13.4 (35)    | 40     | 25.4   | 72     | 25     |
| <i>b</i> -PLGF <sub>73</sub> (40) | 40                        | 6.4 (15)     | 18     | 28.4   | 71     | 11     |

PR (%) = (polymer found)/(polymer in feed) (w/w) × 100.

DL (%) = (drug found)/(micelle found) (w/w) × 100.

EE (%) = [(drug found)/(micelle found)]/[(drug in feed)/(micelle in feed)] (w/w) × 100.

DR (%) = (drug found)/(drug in feed) (w/w) × 100.

TABLE 3: Characterization of micelles versus drugs in 30% feed.

| Drug <sup>a</sup>  | Drug loading (DL) (wt%) |                 |                              |                              |
|--------------------|-------------------------|-----------------|------------------------------|------------------------------|
|                    | <i>b</i> -PLLA          | <i>b</i> -PDLLA | <i>b</i> -PLGL <sub>49</sub> | <i>b</i> -PLGF <sub>49</sub> |
| Fluorescein        | 16.6                    | 20.0            | 29.0                         | 26.2                         |
| 4-Aminofluorescein | 3.0                     | 4.7             | 7.3                          | 7.2                          |
| Pyrene             | 0.5                     | 0.6             | 0.6                          | 0.7                          |
| Doxorubicin        | 30.3                    | 28.6            | 29.7                         | 29.8                         |

DL (%) = (drug found)/(micelle found) (w/w) × 100.

<sup>a</sup>The amount of drug in feed = 30 wt%.

on the drug loading into the micelles. Probably relatively high water solubility of AF had critical influence on the entrapment behavior of the model drug into the micelles. On the other hand, PY and DOX gave contrastive results. Both of PY and DOX are hydrophobic poorly water-soluble aromatic compounds, but DOX has polar hydroxyl and amino groups. PY consisting only of aromatic ring was hardly loaded into all micelles tested, and the DL values were around 0.6%. However, the PR of the PY-loaded micelles was relatively high (78–87%) indicating similar trends observed for AF. On the other hand, DOX showed high level DL values (around 30%) and high PR (83–89%) for all of the micelles tested. Although DL of FL into *b*-PLGL and *b*-PLGF micelles were higher than those into *b*-PLLA and *b*-PDLLA micelles, the DL values of DOX for all of the micelles were not significantly different. These all results mean that the combination of core-forming polymer and drugs has critical influence on the drug loading behavior into polymeric micelles.

#### 4. Conclusions

In this study, we discussed the relationship between the structure of core-forming segment and the structure of drugs to optimize the biodegradable AB-type amphiphilic block copolymer for polymeric micelle-type drug delivery

carriers. Using PEG-*b*-poly(LA-*co*-depsipeptide), the systematic variation of core-forming (hydrophobic) segments could be provided. PEG-*b*-PLGL and PEG-*b*-PLGF with the similar molecular weights and various mole fractions of depsipeptide units were synthesized and used for the preparation of polymeric micelles entrapping model drug (FL). The yields of micelles and a DR were decreased with the increase in the amounts of FL in feed. From the results for PEG-*b*-PLLA and PEG-*b*-PDLLA, noncrystallinity of the hydrophobic segments was suitable to load the FL where the amount of FL in feed was high. Both of PEG-*b*-PLGL micelle with aliphatic (Leu) side-chain groups and PEG-*b*-PLGF micelle with aromatic (Phe) side-chain groups showed higher DL values compared with PEG-*b*-PDLLA micelles. The introduction of aliphatic or aromatic side-chain groups was effective to increase the drug loading, and DL values for PEG-*b*-PLGL and PEG-*b*-PLGF were increased with increase in the mole fraction of depsipeptide units. PEG-*b*-PLGL micelle showed higher DL than PEG-*b*-PLGF micelle only when the amount of FL in feed was high. The interaction of aromatic side chain of PLGF segment with aromatic model drug compound had no significant impact on the drug loading. Comparing the four model drugs (FL, AF, PY, and DOX) used in this study, it was revealed that the combination of the core-forming segments and drugs had great influences on DL and PR. All information obtained in this study should

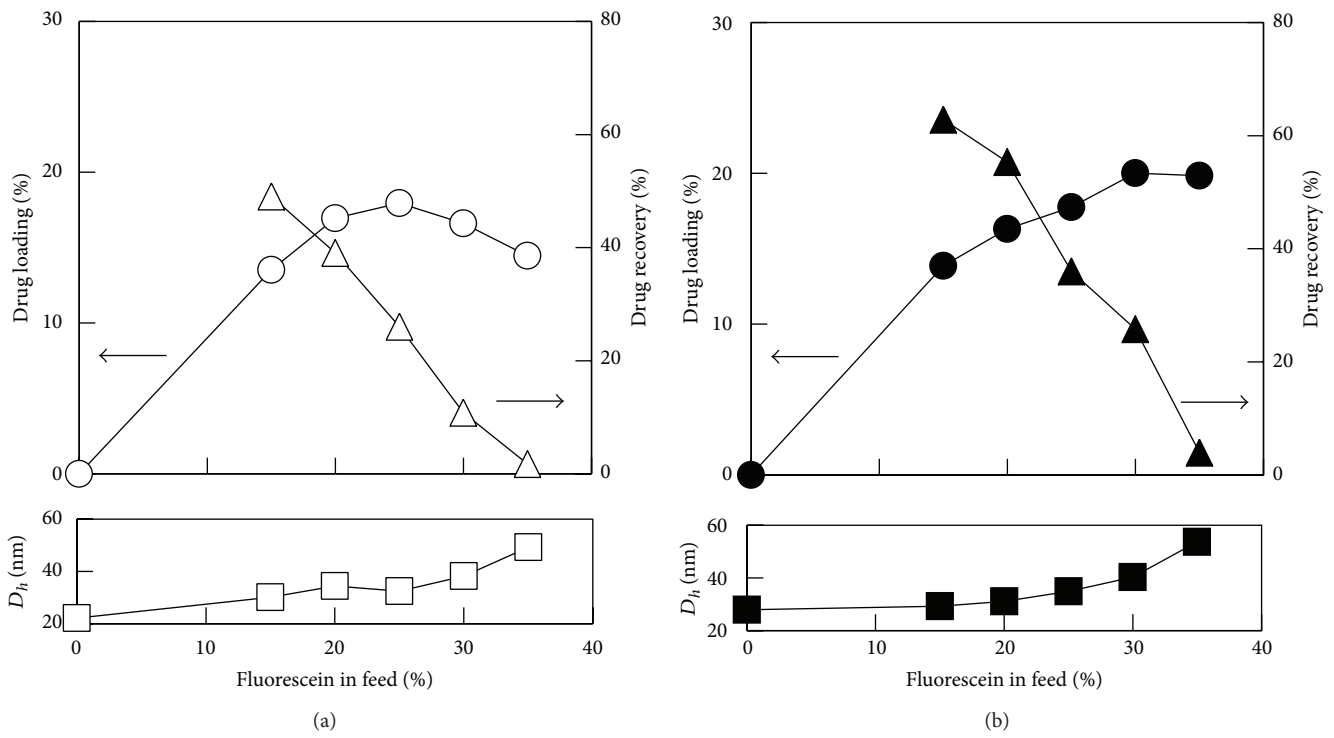


FIGURE 4: Drug loading (circle), drug recovery (triangle), and hydrodynamic diameter (square) for (a) **b-PLLA** and (b) **b-PDLLA** micelles versus the amount of fluorescein in feed.

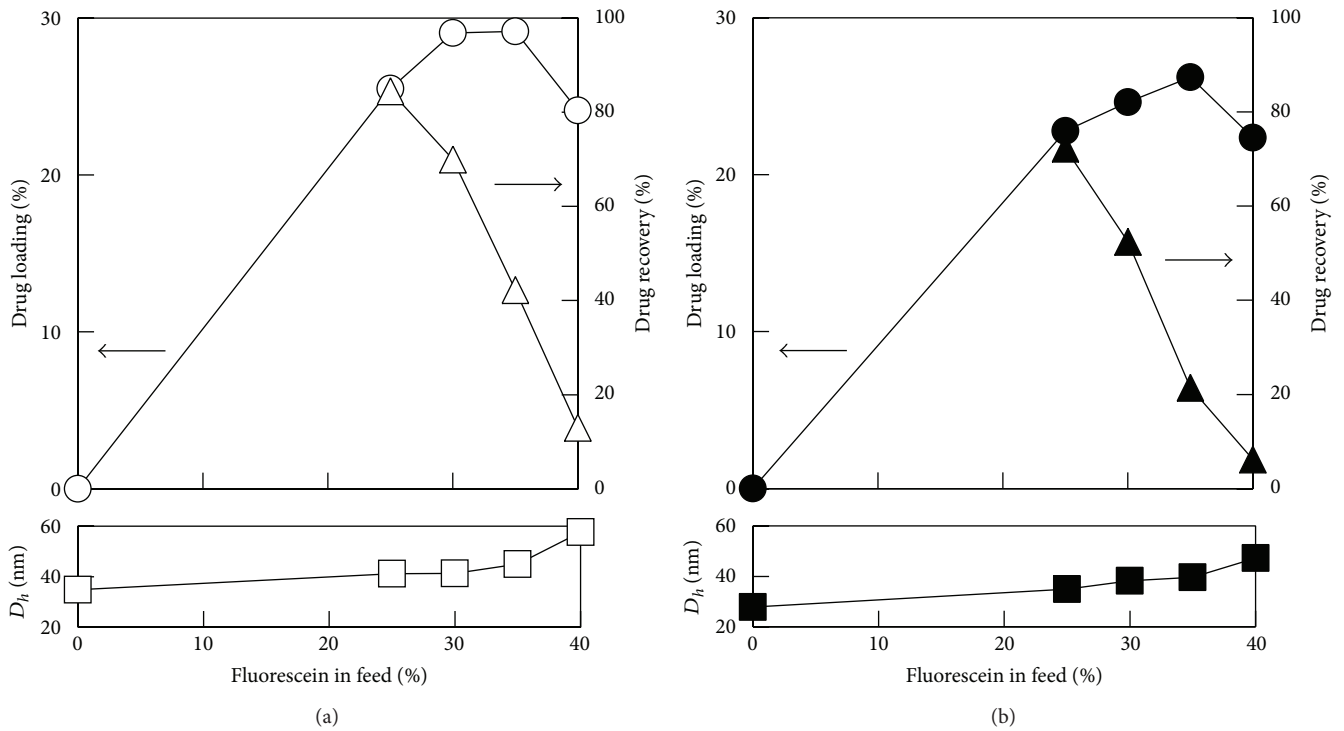


FIGURE 5: Drug loading (circle), drug recovery (triangle), and hydrodynamic diameter (square) for (a) **b-PLGL<sub>49</sub>** and (b) **b-PLGF<sub>49</sub>** micelles versus the amount of fluorescein in feed.

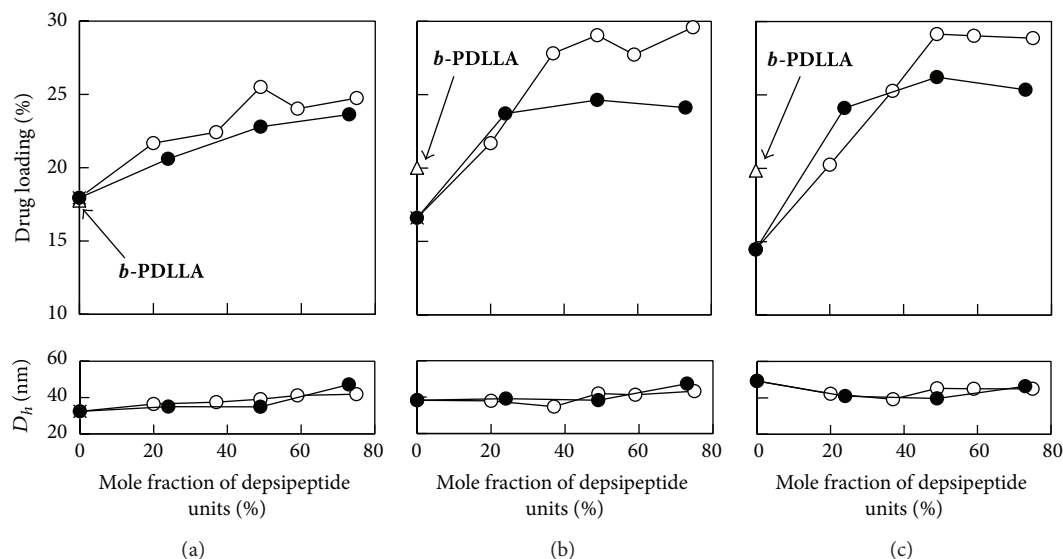


FIGURE 6: Drug loading and hydrodynamic diameter for **b-PLGL** (open circle) and **b-PLGF** (closed circle) micelles versus mole fraction of depsiptide units at various fluorescein in feed (a) 25%, (b) 30%, and (c) 35%. The values for **b-PDLLA** micelle were shown as open triangles.

be useful for rational design of polymeric micelle-type drug delivery carrier with high drug loading efficiency.

### Conflict of Interests

The authors declare that there is no conflict of interests regarding the publication of this paper.

### Acknowledgments

A portion of this work was financially supported by a Grant-in-Aid for Scientific Research (no. 22300172) from the Japan Society for the Promotion of Science (JSPS) and Strategic Project to Support the Formation of Research Bases at Private Universities: Matching Fund Subsidy from Ministry of Education, Culture, Sports, Science and Technology (MEXT), Japan, 2010–2014.

### References

- [1] Y. Lu and K. Park, "Polymeric micelles and alternative nanonized delivery vehicles for poorly soluble drugs," *International Journal of Pharmaceutics*, vol. 453, no. 1, pp. 198–214, 2013.
- [2] S. S. Kulthe, Y. M. Choudhari, N. N. Inamdar, and V. Mourya, "Polymeric micelles: authoritative aspects for drug delivery," *Designed Monomers and Polymers*, vol. 15, no. 5, pp. 465–521, 2012.
- [3] J. Gong, M. Chen, Y. Zheng, S. Wang, and Y. Wang, "Polymeric micelles drug delivery system in oncology," *Journal of Controlled Release*, vol. 159, no. 3, pp. 312–323, 2012.
- [4] K. Miyata, R. J. Christie, and K. Kataoka, "Polymeric micelles for nano-scale drug delivery," *Reactive and Functional Polymers*, vol. 71, no. 3, pp. 227–234, 2011.
- [5] G. Gaucher, P. Satturwar, M.-C. Jones, A. Furtos, and J.-C. Leroux, "Polymeric micelles for oral drug delivery," *European Journal of Pharmaceutics and Biopharmaceutics*, vol. 76, no. 2, pp. 147–158, 2010.
- [6] T. Nakanishi, S. Fukushima, K. Okamoto et al., "Development of the polymer micelle carrier system for doxorubicin," *Journal of Controlled Release*, vol. 74, no. 1–3, pp. 295–302, 2001.
- [7] D. E. Discher and A. Eisenberg, "Polymer vesicles," *Science*, vol. 297, no. 5583, pp. 967–973, 2002.
- [8] C. J. F. Rijcken, O. Soga, W. E. Hennink, and C. F. van Nostrum, "Triggered destabilisation of polymeric micelles and vesicles by changing polymers polarity: an attractive tool for drug delivery," *Journal of Controlled Release*, vol. 120, no. 3, pp. 131–148, 2007.
- [9] S. B. La, T. Okano, and K. Kataoka, "Preparation and characterization of the micelle-forming polymeric drug indomethacin-incorporated poly(ethylene oxide)-poly( $\beta$ -benzyl L-aspartate) block copolymer micelles," *Journal of Pharmaceutical Sciences*, vol. 85, no. 1, pp. 85–90, 1996.
- [10] J. Connor, N. Norley, and L. Huang, "Biodistribution of pH-sensitive immunoliposomes," *Biochimica et Biophysica Acta*, vol. 884, no. 3, pp. 474–481, 1986.
- [11] I. L. Shin, S. Y. Kim, Y. M. Lee, C. S. Cho, and Y. K. Sung, "Methoxy poly(ethylene glycol)/ $\epsilon$ -caprolactone amphiphilic block copolymeric micelle containing indomethacin. I. Preparation and characterization," *Journal of Controlled Release*, vol. 51, no. 1, pp. 1–11, 1998.
- [12] M. Yokoyama, M. Miyauchi, N. Yamada et al., "Characterization and anticancer activity of the micelle-forming polymeric anticancer drug Adriamycin-conjugated poly(ethylene glycol)-poly(aspartic acid) block copolymer," *Cancer Research*, vol. 50, no. 6, pp. 1693–1700, 1990.
- [13] M. Yokoyama, G. S. Kwon, T. Okano, Y. Sakurai, T. Seto, and K. Kataoka, "Preparation of micelle-forming polymer-drug conjugates," *Bioconjugate Chemistry*, vol. 3, no. 4, pp. 295–301, 1992.
- [14] M. Yokoyama, T. Okano, Y. Sakurai, S. Suwa, and K. Kataoka, "Introduction of cisplatin into polymeric micelle," *Journal of Controlled Release*, vol. 39, no. 2-3, pp. 351–356, 1996.

- [15] A. Harada and K. Kataoka, "Novel polyion complex micelles entrapping enzyme molecules in the core: preparation of narrowly-distributed micelles from lysozyme and poly(ethylene glycol)-poly(aspartic acid) block copolymer in aqueous medium," *Macromolecules*, vol. 31, no. 2, pp. 288–294, 1998.
- [16] K. Kataoka, H. Togawa, A. Harada, K. Yasugi, T. Matsumoto, and S. Katayose, "Spontaneous formation of polyion complex micelles with narrow distribution from antisense oligonucleotide and cationic block copolymer in physiological saline," *Macromolecules*, vol. 29, no. 26, pp. 8556–8557, 1996.
- [17] A. Harada and K. Kataoka, "Formation of polyion complex micelles in an aqueous milieu from a pair of oppositely-charged block copolymers with poly(ethylene glycol) segments," *Macromolecules*, vol. 28, no. 15, pp. 5294–5299, 1995.
- [18] H. Yuan, L.-J. Lu, Y.-Z. Du, and F.-Q. Hu, "Stearic acid-g-chitosan polymeric micelle for oral drug delivery: in vitro transport and in vivo absorption," *Molecular Pharmaceutics*, vol. 8, no. 1, pp. 225–238, 2011.
- [19] C. Cui, Y. N. Xue, M. Wu et al., "Cellular uptake, intracellular trafficking, and antitumor efficacy of doxorubicin-loaded reduction-sensitive micelles," *Biomaterials*, vol. 34, no. 15, pp. 3858–3869, 2013.
- [20] P.-Y. Li, P.-S. Lai, W.-C. Hung, and W.-J. Syu, "Poly(l-lactide)-Vitamin e TPGS nanoparticles enhanced the cytotoxicity of doxorubicin in drug-resistant MCF-7 breast cancer cells," *Biomacromolecules*, vol. 11, no. 10, pp. 2576–2582, 2010.
- [21] J. Yue, S. Liu, Z. Xie, Y. Xing, and X. Jing, "Size-dependent biodistribution and antitumor efficacy of polymer micelle drug delivery systems," *Journal of Materials Chemistry B*, vol. 1, pp. 4273–4280, 2013.
- [22] M. Gou, X. Zheng, K. Men et al., "Poly( $\epsilon$ -caprolactone)/poly(ethylene glycol)/poly( $\epsilon$ -caprolactone) nanoparticles: preparation, characterization, and application in doxorubicin delivery," *Journal of Physical Chemistry B*, vol. 113, no. 39, pp. 12928–12933, 2009.
- [23] T. Ouchi, T. Nozaki, A. Ishikawa, I. Fujimoto, and Y. Ohya, "Synthesis and enzymatic hydrolysis of lactic acid-depsipeptide copolymers with functionalized pendant groups," *Journal of Polymer Science A*, vol. 35, no. 2, pp. 377–383, 1997.
- [24] Y. Ohya, H. Matsunami, E. Yamabe, and T. Ouchi, "Cell attachment and growth on films prepared from poly(depsipeptide-co-lactide) having various functional groups," *Journal of Biomedical Materials Research A*, vol. 65, no. 1, pp. 79–88, 2003.
- [25] F. Tasaka, Y. Ohya, and T. Ouchi, "Synthesis of novel comb-type polylactide and its biodegradability," *Macromolecules*, vol. 34, no. 16, pp. 5494–5500, 2001.
- [26] T. Ouchi, H. Seike, T. Nozaki, and Y. Ohya, "Synthesis and characteristics of polydepsipeptide with pendant thiol groups," *Journal of Polymer Science A*, vol. 36, no. 8, pp. 1283–1290, 1998.

## Research Article

# Fabrication and Characterization of Thermoresponsive Polystyrene Nanofibrous Mats for Cultured Cell Recovery

Hwan Hee Oh,<sup>1</sup> Young-Gwang Ko,<sup>1</sup> Hiroshi Uyama,<sup>2</sup> Won Ho Park,<sup>3</sup>  
Donghwan Cho,<sup>1</sup> and Oh Hyeong Kwon<sup>1</sup>

<sup>1</sup> Department of Polymer Science and Engineering, Kumoh National Institute of Technology, 1 Yangho-dong, Gumi, Gyeongbuk 730-701, Republic of Korea

<sup>2</sup> Department of Applied Chemistry, Graduate School of Engineering, Osaka University Suita, Osaka 565-0871, Japan

<sup>3</sup> Department of Advanced Organic Materials and Textile System Engineering, Chungnam National University, 79 Daehangno, Yuseong-gu, Daejeon 305-764, Republic of Korea

Correspondence should be addressed to Oh Hyeong Kwon; ohkwon@kumoh.ac.kr

Received 11 December 2013; Accepted 30 December 2013; Published 20 February 2014

Academic Editor: Inn-Kyu Kang

Copyright © 2014 Hwan Hee Oh et al. This is an open access article distributed under the Creative Commons Attribution License, which permits unrestricted use, distribution, and reproduction in any medium, provided the original work is properly cited.

Rapid cell growth and rapid recovery of intact cultured cells are an invaluable technique to maintain the biological functions and viability of cells. To achieve this goal, thermoresponsive polystyrene (PS) nanofibrous mat was fabricated by electrospinning of PS solution, followed by the graft polymerization of thermoresponsive poly(*N*-isopropylacrylamide)(PIPAAm) on PS nanofibrous mats. Image analysis of the PS nanofiber revealed a unimodal distribution pattern with 400 nm average fiber diameter. Graft polymerization of PIPAAm on PS nanofibrous mats was confirmed by spectroscopic methods such as ATR-FTIR, ESCA, and AFM. Human fibroblasts were cultured on four different surfaces, PIPAAm-grafted and ungrafted PS dishes and PIPAAm-grafted and ungrafted PS nanofibrous mats, respectively. Cells on PIPAAm-grafted PS nanofibrous mats were well attached, spread, and proliferated significantly much more than those on other surfaces. Cultured cells were easily detached from the PIPAAm-grafted surfaces by decreasing culture temperature to 20°C, while negligible cells were detached from ungrafted surfaces. Moreover, cells on PIPAAm-grafted PS nanofibrous mats were detached more rapidly than those on PIPAAm-grafted PS dishes. These results suggest that thermoresponsive nanofibrous mats are attractive cell culture substrates which enable rapid cell growth and recovery from the culture surface for application to tissue engineering and regenerative medicine.

## 1. Introduction

Tissue engineering is a rapidly expanding field that seeks to create specific human tissues and organs by combining cells and scaffolds formed typically using either synthetic or naturally-derived polymers [1–4]. Tissue engineering has three essential components as follows: cells, scaffolds using biomaterials, and bioactive molecules. The most important component among them is highly functional cells, because it is unattainable to develop therapeutic replacement tissue even if the ideal scaffold was prepared when cells lost their natural functionality.

In this point of view, the process of cell culture requires a method to recover cells from the culture surface.

Trypsin, an enzyme commonly found in the digestive tract, can be used to digest proteins, which cleaves adhesion of cells to the surface and cell-cell junctions. Trypsinization process for cultured cell recovery has a big problem [5, 6]. Protease like trypsin dissociates cell membrane proteins and secreted ECM by cells, resulting in decreased specific cell functions and viability, especially on highly differentiated functionalized cell types. To remedy this problem and recover intact cultured cells or cell sheets, thermoresponsive poly(*N*-isopropylacrylamide) (PIPAAm)-grafted PS dishes were mainly used by Okano group [7–11]. PIPAAm exhibits a phase separation behavior in water below its lower critical solution temperature (LCST) at 32°C [12]. The PIPAAm-grafted surface can reversibly change its

surface hydrophilic/hydrophobic properties in response to temperature changes. Accordingly, cells can be attached to the PIPAAm-grafted surface above 32°C and detached below 32°C by hydration of grafted PIPAAm chains. Okano and his colleagues have reported many scientific and clinical results utilizing PIPAAm-grafted PS cell culture dishes [13–15]. However, cell detachment from PIPAAm-grafted PS dish surface is relatively a slow process. Rapid recovery of cultured cells is very important to prevent their functional damage, because lower temperature treatment for a long time might have negative effects on cell functions. We have already reported that cells or cell sheets cultured on PIPAAm-grafted porous membranes can be recovered more rapidly than PIPAAm-grafted nonporous PS surfaces [16, 17]. Cells can be detached by the hydration of grafted PIPAAm chains, which are promoted by the supply of essential water molecules to hydrate PIPAAm-grafted layer. With porous membranes, the water accesses the PIPAAm-grafted surface from underneath and periphery of the attached cells, resulting in rapid hydration of PIPAAm chains and cell detachment.

Recently, electrospun nanofibers have attracted great attention as a new type of scaffolds for tissue engineering [18–24]. It is well known that extracellular environment influences many aspects of cell behavior such as morphology, functionality, and cell-cell interactions [20]. In natural tissues, cells are surrounded by extracellular matrix (ECM), which has structural features ranging from nanometer to micrometer scale. Hence, a nanostructured porous and large surface area is needed as an alternate to natural ECM. To mimic the natural ECM structure, electrospinning is thought to be one of the most suitable methods to fabricate nanofibrous matrices. We have previously reported that cells on highly porous electrospun nanofibrous mat were well attached, spread, and proliferated much more than nonporous surfaces [25–30]. It is considered that highly porous nanofibrous mat with high surface area and nanosized roughness offers a biomimicking structure during cell culture, more structural space for accommodation and attachment and proliferation of cells, and enables the efficient exchange of nutrient and metabolic wastes.

Rapid cell growth and rapid recovery of intact cultured cells are an invaluable technique to maintain the biological functions and viability of cells for tissue engineering and regenerative medicine. In the present study, we fabricated thermoresponsive PS nanofibrous mats to achieve this goal by electrospinning method and subsequent surface graft polymerization of PIPAAm by electron beam irradiation.

## 2. Experimental

**2.1. Materials.** Isopropyl acrylamide (IPAAm) was purchased from TCI Chemicals (Tokyo, Japan) and used after recrystallization from *n*-hexane. Polystyrene (PS, Mw: 1,280,000; Mw/Mn = 1.03) was purchased from Polymer Source, Inc (Montreal, Canada). N,N-Dimethylformamide (DMF) to prepare PS solution was obtained from Daejung Chemicals and Metals (Gyeonggi, Korea) and used as received without further purification. Polystyrene dish (35 × 10 mm) was

purchased from SPL Life Science (Gyeonggi, Korea). Trypsin-EDTA solution, streptomycin, penicillin, and Dulbecco's modified Eagle's medium (DMEM) were bought from Gibco BRL (Grand Island, NY, USA).

**2.2. Preparation of PS Nanofibrous Mats.** Nanofibrous PS mats were fabricated by electrospinning technique as previously reported [30]. Briefly, PS was dissolved in DMF at a concentration of 3 wt%. The PS solution is contained in a glass syringe controlled by syringe pump. A high voltage is applied between syringe needle and collector. When the electric field reached a critical value with increasing voltage, mutual charge repulsion overcame the surface tension of polymer solution and an electrically charged jet was ejected from the syringe needle to the collector. Because of charge repulsion in polymer solution, diameter of fibers significantly decreased during the flight. PS nanofibrous mats were fabricated reproducibly under the voltage of 10 kV, tip-to-collector distance of 15 cm and flow rate of 1 mL/h. Electrospun PS nanofibrous mat was carefully detached from collector and dried *in vacuo* for 2 days at 30°C to remove residual solvent completely.

**2.3. Heat Treatment of PS Nanofibrous Mat.** Because electrospun PS nanofibrous mat has no bonding points between fibers, its mechanical strength was too low to handle it. To remedy this problem, heat treatment was employed. PS nanofibrous mat was placed between two glass plates (20 cm × 20 cm × 3 mm) and then kept heated for 25 minutes at heating oven fixed at 120°C, which is slightly higher temperature than glass transition temperature (T<sub>g</sub>) of PS.

**2.4. PIPAAm Graft Polymerization on PS Nanofibrous Mat.** IPAAm monomer was dissolved in 2-propanol at a concentration of 55 wt%. This monomer solution (40 μL) was spread uniformly over the surface of the PS nanofibrous mat and PS dish, and then electron beam was irradiated using an area beam electron processing system (Curetron BBC-200-AA2, Nissin-High Voltage, Kyoto, Japan) at various radiation doses (acceleration voltage of 150 kV under 1.0 × 10<sup>-4</sup> Pa). Unreacted monomer and ungrafted polymers were removed by washing extensively with cold water, and the PIPAAm-grafted PS matrices were dried *in vacuo* at room temperature.

**2.5. Characterizations.** The morphology and diameter of electrospun nanofibers were determined by SEM and image analyzer. Mechanical properties of PS nanofibrous mat before and after heat treatment were tested by universal testing machine. The specimen was prepared in accordance with ASTM D638. Grafting of PIPAAm on PS nanofibrous mats and PS dishes was confirmed by attenuated total reflection-Fourier transform IR (ATR-FTIR) and electron spectroscopy for chemical analysis (ESCA). The density of PIPAAm grafted onto the PS nanofibrous mats and PS dishes was determined by ATR-FTIR in comparison with standard calibration curve. The control PS substrate has strong absorption bands attributed to aromatic groups at 1600 cm<sup>-1</sup>. As PIPAAm was grafted onto PS surface, an amide I absorption band appeared

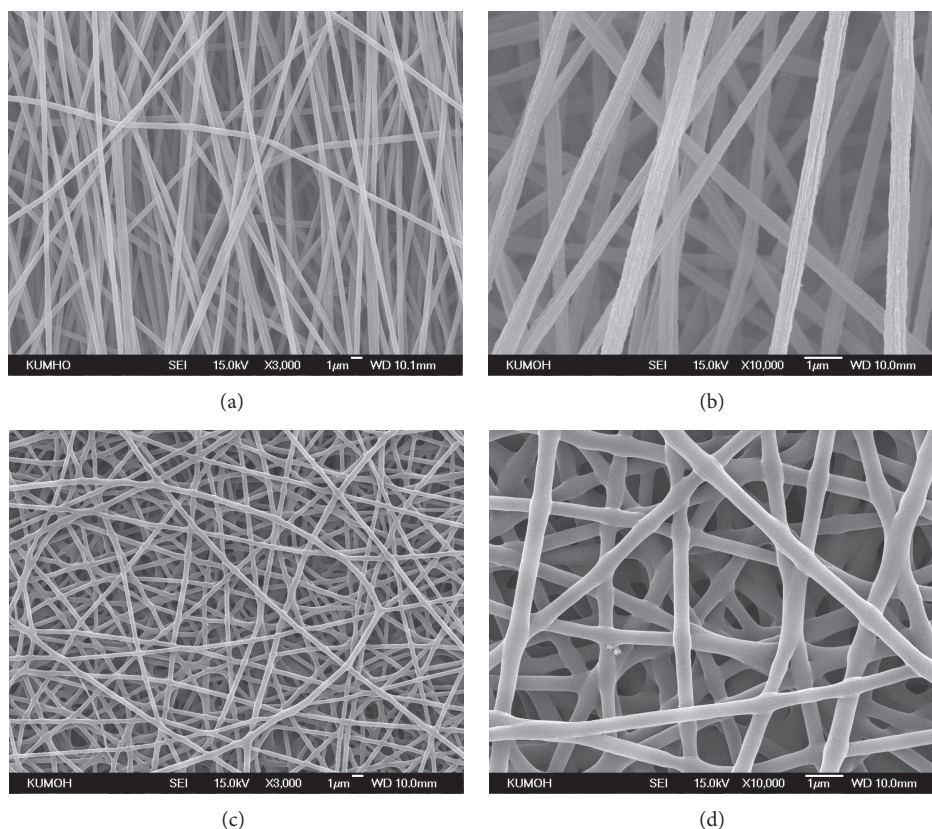


FIGURE 1: SEM micrographs of electrospun polystyrene nanofibrous mat, magnification of  $\times 3,000$  (a) and  $\times 10,000$  (b), respectively. Polystyrene nanofibrous mat after interfiber bonding treatment, magnification of  $\times 3,000$  (c) and  $\times 10,000$  (d), respectively.

in the region of  $1650\text{ cm}^{-1}$ . The peak intensity ratio ( $I_{1650/1600}$ ) was used to determine the amount of PIPAAm grafted on PS surface using a calibration curve of known PIPAAm amount cast on PS surface from solution. Water contact angles were determined by a sessile drop method at 20 and  $37^\circ\text{C}$ . Each sample was cut in size ( $1.0 \times 1.0\text{ cm}$ ) to measure water contact angles. All samples were measured six times and averaged. Contact angles were presented as a mean value ( $n = 6$ ) with a standard deviation.

**2.6. Cell Culture.** To examine the tissue compatibility, human fibroblasts were evenly seeded at 20,000 cells/dish onto each surface of PIPAAm-grafted PS nanofibrous mats, ungrafted PS nanofibrous mats, PIPAAm-grafted PS dishes, and ungrafted PS dishes. Seeded fibroblasts were cultivated in Dulbecco's modified Eagle's medium (DMEM) supplemented with 10% fetal bovine serum and 1% penicillin G-streptomycin. Attached cell morphology and viability of fibroblasts were measured by SEM and MTT assay.

**2.7. Recovery of Cultured Cells.** Detachment of single cells was achieved by lower temperature treatment after incubation at  $37^\circ\text{C}$  for 5 hours. For lower temperature treatment, spread cells on each surface were transferred to a  $\text{CO}_2$  incubator equipped with a cooling unit fixed at  $20^\circ\text{C}$ . The morphology

and detachment rate were determined with SEM and MTT assay as a function of lower temperature treatment time.

### 3. Results and Discussion

**3.1. Characterization of Electrospun Mat.** Polystyrene (PS) nanofibrous mats were prepared via electrospinning with optimized conditions to have an average diameter less than 500 nm to prevent cell penetration into the mat. Electrospun PS mat structures revealed randomly aligned fibers with average diameter of 400 nm (Figures 1(a) and 1(b)). The surface of electrospun nanofibrous mats required heat treatment because of weak mechanical properties. It causes exfoliation of surface layer of nonwoven PS nanofibrous mat during washing process of poly(*N*-isopropylacrylamide) (PIPAAm)-grafted surfaces. For this reason, PS mat was heat-treated at  $120^\circ\text{C}$  (slightly higher temperature than glass transition temperature of the PS mat). After heat treatment, the average diameter of nanofibers was increased to 450 nm and physical crosslinking points appeared (Figures 1(c) and 1(d)). The heat-treated PS nanofibrous mat showed network structure between fibers, while the original PS nanofibrous mat showed a random straightforward structure.

Mechanical properties of the heat-treated PS mat and original PS mat could be compared by using universal testing

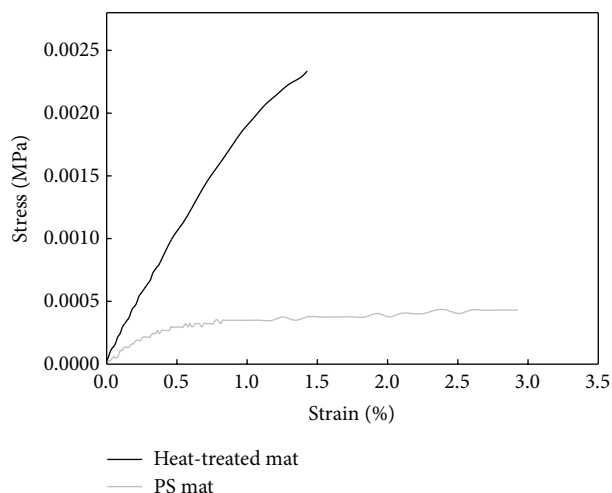


FIGURE 2: Stress-strain curves obtained from tensile test for heat-treated PS mat and original PS mat.

machine (UTM), and the results of tensile strength were indicated in Figure 2. Heat-treated PS mat could resist more stress than PS mat during rinsing process of PIPAAm-grafted PS mat surfaces without separation of outer surfaces. The heat-treated PS mat ( $148.55 \pm 10.55$  MPa) showed higher modulus than original PS mat ( $68.88 \pm 7.96$  MPa). We assumed that this difference of curve shape is due to a presence of physical crosslinking points on the electrospun mat. The load was transferred and absorbed into crosslinking points which appeared after heat treatment. The heat-treated PS mat was altered to be a little bit stiff and rigid than before heat treatment. However, heat treatment of PS mat facilitates washing procedure after PIPAAm graft polymerization.

**3.2. Investigation of PIPAAm-Grafted Surfaces.** The PIPAAm-grafted PS mats and dishes were prepared with various conditions of electron beam irradiation. Grafting of PIPAAm onto surface was performed after preliminary examination for arranging of the irradiation dosage. There was not a morphological deformation of PS nanofibrous mats by electron beam irradiation. To confirm grafting of PIPAAm on PS surface by electron beam irradiation, surface elemental analysis was performed using ESCA. In Figure 3, an atomic percent of nitrogen was observed on the PIPAAm-grafted PS surfaces, while nitrogen was not detected on ungrafted PS surfaces. PIPAAm-grafted PS mat (Figure 3(a)) showed 79.5% of C, 8.8% of N, and 11.7% of O atomic composition. And PIPAAm-grafted PS dish (Figure 3(b)) showed 76.5% of C, 8.3% of N, and 15.2% of O atomic composition, while the ungrafted PS mat and ungrafted PS dish showed 100% of C atomic composition without N and O. Because PS does not contain amide group, nitrogen on the ungrafted surfaces was not surveyed, while PIPAAm has amide groups in the chain. From these results, we infer that PIPAAm was successfully grafted on PS mat and PS dish surfaces by electron beam irradiation.

TABLE 1: Water contact angle ( $^{\circ}$ ) of each surface measured by sessile drop method ( $n = 6$ ).

|                                 | 20 $^{\circ}$ C  | 37 $^{\circ}$ C  |
|---------------------------------|------------------|------------------|
| PIPAAm-grafted polystyrene mat  | $47.83 \pm 2.79$ | $71.60 \pm 1.82$ |
| Ungrafted polystyrene mat       | $75.83 \pm 1.80$ | $74.80 \pm 0.45$ |
| PIPAAm-grafted polystyrene dish | $46.00 \pm 1.87$ | $58.33 \pm 2.50$ |
| Ungrafted polystyrene dish      | $82.50 \pm 1.38$ | $82.80 \pm 0.84$ |

Figure 4 shows ATR-FTIR spectra of PIPAAm-grafted and ungrafted PS surfaces. Significant increase of amide peak at  $1650\text{ cm}^{-1}$  appeared at PIPAAm-grafted surfaces. PS includes aromatic groups that have a characteristic peak at  $1600\text{ cm}^{-1}$  and a characteristic peak of PIPAAm appeared at  $1650\text{ cm}^{-1}$  attributed to amide group in PIPAAm chain. In the cases of PS mat and PS dish without electron beam irradiation (0 kGy), the absorption peak was revealed at  $1600\text{ cm}^{-1}$  only, while PIPAAm-grafted PS mat surface by radiation dose 232, 369 kGy revealed clear peak at  $1650\text{ cm}^{-1}$ . The peak of  $1650\text{ cm}^{-1}$  was increasing as a function of irradiation dosage (Figure 4(a)). Also in PS dishes, amide peak at  $1650\text{ cm}^{-1}$  shows up only at PIPAAm-grafted surfaces and the peak was increased by increasing irradiation strength (Figure 4(b)). It is in accordance with ESCA results of PIPAAm-grafted PS surfaces compared with ungrafted PS surfaces. Grafted amount of PIPAAm on PS dishes and PS mats was analyzed by calculation of peak intensity at  $1650\text{ cm}^{-1}$  and  $1600\text{ cm}^{-1}$ . The peak intensity ratio ( $I_{1650}/I_{1600}$ ) was used to determine the graft density of PIPAAm on the surface using the calibration curve. PIPAAm-grafted PS mat with 369 kGy irradiation and PIPAAm-grafted PS dish with 507 kGy irradiation were grafted approximately  $1.02\text{ g/cm}^2$  and  $1.01\text{ g/cm}^2$  of PIPAAm, respectively.

The topography of polystyrene surfaces was measured by tapping mode of atomic force microscope (AFM) (Figure 5). PS nanofibrous mat showed randomly overlapped logs-like structure (Figure 5(b)) and PS dish showed a lawn-like morphology (Figure 5(d)). The morphology of PIPAAm-grafted surfaces was altered to rough surface compared to neat PS surfaces. In the case of nanofibrous PS mats, PIPAAm-grafted fiber was thicker than ungrafted one. Also, the topography of PS dish surface was changed by the graft of PIPAAm. According to these results, we confirmed that PIPAAm was successfully grafted onto electrospun nanofibrous PS mats and PS dish surfaces.

PIPAAm-grafted surfaces exhibited decreasing contact angles by lowering the temperature from 37 to 20 $^{\circ}$ C, while ungrafted PS surfaces had negligible contact angle changes with changing temperature (Table 1). This result indicates that PIPAAm-grafted surfaces, which are hydrophobic at higher temperature, became remarkably more hydrophilic in response to a temperature reduction due to spontaneous hydration of surface grafted PIPAAm. PIPAAm-grafted PS mats and PIPAAm-grafted PS dishes showed contact angle gaps of 23.77 $^{\circ}$  and 13.33 $^{\circ}$  by temperature change from 37 to 20 $^{\circ}$ C. Water contact angle change of more than 10 $^{\circ}$  which

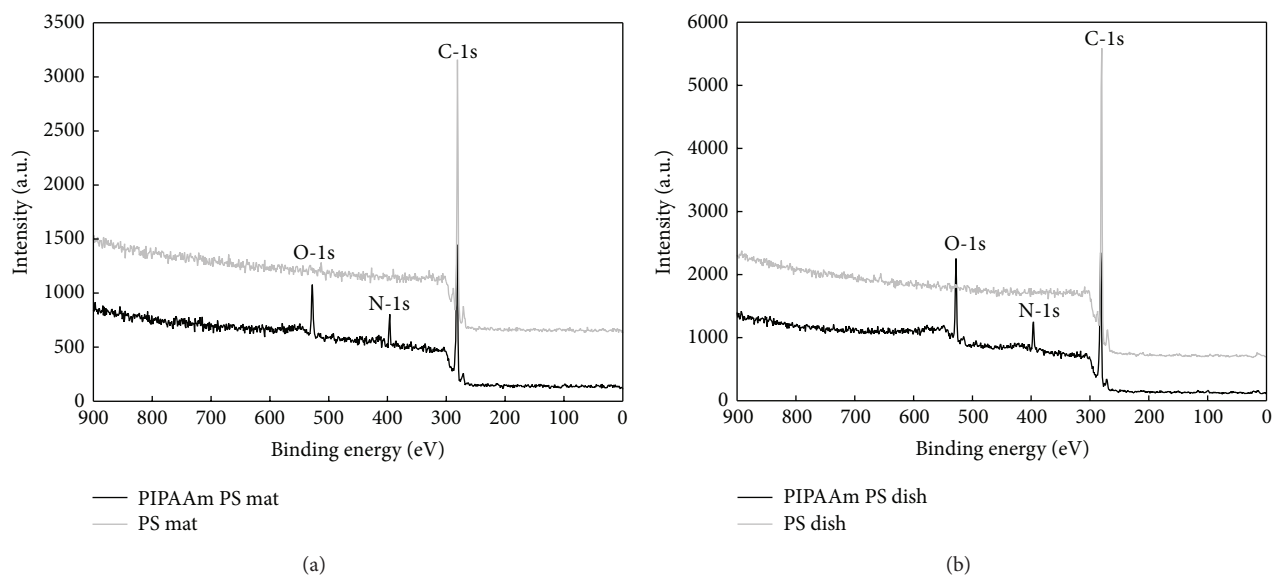


FIGURE 3: ESCA survey scan spectra of PIPAAm-grafted and ungrafted polystyrene mat (a) and PIPAAm-grafted and ungrafted polystyrene dish (b).

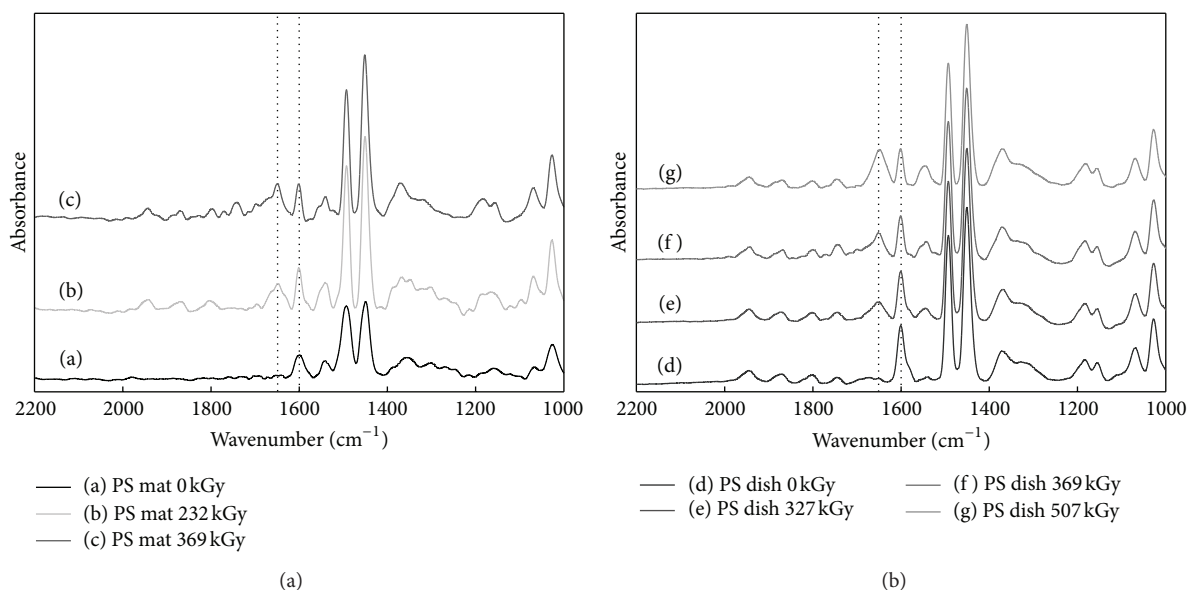


FIGURE 4: ATR-FTIR spectra of PIPAAm-grafted polystyrene mats (a) and polystyrene dishes (b) as a function of radiation dose.

occurred by temperature alteration was enough for cell detachment.

**3.3. Cell Proliferation on Thermoresponsive Matrices.** To demonstrate biocompatibility and cell proliferation, fibroblasts were cultured on PIPAAm-grafted PS surfaces and ungrafted PS surfaces. Attached and spread fibroblasts on nanofibrous PS mat were proliferated more rapidly than those of flat PS dish surface (Figure 6). After 3 hours of culture, initial cell attachment on electrospun nanofibrous PS mat surfaces was higher than PS dish surfaces. Electrospun mat

has a higher specific surface area; the three-dimensional structure of electrospun mats gives good metabolism to cells and the surface morphology was rougher than surface of PS dish. For these reasons, cells were attached easily onto electrospun PS mat surfaces. Proliferation of cells on PIPAAm-grafted surfaces was higher than that of ungrafted surfaces. The surface property changed to be hydrophilic by the graft of PIPAAm, which increased compatibility of surfaces to the cells.

**3.4. Recovery of Cultured Cells.** Detachment of single cells from PIPAAm-grafted PS surfaces was induced by low

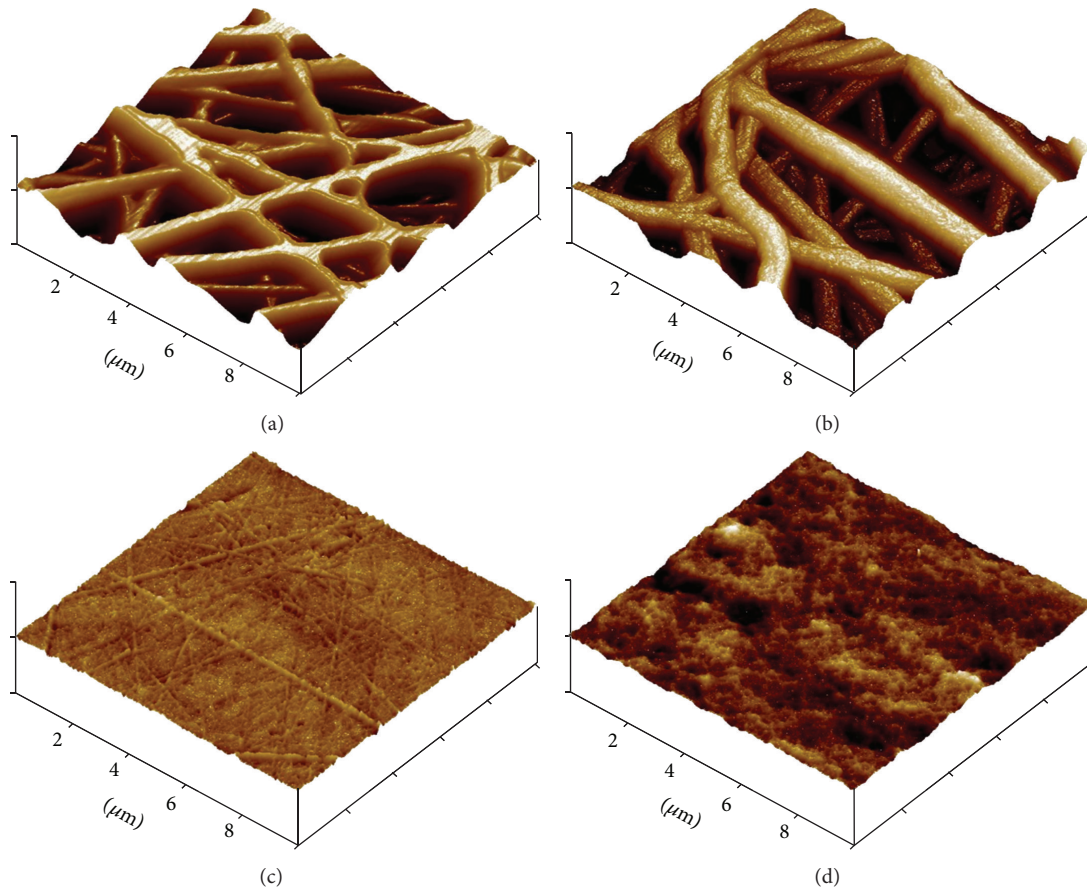


FIGURE 5: Three-dimensional tapping mode AFM topographical images of each surface: (a) ungrafted polystyrene mat, (b) PIPAAm-grafted polystyrene mat, (c) ungrafted polystyrene film, and (d) PIPAAm-grafted polystyrene dish.

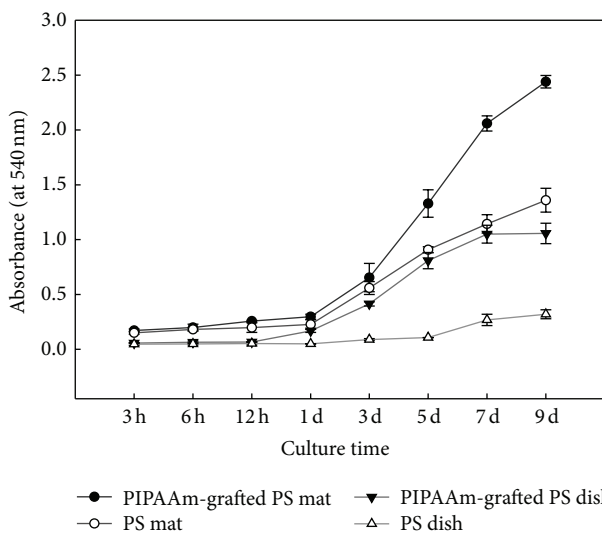


FIGURE 6: MTT assay of cultured fibroblasts on polystyrene mats and polystyrene dishes.

temperature treatment after incubation at 37°C. Almost all of the seeded cells were attached and spread on these surfaces after 5 hours of culture at 37°C. When the culture

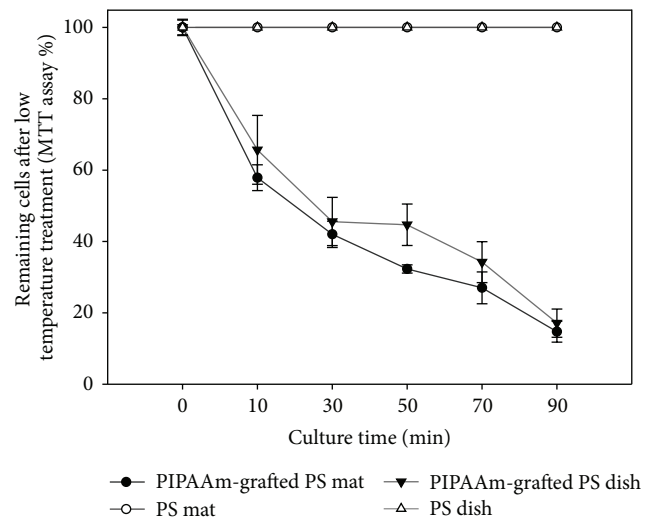


FIGURE 7: The percentage of remaining cells on ungrafted and PIPAAm-grafted polystyrene surfaces as a function of incubation time at 20°C.

temperature was reduced to 20°C after 5 h incubation at 37°C, the spread cells became rounded and detached from both PIPAAm-grafted PS dish and nanofibrous mat surfaces. This

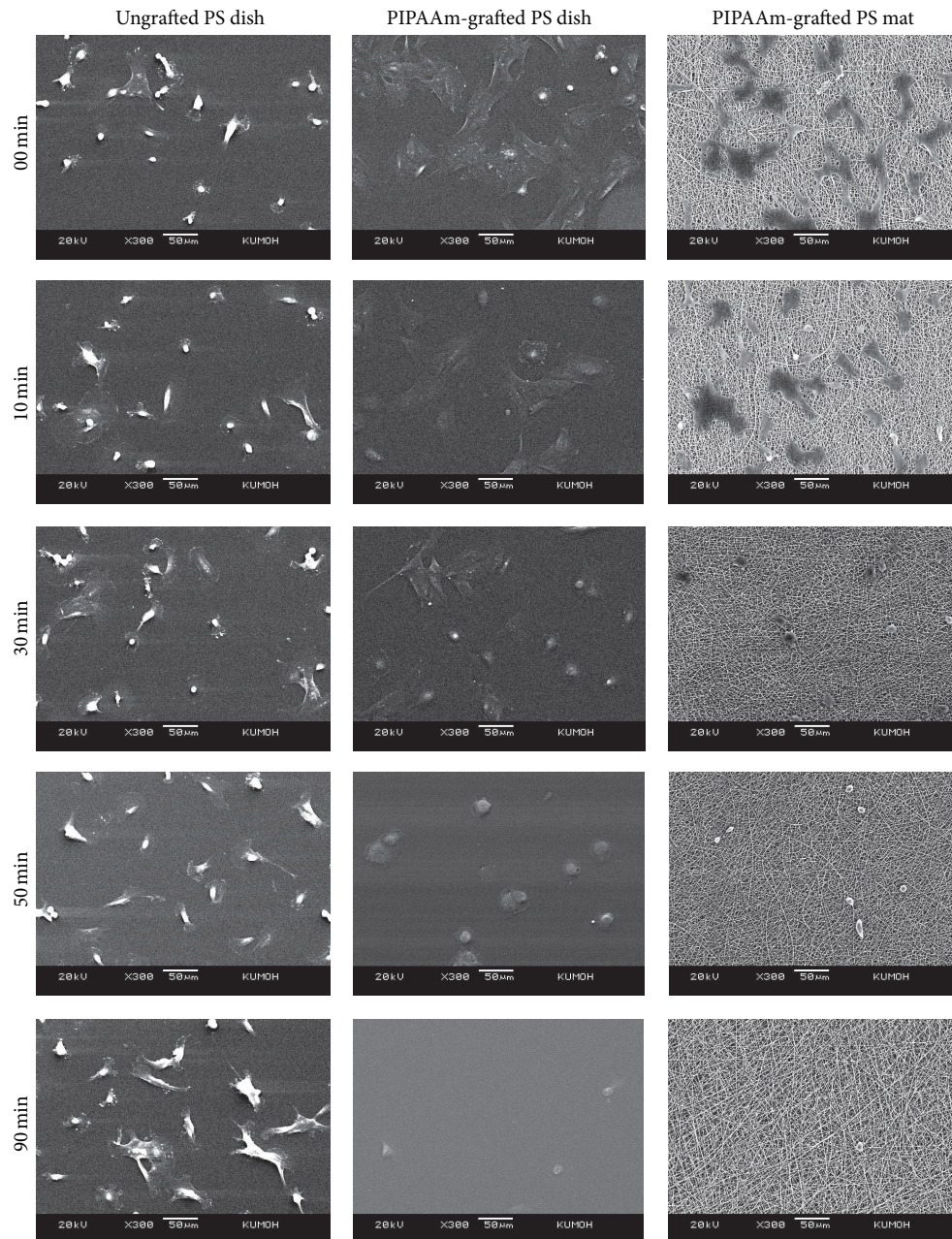


FIGURE 8: SEM micrographs of fibroblasts detachment from the ungrafted polystyrene dish, PIPAAm-grafted polystyrene dish, and PIPAAm-grafted polystyrene mat surface as a function of incubation time at 20°C.

is because PIPAAm is hydrated below its LCST, producing an expanded, swollen, and hydrophilic surface. This surface property changes weakened cellular adhesion, resulting in spontaneous cell detachment.

The percentage of still attached single cells after low temperature treatment decreased rapidly on PIPAAm-grafted surfaces, while there are no cells detached from ungrafted surfaces because of no surface property alternation by reducing culture temperature (Figure 7). Time-lapse images (in minutes) of cell morphology assist the result of MTT

assay (Figure 8). Spread cells were more rapidly detached on PIPAAm-grafted PS mat than PIPAAm-grafted PS dish. This difference is probably because of porous structure, the water molecules rapidly reach to grafted PIPAAm from underneath and peripheral to the attached cells, resulting in rapid hydration of grafted PIPAAm molecules and accelerating detachment of the cells. Initial cell attachment, rapid proliferation, and rapid intact cell recovery are important to maintain biological functions and viability of cell source for the fields of tissue engineering and regenerative medicine.

#### 4. Conclusions

In this study, PS nanofibrous mats prepared by electrospinning method and subsequent grafting of PIPAAm by electron beam irradiation enabled a rapid cultured cells detachment for biological function and viability of cultured cells. Temperature-responsive surface was developed by introducing thermosensitive PIPAAm chains onto PS nanofibrous mats via electron beam irradiation. Heat treatment was employed to provide bonding points between fibers resulting in increase in mechanical property for sufficient washing process.

Also we expected porous substrate would assist more rapid hydration for functionality of cultured cells. From the noticed results, cells were well attached and proliferated on nanofibrous PS mat more than flat PS dish surface. Also cells were detached more rapidly on PIPAAm-grafted PS nanofiber surfaces than PIPAAm-grafted PS dish surfaces probably due to the effective water supply via existing pores on nanofibers. To maintain biological functions and viability of recovered cells, development of rapid cell recovery system is prerequisite. From this view point, PIPAAm-grafted nanofibrous mats could be a promising tool to recover intact cultured cells.

#### Conflict of Interests

The authors declare that there is no conflict of interests regarding the publication of this paper.

#### Acknowledgment

This paper was supported by Research Fund, Kumoh National Institute of Technology.

#### References

- [1] E. D. Hay, "Extracellular matrix," *Journal of Cell Biology*, vol. 91, no. 3, pp. 205–223, 1981.
- [2] R. Langer and J. P. Vacanti, "Tissue engineering," *Science*, vol. 260, no. 5110, pp. 920–926, 1993.
- [3] L. G. Cima, D. E. Ingber, J. P. Vacanti, and R. Langer, "Hepatocyte culture on biodegradable polymeric substrates," *Biotechnology and Bioengineering*, vol. 38, no. 2, pp. 145–158, 1991.
- [4] A. Atala, D. Mooney, J. P. Vacanti, and R. Langer, Eds., *Synthetic Biodegradable Polymer Scaffolds*, Birkhauser, Boston, Mass, USA, 1997.
- [5] J. K. Son, J. J. Park, C. K. Park, B. K. Yang, C. I. Kim, and H. T. Cheong, "Development of somatic cell nuclear transfer embryos following donor cell type and cell treatment in cattle," *Reproductive and Developmental Biology*, vol. 28, pp. 1–6, 2004.
- [6] S. Bae, C. W. Park, H. K. Son, C. J. Jeon, and H. Kim, "Comparison of temperature-responsive polymer and trypsin-mediated passages of mesenchymal stem cells," *Tissue Engineering and Regenerative Medicine*, vol. 4, pp. 388–392, 2007.
- [7] N. Yamada, T. Okano, H. Sakai, F. Karikusa, Y. Sawasaki, and Y. Sakurai, "Thermo-responsive polymeric surfaces; control of attachment and detachment of cultured cells," *Die Makromolekulare Chemie, Rapid Communications*, vol. 11, pp. 571–576, 1990.
- [8] T. Okano, N. Yamada, H. Sakai, and Y. Sakurai, "A novel recovery system for cultured cells using plasma-treated polystyrene dishes grafted with poly(N-isopropylacrylamide)," *Journal of Biomedical Materials Research*, vol. 27, no. 10, pp. 1243–1251, 1993.
- [9] T. Okano, N. Yamada, M. Okuhara, H. Sakai, and Y. Sakurai, "Mechanism of cell detachment from temperature-modulated, hydrophilic-hydrophobic polymer surfaces," *Biomaterials*, vol. 16, no. 4, pp. 297–303, 1995.
- [10] A. Kikuchi, M. Okuhara, F. Karikusa, Y. Sakurai, and T. Okano, "Two-dimensional manipulation of confluent cultured vascular endothelial cells using temperature-responsive poly(N-isopropylacrylamide)-grafted surfaces," *Journal of Biomaterials Science, Polymer Edition*, vol. 9, no. 12, pp. 1331–1348, 1998.
- [11] A. Kushida, M. Yamato, C. Konno, A. Kikuchi, Y. Sakurai, and T. Okano, "Decrease in culture temperature releases monolayer endothelial cell sheets together with deposited fibronectin matrix from temperature-responsive culture surfaces," *Journal of Biomedical Materials Research*, vol. 45, pp. 355–362, 1999.
- [12] M. Heskins, J. E. Guillet, and E. James, "Solution properties of poly(N-isopropylacrylamide)," *Journal of Macromolecular Science A*, vol. 2, pp. 1441–1455, 1968.
- [13] K. Nishida, M. Yamato, Y. Hayashida et al., "Functional bio-engineered corneal epithelial sheet grafts from corneal stem cells expanded *ex vivo* on a temperature-responsive cell culture surface," *Transplantation*, vol. 77, no. 3, pp. 379–385, 2004.
- [14] Y. Shiroyanagi, M. Yamato, Y. Yamazaki, H. Toma, and T. Okano, "Transplantable urothelial cell sheets harvested noninvasively from temperature-responsive culture surfaces by reducing temperature," *Tissue Engineering*, vol. 9, no. 5, pp. 1005–1012, 2003.
- [15] T. Shimizu, M. Yamato, A. Kikuchi, and T. Okano, "Cell sheet engineering for myocardial tissue reconstruction," *Biomaterials*, vol. 24, no. 13, pp. 2309–2316, 2003.
- [16] O. H. Kwon, A. Kikuchi, M. Yamato, Y. Sakurai, and T. Okano, "Rapid cell sheet detachment from poly(N-isopropylacrylamide)-grafted porous cell culture membranes," *Journal of Biomedical Materials Research*, vol. 50, pp. 82–89, 2000.
- [17] H. K. Oh, A. Kikuchi, M. Yamato, and T. Okano, "Accelerated cell sheet recovery by co-grafting of PEG with PIPAAm onto porous cell culture membranes," *Biomaterials*, vol. 24, no. 7, pp. 1223–1232, 2003.
- [18] G. E. Wnek, M. E. Carr, D. G. Simpson, and G. L. Bowlin, "Electrospinning of nanofiber fibrinogen structures," *Nano Letters*, vol. 3, no. 2, pp. 213–216, 2003.
- [19] H. Fong, I. Chun, and D. H. Reneker, "Beaded nanofibers formed during electrospinning," *Polymer*, vol. 40, no. 16, pp. 4585–4592, 1999.
- [20] X. M. Mo, C. Y. Xu, M. Kotaki, and S. Ramakrishna, "Electrospun P(LLA-CL) nanofiber: a biomimetic extracellular matrix for smooth muscle cell and endothelial cell proliferation," *Biomaterials*, vol. 25, no. 10, pp. 1883–1890, 2004.
- [21] M. Shin, O. Ishii, T. Sueda, and J. P. Vacanti, "Contractile cardiac grafts using a novel nanofibrous mesh," *Biomaterials*, vol. 25, no. 17, pp. 3717–3723, 2004.
- [22] W.-J. Li, R. Tuli, X. Huang, P. Laquerriere, and R. S. Tuan, "Multilineage differentiation of human mesenchymal stem cells in a three-dimensional nanofibrous scaffold," *Biomaterials*, vol. 26, no. 25, pp. 5158–5166, 2005.

- [23] X. Zong, K. Kim, D. Fang, S. Ran, B. S. Hsiao, and B. Chu, "Structure and process relationship of electrospun bioabsorbable nanofiber membranes," *Polymer*, vol. 43, no. 16, pp. 4403–4412, 2002.
- [24] H. Yoshimoto, Y. M. Shin, H. Terai, and J. P. Vacanti, "A biodegradable nanofiber scaffold by electrospinning and its potential for bone tissue engineering," *Biomaterials*, vol. 24, no. 12, pp. 2077–2082, 2003.
- [25] S. L. Ik, H. K. Oh, W. Meng, I.-K. Kang, and Y. Ito, "Nanofabrication of microbial polyester by electrospinning promotes cell attachment," *Macromolecular Research*, vol. 12, no. 4, pp. 374–378, 2004.
- [26] Y. Ito, H. Hasuda, M. Kamitakahara et al., "A composite of hydroxyapatite with electrospun biodegradable nanofibers as a tissue engineering material," *Journal of Bioscience and Bioengineering*, vol. 100, no. 1, pp. 43–49, 2005.
- [27] O. H. Kwon, I. S. Lee, Y.-G. Ko et al., "Electrospinning of microbial polyester for cell culture," *Biomedical Materials*, vol. 2, no. 1, article S08, pp. S52–S58, 2007.
- [28] W. Meng, S.-Y. Kim, J. Yuan et al., "Electrospun PHBV/collagen composite nanofibrous scaffolds for tissue engineering," *Journal of Biomaterials Science, Polymer Edition*, vol. 18, no. 1, pp. 81–94, 2007.
- [29] A. Finne-Wistrand, A.-C. Albertsson, O. H. Kwon et al., "Resorbable scaffolds from three different techniques: electrospun fabrics, salt-leaching porous films, and smooth flat surfaces," *Macromolecular Bioscience*, vol. 8, no. 10, pp. 951–959, 2008.
- [30] Y.-J. Kim, C. H. Ahn, H. H. Oh, K. H. Yoon, I.-K. Kang, and O. H. Kwon, "3-D rat hepatocytes' culture on polystyrene nanofibrous scaffold," *Polymer*, vol. 32, no. 2, pp. 131–137, 2008.

## Research Article

# Enhanced Neural Cell Adhesion and Neurite Outgrowth on Graphene-Based Biomimetic Substrates

Suck Won Hong,<sup>1,2</sup> Jong Ho Lee,<sup>1</sup> Seok Hee Kang,<sup>1</sup> Eun Young Hwang,<sup>2</sup> Yu-Shik Hwang,<sup>3</sup> Mi Hee Lee,<sup>4</sup> Dong-Wook Han,<sup>1</sup> and Jong-Chul Park<sup>4</sup>

<sup>1</sup> Department of Cogno-Mechatronics Engineering, Pusan National University, Busan 609-735, Republic of Korea

<sup>2</sup> Education Program for Samsung Advanced Integrated Circuit, Pusan National University, Busan 609-735, Republic of Korea

<sup>3</sup> Department of Maxillofacial Biomedical Engineering, School of Dentistry and Institute of Oral Biology, Kyung Hee University, Seoul 130-701, Republic of Korea

<sup>4</sup> Cellbiocontrol Laboratory, Department of Medical Engineering, Yonsei University College of Medicine, Seoul 120-752, Republic of Korea

Correspondence should be addressed to Dong-Wook Han; [nanohan@pusan.ac.kr](mailto:nanohan@pusan.ac.kr) and Jong-Chul Park; [parkjc@yuhs.ac](mailto:parkjc@yuhs.ac)

Received 15 November 2013; Accepted 19 December 2013; Published 30 January 2014

Academic Editor: Inn-Kyu Kang

Copyright © 2014 Suck Won Hong et al. This is an open access article distributed under the Creative Commons Attribution License, which permits unrestricted use, distribution, and reproduction in any medium, provided the original work is properly cited.

Neural cell adhesion and neurite outgrowth were examined on graphene-based biomimetic substrates. The biocompatibility of carbon nanomaterials such as graphene and carbon nanotubes (CNTs), that is, single-walled and multiwalled CNTs, against pheochromocytoma-derived PC-12 neural cells was also evaluated by quantifying metabolic activity (with WST-8 assay), intracellular oxidative stress (with ROS assay), and membrane integrity (with LDH assay). Graphene films were grown by using chemical vapor deposition and were then coated onto glass coverslips by using the scooping method. Graphene sheets were patterned on SiO<sub>2</sub>/Si substrates by using photolithography and were then covered with serum for a neural cell culture. Both types of CNTs induced significant dose-dependent decreases in the viability of PC-12 cells, whereas graphene exerted adverse effects on the neural cells just at over 62.5 ppm. This result implies that graphene and CNTs, even though they were the same carbon-based nanomaterials, show differential influences on neural cells. Furthermore, graphene-coated or graphene-patterned substrates were shown to substantially enhance the adhesion and neurite outgrowth of PC-12 cells. These results suggest that graphene-based substrates as biomimetic cues have good biocompatibility as well as a unique surface property that can enhance the neural cells, which would open up enormous opportunities in neural regeneration and nanomedicine.

## 1. Introduction

Graphene is a single-atom thick and is defined as a two-dimensional sheet of hexagonally arranged carbon atoms isolated from its three-dimensional parent material, graphite [1]. As with many novel materials, applications of graphene and its family nanomaterials, such as graphene oxide (GO), reduced GO (rGO), and graphene nanosheets, offer many technological opportunities since they exhibit interesting electrical, thermal, mechanical, and optical properties [2]. The practical uses of graphene family nanomaterials are extensive, covering applications as diverse as battery electrodes, super-capacitors, nanoelectronics (e.g., transistors

and sensors), antibacterial paper, and many biomedical uses for drug delivery, diagnosis, and therapy [3–7]. These numerous potential applications of graphene and related materials make them very attractive to both the scientific and industrial community. However, to ensure the safe development of graphene and its family nanomaterials, their potential impact on health and environment remains unelucidated yet.

Carbon nanotubes (CNTs) and graphene, despite both being carbon-based, are two very distinct nanomaterials, and their biological applications still keep wide open. During the last decade, many studies of interactions between neural cells and carbon nanomaterials (CNMs) including CNTs,

graphene, and their derivatives were carried out with terminally differentiated primary cells or cell lines [8, 9]. The primary focuses of very recent studies were on establishing biocompatibility and biofunctionality of the proposed materials, revealing that by pretreating rats with amine-modified single-walled CNTs (SWCNTs) neurons could be protected and the recovery of behavioural functions in rats with induced stroke could be enhanced [10], and graphene substrates exhibited excellent biocompatibility and significantly promoted neurite sprouting and outgrowth of mouse hippocampal cells [11].

In the present study, the biocompatibility between neural cells and three CNMs, namely, graphene, SWCNTs, and multiwalled CNTs (MWCNTs), was evaluated and compared by quantifying metabolic activity, intracellular oxidative stress, and membrane integrity. Neural cell adhesion and neurite outgrowth were examined onto graphene-based biomimetic substrates.

## 2. Experimental

**2.1. Synthesis and Morphological Observation of Carbon Nanomaterials (CNMs).** Graphene and SWCNTs were grown by using chemical vapor deposition (CVD), as previously described [12, 13]. MWCNTs were synthesized by using spray pyrolysis combined with a subsequent thermal CVD process, as described elsewhere [14, 15]. After being synthesized, each CNM was weighed by using an electronic balance (with a readability of 0.1 mg, Adventurer Analytical Balance, Ohaus, Bradford, MA). The surface morphology of each CNM was observed by using scanning electron microscopy (SEM). In brief, all CNMs were coated with an ultrathin layer of gold/platinum by an ion sputter (E1010, Hitachi, Tokyo, Japan) and were then observed with a field emission scanning electron microscope (FESEM, Hitachi S-4700) at an accelerating voltage of 5 kV for graphene and 15 kV for both CNTs. A colloidal dispersive solution of each CNM was prepared in Dulbecco's phosphate-buffered saline (DPBS, Sigma-Aldrich Co., St Louis, MO, pH 7.4) with a final concentration of 500 ppm and was then sonicated for homogenous dispersions under mild conditions by using a water bath sonicator with a bath temperature of 25°C overnight. For biocompatibility evaluations, the suspension of each CNM was serially diluted with 2 × Dulbecco's modified Eagle's medium (DMEM, Sigma-Aldrich Co.) and was then treated to the cultured monolayer of neural cells.

**2.2. Preparation of Graphene-Based Substrates.** Graphene films were grown on catalytic copper (Cu) surface by using a CVD method [12, 13]. For the preparation of a graphene-coated substrate, the grown graphene film on a Cu foil was transferred onto a glass coverslip by using the scooping process. In detail, 10 wt% of poly(methyl methacrylate) (PMMA, Sigma-Aldrich Co.) was spin-casted on a Cu foil at 3000 rpm for 30 seconds and was then placed into an Cu etchant solution (Transene Company, Inc., Danvers, MA) to completely remove the Cu foil. Next, graphene covered with a PMMA substrate was scooped onto a glass coverslip, followed by removal of the PMMA by adding acetone for 40 min.

For the neural cell adhesion, the top surface of graphene coated on the glass coverslip was covered with 50% fetal bovine serum (FBS, Sigma-Aldrich Co.) for 1 hour while shaking at 37°C and 80 rpm [16]. In the case of the graphene-patterned substrate, a patterned array of graphene films with rectangular shapes (100 μm × 150 μm) was fabricated on a SiO<sub>2</sub>/Si substrate by using a conventional photolithography (AZ 5214) as described elsewhere [12]. The morphology of the patterned graphene array was observed under a scanning electron microscope (SEM, Hitachi S-4800, Tokyo, Japan) at an accelerating voltage of 1.0 kV. To observe the neurite outgrowth, the top surface of the patterned graphene was covered with FBS by using the same method as mentioned above.

**2.3. Cell Cultures and Conditions.** PC-12 cells (derived from pheochromocytoma of rat adrenal medulla) were obtained from American Type Culture Collection (ATCC, Rockville, MD). Cells were routinely maintained in RPMI-1640 media (Sigma-Aldrich Co.) supplemented with 10% horse serum, 5% FBS, and 1% antibiotic antimycotic solution (including 10,000 U penicillin, 10 mg streptomycin, and 25 μg amphotericin B per mL, Sigma-Aldrich Co.) at 37°C in a humidified atmosphere of 5% CO<sub>2</sub> in air.

**2.4. WST-8 Assay for Metabolic Activity Determination.** The number of viable cells was quantified indirectly by using highly water-soluble tetrazolium salt (WST-8, 2-(2-methoxy-4-nitrophenyl)-3-(4-nitrophenyl)-5-(2,4-disulphophenyl)-2H-tetrazolium, monosodium salt; Dojindo Lab., Kumamoto, Japan), reduced to a water-soluble formazan dye by mitochondrial dehydrogenases. The cell viability was found to be directly proportional to the metabolic reaction products obtained in WST-8 [17]. Briefly, the WST-8 assay was conducted as follows: PC-12 cells were treated with increasing concentrations (0.5~500 ppm) of each CNM and were then incubated with WST-8 reagent for the last 4 hours of the culture period (24 hours) at 37°C in the dark. Parallel sets of wells containing freshly cultured cells, which were not treated with any CNMs suspended in the same concentration ratio of DPBS and DMEM, were regarded as negative controls. The absorbance was determined at 450 nm by using an ELISA reader (SpectraMax 340, Molecular Device Co., Sunnyvale, CA). The relative cell viability was determined as the percentage ratio of the optical densities in the media (containing CNMs at each concentration) to that of the fresh control medium.

**2.5. DCF Assay for Oxidative Stress Determination.** The 2',7'-dichlorodihydrofluorescein (DCF) assay is a widely used method to detect intracellular reactive oxygen species (ROS) levels in pharmacological studies [18, 19]. The accumulation of intracellular free radicals from CNMs was quantified using a ROS assay kit (OxiSelect, Cell Biolabs, Inc., San Diego, CA), which employs the cell-permeable fluorogenic probe 2',7'-dichlorodihydrofluorescein diacetate (DCFH-DA). DCFH-DA is an ROS detector that can cross cell membranes and be deacetylated by intracellular esterases to nonfluorescent

2',7'-dichlorodihydrofluorescein (DCFH). In the presence of ROS, DCFH is rapidly oxidized to the highly fluorescent DCF, which is readily detectable. The fluorescence intensity is proportional to the ROS levels within the cell cytosol. PC-12 cells were exposed to increasing concentrations (0.5~500 ppm) of each CNM for 24 h and were then incubated with DCHF-DA for 30 minutes at 37°C in the dark. Parallel sets of wells containing freshly cultured cells, which were not treated with any CNMs suspended in the same concentration ratio of DPBS and DMEM, were regarded as negative controls. The fluorescence emission of DCF was monitored at regular intervals at an excitation wavelength of 480 nm and an emission wavelength of 530 nm in a fluorescence plate reader (VICTOR3 Multilabel Counter, PerkinElmer, Inc., Waltham, MA). The amount of DCF formed was calculated from a calibration curve constructed using an authentic DCF standard. The relative DCF intensity was determined as the percentage ratio of the fluorescence intensities in the wells (containing CNMs at each concentration) to that in the fresh control well.

**2.6. LDH Assay for Membrane Integrity Determination.** Cell membrane integrity was monitored using a lactate dehydrogenase (LDH) assay kit (Takara Bio Inc, Shiga, Japan) to determine the release of LDH into the medium according to the manufacturer instructions. In this assay, LDH released from damaged cells oxidizes lactate to pyruvate, which promotes conversion of the tetrazolium salt INT to a water-soluble red formazan product [19]. Briefly, after 24 hours exposure to increasing concentrations (0.5~500 ppm) of each CNM, the supernatant from each well was transferred to a new 96-well plate. Reconstituted substrate mix was added to each well and the plates were kept for 30 minutes in the dark at room temperature. Stop solution was then added to each well. Parallel sets of wells containing freshly cultured cells, which were not treated with any CNMs suspended in the same concentration ratio of DPBS and DMEM, were regarded as negative controls. Released LDH catalyzed the oxidation of lactate to pyruvate with simultaneous reduction of  $\text{NAD}^+$  to NADH. The rate of  $\text{NAD}^+$  reduction was directly proportional to LDH activity in the cell medium. The intensity of red color formed in the assay was measured at a wavelength of 490 nm with an ELISA reader (SpectraMax 340, Molecular Device Co.), which was proportional to the number of damaged cells. The relative LDH release was determined as the percentage ratio of the optical densities in the media (containing CNMs at each concentration) to that of the fresh control medium.

**2.7. Assays for Neural Cell Adhesion, Neurite Outgrowth, and Proliferation.** The adhesion of PC-12 cells and their neurite outgrowth were investigated onto graphene-coated and graphene-patterned substrates, respectively, under the conditions of the culture media without neural growth factors for neuronal differentiation. Neural cells were seeded with high density of  $2 \times 10^5$  cells/mL onto glass coverslips with FBS-covered graphene on them lying in a 48-well plate and were then incubated for 3 days. After incubation, cellular

morphology adhered onto graphene-coated substrates was observed under an inverted microscope (IX81-F72, Olympus Optical, Osaka, Japan). For observing neurite outgrowth, PC-12 cells (low density of initial seeding,  $1 \times 10^4$  cells/mL) were cultured for 7 days onto FBS-covered graphene patterned on a  $\text{SiO}_2/\text{Si}$  substrate lying in a 12-well plate. After cultivation, neurite outgrowth onto graphene-patterned substrate was visualized by using atomic force microscopy (AFM, Innova, Veeco Instruments Inc., Plainview, NY). In order to compare the proliferation pattern of PC-12 cells, cells were seeded on glass coverslips without and with FBS-covered graphene on them and then cultivated for 1, 3, 5, and 7 days at 37°C in a  $\text{CO}_2$  incubator. After incubation, the cell proliferation was determined by the WST-8 assay as described above.

**2.8. Statistical Analysis.** All variables were tested in three independent cultures for each cytotoxicity assay, which was repeated twice ( $n = 6$ ). Quantitative data are expressed as mean  $\pm$  standard deviation (SD). Data were tested for homogeneity of variances using Levene's test, prior to statistical analysis. Multiple comparisons to detect the dose-dependent effects of CNMs on PC-12 cells were carried out using one-way analysis of variance (ANOVA, SAS Institute, Cary, NC), which was followed by the Bonferroni test when variances were homogeneous and the Tamhane test when variances were not. Statistical analysis for the proliferation study was made by using the Student's *t*-test. A value of  $P < 0.05$  was considered statistically significant.

### 3. Results and Discussion

**3.1. SEM Analysis.** Figure 1 shows FESEM images of pristine graphene, SWCNTs, and MWCNTs. All the CNMs were well dispersed in the culture medium (DMEM) with serum. Most of graphene nanoplatelets existed as single or few layers and presented both large and small sheets. Several graphene nanoplatelets with lateral sizes of around 200~500 nm have been observed while a few nanoplatelets showed smaller sizes within the range of 50~100 nm. SWCNTs and MWCNTs mostly formed nanofibrous bundles of 2~5 nm and 10~15 nm in diameter, respectively, and several  $\mu\text{m}$  in length in the suspension.

**3.2. Effects of CNMs on Metabolic Activity.** In order to evaluate the neural cell biocompatibility of CNMs, the effects of CNMs on the metabolic activity of PC-12 cells were examined with the WST-8 assay where the formation of formazan dye depends on the mitochondrial enzyme activity. As shown in Figure 2, the viability of PC-12 cells decreased in a dose-dependent manner after 24 hours of exposure to increasing concentrations of each CNM. Graphene started to record significant ( $P < 0.05$ ) mitochondrial toxicity from 62.5 ppm and showed about 18% loss in the cell viability even at the top concentration tested (500 ppm) in comparison to unexposed controls. In contrast, significant ( $P < 0.05$ ) cytotoxicity was induced at 31.3 ppm of both CNTs, which resulted in approximately 18%~20% inhibition of the viability in comparison to untreated controls. A recent study reported

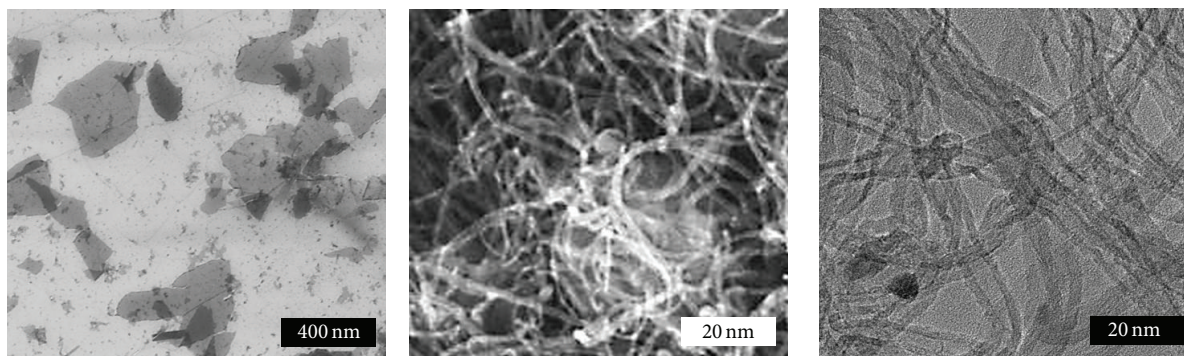


FIGURE 1: FESEM images of the surface morphologies of graphene nanoplatelets, SWCNTs, and MWCNTs.

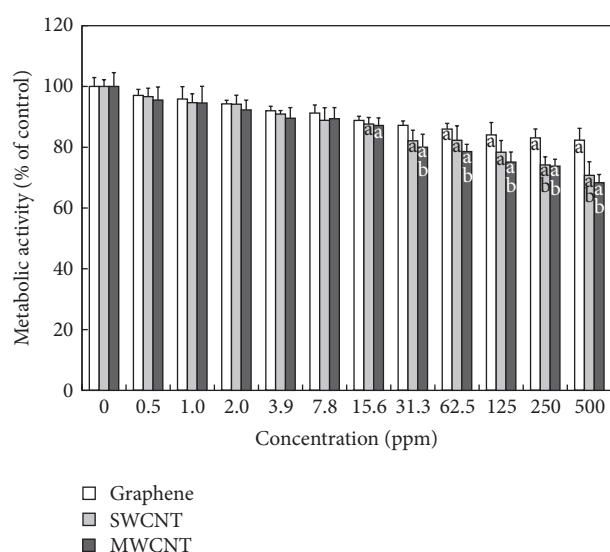


FIGURE 2: Effects of graphene, SWCNTs, and MWCNTs on mitochondrial toxicity of PC-12 cells. Cells were treated with different concentrations of CNMs for 24 hours. At the end of the incubation period, the WST-8 assay was performed to evaluate the cytotoxicity as described in Section 2. Data were expressed as mean  $\pm$  standard deviation (SD) based on at least duplicate observations from three independent experiments. The letter “a” indicates statistically significant difference from the untreated control; the letter “b” indicates statistically significant difference from cells treated with graphene at the same concentration ( $P < 0.05$ ).

that GO showed stronger hemolytic activity against red blood cells than aggregated graphene sheets whereas compacted graphene sheets were more damaging to mammalian fibroblasts than less densely packed GO [20]. Moreover, it was revealed that 7.5~30 ppm of SWCNTs reduced the total DNA content of mixed neuroglial cultures [21]. MWCNTs have been shown to induce massive loss of cell viability in human dermal fibroblasts through cell cycle arrest in the  $G_1$  phase, downregulation of adhesion-related genes, DNA damage, and programmed cell death as well as cause cytoskeleton damage and disturbance of actin stress fibers in the range of 40~200 ppm [22, 23]. In addition, our previous study revealed

that primary-cultured fibroblasts were more susceptible to CNMs than the fibroblast cell line [24]. As a result, it is considered that the WST assay has any detection limit to find out cytotoxic effects of CNMs at relatively low concentrations ( $<31.3$  ppm) on neural cells. Numerous previous studies have employed the methylthiazolyldiphenyl-tetrazolium bromide (MTT) assay, a typical nanotoxicity assay, but this assay sometimes failed to predict the toxicity of CNMs because of the spontaneous reduction of MTT by CNMs, resulting in a false positive signal [20, 25]. Therefore, cytotoxicity against cells exposed to CNMs should be also determined by alternative *in vitro* cell endpoint assays, such as ROS production, lipid peroxidation, and LDH leakage, because a WST-8 assay is based only on the activity of mitochondrial dehydrogenases.

**3.3. Effects of CNMs on Intracellular Oxidative Stress.** The DCF assay has been well verified as an effective index for evaluating the toxicity of nanomaterials attributable to ROS generation [19, 26]. Following exposure of PC-12 cells for 24 hours to each CNM, the state of oxidative stress in the cells was observed. As shown in Figure 3, the ROS generation increased in a dose-dependent manner as the concentration of each CNM increased, with the exception of graphene at the concentrations lower than 125 ppm. However, significant ( $P < 0.05$ ) ROS generation started to be recorded from 3.9 ppm of both CNTs, which resulted in 130% increase in comparison to unexposed controls. These results roughly correlated with results from the WST-8 assay, suggesting that toxicity in cells exposed to CNTs might result from oxidative stress mediated by ROS generated from CNTs internalized into cells [9]. There is convincing evidence supporting this suggestion. It was demonstrated that long SWCNTs led to significant increases in ROS generation and malondialdehyde (a product of lipid peroxidation) level in PC-12 cells in time and dose-dependent manners [27]. Other evidence showed that exposure to MWCNTs resulted in a concentration-dependent cytotoxicity in cultured human embryonic kidney cells, which was associated with increased oxidative stress [28]. On the other hand, surface functionalization (e.g., PEGylation) of SWCNTs has been shown to decrease ROS-mediated toxicological response in PC-12 cells [29].

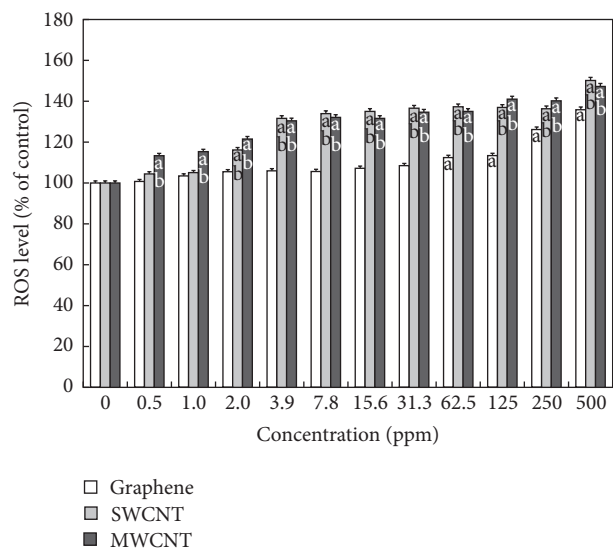


FIGURE 3: Effects of graphene, SWCNTs, and MWCNTs on ROS generation in PC-12 cells. Cells were treated with different concentrations of CNMs for 24 hours. At the end of the incubation period, the DCF assay was performed to evaluate the cytotoxicity as described in Section 2. Data were expressed as mean  $\pm$  standard deviation (SD) based on at least duplicate observations from three independent experiments. The letter “a” indicates statistically significant difference from the untreated control; the letter “b” indicates statistically significant difference from cells treated with graphene at the same concentration ( $P < 0.05$ ).

Furthermore, it was reported that vitamin E might protect PC-12 cells from the injury induced by SWCNTs through the downregulation of oxidative stress and prevention of mitochondrial-mediated apoptosis [30].

**3.4. Effects of CNMs on Cell Membrane Integrity.** LDH leakage is well known as a useful index for cytotoxicity on the basis of loss of membrane integrity, a hallmark of necrosis. All the CNMs induced apparent LDH release from PC-12 cells, revealing the adverse effect of CNMs on cell membrane integrity (Figure 4). Significant LDH release was noted only after 24 hours of exposure to graphene at higher concentrations (250 and 500 ppm). At lower concentrations (0.5~125 ppm), graphene had no effect on the release of LDH. In contrast, both SWCNTs and MWCNTs began to induce a significant ( $P < 0.05$ ) increase in LDH release from 0.5 ppm and resulted in 235% and 296%, respectively at the highest concentration (500 ppm) in comparison to untreated controls. Some reasons can be evoked to explain the difference in cytotoxicity between graphene and CNTs. Generally, the size (namely, dimensions), shape, composition, surface charge, and surface chemistry (e.g., functionalization) of nanomaterials as well as the target cell type are critical determinants of intracellular responses, degree of cytotoxicity and potential mechanisms of toxicity [31]. The chemical composition and dimensions of graphene are similar to those of CNTs, but the shape of graphene is completely different from that of CNTs (planar versus cylindrical) [32].

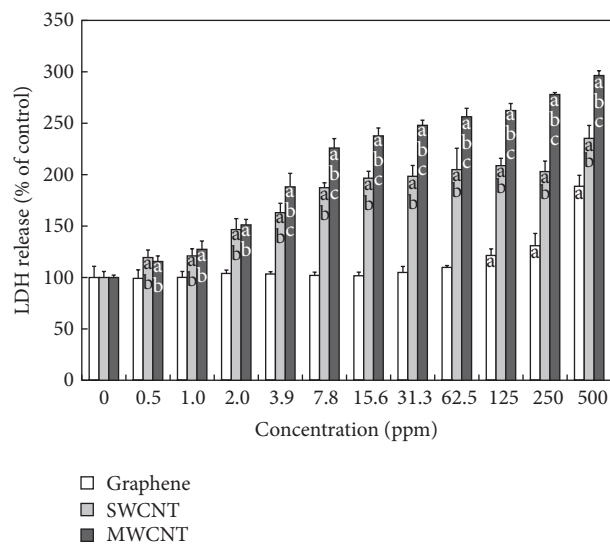


FIGURE 4: Effects of graphene, SWCNTs, and MWCNTs on LDH release from PC-12 cells. Cells were treated with different concentrations of CNMs for 24 hours. At the end of the incubation period, the LDH assay was performed to evaluate the cytotoxicity as described in Section 2. Data were expressed as mean  $\pm$  standard deviation (SD) based on at least duplicate observations from three independent experiments. The letter “a” indicates statistically significant difference from the untreated control; the letters “b” and “c” indicate statistically significant differences from cells treated with graphene and SWCNTs, respectively, at the same concentration ( $P < 0.05$ ).

Thus, it is likely that the piercing, needle-like CNT may be more mobile than the sheet-like graphene and can more readily penetrate the cell membrane, resulting in greater cell membrane damage [33]. These dose-dependent responses of PC-12 cells to CNMs correlated exactly with those from the DCF assay, implying that cell membrane damage is another mechanism for the toxicity of CNMs. In this study, the  $>250$  ppm of graphene increased the LDH release and ROS generation. However, lower doses (0.5~31.3 ppm) of graphene had no effect on multiple endpoints such as metabolic activity, LDH leakage, and ROS production. Therefore, lower levels of exposure ( $<30$  ppm) to graphene could theoretically be useful in biomedical applications including imaging, drug delivery, tissue engineering, and biosensors [34, 35]. Future studies will focus on the mechanistic studies regarding the interaction between CNMs and immune cells or tissues in order to ensure that these materials are developed in a safe and responsible manner to help confirm their long-term sustainability.

**3.5. Neural Cell Adhesion and Neurite Outgrowth on Graphene-Based Biomimetic Substrates.** After PC-12 cells were cultured on a glass coverslip with FBS-covered graphene on it, their morphology was observed by using the optical microscopy. Cells were able to grow under the conditions of culture media without neural growth factors for neuronal differentiation. As shown in Figure 5(a), more cells were found to be adhered on the glass coverslip with FBS-covered graphene on it than on the glass coverslip

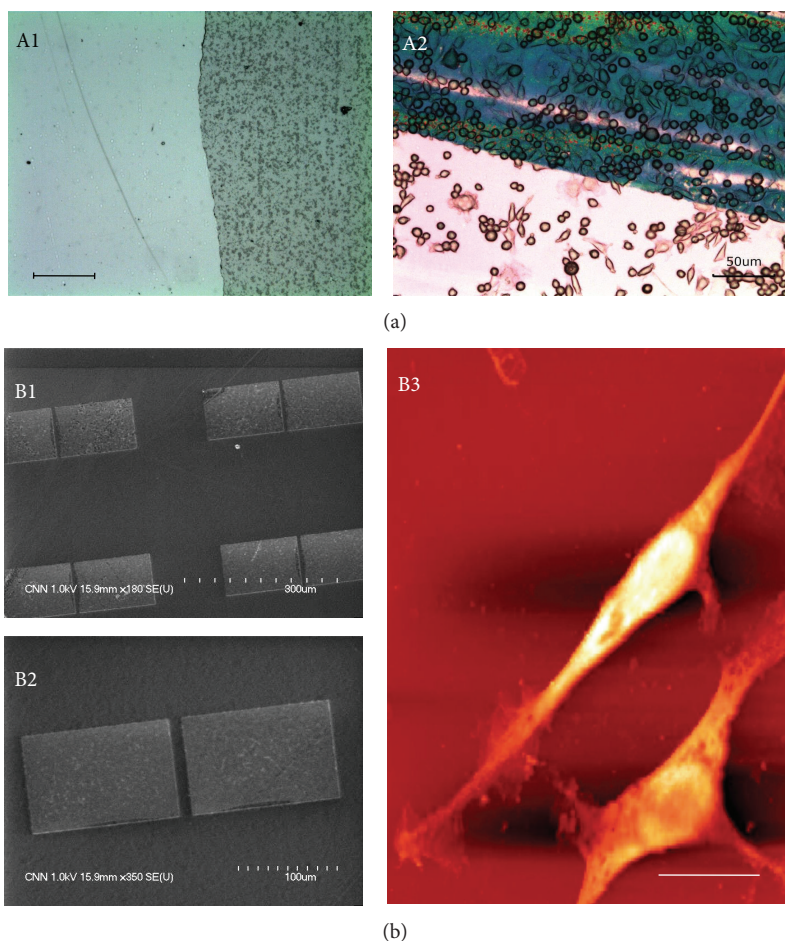


FIGURE 5: Neural cell adhesion (a) and neurite outgrowth (b) on graphene-based biomimetic substrates. Bright-field images of a glass coverslip with FBS-covered graphene on it (A1, scale bar = 10  $\mu\text{m}$ ) and PC-12 cells on the boundary area between glass (lower) and graphene (upper) 3 days after cell culture (A2). SEM images (B1 and B2) of graphene patterned on a  $\text{SiO}_2/\text{Si}$  substrate (B2, enlarged image of B1) and AFM image of neurite outgrowth from PC-12 cells on patterned graphene covered with FBS after 7 days of incubation (B3, scale bar = 20  $\mu\text{m}$ ).

without graphene-coated layers after 3 days of incubation. Moreover, PC-12 cells adhered on the bare glass coverslip appeared to partly take a spindle shape, while the graphene-coated substrate did not seem to have the same effect on cells. This pattern in the cellular adhesion was in good agreement with our previous study showing that adhesion and proliferation of PC-12 cells cultured onto graphene-coated glass coverslips were superior to those onto uncoated ones [16]. It has been reported that NIH-3T3 fibroblasts, although the cell type is different from neural cells, show highly improved cell growth, adhesion, and gene transfection efficiency on rGO/MWCNT-coated substrates [36]. Another report has revealed that rGO is biocompatible with PC-12 cells, whereas the SWCNT network is inhibitory to the proliferation, viability, and neuritegenesis of PC-12 cells [37]. This contrasting phenomenon was explained by the hypothesis that could be attributed to the distinct nanotopographic features of these two kinds of nanocarbon substrates. Controlling microenvironments of cells on certain substrates makes it possible to mimic *in vivo* situations and consequently contributes to the differentiation

of stem cells into specific cell types [38]. On the other hand, PC-12 cells were shown to spread with apparent neurite outgrowth on the patterned graphene covered with FBS after 7 days of incubation (Figure 5(b)). As shown in Figure 6, PC-12 cells were cultured on glass coverslips without and with FBS-covered graphene on them, and their proliferation was examined by using the WST-8 assay. The time-dependant proliferation pattern of PC-12 cells on the glass coverslip with FBS-covered graphene on it was almost similar to that of the cells on the bare glass coverslip. However, PC-12 cells on the glass coverslip with FBS-covered graphene on it better proliferated than on the bare glass coverslip. The differentiation of PC-12 cells could be initiated simply by exchanging culture media without any neural growth factors for neuronal differentiation. This result suggests that graphene-patterned substrates as biomimetic cues have a specific surface property that can promote neural cells. Recent evidence supports this suggestion, showing that behaviors of neural stem cells, such as attachment, proliferation, and differentiation on the surface-functionalized graphene with laminin, were

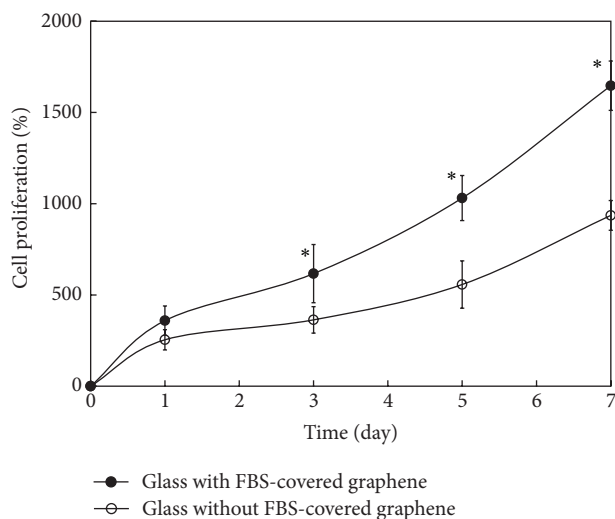


FIGURE 6: Proliferation of PC-12 cells cultured on bare glass coverslips with and without FBS-covered graphene on them after 1, 3, 5, and 7 days of incubation. At the end of each incubation period, the WST-8 assay was performed to examine the cell proliferation as described in materials and methods. Data were expressed as mean  $\pm$  standard deviation (SD) based on at least duplicate observations from three independent experiments. The asterick denotes significant difference in the proliferation between bare glass coverslips with and without FBS-covered graphene,  $P < 0.05$ .

significantly better than those of the pure graphene surface [39]. In addition to this evidence, it has been reported that CNTs enhance the excitability of neurons by forming tight contacts with the cell membrane so that electrical activity is diverted through the nanotubes [40, 41].

#### 4. Conclusion

From evaluation of the biocompatibility between neural cells and CNMs, it was demonstrated that graphene exerted much less adverse effects on neural cells than both types of CNTs, namely, SWCNTs and MWCNTs, at the concentrations lower than 62.5 ppm. Graphene-coated or graphene-patterned substrates were shown to substantially enhance the adhesion, neurite outgrowth, and proliferation of neural cells. Therefore, it is concluded that graphene-based biomimetic substrates have good biocompatibility as well as a unique surface property that can enhance neural cells, which would be potentially applied to neural regeneration and nanomedicine.

#### Conflict of Interests

All the authors of this study do not have any direct financial relationship with commercial identities.

#### Acknowledgments

This research was supported by the Basic Science Research Program through the National Research Foundation of Korea

(NRF) funded by the Ministry of Education, Science and Technology (2012R1A2A2A02010181 and 2011-0014412).

#### References

- [1] V. C. Sanchez, A. Jachak, R. H. Hurt, and A. B. Kane, "Biological interactions of graphene-family nanomaterials: an interdisciplinary review," *Chemical Research in Toxicology*, vol. 25, no. 1, pp. 15–34, 2012.
- [2] V. Singh, D. Joung, L. Zhai, S. Das, S. I. Khondaker, and S. Seal, "Graphene based materials: past, present and future," *Progress in Materials Science*, vol. 56, no. 8, pp. 1178–1271, 2011.
- [3] C. Fisher, A. E. Rider, Z. J. Han, S. Kumar, I. Levchenko, and K. (Ken) Ostrikov, "Applications and nanotoxicity of carbon nanotubes and graphene in biomedicine," *Journal of Nanomaterials*, vol. 2012, Article ID 315185, 13 pages, 2012.
- [4] M. Zhi, C. Xiang, J. Li, M. Li, and N. Wu, "Nanostructured carbon-metal oxide composite electrodes for supercapacitors: a review," *Nanoscale*, vol. 5, no. 1, pp. 72–88, 2012.
- [5] X. Huang, Z. Zeng, Z. Fan, J. Liu, and H. Zhang, "Graphene-based electrodes," *Advanced Materials*, vol. 24, no. 45, pp. 5979–6004, 2012.
- [6] W. Hu, C. Peng, W. Luo et al., "Graphene-based antibacterial paper," *ACS Nano*, vol. 4, no. 7, pp. 4317–4323, 2010.
- [7] L. Feng, L. Wu, and X. Qu, "New horizons for diagnostics and therapeutic applications of graphene and graphene oxide," *Advanced Materials*, vol. 25, no. 2, pp. 168–186, 2013.
- [8] E. Jan and N. A. Kotov, "Successful differentiation of mouse neural stem cells on layer-by-layer assembled single-walled carbon nanotube composite," *Nano Letters*, vol. 7, no. 5, pp. 1123–1128, 2007.
- [9] H. He, L. A. Pham-Huy, P. Dramou, D. Xiao, P. Zuo, and C. Pham-Huy, "Carbon nanotubes: applications in pharmacy and medicine," *Biomedical Research International*, vol. 2013, Article ID 578290, 12 pages, 2013.
- [10] H. J. Lee, J. Park, O. J. Yoon et al., "Amine-modified single-walled carbon nanotubes protect neurons from injury in a rat stroke model," *Nature Nanotechnology*, vol. 6, no. 2, pp. 121–125, 2011.
- [11] N. Li, X. Zhang, Q. Song et al., "The promotion of neurite sprouting and outgrowth of mouse hippocampal cells in culture by graphene substrates," *Biomaterials*, vol. 32, no. 35, pp. 9374–9382, 2011.
- [12] S. W. Hong, F. Du, W. Lan, S. Kim, H.-S. Kim, and J. A. Rogers, "Monolithic integration of arrays of single-walled carbon nanotubes and sheets of graphene," *Advanced Materials*, vol. 23, no. 33, pp. 3821–3826, 2011.
- [13] R.-H. Kim, M.-H. Bae, D. G. Kim et al., "Stretchable, transparent graphene interconnects for arrays of microscale inorganic light emitting diodes on rubber substrates," *Nano Letters*, vol. 11, no. 9, pp. 3881–3886, 2011.
- [14] S. H. Kim, W. D. Kim, J. M. Park, and J. Y. Ahn, "Gas-phase growth of heterostructures of carbon nanotubes and bimetallic nanowires," *Journal of Nanomaterials*, vol. 2011, Article ID 736219, 7 pages, 2011.
- [15] W. D. Kim, J. Y. Ahn, D. G. Lee et al., "Tailoring the carbon nanostructures grown on the surface of Ni-Al bimetallic nanoparticles in the gas phase," *Journal of Colloid and Interface Science*, vol. 362, no. 2, pp. 261–266, 2011.
- [16] J. H. Lee, S. H. Kang, Y. C. Shin et al., "Enhanced neurite outgrowth of PC-12 cells on graphene-monolayer-coated substrates

- as biomimetic cues,” *Journal of the Korean Physical Society*, vol. 61, no. 10, pp. 1696–1699, 2012.
- [17] T. Sh. Atabaev, O. S. Jin, J. H. Lee et al., “Facile synthesis of bifunctional silica-coated core-shell  $Y_2O_3:Eu^{3+}$ ,  $Co^{2+}$  composite particles for biomedical applications,” *RSC Advances*, vol. 2, no. 25, pp. 9495–9501, 2012.
- [18] D. P. Maxwell, Y. Wang, and L. McIntosh, “The alternative oxidase lowers mitochondrial reactive oxygen production in plant cells,” *Proceedings of the National Academy of Sciences of the United States of America*, vol. 96, no. 14, pp. 8271–8276, 1999.
- [19] S. C. Hong, J. H. Lee, J. Lee et al., “Subtle cytotoxicity and genotoxicity differences in superparamagnetic iron oxide nanoparticles coated with various functional groups,” *International Journal of Nanomedicine*, vol. 6, pp. 3219–3231, 2011.
- [20] K.-H. Liao, Y.-S. Lin, C. W. MacOsko, and C. L. Haynes, “Cytotoxicity of graphene oxide and graphene in human erythrocytes and skin fibroblasts,” *ACS Applied Materials and Interfaces*, vol. 3, no. 7, pp. 2607–2615, 2011.
- [21] L. Belyanskaya, S. Weigel, C. Hirsch, U. Tobler, H. F. Krug, and P. Wick, “Effects of carbon nanotubes on primary neurons and glial cells,” *Neurotoxicology*, vol. 30, no. 4, pp. 702–711, 2009.
- [22] Y. Zhang, B. Wang, X. Meng, G. Sun, and C. Gao, “Influences of acid-treated multiwalled carbon nanotubes on fibroblasts: proliferation, adhesion, migration, and wound healing,” *Annals of Biomedical Engineering*, vol. 39, no. 1, pp. 414–426, 2011.
- [23] A. Patlolla, B. Patlolla, and P. Tchounwou, “Evaluation of cell viability, DNA damage, and cell death in normal human dermal fibroblast cells induced by functionalized multiwalled carbon nanotube,” *Molecular and Cellular Biochemistry*, vol. 338, no. 1–2, pp. 225–232, 2010.
- [24] J. H. Lee, Y. C. Shin, S. H. Kang et al., “Cytotoxicity evaluations of pristine graphene and carbon nanotubes in fibroblastic cells,” *Journal of the Korean Physical Society*, vol. 61, no. 6, pp. 873–877, 2012.
- [25] L. Belyanskaya, P. Manser, P. Spohn, A. Bruinink, and P. Wick, “The reliability and limits of the MTT reduction assay for carbon nanotubes-cell interaction,” *Carbon*, vol. 45, no. 13, pp. 2643–2648, 2007.
- [26] T. Xia, M. Kovochich, J. Brant et al., “Comparison of the abilities of ambient and manufactured nanoparticles to induce cellular toxicity according to an oxidative stress paradigm,” *Nano Letters*, vol. 6, no. 8, pp. 1794–1807, 2006.
- [27] J. Wang, P. Sun, Y. Bao, J. Liu, and L. An, “Cytotoxicity of single-walled carbon nanotubes on PC12 cells,” *Toxicology in Vitro*, vol. 25, no. 1, pp. 242–250, 2011.
- [28] A. R. N. Reddy, Y. N. Reddy, D. R. Krishna, and V. Himabindu, “Multi wall carbon nanotubes induce oxidative stress and cytotoxicity in human embryonic kidney (HEK293) cells,” *Toxicology*, vol. 272, no. 1–3, pp. 11–16, 2010.
- [29] Y. Zhang, Y. Xu, Z. Li et al., “Mechanistic toxicity evaluation of uncoated and PEGylated single-walled carbon nanotubes in neuronal PC12 cells,” *ACS Nano*, vol. 5, no. 9, pp. 7020–7033, 2011.
- [30] J. Wang, P. Sun, Y. Bao, B. Dou, D. Song, and Y. Li, “Vitamin E renders protection to PC12 cells against oxidative damage and apoptosis induced by single-walled carbon nanotubes,” *Toxicology in Vitro*, vol. 26, no. 1, pp. 32–41, 2012.
- [31] W. J. Yang, J. H. Lee, S. C. Hong, J. Lee, J. Lee, and D. W. Han, “Difference between toxicities of iron oxide magnetic nanoparticles with various surface-functional groups against human normal fibroblasts and fibrosarcoma cells,” *Materials*, vol. 6, no. 10, pp. 4689–4706, 2013.
- [32] C. Bussy, H. Ali-Boucetta, and K. Kostarelos, “Safety considerations for graphene: lessons learnt from carbon nanotubes,” *Accounts of Chemical Research*, vol. 46, no. 3, pp. 692–701, 2013.
- [33] Y. Zhang, S. F. Ali, E. Dervishi et al., “Cytotoxicity effects of graphene and single-wall carbon nanotubes in neural pheochromocytoma-derived pc12 cells,” *ACS Nano*, vol. 4, no. 6, pp. 3181–3186, 2010.
- [34] Y. Zhang, T. R. Nayak, H. Hong, and W. Cai, “Graphene: a versatile nanoplatform for biomedical applications,” *Nanoscale*, vol. 4, no. 13, pp. 3833–3842, 2012.
- [35] S. H. Ku, M. Lee, and C. B. Park, “Carbon-based nanomaterials for tissue engineering,” *Advanced Healthcare Materials*, vol. 2, no. 2, pp. 244–260, 2013.
- [36] S.-R. Ryoo, Y.-K. Kim, M.-H. Kim, and D.-H. Min, “Behaviors of NIH-3T3 fibroblasts on graphene/carbon nanotubes: proliferation, focal adhesion, and gene transfection studies,” *ACS Nano*, vol. 4, no. 11, pp. 6587–6598, 2010.
- [37] S. Agarwal, X. Zhou, F. Ye et al., “Interfacing live cells with nanocarbon substrates,” *Langmuir*, vol. 26, no. 4, pp. 2244–2247, 2010.
- [38] J.-Y. Jang, S. W. Lee, S. H. Park et al., “Combined effects of surface morphology and mechanical straining magnitudes on the differentiation of mesenchymal stem cells without using biochemical reagents,” *Journal of Biomedicine and Biotechnology*, vol. 2011, Article ID 860652, 9 pages, 2011.
- [39] S. Y. Park, J. Park, S. H. Sim et al., “Enhanced differentiation of human neural stem cells into neurons on graphene,” *Advanced Materials*, vol. 23, no. 36, pp. H263–H267, 2011.
- [40] G. Cellot, E. Cilia, S. Cipollone et al., “Carbon nanotubes might improve neuronal performance by favouring electrical shortcuts,” *Nature Nanotechnology*, vol. 4, no. 2, pp. 126–133, 2009.
- [41] G. A. Silva, “Nanomedicine: shorting neurons with nanotubes,” *Nature Nanotechnology*, vol. 4, no. 2, pp. 82–83, 2009.

## Research Article

# Specific Intracellular Uptake of Herceptin-Conjugated CdSe/ZnS Quantum Dots into Breast Cancer Cells

Seung-Jin Han,<sup>1</sup> Pierson Rathinaraj,<sup>1</sup> Soo-Young Park,<sup>1</sup> Young Kyoo Kim,<sup>1</sup>  
Joon Hyung Lee,<sup>2</sup> Inn-Kyu Kang,<sup>1</sup> Jong-Sik Moon,<sup>3</sup> and Jeffrey G. Winiarz<sup>3</sup>

<sup>1</sup> School of Applied Chemical Engineering, Kyungpook National University, Daegu 702-701, Republic of Korea

<sup>2</sup> School of Advanced Materials Engineering, Kyungpook National University, Daegu 702-701, Republic of Korea

<sup>3</sup> Department of Chemistry, Missouri University of Science and Technology, Missouri, MO 65409, USA

Correspondence should be addressed to Inn-Kyu Kang; [ikkang@knu.ac.kr](mailto:ikkang@knu.ac.kr)

Received 14 November 2013; Accepted 14 December 2013; Published 9 January 2014

Academic Editor: Oh Hyeong Kwon

Copyright © 2014 Seung-Jin Han et al. This is an open access article distributed under the Creative Commons Attribution License, which permits unrestricted use, distribution, and reproduction in any medium, provided the original work is properly cited.

Herceptin, a typical monoclonal antibody, was immobilized on the surface of CdSe/ZnS core-shell quantum dots (QDs) to enhance their specific interactions with breast cancer cells (SK-BR3). The mean size of the core-shell quantum dots (28 nm), as determined by dynamic light scattering, increased to 86 nm after herceptin immobilization. The *in vitro* cell culture experiment showed that the keratin forming cancer cells (KB) proliferated well in the presence of herceptin-conjugated QDs (QD-Her, 5 nmol/mL), whereas most of the breast cancer cells (SK-BR3) had died. To clarify the mechanism of cell death, the interaction of SK-BR3 cells with QD-Her was examined by confocal laser scanning microscopy. As a result, the QD-Her bound specifically to the membrane of SK-BR3, which became almost saturated after 6 hours incubation. This suggests that the growth signal of breast cancer cells is inhibited completely by the specific binding of herceptin to the Her-2 receptor of SK-BR3 membrane, resulting in cell death.

## 1. Introduction

The development of noncytotoxic quantum dots (QDs) has attracted considerable interest as luminescence probes in biological and medical research because of their some unique optical and chemical properties [1], such as a tunable fluorescence wavelength according to size, a sharp and symmetrical fluorescence peak, strong and stable emission, high quantum yield, brightness, and photo stability [2–5]. QDs have several advantages over traditional dyes and fluorescent proteins used as imaging probes, such as tunable emission from visible to infrared wavelengths, broader excitation spectra, and high resistance to photo bleaching [6, 7]. On the other hand, the potential applications of QDs in biology and medicine are limited because of their toxic effects [8]. QDs contain toxic components, such as cadmium or lead. Cd<sup>2+</sup> and Pb<sup>2+</sup> can be released from QDs to kill the cells [9]. Recently, a number of techniques, such as a gold outer shell [10], targeted ligand-like peptide [11], proteins [12, 13], and polymer coating [14] have been developed to minimize the cytotoxicity of QDs. Consequently, many approaches for transforming QDs

from hydrophobic to hydrophilic have been developed for a range of biomedical applications. Accordingly, researchers have also used noncytotoxic materials, such as polyethylene glycol (PEG) and polymaleic anhydride salt-1-tetradecene, to coat the surfaces of QDs [15].

Thus far, a range of surface coatings of QDs have been explored including the conjugation of mercaptoacetic acid [16], mercaptopropionic acid [17], mercaptobenzoic acid [18], and biocompatible and chemically functionalizable inorganic shells, such as silica or zinc sulfide [19]. These coatings can guarantee the water solubility of QDs but cannot enhance the biocompatibility significantly. Therefore, further coatings with suitable water-soluble organic ligand/biomolecules are necessary to enhance the biocompatibility of QDs. To that end, QDs have been linked covalently with biorecognition molecules, such as biotin [20], oleic acid [21], peptides [22], bovine serum albumin [23], transferrin [24], antibodies [25], and DNA [26].

Polymeric micelles have been studied extensively for the solubilization of hydrophobic drugs and bioactive agents because of their unique properties, including nanoscale size,

high water solubility, high structural stability, high carrying capacity of hydrophobic agents, and easy introduction of functional moieties to the outer shell. The polymers generally leave the fluorescent properties of QDs unchanged but allow the introduction of other moieties to the QD surfaces [27]. CdSe/ZnS QD is a versatile core shell material with a wide band gap of 3.37 eV and a rather large exciton binding energy that makes the exciton state stable, even at room temperature. Zinc is a very important trace element in humans [28] and has been found to play an important part in many biological systems [29–32]. Therefore, CdSe/ZnS core-shell QDs are expected to be environmentally friendly and more suitable for bioimaging and cancer detection than CdSe QD.

In this study, breast cancer cells were targeted with herceptin-conjugated quantum dots for cancer therapy and diagnosis. Phospholipid-immobilized CdSe/ZnS core-shell quantum dots (QDs) were prepared by a coupling reaction of trioctylphosphine oxide-coated CdSe/ZnS core-shell quantum dots with carboxylic acid-terminated PEG and methoxy-terminated PEG. Herceptin was then introduced to the surface of the QDs (QD-Her) to enhance the antitumor effects of chemotherapeutic agents without increasing their toxicity [33–36]. The surface properties of the QDs and QD-Her were characterized by Fourier transform infrared (FT-IR) spectroscopy, electron spectroscopy for chemical analysis (ESCA), UV-Vis spectrometry, dynamic light scattering (DLS), and zeta potential measurements. To evaluate the cell compatibility and cytotoxicity of the QDs and QD-Her, human breast cancer cells (SK-BR3) were cultured in the presence of Q-dots. The intracellular uptake of QD-Her to the cells was also observed by confocal laser scanning microscopy (CLSM).

## 2. Materials and Methods

Trioctyl phosphine oxide (TOPO), trioctyl phosphine (TOP), and hexadecylamine (HDA) were purchased from Sigma-Aldrich Co., USA. DSPE-PEG 2000 {1,2-distearoyl-*sn*-glycero-3-phosphoethanolamine-N-[carboxy(polyethylene glycol)-2000]} and PEG-2-PE {1,2-palmitoyl-*sn*-glycero-3-phosphoethanolamine-N-[methoxy(polyethylene glycol)-2000]} were purchased from Avanti Polar Lipids, USA. Herceptin was obtained from Roche Pharma Ltd. (Basel, Switzerland). Cell culture reagents, fetal bovine serum (FBS), Dulbecco's modified eagle medium (DMEM, high glucose), penicillin-streptomycin, trypsin/EDTA, and Dulbecco's phosphate buffer saline (PBS) were supplied by Gibco BRL (Carlsbad, CA), and the SK-BR3 cells (breast cancer cells) were purchased from Korean Cell Line Bank.

**2.1. Synthesis of CdSe/ZnS Core/Shell QDs.** The synthesis of CdSe/ZnS quantum dots was performed using recently reported methods [27, 35]. A mixture of 9 mmol of trioctylphosphine oxide (TOPO), 7 mmol of tetradecyl phosphonic acid (TDPA), and 0.2 g of cadmium oxide (CdO) was heated to 240°C for 20 minutes to obtain a clear solution. A solution containing 0.01 g of Se powder dissolved in 5 mmol of trioctylphosphine (TOP) was injected quickly into the hot

solution, and the reaction mixture was allowed to cool to 100°C for the growth of CdSe nanocrystals. To obtain the CdSe/ZnS nanoparticles, the solution was cooled to room temperature and highly luminescent CdSe nanocrystals were isolated and purified by centrifugation followed by precipitation with methanol and finally dissolved in 5 mL of toluene.

To obtain the CdSe/ZnS core-shell quantum dots, the precipitated CdSe nanocrystals were dispersed in 2 mL of TOP in a three-necked flask. In addition, ZnS (0.092 g) was dissolved in 2 mmol TOP upon gentle heating. After cooling to room temperature, the resulting mixture was injected dropwise into a reaction flask containing the core nanocrystal at 140°C for 6 hrs. After the addition was complete, the particles were annealed at 90°C for 6 hrs. Core-shell quantum dots of various sizes were obtained by adjusting the concentration of CdO and ZnS in TOP, as well as the corresponding injection periods. The prepared CdSe/ZnS QDs were dissolved in chloroform and purified further by centrifugation and double reprecipitation from methanol.

**2.2. Preparation of Hydrophilic CdSe/ZnS QDs.** DSPE-PEG and PEG-2 PE (2:8) were dissolved in 5 mL of chloroform (CHCl<sub>3</sub>) and 1 mL of the mixture was transferred to a 250 mL three neck round-bottom flask containing CdSe/ZnS QDs in 5 mL of chloroform. The clear solution was stirred overnight under nitrogen. When the reaction was complete, the chloroform was removed by vacuum, and the residue was mixed with 4 mL of water and transferred to a centrifuge tube. Subsequently, 40 mL of water was added to the mixed solution, and the precipitated product was separated by centrifugation (3,000 rpm for 15 min) and washed with water. The precipitated product was dissolved in 10 mL of methanol, and water was then added to ensure that polymer-coated QDs were suspended.

**2.3. Immobilization of Herceptin on the Surface of CdSe/ZnS QDs.** The immobilization of herceptin on CdSe/ZnS (QD-Her) was carried out by a reaction of water-soluble QDs with herceptin, as shown in Figure 1. Water soluble QDs (18 mg/mL) and herceptin (108 mg/mL) were added to a two-necked round-bottom flask and dissolved in 10 mL of PBS buffer (pH 6.0). EDC (1 mmol) and NHS (1 mmol) were added to the reaction solution followed by stirring for 5 hrs at room temperature. The reaction solution was filtered to remove the precipitate and then added to a dialysis membrane (MWCO: 100,000) in deionized water media for 24 h to remove the unreacted EDC, NHS, and herceptin. Finally, the solution was filtered through a 0.45 μm membrane and dried for 24 hrs under vacuum.

## 3. Results

**3.1. Physical Characterization.** Quantum dot nanoparticles were ground with KBr powder, compressed into pellets, and examined by FTIR (Jasco FTIR 300 E spectrometer) spectroscopy with a resolution of 4 cm<sup>-1</sup>. Transmission electron microscopy (TEM, Philips, CM 200 TEM, applied operation voltage; 120 kV) was used to observe the morphology of

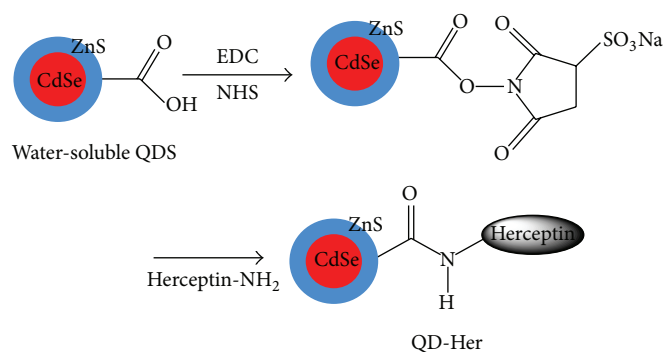


FIGURE 1: Schematic diagram showing the immobilization of herceptin on the CdSe/ZnS core-shell quantum dots (QD-Her).

the nanoparticles. To obtain the samples for the TEM observations, the particles were diluted with distilled water and deposited on Formvar-coated 400 mesh copper grids. After drying the nanoparticle-fluid thin film on the copper grid, a thin carbon film, approximately 10–30 nm in thickness, was deposited on the nanoparticles fluid film. The hydrodynamic diameter and size distribution of the quantum dots were determined by dynamic light scattering (DLS) using a standard laboratory built light scattering spectrometer using a BI90 particle sizer (Brookhaven Instruments Corp., Holtsville, NY). The system had a vertically polarized incident light of 514.5 nm supplied by an argon ion laser (Lexel laser, model 95). The UV-Vis absorption spectrum was recorded from aqueous dispersions at room temperature using a Hitachi U-3000 spectrophotometer.

**3.2. Cell Culture.** SK-BR3 (breast cancer cells) was used as the target cell, and KB (epithelial cancer cells) was used as the control cell line. The cells were cultured routinely at 37°C in a humidified atmosphere containing 5% CO<sub>2</sub> in a polystyrene dish containing 10 mL of McCoy medium or DMEM medium, supplemented with 10% fetal bovine serum and 1% penicillin streptomycin G sodium (PGS). The medium was changed every third day. For subculture, the cells were washed twice with PBS and incubated with a trypsin-EDTA solution (0.25% trypsin, 1 mM EDTA) for 10 min at 37°C to detach the cells. Complete media were then added to the polystyrene dish at room temperature to inhibit the effects of trypsin. The cells were washed twice by centrifugation and resuspended in complete media for reseeding and growing in new culture flasks. To observe the morphology of cells, the cells were seeded at a concentration of  $1 \times 10^5$ /mL in a 10 mL Petri dish and incubated for 3 days with QDs-or QD-Her-containing media at a concentration of 0.2 mg/mL. The morphology of adhered cells was observed by optical microscopy (Nikon Eclipse TS100, Japan).

To examine the cellular uptake of nanoparticles via fluorescence microscope and confocal laser microscope, the cells were seeded at a concentration of  $1 \times 10^5$ /mL in a 10 mL Petri dish and incubated for 1 day. After 1 day, the medium was replaced with QDs and QD-Her-containing media at a particle concentration of 50 µg/mL and incubated for certain time (1–6 hrs) for the internalization of the nanoparticles into

the cells. The cells were then washed three times with Dulbecco's PBS (D-PBS) and images were taken using fluorescence and confocal laser microscopes. The fluorescence images were obtained using an Olympus IX70 fluorescence microscope equipped with a cooled charge-coupled device (CCD) camera. The images were processed using DVC view software (version 2.2.8, DVC Company). A Zeiss LSM 410 confocal laser scanning microscope (Brightness: 700 cd/mm<sup>2</sup>, Zeiss, Oberkochen, Germany) was used to obtain the confocal images. The position and integrity of the internalized QD-Her conjugates were evaluated by confocal microscopy using 4,6-diamidino-2-phenylindole dihydrochloride (DAPI, blue) as a marker, which stains the nuclei of the cells. The cell nuclei were stained by the addition of DAPI solution (10 µL) with proper mixing and incubated for 10 min. To track the QD-Her nanoparticles, herceptin-conjugated QDs and DAPI (488 nm) were added to the cells. The stained cells were washed at least three times with 1 mL of fresh McCoy medium and images were then taken by confocal laser microscopy [37].

The comparative proliferation of SK-BR3 and KB cells in a medium containing QDs and QD-Her was determined using a MTT (3-(4,5-dimethylthiazol-2-yl)-2,5-diphenyltetrazolium bromide) assay. Briefly, the SK-BR3 and KB cells were seeded separately ( $1 \times 10^5$  cell/mL) on 24 well plates in the presence of a cell culture medium. After 24 h, the culture medium was replaced with fresh medium containing QDs and QD-Her at a particle concentration of 200 µg/mL. After incubation for 1, 2, and 3 days, a 50 µL MTT solution (5 mg/mL in PBS) was added to each well and incubated in a humidified atmosphere of 5% CO<sub>2</sub> at 37°C for 4 h. After removing the medium, the converted dye was dissolved in acidic isopropanol (0.04 N HCl-isopropanol) and kept for 30 min in the dark at room temperature. From each sample, the medium (100 µL) was taken, transferred to a 96-well plate, and subjected to the ultraviolet measurements of the converted dye. This was achieved at a wavelength of 570 nm on a kinetic microplate reader. The experiment was repeated at least three times.

The phase contrast and fluorescence images of the cells were obtained using a combined explorer system with a motorized inverted fluorescence microscope (Carl Zeiss LSM700, Germany), using the topographic images that can be detected simultaneously. The cell proliferation experiment

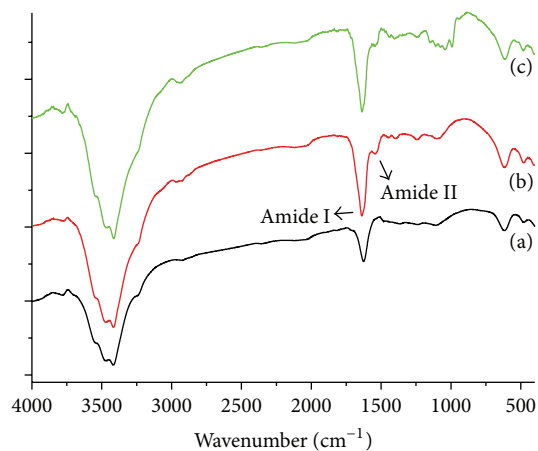


FIGURE 2: FT-IR spectra of the QDs (a), QD-Her (b), and herceptin (c) measured using the KBr method.

was performed in triplicate and the results were expressed as mean  $\pm$  standard deviation (SD). Student's *t*-test was used to assess the statistical significant differences in the results. A *P* value  $<0.05$  was considered significant.

## 4. Discussions

### 4.1. Surface Characterization of Herceptin-Immobilized QDs.

The surface modification of QDs with herceptin was confirmed by FTIR, as shown in Figure 2. In the case of the QDs spectrum, the introduction of DSPE-PEG 2000 to the surface of the QDs was confirmed by observing the characteristic peaks at  $1700$  and  $3500\text{ cm}^{-1}$ , as shown in Figure 2(a), which was attributed to free carboxyl ( $-\text{COOH}$ ) and hydroxyl ( $-\text{OH}$ ) groups [38, 39]. Again, after the reaction of the QDs with herceptin, two new peaks at positions approximately  $1648\text{ cm}^{-1}$  and  $1540\text{ cm}^{-1}$  were observed in the spectrum of QD-Her (Figure 2(b)), which were assigned to amide I ( $-\text{CO}-\text{NH}-$ ) and amide II ( $-\text{CO}-\text{NH}-$ ) bonds, respectively, indicating the successful immobilization of herceptin on the surface of the QDs [29, 32].

Figures 3(a) and 3(b) present TEM images of the QDs and QD-Her, respectively. The QDs have a spherical morphology with a mean diameter of  $\sim 4.1\text{ nm}$ . Because of the small dimensions and high surface energy of the particles, it was easy for them to aggregate, as seen in Figure 3(a). On the other hand, in the case of QD-Her, the particles had a mean diameter of  $4.5\text{ nm}$ , were spherical in shape, and showed significantly less aggregation (Figure 3(b)). The larger particle size and nonaggregated particles morphology was attributed to the conjugation of herceptin on the surface of the QDs. Figure 4 shows the typical size and size distribution of the synthesized QDs (Figure 4(a)) and QD-Her (Figure 4(b)) measured by DLS. The mean size of the QDs as determined by DLS was  $\sim 28\text{ nm}$ . On the other hand, the mean size of the QD-Her was approximately  $86\text{ nm}$ . The particle size, as determined by DLS, was considerably larger than that determined by TEM. This is because the DLS technique measures the mean hydrodynamic diameter of the QDs core surrounded by the organic and solvation layers, and this hydrodynamic

TABLE 1: Atomic percentage of QDs and QD-Her calculated from the ESCA survey scan spectra.

| Substrates | Atomic (%) |      |      |     |
|------------|------------|------|------|-----|
|            | C          | O    | N    | P   |
| QDs        | 69.3       | 24.0 | 0.7  | 6.0 |
| QD-Her     | 73.1       | 15.5 | 10.5 | 0.5 |

diameter is affected by the viscosity and concentration of the solution. TEM, however, gives the diameter of the core alone [29]. The synthesis of CdSe/ZnS core-shell QDs and herceptin-immobilized QDs was also confirmed by UV-Vis absorption spectroscopy, as shown in Figure 5. The QDs showed an absorption onset at  $526\text{ nm}$  (Figure 5(a)) and after herceptin immobilization, it exhibited a red shift to  $529\text{ nm}$  [31]. This red shift was caused by strong quantum confinement due to the increase in particle size. In addition, the peak at  $529\text{ nm}$  attributed to the herceptin labels on the surface of QDs, because of metal to ligand charge transfer [34].

The immobilization of herceptin on the surface of QDs was confirmed by ESCA, as shown in Figure 6. The QDs showed peaks for five elements corresponding to Cls (binding energy,  $284.0\text{ eV}$ ) and OIs (binding energy,  $526.5\text{ eV}$ ), P2s, 2p (binding energy,  $197.0\text{ eV}$ ,  $132\text{ eV}$ ), and N1s (binding energy,  $397.0\text{ eV}$ ), as shown in Figure 6(a). On the other hand, after herceptin immobilization, the QD-Her showed three typical peaks corresponding to Cls, OIs, and N1s. Table 1 lists the chemical compositions of the QDs and QD-Her, which were calculated from the ESCA survey scan spectra. In the case of the QD-Her, the carbon content ( $73.1\%$ ) was higher than in the QDs ( $69.3\%$ ). Furthermore, one new element, sulfur ( $0.4\%$ ), was observed on the surfaces of the QD-Her, and in the case of QD-Her, the nitrogen content increased from  $0.7\%$  to  $10.5\%$ , indicating the successful immobilization of herceptin on the surface of the QDs. One possible explanation for the reduction in the P2s, 2p, and S2p peaks is the photoelectrons with energy loss and the increase in the binding energy during immobilization with herceptin [40].

### 4.2. Evaluation of Cytotoxicity.

Figure 7 shows the status of the "Live/Dead" dye-stained SK-BR3 and KB cell cultured in the presence of QDs and QD-Her for 1 and 3 days of incubation. Using this qualitative method, the living and dead cells were stained in green and red under the fluorescence microscope, respectively. Figure 7 shows that all the KB cells remained viable after 3 days of incubation, irrespective of the presence or absence of nanoparticles. On the other hand, after a culture of 1 and 3 days, in the presence of QD-Her, most of the SK-BR3 cells had died, as shown in Figures 8(e) and 8(f). On the other hand, most of the SK-BR3 cells remained viable in the presence of the QDs and in the polystyrene culture dish (Figures 7(a)–7(d)), but a nonsignificant number of cells were dead in the QD-Her case. A possible explanation of this large decrease in cell viability in the case of QD-Her is that intracellularly delivered herceptin exhibits acute apoptotic activity

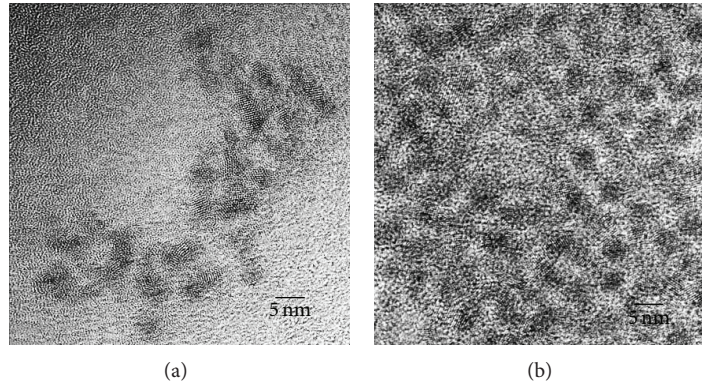


FIGURE 3: TEM images of the QDs (a) and QD-Her (b).

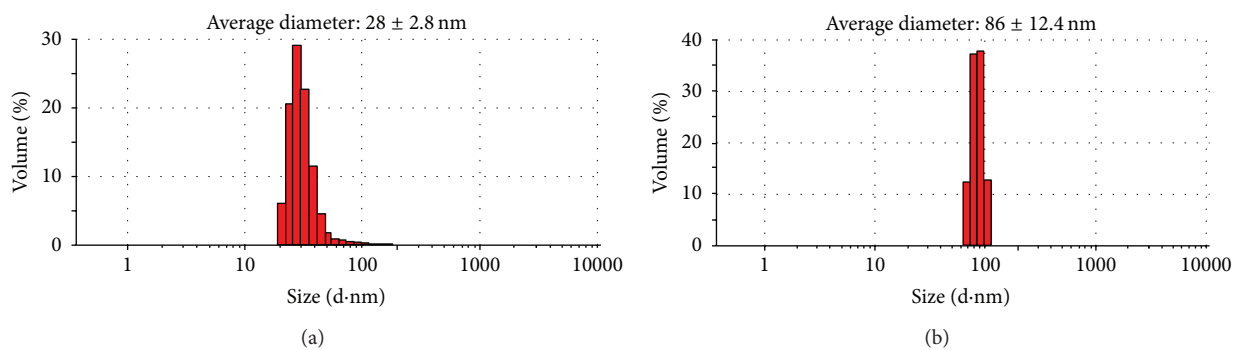


FIGURE 4: Particle size distribution of the QDs (a) and QD-Her (b) measured by dynamic light scattering (DLS).

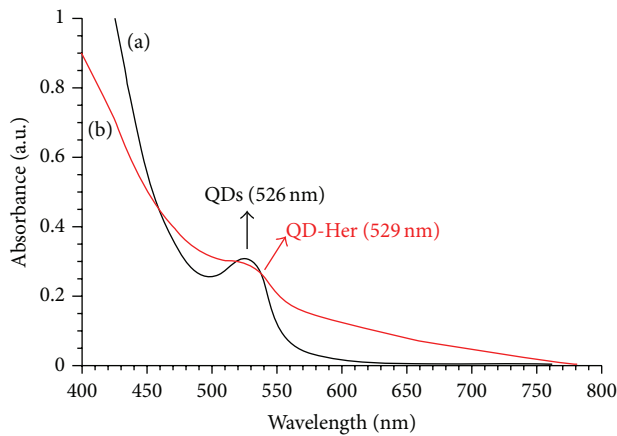


FIGURE 5: UV-Vis absorption spectra of the QDs (a) and QD-Her (b) in aqueous solution.

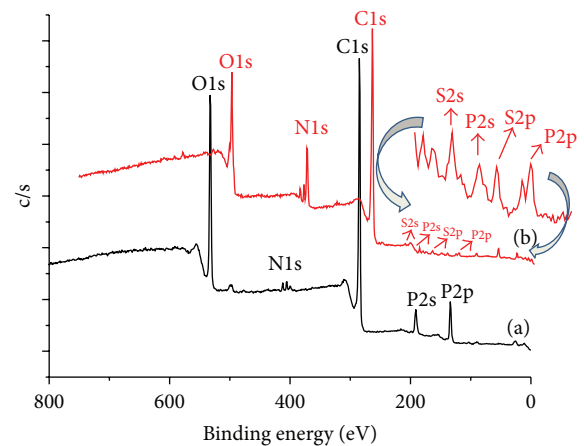


FIGURE 6: ESCA survey scan spectra of the QDs (a) and QD-Her (b).

by interacting with several transcription factors related to cell proliferation [39]. Previously, Bae et al. reported that degradable heparin nanogels and heparin/chitosan polyelectrolyte nanocomplexes could effectively induce apoptosis via receptor-mediated endocytosis through specific herceptin-HER2 integrin interaction [39]. The endocytosed QD-Her within the cells would release free herceptin molecules in the cytoplasm by cleaving the QD-herceptin linkage under the reductive intracellular environment, which has 300 times

higher glutathione (GSH) concentration (20 Mm) than the extracellular level [41]. GSH is the most abundant reducing agent in the cytoplasm, facilitating the detachment of herceptin from the QDs by breaking the PEG-herceptin linkage. In addition, nanoparticles are taken up by the cells through endocytosis, which disrupts the cell membrane [32], or weak cell adhesive interactions with QDs promote apoptosis (programmed cell death). The core-shell nanoparticles conjugated with herceptin may act as cellular markers and target the receptors expressed on the cell surface with cellular

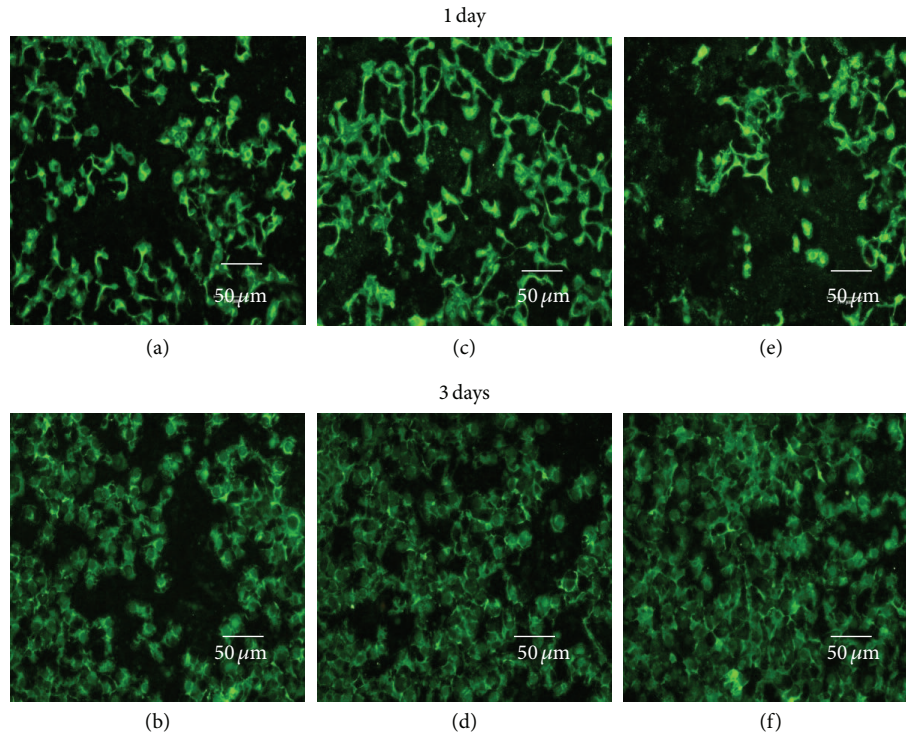


FIGURE 7: Fluorescence microscopy images of live and dead KB cells after culturing for 1 and 3 days in a polystyrene culture dish ((a), (b)) and in the presence of QDs ((b), (d)) and QD-Her ((e), (f)). The live and dead cells were stained and visualized in green and red, respectively, under a fluorescence microscope.

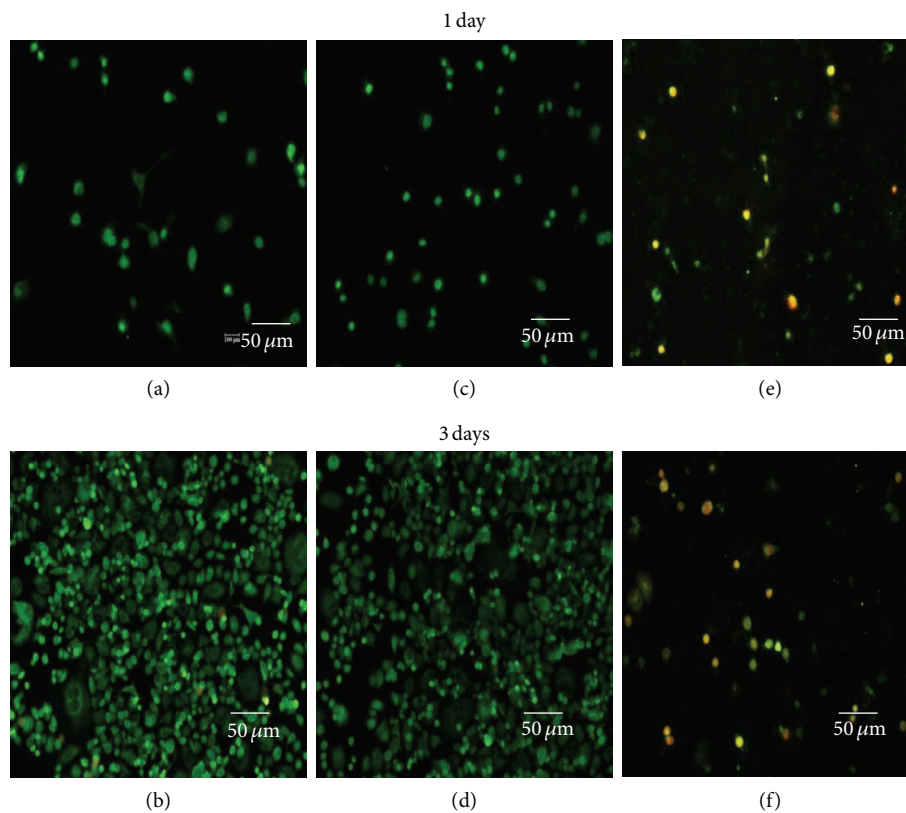


FIGURE 8: Fluorescence microscopy image of the live and dead SK-BR3 cells after culturing for 1 and 3 days in a polystyrene culture dish ((a), (b)) and in the presence of QDs ((b), (d)) and QD-Her ((e), (f)). Live and dead cells were stained in green and red, respectively, under a fluorescence microscope.

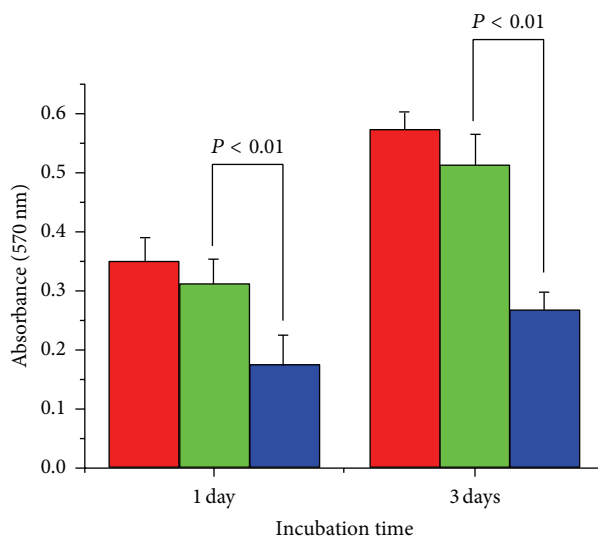


FIGURE 9: MTT assay, absorbance as a measure of the cell proliferation of SK-BR3 cells cultured in the PS culture dish (the red bar), in the presence of QDs (the green bar) and QD-Her (the blue bar) for different time.

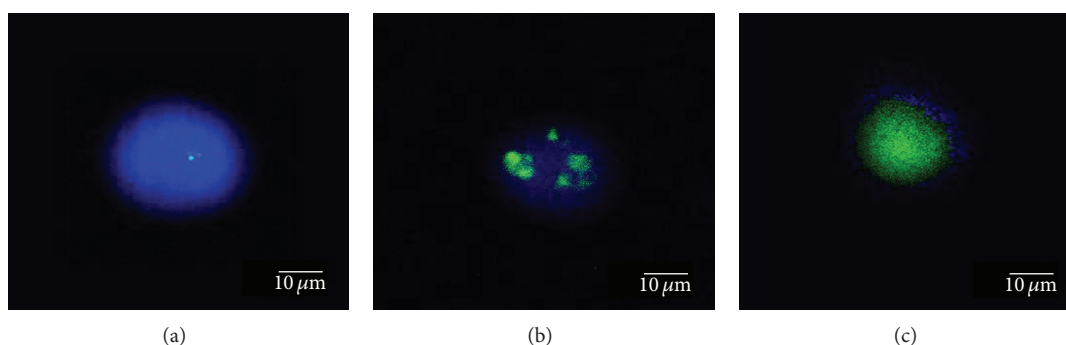


FIGURE 10: Fluorescence images obtained from the culture of SK-BR3 cells for 1, 3, and 6 hrs in the presence of DAPI and QD-Her.

internalization. The receptors are highly regulated by the cell surface proteins [37], which mediate the specific interactions between the cells and their extracellular milieu, and they are generally localized on the plasma membrane [33]. This suggests that the cytotoxicity of QDs was improved by the conjugation of DSPE-PEG and PEG-2-PE (Figures 7(c), 7(d)) and herceptin (Figures 7(e), 7(f)), as determined by the viability of KB cells (see Figure 7).

Figure 9 shows the viability of SK-BR3 cells cultured for 1 and 3 days in the presence of QD-Her, as determined by the MTT assay. After 1 and 3 days of incubation, the level of SK-BR3 cell proliferation in the presence of QDs was similar to that of the cells cultured in the absence of nanoparticles (PS culture dish). On the other hand, cell proliferation in the presence of QD-Her was significantly lower than that of the QDs. Therefore, the CdSe/ZnS quantum dots conjugated with herceptin could increase the death of SK-BR3 cells considerably compared to the CdSe/ZnS quantum dots without herceptin.

**4.3. Evaluation of Intracellular Uptake.** The uptake of QD-Her into the target cells was visualized by fluorescence microscopy. Figure 10 shows fluorescence images obtained from the cultured SK-BR3 cells that had been incubated for up to 6 hrs in the presence QD-Her. During the cell culture in the presence of QD-Her, a significant number of nanoparticles were transported into the cells and emitted intense fluorescence. This suggests that the QDs carrying herceptin provide specific recognition signals for the nanoparticles to facilitate internalization into the target cells (SK-BR3 cells). The interaction of the herceptin from the QDs with the HER-2 receptors expressed on the membrane surface of the SK-BR3 cells might have contributed to the improvement in the internalization of QD-Her into the cells, based on receptor-mediated endocytosis [29]. Gan et al. reported similar results [42]. They introduced a hepatocarcinoma binding peptide (A54) onto the surface of the magnetite nanoparticles and examined their interaction with hepatocellular carcinoma cells *in vitro* by fluorescence microscopy. Internalization of the herceptin-conjugated nanoparticles (QD-Her) into SK-BR3 occurred. Breast cancer cells expressing HER-2 receptor

were quite sensitive to herceptin. Figure 10 shows that herceptin is an effective antibody, binding specifically to the HER-2 receptor-bearing breast cancer cells. The internalization of QD-Her into SK-BR3 cells was confirmed by confocal laser microscopy to characterize the delivery of QD-Her to the cytoplasm of the SK-BR3 cells. Figure 10 shows the fluorescence image derived from the nucleus of the SK-BR3 cells (DAPI, blue) and QD-Her internalized (green). The cells were cultured in the presence of QD-Her at various incubation times (Figure 10). Weak QD-Her conjugates were observed in the fluorescence image (green color) after 1 hr (Figure 10(a)) and slightly higher fluorescence image was observed after 3 hrs (Figure 10(b)). Intense fluorescence image was noted after 6 hrs (Figure 10(c)). On the other hand, the blue fluorescence image derived from the nuclei stained with DAPI was strong after 1 hr incubation but it decreased with increasing incubation time and almost disappeared after 6 hrs incubation. In particular, the interaction of SK-BR3 with QD-Her began after 1 hr incubation and was accelerated and saturated after 6 hrs. The confocal microscopy images suggest that the nanoparticle-mediated delivery of monoclonal antibodies was achieved efficiently, resulting in cell death. The mechanism of internalization involves endocytosis followed by the release of herceptin-conjugated nanoparticles to the cytoplasm [37]. This suggests that the growth signal of breast cancer cells is inhibited completely by the specific binding of the herceptin to the Her-2 receptor of SK-BR3 membrane, resulting in cell death [38].

## 5. Conclusions

DSPE-PEG-coated CdSe/ZnS core-shell quantum dots (QDs) were conjugated successfully with the herceptin antibody. Herceptin immobilized QDs (QD-Her) were confirmed by FTIR and XPS. The QD-Her size determined by DLS was ~86 nm. The QD-Her had no cytotoxicity on the control cells (KB) compared to the target cells (SK-BR3). QD-Her was internalized selectively into the target cells (SK-BR3), and free herceptin was released in the cytoplasm, which induced acute apoptosis. The QD-Her nanoparticles were endocytosed by breast cancer cells (SK-BR3) to a large extent via a receptor-mediated mechanism, where herceptin conjugated on the nanoparticles targets the HER-2 receptor expressed on the membrane of the cancer cells [39]. Therefore, QD-Her has a potential use in optical imaging and the treatment of breast cancer cells.

## Conflict of Interest

The authors declare that there is no conflict of interest regarding the publication of this manuscript

## Authors' Contribution

Seung-Jin Han and Pierson Rathinaraj contributed equally to this work.

## Acknowledgments

This study was supported by the Basic Research Laboratory Program (no. 2011-0020264) and the General Research Program (2013 RIA 2005148) from the Ministry of Education, Science and Technology of Korea.

## References

- [1] J. Pan, Y. Wang, and S.-S. Feng, "Formulation, characterization, and in vitro evaluation of quantum dots loaded in poly(Lactide)-Vitamin E TPGS nanoparticles for cellular and molecular imaging," *Biotechnology and Bioengineering*, vol. 101, no. 3, pp. 622–633, 2008.
- [2] F. Pinaud, X. Michalet, L. A. Bentolila et al., "Advances in fluorescence imaging with quantum dot bio-probes," *Biomaterials*, vol. 27, no. 9, pp. 1679–1687, 2006.
- [3] J. Pan and S.-S. Feng, "Targeting and imaging cancer cells by Folate-decorated, quantum dots (QDs)-loaded nanoparticles of biodegradable polymers," *Biomaterials*, vol. 30, no. 6, pp. 1176–1183, 2009.
- [4] K. S. Soppimath, T. M. Aminabhavi, A. R. Kulkarni, and W. E. Rudzinski, "Biodegradable polymeric nanoparticles as drug delivery devices," *Journal of Controlled Release*, vol. 70, no. 1-2, pp. 1679–1687, 2001.
- [5] T. Jamieson, R. Bakhshi, D. Petrova, R. Pocock, M. Imani, and A. M. Seifalian, "Biological applications of quantum dots," *Biomaterials*, vol. 28, no. 31, pp. 4717–4732, 2007.
- [6] A. P. Alivisatos, W. Gu, and C. Larabell, "Quantum dots as cellular probes," *Annual Review of Biomedical Engineering*, vol. 7, pp. 55–76, 2005.
- [7] X. Michalet, F. F. Pinaud, L. A. Bentolila et al., "Quantum dots for live cells, in vivo imaging, and diagnostics," *Science*, vol. 307, no. 5709, pp. 538–544, 2005.
- [8] A. M. Derfus, W. C. W. Chan, and S. N. Bhatia, "Probing the cytotoxicity of semiconductor quantum dots," *Nano Letters*, vol. 4, no. 1, pp. 11–18, 2004.
- [9] E. T. Ben-Ari, "Nanoscale quantum dots hold promise for cancer applications," *Journal of the National Cancer Institute*, vol. 95, no. 7, pp. 502–504, 2003.
- [10] H. Mattoussi, J. Matthew Mauro, E. R. Goldman et al., "Self-assembly of CdSe-ZnS quantum dot bioconjugates using an engineered recombinant protein," *Journal of the American Chemical Society*, vol. 122, no. 49, pp. 12142–12150, 2000.
- [11] A. M. Smith, H. Duan, A. M. Mohs, and S. Nie, "Bioconjugated quantum dots for *in vivo* molecular and cellular imaging," *Advanced Drug Delivery Reviews*, vol. 60, no. 11, pp. 1226–1240, 2008.
- [12] M. T. Fernández-Arguelles, A. Yakovlev, R. A. Sperling et al., "Synthesis and characterization of polymer-coated quantum dots with integrated acceptor dyes as FRET-based nanoprobe," *Nano Letters*, vol. 7, no. 9, pp. 2613–2617, 2007.
- [13] Z. Chen, H. Chen, H. Meng et al., "Bio-distribution and metabolic paths of silica coated CdSeS quantum dots," *Toxicology and Applied Pharmacology*, vol. 230, no. 3, pp. 364–371, 2008.
- [14] J. G. Rouse, C. M. Haslauer, E. G. Lobo, and N. A. Monteiro-Riviere, "Cyclic tensile strain increases interactions between human epidermal keratinocytes and quantum dot nanoparticles," *Toxicology In Vitro*, vol. 22, no. 2, pp. 491–497, 2008.
- [15] W. C. Chan, D. J. Maxwell, X. Gao, R. E. Bailey, M. Han, and S. Nie, "Luminescent quantum dots for multiplexed biological det-

- ection and imaging," *Current Opinion in Biotechnology*, vol. 13, no. 2, pp. 40–47, 2002.
- [16] H. M. Chen, X. F. Huang, L. Xu, J. Xu, K. J. Chen, and D. Feng, "Surface-defect-states photoluminescence in CdS nanocrystals prepared by one-step aqueous synthesis method," *Superletter Microstructure*, vol. 27, no. 3, pp. 1–5, 2000.
- [17] X. Gao, W. C. W. Chan, and S. Nie, "Quantum-dot nanocrystals for ultrasensitive biological labeling and multicolor optical encoding," *Journal of Biomedical Optics*, vol. 7, no. 4, pp. 532–537, 2002.
- [18] C.-C. Chen, C.-P. Yet, H.-N. Wang, and C.-Y. Chao, "Self-assembly of monolayers of cadmium selenide nanocrystals with dual color emission," *Langmuir*, vol. 15, no. 20, pp. 6845–6850, 1999.
- [19] F. Chen and D. Gerion, "Fluorescent CdSe/ZnS nanocrystal-peptide conjugates for long-term, nontoxic imaging and nuclear targeting in living cells," *Nano Letters*, vol. 4, no. 10, pp. 1827–1832, 2004.
- [20] M. Bruchez Jr., M. Moronne, P. Gin, S. Weiss, and A. P. Alivisatos, "Semiconductor nanocrystals as fluorescent biological labels," *Science*, vol. 281, no. 5385, pp. 2013–2016, 1998.
- [21] W. C. W. Chan, D. J. Maxwell, X. Gao, R. E. Bailey, M. Han, and S. Nie, "Luminescent quantum dots for multiplexed biological detection and imaging," *Current Opinion in Biotechnology*, vol. 13, no. 1, pp. 40–46, 2002.
- [22] F. Pinaud, D. King, H.-P. Moore, and S. Weiss, "Bioactivation and cell targeting of semiconductor CdSe/ZnS nanocrystals with phytochelatin-related peptides," *Journal of the American Chemical Society*, vol. 126, no. 19, pp. 6115–6123, 2004.
- [23] K.-I. Hanaki, A. Momo, T. Oku et al., "Semiconductor quantum dot/albumin complex is a long-life and highly photostable endosome marker," *Biochemical and Biophysical Research Communications*, vol. 302, no. 3, pp. 496–501, 2003.
- [24] W. C. W. Chan and S. Nie, "Quantum dot bioconjugates for ultrasensitive nonisotopic detection," *Science*, vol. 281, no. 5385, pp. 2016–2018, 1998.
- [25] E. R. Goldman, G. P. Anderson, P. T. Tran, H. Mattoussi, P. T. Charles, and J. M. Mauro, "Conjugation of luminescent quantum dots with antibodies using an engineered adaptor protein to provide new reagents for fluoroimmunoassays," *Analytical Chemistry*, vol. 74, no. 4, pp. 841–847, 2002.
- [26] D. Gerion, W. J. Parak, S. C. Williams, D. Zanchet, C. M. Micheel, and A. P. Alivisatos, "Sorting fluorescent nanocrystals with DNA," *Journal of the American Chemical Society*, vol. 124, no. 24, pp. 7070–7074, 2002.
- [27] M. Nurunnabi, K. J. Cho, J. S. Choi, K. M. Huh, and Y.-K. Lee, "Targeted near-IR QDs-loaded micelles for cancer therapy and imaging," *Biomaterials*, vol. 31, no. 20, pp. 5436–5444, 2010.
- [28] Y.-K. Lee, S. M. Hong, J. S. Kim et al., "Encapsulation of CdSe/ZnS quantum dots in poly(ethylene glycol)-poly(D,L-lactide) micelle for biomedical imaging and detection," *Macromolecular Research*, vol. 15, no. 4, pp. 330–336, 2007.
- [29] Z.-C. Xing, M.-J. Park, S.-J. Han et al., "Intracellular uptake of magnetite nanoparticles conjugated with RGDS-peptide," *Macromolecular Research*, vol. 19, no. 9, pp. 897–903, 2011.
- [30] Y. L. Wu, C. S. Lim, S. Fu et al., "Surface modifications of ZnO quantum dots for bio-imaging," *Nanotechnology*, vol. 18, no. 21, Article ID 215604, 2007.
- [31] Y. Zhang, N. Kohler, and M. Zhang, "Surface modification of superparamagnetic magnetite nanoparticles and their intracellular uptake," *Biomaterials*, vol. 23, no. 7, pp. 1553–1561, 2002.
- [32] K. M. K. Selim, Z.-C. Xing, M.-J. Choi, Y. Chang, H. Guo, and I.-K. Kang, "Reduced cytotoxicity of insulin-immobilized CdS quantum dots using PEG as a spacer," *Nanoscale Research Letters*, vol. 6, article 528, pp. 1–9, 2011.
- [33] A. K. Gupta and M. Gupta, "Cytotoxicity suppression and cellular uptake enhancement of surface modified magnetic nanoparticles," *Biomaterials*, vol. 26, no. 13, pp. 1565–1573, 2005.
- [34] M. Yamaura, R. L. Camilo, L. C. Sampaio, M. A. Macêdo, M. Nakamura, and H. E. Toma, "Preparation and characterization of (3-aminopropyl)triethoxysilane-coated magnetite nanoparticles," *Journal of Magnetism and Magnetic Materials*, vol. 279, no. 2–3, pp. 210–217, 2004.
- [35] M. Protiere and P. Reiss, "Highly luminescent Cd–ZnSe/ZnS Core/Shell nanocrystal emitting in the blue-green spectral range," *Small*, vol. 3, no. 3, pp. 468–473, 2007.
- [36] W. B. Tan and Y. Zhang, "Multifunctional quantum-dot-based magnetic chitosan nanobeads," *Advanced Materials*, vol. 17, no. 19, pp. 2375–2380, 2005.
- [37] S. S. Bale, S. J. Kwon, D. A. Shah, A. Banerjee, J. S. Dordick, and R. S. Kane, "Nanoparticle-mediated cytoplasmic delivery of proteins to target cellular machinery," *ACS Nano*, vol. 4, no. 3, pp. 1493–1500, 2010.
- [38] K. H. Bae, H. Mok, and T. G. Park, "Synthesis, characterization, and intracellular delivery of reducible heparin nanogels for apoptotic cell death," *Biomaterials*, vol. 29, no. 23, pp. 3376–3383, 2008.
- [39] K. H. Bae, C. W. Moon, Y. Lee, and T. G. Park, "Intracellular delivery of heparin complexed with chitosan-g-poly(ethylene glycol) for inducing apoptosis," *Pharmaceutical Research*, vol. 26, no. 1, pp. 93–100, 2009.
- [40] P. F. Gomes, M. P. F. Godoy, A. B. Veloso et al., "Exciton binding energy in type II quantum dots," *Physica Status Solidi B*, vol. 4, no. 2, pp. 385–388, 2007.
- [41] R. Hong, G. Han, J. M. Fernández, B.-J. Kim, N. S. Forbes, and V. M. Rotello, "Glutathione-mediated delivery and release using monolayer protected nanoparticle carriers," *Journal of the American Chemical Society*, vol. 128, no. 4, pp. 1078–1079, 2006.
- [42] Z.-F. Gan, J.-S. Jiang, and Y. Yang, "Immobilization of homing peptide on magnetite nanoparticles and its specificity in vitro," *Journal of Biomedical Materials Research A*, vol. 27, no. 1, pp. 468–476, 2008.

## Research Article

# Immobilization of Bone Morphogenetic Protein on DOPA- or Dopamine-Treated Titanium Surfaces to Enhance Osseointegration

Jeonghwa Kang,<sup>1,2</sup> Seiichi Tada,<sup>1</sup> Takashi Kitajima,<sup>1</sup> Tae Il Son,<sup>1,3</sup>  
Toshiro Aigaki,<sup>1,2</sup> and Yoshihiro Ito<sup>1,2</sup>

<sup>1</sup> Nano Medical Engineering Laboratory, RIKEN, 2-1 Hirosawa, Wako-shi, Saitama 351-0198, Japan

<sup>2</sup> Department of Biological Science, Tokyo Metropolitan University, Minami-Osawa, Tokyo 192-0938, Japan

<sup>3</sup> Department of Biotechnology and Bio-Environmental Technology (BET) Research Institute, Chung-Ang University, 40-1 San, Nae-Ri, Daeduck-myun, Ansong-si, Kyungki-do 456-756, Republic of Korea

Correspondence should be addressed to Yoshihiro Ito; [y-ito@riken.jp](mailto:y-ito@riken.jp)

Received 15 October 2013; Revised 16 November 2013; Accepted 25 November 2013

Academic Editor: Oh Hyeong Kwon

Copyright © 2013 Jeonghwa Kang et al. This is an open access article distributed under the Creative Commons Attribution License, which permits unrestricted use, distribution, and reproduction in any medium, provided the original work is properly cited.

Titanium was treated with 3,4-dihydroxy-L-phenylalanine (DOPA) or dopamine to immobilize bone morphogenetic protein-2 (BMP2), a biomolecule. DOPA and dopamine solutions turned into suspensions, and precipitates were produced at high pH. Both treatments produced a brown surface on titanium that was thicker at high pH than low pH. Dopamine produced a thicker layer than DOPA. The hydrophobicity of the surfaces increased after treatment with dopamine independent of pH. Furthermore, there were more amino groups in the layers formed at pH 8.5 than pH 4.5 in both treatments. Dopamine treatment produced more amino groups in the layer than DOPA. BMP2 was immobilized on the treated surfaces via a coupling reaction using carbodiimide. More BMP2 was immobilized on surfaces treated at pH 8.5 than pH 4.5 in both treatments. The immobilized BMP induced specific signal transduction and alkali phosphatase, a differentiation marker. Thus, the present study demonstrates that titanium treated with DOPA or dopamine can become bioactive via the surface immobilization of BMP2, which induces specific signal transduction.

## 1. Introduction

Biomedical engineering has the potential to improve the quality of human life. Chemical modification of biological signaling molecules such as cell growth factors on implants is important in clinical therapeutics. Titanium is a biocompatible implant material but does not have specific biofunctionality. The adsorption of plasma proteins onto titanium surfaces plays an essential role in implant integration. The bioactivation of implants requires the functionalization of an implant surface with signaling molecules [1–3].

The formation of new bone is required for successful outcomes in bone fracture repair and dental implants. Efficient bone formation depends on the recruitment of osteoblast precursors to the site followed by osteoblast maturation, matrix deposition, and mineralization [4, 5]. Bone morphogenetic protein-2 (BMP2) is a signaling protein known to play

important roles in the bone healing process and enhancing therapeutic efficacy [6, 7]. Therefore, coating or immobilizing BMP2 onto organic or inorganic surfaces is reported to enhance the osseointegration of materials [8–16].

Some researchers report physically coating titanium with BMP [17–19]. In addition, Kashiwagi et al. [20] prepared titanium-binding BMP using their selective titanium-binding peptide. On the other hand, in order to create stable covalent immobilization, Puleo et al. [21] performed plasma polymerization of allylamine on a titanium surface. Meanwhile, others prepared chitosan, dextran, or polymer layers on titanium to covalently immobilize BMP [22–25].

However, the covalent modification method of inorganic surfaces is limited, although there are some specific methodologies such as silane coupling. Therefore, Lee et al. [26, 27] devised a new convenient and universal method.

Underwater adhesive proteins containing 3,4-dihydroxy-*l*-phenylalanine (DOPA) from mussel protein play important roles in adhesion to various materials including polymers, metals, and ceramics. Therefore, Lee et al. hypothesized that the coexistence of catechol (i.e., DOPA) and amine (i.e., lysine) groups is crucial for achieving adhesion to a wide variety of materials. They consequently identified dopamine as a small-molecule compound that contains both functionalities and found that it is useful for the surface modification of various materials [26, 27]. Material surfaces were treated with dopamine to immobilize biological molecules including growth factors [28–34]. This dopamine treatment resulted in “polydopamine” or “melanin-like” films produced through the oxidation of dopamine or other catecholamines such as norepinephrine. Thus, this represents a very convenient and universal method for adding an organic layer to various materials including polymers, metals, and ceramics.

Meanwhile, Lai et al. [35] utilized this dopamine treatment method to conjugate BMP on titanium for the first time; the covalent conjugation was performed under alkaline conditions as suggested by Lee et al. [28]. The surface functionalization of TiO<sub>2</sub> nanotubes with BMP2 was beneficial for mesenchymal stem cell proliferation and differentiation. Their approach hints at potential applications in enhanced bone osseointegration stemming from the development of titanium-based implants.

We previously found that dopamine-treated surfaces contain amino groups that can be utilized for protein immobilization [33]. Therefore, in this study, we covalently immobilized BMP2 on dopamine-treated titanium surfaces using the amino groups. In addition to dopamine, DOPA was used for surface treatment as a link between titanium and BMP2, and the effect of BMP2 immobilization on titanium surfaces was investigated.

## 2. Materials and Methods

**2.1. Materials.** DOPA was purchased from Sigma (St. Louis, MO, USA). 3,4-Dihydroxyphenethylamine hydrochloride (dopamine) and *N*-hydroxysuccinimide (NHS) were purchased from Wako Pure Chemical Industries (Osaka, Japan). 1-Ethyl-3-(3-dimethylaminopropyl) carbodiimide hydrochloride (water-soluble carbodiimide (WSC)) was obtained from Dojindo (Kumamoto, Japan).

A glass plate (diameter, 15 mm; thickness, 1 mm) was coated by vacuum deposition with titanium (400 nm thick ( $\pm 25\%$ )) by Osaka Vacuum Industries Co. (Osaka, Japan) as previously reported [33].

Recombinant human BMP2 was purchased from R&D Systems Inc. (Minneapolis, MN, USA). Polyclonal anti-human BMP2 antibody was purchased from Abcam (Cambridge, UK). Horseradish peroxidase (HRP)-conjugated secondary antibody was obtained from Zymed (Carlsbad, CA, USA). Block Ace Powder was obtained from DS Pharma Biomedical (Sapporo, Japan).

**2.2. Solution Measurement.** Dopamine solution (2 mg/mL) was prepared in 10 mM Tris-buffer (adjusted to various

pH values). After reacting at room temperature for 24 h, ultraviolet (UV) measurement was performed. Detection was carried out on the basis of using the absorbance at 500 nm. UV measurement was performed using a JASCO V-550 (Tokyo, Japan).

**2.3. Surface Treatment.** The surfaces of the plates were washed in hexane solution, cleaned with 6 M hydrogen chloride for 10 min, rinsed twice with triple-distilled water, dried in a vacuum oven for 24 h, and cleaned photochemically using an excimer UV lamp (USHIO Inc., Tokyo, Japan) for 10 min before incubation in dopamine solution; this method was applied to completely remove C–C bonds and avoid the subsequent decomposition of organic molecules. The complete removal of organic material was confirmed by the observed decrease in the water contact angle.

Next, DOPA or dopamine treatment was performed. The cleaned plates were placed in a flask containing 2 mg/mL dopamine or DOPA solution in water (pH 4.5) or 10 mM Tris-buffer (adjusted to pH 8.5). The reaction was performed at room temperature for 24 h. The treated TiO<sub>2</sub> was rinsed in fresh water and dried in a clean vacuum oven at room temperature for 24 h.

To immobilize BMP2 on the surfaces of the plates, BMP2 solution was mixed with an aqueous solution of 50 mM WSC and 20 mM NHS. The treated plates were immersed in the mixed solution for 48 h at 4°C. After incubation, the plates were washed 3 times with phosphate-buffered saline (PBS).

**2.4. Surface Analysis.** The static water contact angles of the sample surfaces were measured at 25°C in air by a contact-angle meter (Kyowa Interface Science Co., Tokyo, Japan) based on the sessile drop method. All contact angles were determined by averaging 10 different point values measured on each dopamine-treated surface.

The thickness of the polymer was measured by an ellipsometer M-2000DI (JA Woollam Company, NE, USA) from 195 to 1,500 nm at 3 angles: 65°, 70°, and 75°. The surface roughness was analyzed by a New View 5032 apparatus (Zygo Co., Middlefield, CT, USA).

Fluorescein isothiocyanate (FITC) was used to determine the amount of amino groups on a surface. FITC solution (100  $\mu$ L, 10 mg/mL) in dimethylsulfoxide was mixed with 1 mL 0.1 M sodium bicarbonate solution (pH 9.0). The sample plate modified with DOPA or dopamine was incubated in the solution at room temperature for 1 h and subsequently rinsed 10 times with PBS. FITC was quantified by an AxioVision instrument (Zeiss, Oberkochen, Germany) with a Cool SNAP HQ camera (Photometrics, Tokyo, Japan).

Immobilized BMP2 was detected using an anti-BMP2 antibody. The plate was rinsed with PBS-Tween (PBS-T) (0.1%) and blocked by incubation in an aqueous solution of 1% nonfat milk for 30 min. The plate was subsequently incubated with an anti-BMP2 antibody (1:2,000 dilution) overnight at 4°C and washed 3 times with PBS-T (0.1%) before being incubated with an HRP-conjugated secondary antibody (1:10,000 dilution) for 1 h at room temperature. After washing 3 times with PBS-T (0.1%), a chemiluminescence

reaction was performed using an ECL Plus Western Blotting Detection System (GE Healthcare, Fairfield, CT, USA) and was observed by Light-Capture (ATTO, Tokyo, Japan).

**2.5. Cell Culture.** BRE-Luc C2C12 cells, which have a luciferase reporter gene with a BMP2-specific enhancer derived from inhibitor of differentiation (Id)1 promoter, were cultured in DMEM (Sigma, St. Louis, MO, USA) supplemented with 5% fetal bovine serum (Moregate Inc., Hamilton, Waikato, New Zealand) and 1% penicillin-streptomycin (Wako Pure Chemical Industries, Osaka, Japan) at 37°C in 95% humidified air/5% CO<sub>2</sub>. The cells were then washed with 5 mL PBS and harvested using a 0.25% trypsin solution containing 1 mM EDTA (Wako Pure Chemical Industries, Osaka, Japan) for 3 min at 37°C. Finally, the recovered cells were suspended in medium for the subsequent *in vitro* examination.

To monitor BMP signaling, the cell suspension was added to 24-well tissue culture polystyrene plates (0.5 mL/well,  $1 \times 10^5$  cells/mL) containing the samples, which were previously washed with sterilized PBS. After the cells were cultured in a 5% CO<sub>2</sub> atmosphere at 37°C for 48 h, they were washed with PBS and disrupted with lysis reagent (Promega, Madison, WI, USA). The luciferase activity in the lysate was measured using a luciferase assay reagent kit (Promega, Madison, WI, USA) with a Mithras LB940 luminescence plate reader (Berthold Technologies, Bad Wildbad, Germany). The observed activity was normalized to the protein content in the cell lysate, which was determined using a BCA protein assay kit (Pierce, Rockford, IL, USA).

As a marker of osteogenetic differentiation, alkaline phosphatase activity was measured as previously reported [36]. C2C12 cells suspension was added to 24-well tissue culture polystyrene plates (0.5 mL/well,  $5 \times 10^3$  cells/mL) containing the samples, which were previously washed with sterilized PBS. The cells were cultured in a 5% CO<sub>2</sub> atmosphere at 37°C for 10 days (changing the media every 2 days), washed with Tris-buffered saline, and disrupted with Tris-buffered saline containing 0.2% Triton X-100. The alkaline phosphatase activity was measured using the fluorescent substrate, 4-methylumbelliferyl phosphate (Sigma, St. Louis, MO, USA), with a Mithras LB940 luminescence plate reader. The observed activity was normalized to the protein content in the cell lysate, which was determined using a BCA protein assay kit.

**2.6. Statistical Analysis.** Statistical analyses were performed using Student's *t*-test for paired samples and analysis of variance for multiple samples.

### 3. Results and Discussion

**3.1. DOPA and Dopamine Treatment.** The properties of DOPA and dopamine solution were investigated on the basis of turbidity (Figure 1). Both solutions were transparent at low pH even after 24 h and turned turbid and brown at high pH. After 24 h, some precipitate was found in dopamine solution at high pH. Although the turbidity change of the DOPA

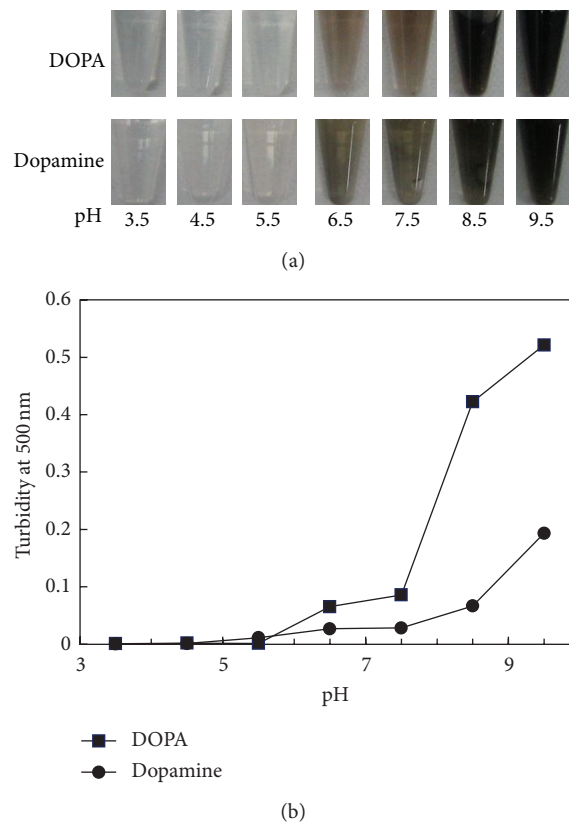


FIGURE 1: Photograph (a) and turbidity (b) of DOPA and dopamine solutions at different pH values. The turbidity data of dopamine solution are from Kang et al. [33].

solution appeared to be greater than that of dopamine, the lower turbidity was due to the precipitation of aggregated dopamine. Therefore, dopamine was considered more reactive than on DOPA.

When titanium-coated glass was treated with either DOPA or dopamine, the surface turned brown at pH 8.5 (Figure 2). The brown color was denser on dopamine-treated surfaces than DOPA-treated surfaces. In contrast, no significant color change was observed when the surfaces were treated at pH 4.5. The color change coincided with the thickness. The layer formed by DOPA was thinner than that formed by dopamine (Table 1). In the case of dopamine, the formed layer at pH 8.5 was about 28 times thicker than that formed at pH 4.5 (Table 1); in the case of DOPA, the surface was less than 5 times thicker.

However, the assessment of surface hydrophilicity on the basis of contact angle measurements revealed that the water contact angle of surfaces increased with DOPA or dopamine treatment even at pH 4.5; the contact angles on the surface were almost the same with treatment at pH 4.5 and pH 8.5 (Table 1). This indicates that the titanium surfaces were fully covered by DOPA or dopamine at pH 4.5 as described previously [33]. Therefore, the present results indicate the effect of dopamine is stronger than that of DOPA. The carboxyl group in DOPA is specifically considered to reduce the reactivity.

TABLE 1: Water contact angle and thickness of the DOPA and dopamine layers formed on titanium.

| Treatment | pH  | Water contact angle (°) | Thickness (nm) |
|-----------|-----|-------------------------|----------------|
| —         | —   | 0                       | 0              |
| DOPA      | 4.5 | 64.0 ± 1.9              | 0.676 ± 0.017  |
|           | 8.5 | 67.8 ± 1.4              | 3.225 ± 0.073  |
| Dopamine  | 4.5 | 51.4 ± 1.9              | 0.798 ± 0.073  |
|           | 8.5 | 54.7 ± 1.1              | 22.05 ± 1.048  |

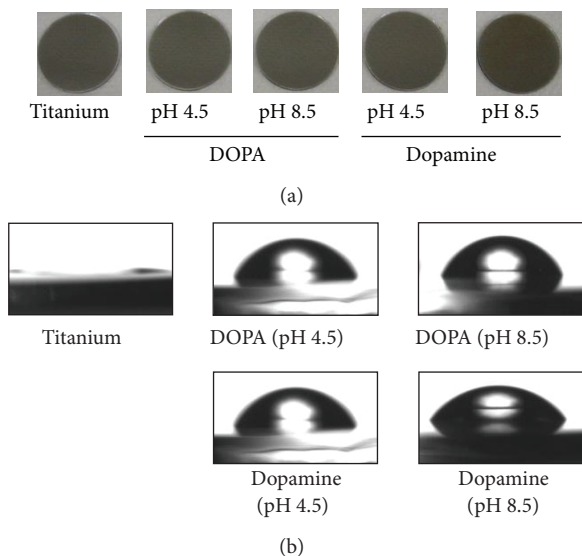


FIGURE 2: Images (a) and water contact angle (b) of DOPA- and dopamine-treated titanium.

The amount of amino groups present on DOPA- or dopamine-treated surfaces was measured using FITC (Figure 3). The amount of amino groups in the organic layer was about 3-fold greater at pH 8.5 than pH 4.5 in both treatments; the increase was greater than that of thickness. On the other hand, more amino groups were formed by dopamine than DOPA. Because the amount of amino groups did not increase linearly with increasing thickness, the carboxyl group in DOPA reacted with amino group and reduced it.

BMP2 was immobilized by WSC on both the DOPA- and dopamine-treated titanium surfaces, and the immobilization was confirmed by anti-BMP2 antibody (Figure 4). The surface was treated with the BMP2 solution in the absence of WSC and subsequently washed until no nonspecific BMP2 adsorption was detected by anti-BMP2 antibody. The same washing condition was employed for the surfaces treated in the presence of WSC. More BMP2 was immobilized on the surface treated with dopamine at pH 8.5 than pH 4.5. In addition, there was more BMP2 immobilized on the dopamine-treated surfaces than the DOPA-treated surfaces. BMP2 immobilization increased monotonously with increasing amino groups in the layer as shown in Figure 5.

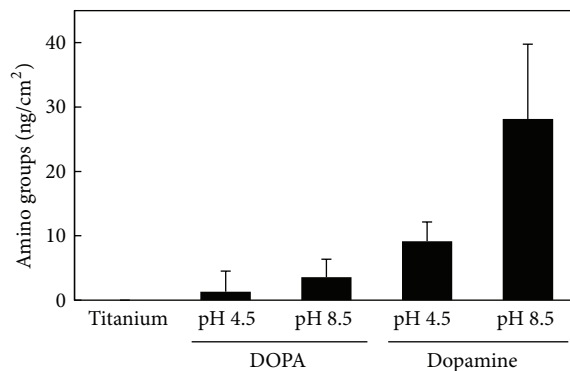


FIGURE 3: Amounts of amino groups on DOPA- and dopamine-treated titanium.

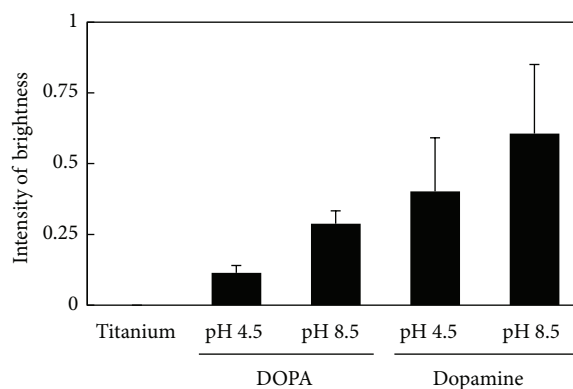


FIGURE 4: Amounts of BMP2 immobilized on DOPA- and dopamine-treated titanium.

**3.2. Biological Activity.** After confirming the immobilization of BMP2 on titanium surfaces, BRE-Luc C2C12 cells were seeded and incubated for 2 days. Id proteins act as dominant-negative inhibitors of basic helix-loop-helix transcription factors. Id and basic helix-loop-helix proteins dictate cellular programs of differentiation and proliferation in various cell types in an opposing manner. BMP2 inhibits myogenic differentiation and regulates bone formation. Id1 is strongly induced by BMP2 and is an important mediator of the inhibitory effect of BMP2 on myogenic differentiation [36, 37]. The results of luciferase activity indicate that BMP2 immobilized on titanium surfaces significantly activated the reporter gene (Figure 6). Thus, the results demonstrate that BMP2 interacts with the receptor even after immobilization. The induction on dopamine-treated and BMP2-immobilized surfaces was more enhanced than on DOPA-treated and BMP-immobilized surfaces, although the difference was not significant.

An alkaline phosphatase assay was performed on C2C12 cells cultured for 10 days on the titanium surface with immobilized BMP2 (Figure 7). These cells are usually employed to study the differentiation of myoblasts and osteoblasts. Alkaline phosphatase is a marker of bone formation; its induction indicates cell differentiation from the myoblastic to the osteoblastic lineage. Although no significant difference of cultured cells was observed by microscopy, the immobilized

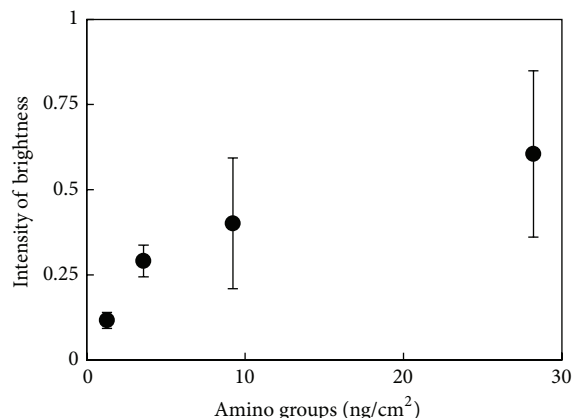


FIGURE 5: The relationship between the amino groups (from Figure 3) and immobilized BMP2 (from Figure 4).

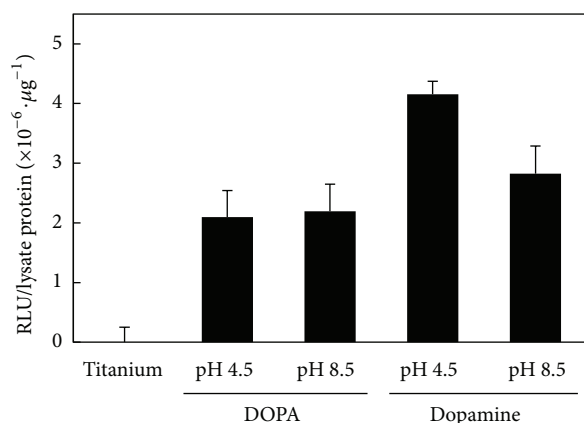


FIGURE 6: Induction of luciferase activity in BRE-Luc C2C12 cells by immobilized BMP2 on titanium.

BMP2 induced osteogenic differentiation. There was no significant difference between BMP2-immobilized surfaces.

Covalent immobilization using functional groups in BMP is categorized into amino groups and carboxyl groups. Tsujigiwa et al. [9], Park et al. [11], Schmoekel et al. [12], and Lai et al. [35] used amino groups in BMP. On the other hand, Puleo et al. [21] used carboxyl groups in BMP. In this study, we employed carboxyl groups in BMP for covalent immobilization and found a significant effect of immobilized BMP.

#### 4. Conclusions

BMP2 is covalently immobilized on dopamine-treated titanium surfaces. The immobilized BMP2 specifically interacts with myoblasts and induces osteogenic differentiation. Therefore, the present method is convenient for covalently immobilizing BMP2 while retaining its biological activity.

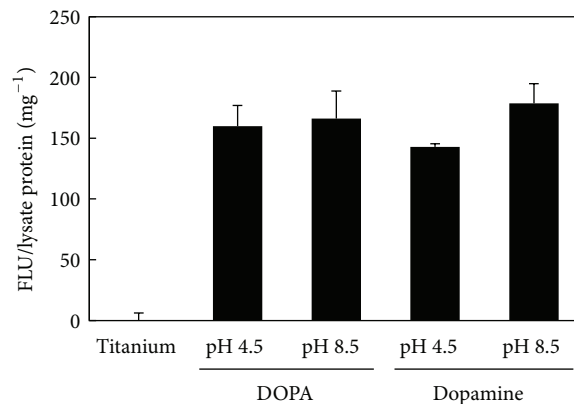


FIGURE 7: Induction of alkaline phosphatase activity in BRE-Luc C2C12 cells by immobilized BMP2 on titanium.

#### Acknowledgments

BRE-Luc C2C12 cells were kindly provided by Dr. Kiyotaka Shiba of the Cancer Institute of the JFCR. This work was supported by JSPS KAKENHI (Grant no. 22220009).

#### References

- [1] M. Bongio, J. J. P. van der Beuken, S. C. G. Leeuwenburgh, and J. A. Jansen, "Development of bone substitute materials: from "biocompatible" to "instructive," *Journal of Materials Chemistry*, vol. 20, no. 40, pp. 8747–8759, 2010.
- [2] B. Joddar and Y. Ito, "Biological modifications of materials surfaces with proteins for regenerative medicine," *Journal of Materials Chemistry*, vol. 21, no. 36, pp. 13737–13755, 2011.
- [3] D. Zhou and Y. Ito, "Inorganic material surfaces made bioactive by immobilizing growth factors for hard tissue engineering," *RSC Advances*, vol. 3, no. 28, pp. 11095–11106, 2013.
- [4] N. Jaiswal, S. E. Haynesworth, A. I. Caplan, and S. P. Bruder, "Osteogenic differentiation of purified, culture-expanded human mesenchymal stem cells in vitro," *Journal of Cellular Biochemistry*, vol. 64, no. 2, pp. 295–312, 1997.
- [5] L. X. Bi, D. J. Simmons, and E. Mainous, "Expression of BMP-2 by rat bone marrow stromal cells in culture," *Calcified Tissue International*, vol. 64, no. 1, pp. 63–68, 1999.
- [6] N. Nishii, M. Arai, N. Yanai, A. Togari, and T. Nakabayashi, "Effect of bone morphogenetic protein-2 (BMP-2) or troglitazone, as an inducer of osteogenic cells or adipocytes, on differentiation of a bone marrow mesenchymal progenitor cell line established from temperature-sensitive (ts) simian virus (SV) 40 T-antigen gene transgenic mice," *Biological and Pharmaceutical Bulletin*, vol. 32, no. 1, pp. 10–17, 2009.
- [7] W. K. Hsu, O. Sugiyama, S. H. Park et al., "Lentiviral-mediated BMP-2 gene transfer enhances healing of segmental femoral defects in rats," *Bone*, vol. 40, no. 4, pp. 931–938, 2007.
- [8] V. Karageorgiou, L. Meinel, S. Hofmann, A. Malhotra, V. Volloch, and D. Kaplan, "Bone morphogenetic protein-2 decorated silk fibroin films induce osteogenic differentiation of human bone marrow stromal cells," *Journal of Biomedical Materials Research A*, vol. 71, no. 3, pp. 528–537, 2004.
- [9] H. Tsujigiwa, H. Nagatsuka, M. Gunduz et al., "Effects of immobilized recombinant human bone morphogenetic protein-2/succinylated type I atelocollagen on cellular activity of ST2

- cells," *Journal of Biomedical Materials Research A*, vol. 75, no. 1, pp. 210–215, 2005.
- [10] B. Han, N. Perelman, B. Tang, F. Hall, E. C. Shors, and M. E. Nimmi, "Collagen-targeted BMP3 fusion proteins arrayed on collagen matrices or porous ceramics impregnated with type I collagen enhance osteogenesis in a rat cranial defect model," *Journal of Orthopaedic Research*, vol. 20, no. 4, pp. 747–755, 2002.
  - [11] Y. J. Park, K. H. Kim, J. Y. Lee et al., "Immobilization of bone morphogenetic protein-2 on a nanofibrous chitosan membrane for enhanced guided bone regeneration," *Biotechnology and Applied Biochemistry*, vol. 43, no. 1, pp. 17–24, 2006.
  - [12] H. G. Schmoekel, F. E. Weber, J. C. Schense, K. W. Grätz, P. Schawwalder, and J. A. Hubbell, "Bone repair with a form of BMP-2 engineered for incorporation into fibrin cell ingrowth matrices," *Biotechnology and Bioengineering*, vol. 89, no. 3, pp. 253–262, 2005.
  - [13] U. Edlund, S. Danmark, and A. Albertsson, "A strategy for the covalent functionalization of resorbable polymers with heparin and osteoinductive growth factor," *Biomacromolecules*, vol. 9, no. 3, pp. 901–905, 2008.
  - [14] H. Shen, X. Hu, F. Yang, J. Bei, and S. Wang, "The bioactivity of rhBMP-2 immobilized poly(lactide-co-glycolide) scaffolds," *Biomaterials*, vol. 30, no. 18, pp. 3150–3157, 2009.
  - [15] A. Schuessle, H. Mayr, J. Tessmar, and A. Goepferich, "Enhanced bone morphogenetic protein-2 performance on hydroxyapatite ceramic surfaces," *Journal of Biomedical Materials Research A*, vol. 90, no. 4, pp. 959–971, 2009.
  - [16] F. R. Kloss, R. Gassner, J. Preiner et al., "The role of oxygen termination of nanocrystalline diamond on immobilisation of BMP-2 and subsequent bone formation," *Biomaterials*, vol. 29, no. 16, pp. 2433–2442, 2008.
  - [17] M. Wiemann, H. P. Jennissen, H. Rumpf et al., "A reporter-cell assay for the detection of BMP-2 immobilized on porous and nonporous materials," *Journal of Biomedical Materials Research*, vol. 62, no. 1, pp. 119–127, 2002.
  - [18] H. Schliephake, A. Aref, D. Scharnweber, S. Bierbaum, S. Roessler, and A. Sewing, "Effect of immobilized bone morphogenic protein 2 coating of titanium implants on peri-implant bone formation," *Clinical Oral Implants Research*, vol. 16, no. 5, pp. 563–569, 2005.
  - [19] J. Hall, R. G. Soransen, J. M. Wozney, and U. M. E. Wikesjö, "Bone formation at rhBMP-2-coated titanium implants in the rat ectopic model," *Journal of Clinical Periodontology*, vol. 34, no. 5, pp. 444–451, 2007.
  - [20] K. Kashiwagi, T. Tsuji, and K. Shiba, "Directional BMP-2 for functionalization of titanium surfaces," *Biomaterials*, vol. 30, no. 6, pp. 1166–1175, 2009.
  - [21] D. A. Puleo, R. A. Kissling, and M.-S. Sheu, "A technique to immobilize bioactive proteins, including bone morphogenetic protein-4 (BMP-4), on titanium alloy," *Biomaterials*, vol. 23, no. 9, pp. 2079–2087, 2002.
  - [22] T. Y. Lim, W. Wang, Z. Shi, C. K. Poh, and K. G. Neoh, "Human bone marrow-derived mesenchymal stem cells and osteoblast differentiation on titanium with surface-grafted chitosan and immobilized bone morphogenetic protein-2," *Journal of Materials Science*, vol. 20, no. 1, pp. 1–10, 2009.
  - [23] Z. L. Shi, K. G. Neoh, E. T. Kang, K. P. Chye, and W. Wang, "Surface functionalization of titanium with carboxymethyl chitosan and immobilized bone morphogenetic protein-2 for enhanced osseointegration," *Biomacromolecules*, vol. 10, no. 6, pp. 1603–1611, 2009.
  - [24] Z. Shi, K. G. Neoh, E. Kang, C. Poh, and W. Wang, "Titanium with surface-grafted dextran and immobilized bone morphogenetic protein-2 for inhibition of bacterial adhesion and enhancement of osteoblast functions," *Tissue Engineering A*, vol. 15, no. 2, pp. 417–426, 2009.
  - [25] C. Lorenz, A. Hoffmann, G. Gross et al., "Coating of titanium implant materials with thin polymeric films for binding the signaling protein BMP2," *Macromolecular Bioscience*, vol. 11, no. 2, pp. 234–244, 2011.
  - [26] H. Lee, S. M. Dellatore, W. M. Miller, and P. B. Messersmith, "Mussel-inspired surface chemistry for multifunctional coatings," *Science*, vol. 318, no. 5849, pp. 426–430, 2007.
  - [27] C. E. Brubaker and P. B. Messersmith, "The present and future of biologically inspired adhesive interfaces and materials," *Langmuir*, vol. 28, no. 4, pp. 2200–2205, 2012.
  - [28] H. Lee, J. Rho, and P. B. Messersmith, "Facile conjugation of biomolecules onto surfaces via mussel adhesive protein inspired coatings," *Advanced Materials*, vol. 21, no. 4, pp. 431–434, 2009.
  - [29] C. K. Poh, Z. Shi, T. Y. Lim, K. G. Neoh, and W. Wang, "The effect of VEGF functionalization of titanium on endothelial cells in vitro," *Biomaterials*, vol. 31, no. 7, pp. 1578–1585, 2010.
  - [30] Y. B. Lee, Y. M. Shin, J. H. Lee et al., "Polydopamine-mediated immobilization of multiple bioactive molecules for the development of functional vascular graft materials," *Biomaterials*, vol. 33, no. 33, pp. 8343–8352, 2012.
  - [31] K. K. Yang, J. S. Lee, J. J. Kim et al., "Polydopamine-mediated surface modification of scaffold materials for human neural stem cell engineering," *Biomaterials*, vol. 33, no. 29, pp. 6952–6964, 2012.
  - [32] Y. M. Shin, Y. B. Lee, S. J. Kim et al., "Mussel-inspired immobilization of vascular endothelial growth factor (VEGF) for enhanced endothelialization of vascular grafts," *Biomacromolecules*, vol. 13, no. 7, pp. 2020–2028, 2012.
  - [33] J. Kang, M. Sakuragi, A. Shibata et al., "Immobilization of epidermal growth factor on titanium and stainless steel surfaces via dopamine treatment," *Materials Science and Engineering C*, vol. 32, no. 8, pp. 2552–2561, 2012.
  - [34] B. Joddar, A. Albayrak, J. Kang, M. Nishihara, H. Abe, and Y. Ito, "Sustained delivery of siRNA from dopamine-coated stainless steel surfaces," *Acta Biomaterialia*, vol. 9, no. 5, pp. 6753–6761, 2013.
  - [35] M. Lai, K. Cai, L. Zhao, X. Chen, Y. Hou, and Z. Yang, "Surface functionalization of TiO<sub>2</sub> nanotubes with bone morphogenetic protein 2 and its synergistic effect on the differentiation of mesenchymal stem cells," *Biomacromolecules*, vol. 12, no. 4, pp. 1097–1105, 2011.
  - [36] T. Mazaki, T. Kitajima, Y. Shiozaki et al., "In vitro and in vivo enhanced osteogenesis by kaempferol found by a high-throughput assay using human mesenchymal stromal cells," *Journal of Functional Foods*, 2013.
  - [37] O. Korchynskiy and P. Ten Dijke, "Identification and functional characterization of distinct critically important bone morphogenetic protein-specific response elements in the Id1 promoter," *Journal of Biological Chemistry*, vol. 277, no. 7, pp. 4883–4891, 2002.

## Research Article

# Fabrication of Microfibrous and Nano-/Microfibrous Scaffolds: Melt and Hybrid Electrospinning and Surface Modification of Poly(L-lactic acid) with Plasticizer

Young Il Yoon,<sup>1</sup> Ko Eun Park,<sup>1</sup> Seung Jin Lee,<sup>2</sup> and Won Ho Park<sup>1</sup>

<sup>1</sup> Department of Advance Organic Materials and Textile System Engineering, Chungnam National University, Daejeon 305-764, Republic of Korea

<sup>2</sup> College of Pharmacy, Ewha Womans University, Seoul 120-750, Republic of Korea

Correspondence should be addressed to Won Ho Park; parkwh@cnu.ac.kr

Received 9 October 2013; Accepted 2 November 2013

Academic Editor: Yoshihiro Ito

Copyright © 2013 Young Il Yoon et al. This is an open access article distributed under the Creative Commons Attribution License, which permits unrestricted use, distribution, and reproduction in any medium, provided the original work is properly cited.

Biodegradable poly(L-lactic acid) (PLA) fibrous scaffolds were prepared by electrospinning from a PLA melt containing poly(ethylene glycol) (PEG) as a plasticizer to obtain thinner fibers. The effects of PEG on the melt electrospinning of PLA were examined in terms of the melt viscosity and fiber diameter. Among the parameters, the content of PEG had a more significant effect on the average fiber diameter and its distribution than those of the spinning temperature. Furthermore, nano-/microfibrous silk fibroin (SF)/PLA and PLA/PLA composite scaffolds were fabricated by hybrid electrospinning, which involved a combination of solution electrospinning and melt electrospinning. The SF/PLA (20/80) scaffolds consisted of a randomly oriented structure of PLA microfibers (average fiber diameter = 8.9  $\mu\text{m}$ ) and SF nanofibers (average fiber diameter = 820 nm). The PLA nano-/microfiber (20/80) scaffolds were found to have similar pore parameters to the PLA microfiber scaffolds. The PLA scaffolds were treated with plasma in the presence of either oxygen or ammonia gas to modify the surface of the fibers. This approach of controlling the surface properties and diameter of fibers could be useful in the design and tailoring of novel scaffolds for tissue engineering.

## 1. Introduction

Electrospinning from melt is an attractive solvent-free manufacturing process for tissue engineering scaffolds [1]. Melt electrospinning has inherent advantages, such as cleaner processing with environmental safety and higher productivity (with lower production cost) due to the absence of solvent. In addition, melt electrospinning is particularly attractive for its applicability to commodity polymers, such as polypropylene and polyethylene, which are only soluble in limited solvents and require high temperature for dissolution [2–7]. However, a polymer melt has higher viscosity than the solution state, which usually generates thicker micron-sized fibers than those of solution electrospinning. In addition, the tendency of the polymer to solidify as it flows out of a nozzle hinders the stretching of the polymer jet, thus resulting in microfibers [8].

In order to fabricate thinner fibers via melt electrospinning, the viscosity of a polymer melt should be reduced by

adjusting the processing parameters or polymer parameters. Important parameters reported for melt electrospinning are the molecular weight, tacticity, melting point of the polymer, electric field strength, distance from the nozzle, mass flow rate, and process temperatures (electrospinning temperature, heating chamber temperature) [9–13]. Detta et al. [14] melt electrospun a novel blend of a high molecular weight polymer, poly( $\epsilon$ -caprolactone), with a low molecular weight polymer, poly(ethylene glycol)-*block*-poly( $\epsilon$ -caprolactone). It was noted that the diameter of the fiber obtained was in the micron range and was directly related to the mass flow rate. Dalton et al. [9] employed a viscosity-reducing additive to reduce the diameter of fiber electrospun from the polymer melt. They found that the additive reduces the average chain length and thus reduces the viscosity of the polymer solution and, with it, the fiber diameter.

Nanofibrous structures produced by electrospinning (with nanosized fiber diameter, appropriate pore size, and

high surface area) are very useful in the design of scaffolds for tissue engineering via higher cell absorption on a material. Melt electrospinning can be a better technology for fibrous scaffolds, because it avoids toxic solvents. Several polymers to date have been melt electrospun into microfibrillar scaffolds for tissue engineering applications [15–17]. Poly(lactic acid) (PLA) is one of the most widely used synthetic polymers in biomedical applications. PLA has been widely used in the areas of surgical suture, implant materials, drug carriers, and scaffolds for tissue engineering [18, 19]. However, PLA has poor hydrophilicity, and no natural cell recognition sites exist on its surface [20].

This study examined the melt- and hybrid electrospinning of PLA, which is a promising biomaterial for scaffolds with good biocompatibility and biodegradability. To this end, a plasticizer additive for the PLA melt was used to reduce the viscosity of the polymer melt and decrease the fiber diameter. Also, the effects of the processing parameters, such as spinning (syringe) temperature ( $T_s$ ), mass flow rate ( $Q$ ), and heating chamber temperature (atmospheric temperature), were investigated. In addition, the melt- and hybrid electrospun PLA fibers were treated with oxygen or ammonia plasma in order to improve their surface hydrophilicity. Changes in the surface characteristics, including the hydrophilicity and chemical composition, were investigated using contact angle measurement, moisture content, and X-ray photoelectron spectroscopy.

## 2. Materials and Methods

**2.1. Materials.** PLA ( $M_v = 70,000$ ) with  $L$  content >95% was supplied by Huvis Co., Korea. PEG ( $M_n = 2,000$ ) was purchased from Yakuri Pure Chemicals Co., Japan, and used as received. Raw 12-denier silk fibers (*B. mori*) were supplied by Daejeon Sangsa Co., Korea, and silk fibroin (SF) was regenerated according to the methods in a previous study [21]. Dimethyl formamide (DMF), chloroform, and 1,1,1,3,3,3-hexafluoro-2-propanol (HFIP) were purchased from Sigma-Aldrich Co., USA, and used without further purification.

**2.2. Melt- and Hybrid Electrospinning.** Figure 1 shows a schematic diagram of the hybrid electrospinning apparatus (Nano NC, Korea). The spinneret for melt electrospinning consisted of a stainless steel tube capable of oil circulation and a glass syringe placed inside the stainless steel tube. The temperature of the glass syringe was controlled using an oil circulator with a temperature controller. In the melt electrospinning process, PLA microfibers were prepared by electrospinning a PLA melt at temperatures ranging from 185 to 225°C and were collected on a target drum at a distance of 8 cm from the syringe tip (21 G, 0.495 mm). A voltage of 21 kV was applied to the collecting target using a high-voltage power supply (Chungpa EMT, CPS-40K03), and the mass flow rate of the melt was varied from 0.65 to 5.40 mL/h using a syringe pump (KD Scientific, Model 100). The atmosphere temperature in the heating chamber was controlled in the range from 25 to 65°C.

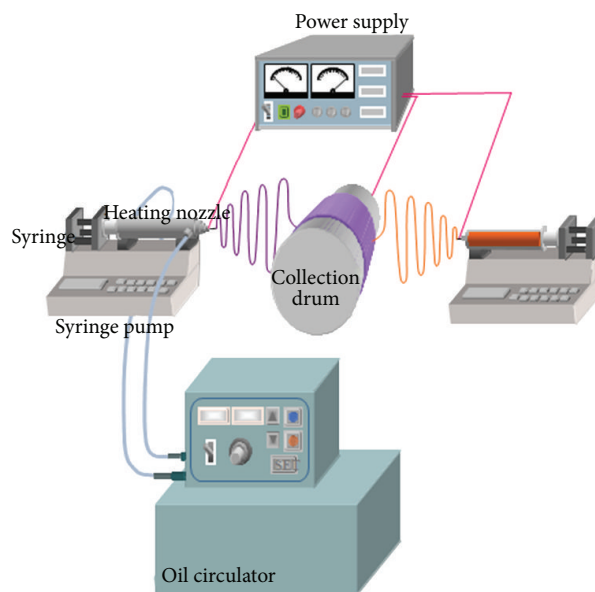


FIGURE 1: Schematic diagram of the hybrid electrospinning apparatus.

In the solution electrospinning compartment, the PLA and SF nanofibers were prepared by electrospinning a PLA solution (14 wt%) in chloroform/DMF (5/1, v/v) and an SF solution (7 wt%) in HFIP, respectively. The nanofibers were collected on a target drum placed 5 cm from the syringe tip (21 G). A voltage of 8 kV was applied to the collecting target by a high-voltage power supply, and the flow rate of the solution was 4 mL/h.

For the PLA/PLA or SF/PLA nano-/microfiber composite scaffolds, a PLA solution (14 wt%) and SF solution (7 wt%) and PLA melt were electrospun simultaneously in opposite directions facing the rotating target. The compositions (10/90, 20/80, 30/70, w/w) of the nano-/microfiber composite scaffold were controlled by adjusting the mass flow rate of the PLA melt from 0.65 to 5.40 mL/h at a fixed flow rate of the solution (4 mL/h). The melt- and hybrid electrospinning conditions for PLA microfibrillar and nano-/microfibrillar scaffolds are summarized in Table 1.

**2.3. Plasma Treatment.** Plasma treatment is known to be an environmentally friendly process to improve the surface hydrophilicity of polymer scaffolds. The  $O_2$  or  $NH_3$  plasma treatments were carried out with the melt electrospun PLA or hybrid electrospun PLA/PLA fibers in a chamber (36 cm × 25 cm × 15 cm) connected to a two-stage rotary pump via a liquid nitrogen cold trap with a base pressure of  $4 \times 10^{-3}$  mbar. An L-S matching unit was used to minimize the standing wave ratio (SWR) of the power transmitted from the 13.56 MHz radio frequency generator. Prior to each plasma treatment, the chamber was cleaned using 50 W air plasma for 30 min. A piece of the PLA fibers was then placed at the center of the chamber, followed by evacuation to the base pressure.  $O_2$  or  $NH_3$  gases were admitted into the system through a needle valve at a pressure of 0.2 mbar, and

TABLE 1: Melt- and hybrid electrospinning conditions of PLA microfibers and PLA composite fibers.

| Sample                            | PEG content (wt%) | Melt electrospinning |           |            |        |          | Solution electrospinning |          |            |        |          |
|-----------------------------------|-------------------|----------------------|-----------|------------|--------|----------|--------------------------|----------|------------|--------|----------|
|                                   |                   | $T_s$ (°C)           | Q (mL/h)  | $D_n$ (mm) | V (kV) | TCD (cm) | $T_s$ (°C)               | Q (mL/h) | $D_n$ (mm) | V (kV) | TCD (cm) |
| PLA microfiber                    | 0~20              | 215                  | 0.65~5.40 | 0.495      | 21     | 8        |                          |          |            |        |          |
| PLA/PLA (20/80) Nano-/microfibers | 10                | 215                  | 1.12      | 0.495      | 21     | 8        | 25                       | 4        | 0.495      | 10     | 5        |
| SF/PLA (20/80) Nano-/microfibers  | 10                | 215                  | 1.12      | 0.495      | 21     | 8        | 25                       | 4        | 0.495      | 10     | 5        |

$T_s$ : spinning temperature.

Q: mass flow rate.

$D_n$ : needle diameter.

V: applied voltage.

TCD: tip to collector distance.

the electrical discharge was initiated. To detect the effect of plasma gas on the PLA fiber, the plasma treatment was carried out under the conditions for 0–300 sec with O<sub>2</sub> gas and for 0–60 sec with NH<sub>3</sub> gas, respectively. Upon the completion of surface modification, the gas feed was turned off and the chamber was vented to the atmosphere. All plasma treatments were carried out at room temperature (22 ± 1 °C).

**2.4. Moisture Content.** The moisture content of the melt electrospun PGA microfibers and hybrid electrospun composite fibers (200 mg) was determined by immersing the fibers in distilled water for 1 h at room temperature [22]. The hydrated samples were then taken out and immediately weighed after removing the surface water with filter paper. The water content (WC, %) was calculated as follows:  $WC(\%) = (W - W_0)/W_0 \times 100$ , where  $W_0$  and  $W$  denote the weight of the sample before and after immersion in water for 1 h, respectively.

**2.5. Measurements and Characterization.** The melt viscosity was measured using a rheometer (ARES, Rheometrics, USA) with a shear rate of 10 rad/sec from 150 to 210 °C. The morphology of electrospun PLA fibers was observed by field emission scanning electron microscopy (FE-SEM, JSM-7000F, JEOL, Japan). Prior to the observations, the samples were coated with platinum by ion sputtering for a few seconds. The average fiber diameter and diameter distribution were obtained by analyzing the SEM images with a custom-code image analysis program (Scope Eye II, Korea). The porosity and pore parameters in the interfiber region of PLA fibers were determined using a mercury intrusion technique with an AutoPore III mercury porosimeter (Micromeritics Instrument, Norcross, GA, USA). Differential scanning calorimetry (DSC) was conducted using a TA instruments 2920 (duPont Co.). Samples were heated from 20 °C to 200 °C at a rate of 10 °C/min (first heating) and held at the final temperature for 1 min to eliminate the thermal history applied to the samples. After cooling to -100 °C, they were then reheated to 200 °C at a rate of 10 °C/min (second heating). The glass transition temperature ( $T_g$ ), melting temperature ( $T_m$ ), and cold crystallization temperature ( $T_c$ ) were obtained from the second run. The mechanical

properties of the electrospun PLA scaffolds were measured using an Instron tensile tester (Instron 8511, Canton, MA, USA) at a crosshead speed of 5 mm/min. The samples were prepared using the D-638-5 ASTM method and tested at 25 °C and 50% humidity ( $n = 10$ ). The contact angle of water droplets on the samples was measured using a DSA100 Drop Shape Analyzer System (KRÜSS, Germany). Deionized water was used, and ten independent measurements were averaged. The surface chemical composition of PLA fibers was investigated before and after plasma treatment using X-ray photoelectron spectroscopy (XPS). XPS spectra of the plasma-treated samples were acquired on an ESCALAB 250 XPS spectrometer (VG Scientific, USA).

### 3. Results and Discussion

**3.1. Effect of Plasticizer on the Thermal Properties of PLA.** The melt electrospinning process is strongly affected by the viscosity of the polymer melt, which is strongly dependent on the temperature for thermoplastic polymers. Therefore, it is important to examine the melt viscosity of a polymer in the temperature range of possible processing. Figure 2 shows the change in melt viscosity of PLA with temperature and PEG plasticizer content. The melt viscosity of neat PLA was 5,300 Poise at 185 °C and gradually decreased to 500 Poise with increasing PEG content up to 20 wt%. The melt viscosities of PLA samples decreased gradually with increasing temperature from 185 to 225 °C. The difference in melt viscosity between 185 °C and 225 °C was approximately 3 times, compared with the neat PLA sample, and the differences were narrower with increasing PEG content up to 20 wt%. To investigate the efficiency of the PEG on PLA, DSC was carried out using the PLA blends with different PEG content up to 20 wt%. Figure 3 shows the DSC thermograms obtained from a second heating for PLA/PEG blends. A gradual depression of the glass transition temperature ( $T_g$ ) from 50 to 25 °C was observed with increasing PEG content. Effective plasticization induces the depression of the glass transition temperature in the polymer/plasticizer system. Therefore, PEG was expected to be compatible with PLA. The cold crystallization temperature ( $T_c$ ) of PLA was lower than

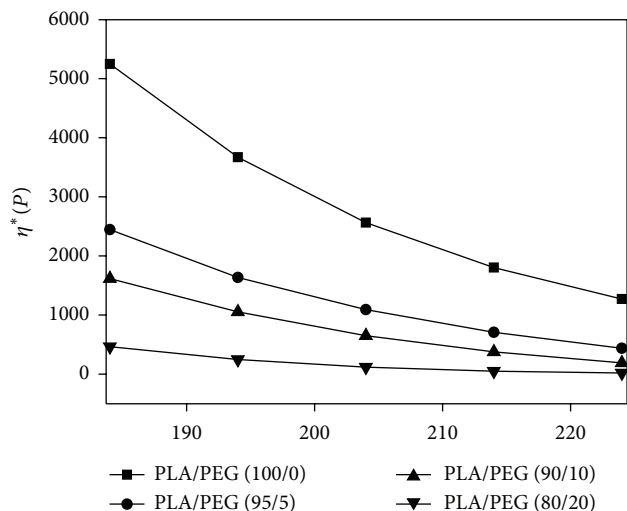


FIGURE 2: Melt viscosity of PLA containing plasticizer (PEG) as a function of temperature.

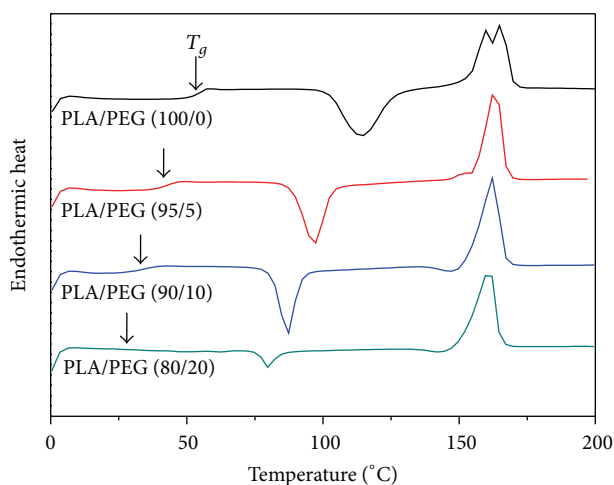


FIGURE 3: DSC thermograms obtained from a second heating for PLA/PEG blends.

that of neat PLA, while the melting temperatures ( $T_m$ ) were nearly unchanged.

**3.2. Effect of Plasticizer on the Diameter of Melt Electrospun PLA Fibers.** Figure 4 shows representative SEM images of the melt electrospun PLA fibers with different PEG contents at syringe temperatures of 215°C. The average diameter and deviation of electrospun PLA fibers decreased significantly from  $24.7 \pm 3.8$  to  $8.97 \pm 1.63$  by adding 5% of PEG (Figures 4(a)-4(b)), but a slight decrease was observed when further increasing PEG contents from 5% to 20% (Figures 4(b)-4(d)). This seems to be associated with the change in viscosity of PLA melt containing PEG plasticizer, as shown in Figure 2. Therefore, it was found that the plasticizer content is a critical parameter affecting the fiber diameter and morphology.

**3.3. Effect of Atmospheric Temperature on the Diameter of Melt Electrospun PLA Fibers.** The atmospheric temperature

determined from the glass transition region of neat PLA was varied from 25 to 65°C in order to investigate its effect on the fiber diameter of melt electrospun PLA fibers. Figure 5 shows the change in the average diameter of PLA fibers with different PEG contents as a function of atmospheric temperature. The average diameter of PLA fibers and its standard deviation were decreased with increasing PEG content. Particularly, the addition of 5 wt% PEG to PLA induced a dramatic decrease in the average fiber diameter of PLA fibers. However, the effect of atmospheric temperature ranging from 25 to 65°C on the average diameter of PLA fibers was not significant.

**3.4. Effect of Mass Flow Rate on the Diameter of Melt Electrospun PLA Fibers.** In a previous study [23], the effects of processing parameters on the average diameter and morphology of melt electrospun PLGA fibers were examined. Among the processing parameters, the mass flow rate had the most influence on the fiber diameter of PLGA. Figure 6(a) shows representative SEM images of the melt electrospun PLA fibers containing 10 wt% PEG at different mass flow rates of 5.40, 2.54, 1.12, and 0.65 mL/h. The average diameter (and standard deviation) of the PLA fibers decreased significantly by about half with decreasing mass flow rate from 5.4 to 0.65 mL/h. Figure 6(b) shows the change in the fiber diameter of PLA with different mass flow rates under fixed spinning conditions. Interestingly, the average fiber diameter and its deviation decreased significantly with decreasing mass flow rate from 5.40 to 0.65 mL/h. This significant decrease in the fiber diameter at the lower mass flow rate may have been due to the formation of a smaller Taylor cone due to the decreased volume supplied from the polymer melt. In contrast, the fiber diameter was not influenced significantly by the flow rate in solution electrospinning.

**3.5. PLA Composite Fibers from Hybrid Electrospinning.** To fabricate a randomly mixed and interconnected network structure between the nanofibers and microfibers, a novel hybrid electrospinning process was designed, combining melt electrospinning with solution electrospinning [24]. This hybrid electrospinning could provide a randomly mixed nano-/microfibrous composite scaffold with higher pore diameters by simultaneous electrospinning. Figure 7 shows SEM images of the PLA/PLA (20/80) and SF/PLA (20/80) nano-/microfiber composite scaffolds fabricated using PLA and SF solution and PLA melt under fixed electrospinning conditions. The PLA/PLA (20/80) and SF/PLA (20/80) nanofiber/microfiber composite scaffolds were fabricated using 14 wt% PLA and 7 wt% SF solution in the solution electrospinning compartment, respectively. In order to vary the composition of the nanofiber/microfiber composite scaffolds, the change in mass flow rate of the PLA melt was feasible and desirable because it is difficult to obtain a desired composition of nano-/microfiber scaffolds by changing the flow rate of the polymer solution. As shown in Figure 7, the PLA microfibers in nano-/microfiber composite scaffolds had a larger average diameter of  $8.86 \pm 0.25 \mu\text{m}$ , whereas PLA and SF nanofibers had smaller average diameters of  $1260 \pm 230 \text{ nm}$

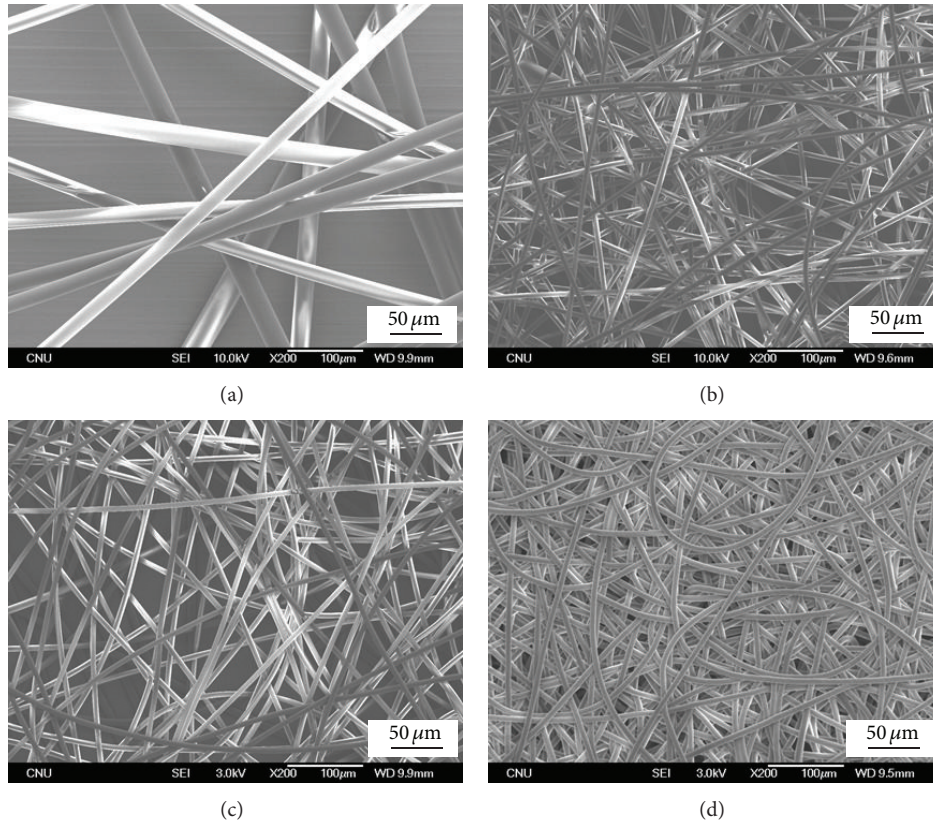


FIGURE 4: SEM images of the melt electrospun PLA fibers with different PEG contents: (a) PLA/PEG (100/0), (b) PLA/PEG (95/5), (c) PLA/PEG (90/10), and (d) PLA/PEG (80/20).

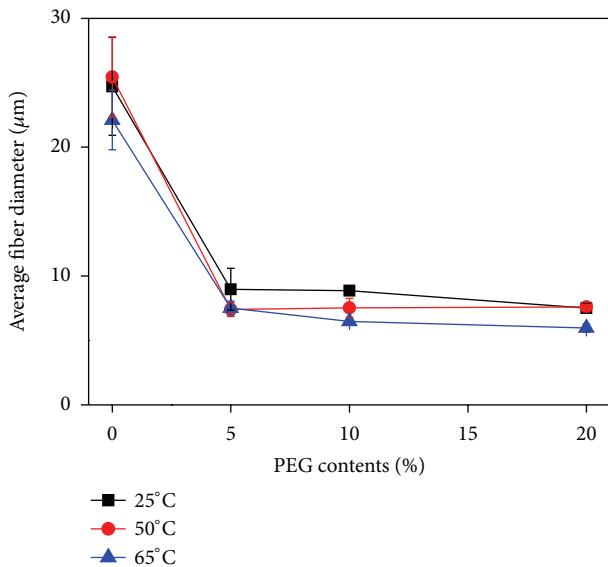


FIGURE 5: Change in the average diameter of PLA fibers with different PEG contents as a function of atmosphere temperature.

and  $820 \pm 240$  nm, respectively. The difference in average fiber diameters between the nanofibers and microfibers was approximately one order of magnitude.

The pore parameter (pore size, porosity) of the scaffolds is a crucial factor affecting the cell attachment, spreading, and migration. Table 2 summarizes the pore parameters of the PLA microfibers and PLA nano-/microfiber (20/80) composite scaffolds determined by mercury porosimetry. The porosities of the PLA/PLA and SF/PLA nano-/microfiber (20/80) composite scaffolds were 91.6% and 95.0%, respectively, indicating high porosity. The total pore volumes of PLA/PLA and SF/PLA samples were 9.9 mL/g and 6.4 mL/g, respectively. In contrast, the porosity and pore volume of the PLA microfiber scaffolds were 94.2% and 13.3 mL/g, respectively. The average pore diameters (APD) in terms of the volumes ( $V$ ) of the PLA/PLA nano-/microfiber (20/80) composite scaffold and PLA microfibrous scaffold were  $34.5 \mu\text{m}$  and  $44.7 \mu\text{m}$ , respectively. This decrease in pore diameter of the PLA/PLA composite scaffold might be due to the introduction of a small amount of nanofibers (20 wt%). However, a pore size of approximately  $40 \mu\text{m}$  is large enough to allow cells to freely migrate in many cases [25].

The mechanical properties of the PLA microfibers and PLA-based nano-/microfiber composite scaffold were assessed using a tensile test. The maximum load value of the PLA scaffolds was evaluated. Table 2 shows the tensile strength and breaking elongation of the PLA microfibers and PLA composite scaffolds. The PLA/PLA (20/80) nano-/microfiber composite scaffold had higher tensile strength ( $26.8 \text{ gf/mm}^2$ ) and modulus ( $2.7 \text{ gf/mm}^2$ ) than

TABLE 2: Pore parameters and mechanical properties of the PLA microfibers and nano-/microfiber (20/80) composite scaffolds.

| Sample                               | Pore properties |                       |         | Mechanical properties                        |                      |                                     |
|--------------------------------------|-----------------|-----------------------|---------|--|----------------------|-------------------------------------|
|                                      | TIV (mL/g)      | APD ( $\mu\text{m}$ ) | $P$ (%) | Tensile strength ( $\text{gf}/\text{mm}^2$ ) | Elongation break (%) | Modulus ( $\text{gf}/\text{mm}^2$ ) |
| PLA microfiber                       | 13.3            | 44.7                  | 94.2    | $1.5 \pm 0.2$                                | $46.1 \pm 6.5$       | $0.3 \pm 0.04$                      |
| PLA/PLA (20/80)<br>Nano-/microfibers | 9.9             | 34.5                  | 91.6    | $26.8 \pm 13.6$                              | $20.6 \pm 2.9$       | $2.7 \pm 0.4$                       |
| SF/PLA (20/80)<br>Nano-/microfibers  | 6.4             | 39.2                  | 95.0    | $20.6 \pm 3.6$                               | $11.0 \pm 1.5$       | $2.1 \pm 0.4$                       |

TIV: total intrusion volume.  
 APD: average pore diameter.  
 $P$ : porosity.

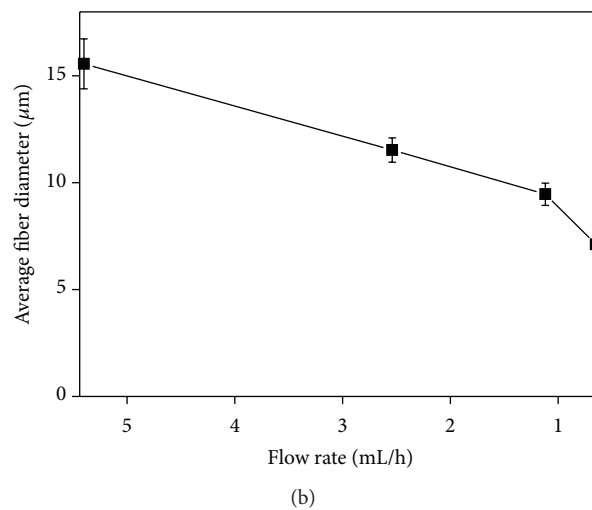
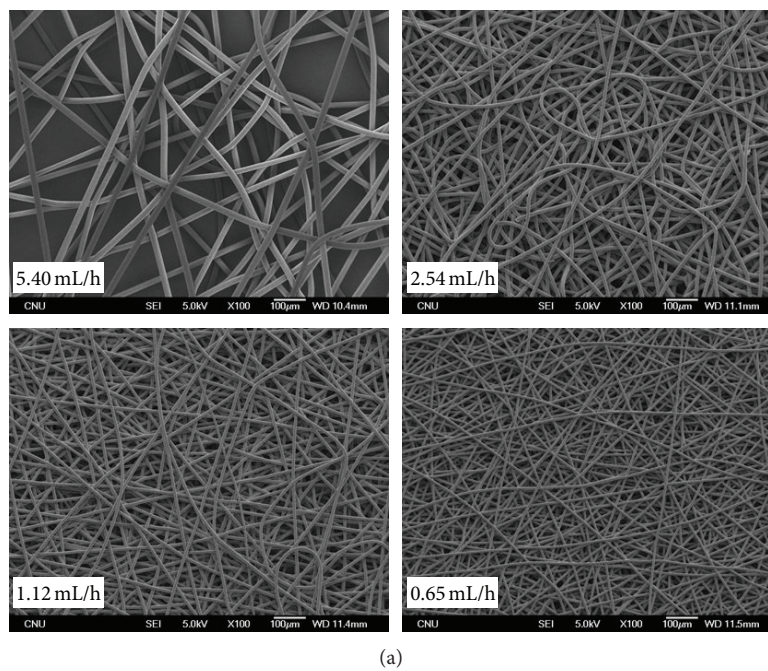


FIGURE 6: (a) SEM images and (b) change in the fiber diameter of the melt electrospun PLA fibers containing 10 wt% PEG at different mass flow rates.

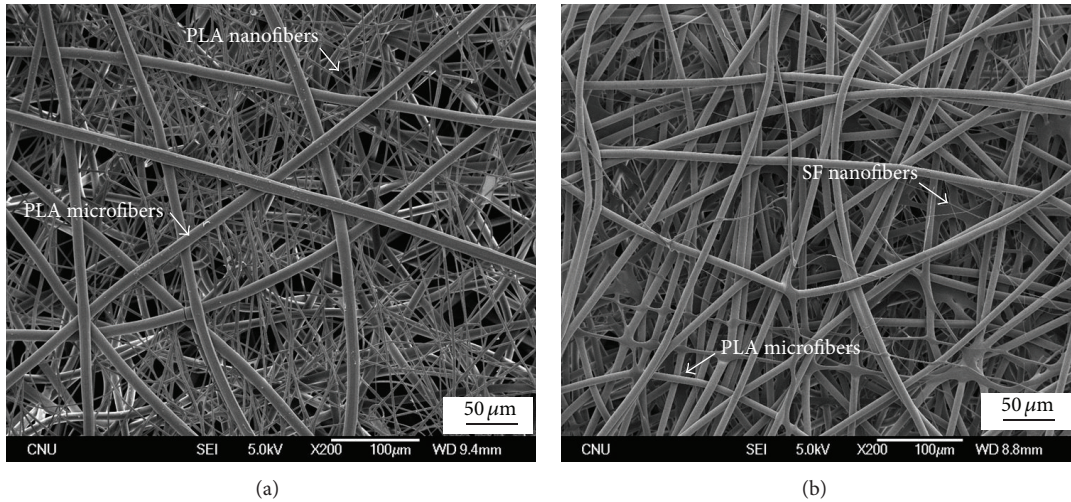


FIGURE 7: SEM images of (a) PLA/PLA (20/80) and (b) SF/PLA (20/80) nano-/microfiber composite scaffolds.

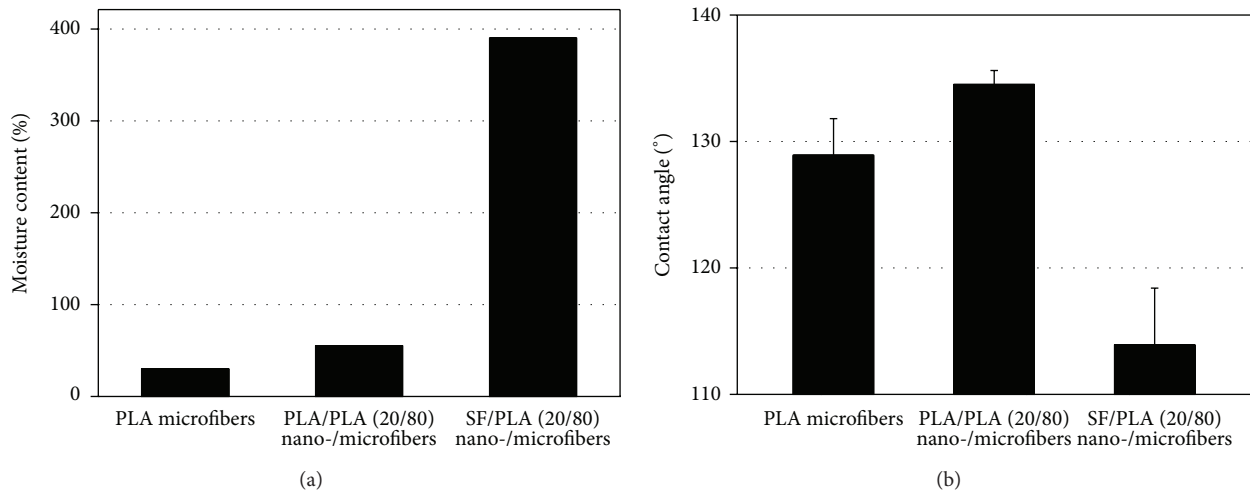


FIGURE 8: Moisture content (MC) and water contact angle (WCA) of PLA microfibers and PLA-based nano-/microfibers (20/80) composite scaffolds.

those (1.5 gf/mm<sup>2</sup> and 0.3 gf/mm<sup>2</sup>) of the PLA microfiber scaffolds. This may be explained by the nanofibrous structure entangled with microfibers. The nanofibers in the nano-/microfiber scaffolds can provide higher contacts or physical junctions with the microfibers or nanofibers and thus act as physical crosslinks.

**3.6. Effect of Plasma Treatment on the Hydrophilicity of the Hybrid Electrospun PLA Fibers.** Biodegradable aliphatic polyesters such as PLA and poly( $\epsilon$ -caprolactone) (PCL) are studied widely in scaffolds for tissue engineering. However, it is desirable to improve their surface properties because they have poor hydrophilicity and no functional sites for cell recognition. Plasma treatment provides an environmentally friendly process to improve the surface hydrophilicity of polymers without a serious loss of their bulk properties [26, 27].

Figure 8 represents the moisture content (MC) and water contact angle (WCA) of PLA microfibers and PLA-based nano-/microfiber (20/80) composite scaffolds. Both PLA microfibers and PLA/PLA (20/80) composite fibers showed a low MC (30% for PLA, 55% for PLA/PLA) and a high WCA (129° for PLA, 135° for PLA/PLA), whereas SF/PLA (20/80) composite fibers showed a high MC (390%) together with a WCA of 114° because of the relatively hydrophilic SF. The higher MC in the PLA/PLA sample compared to the PLA microfibers may be associated with a higher surface area due to the combined nanofibrous structure. The WCA is strongly dependent on the surface roughness and surface hydrophilicity, and thus the higher WCA of PLA/PLA composite fibers may be affected by the surface roughness.

The hybrid electrospun PLA/PLA (20/80) composite fibers were treated with plasma in the presence of either oxygen or ammonia gas to modify the surface properties of the fibers and to further compare the effects of two gases

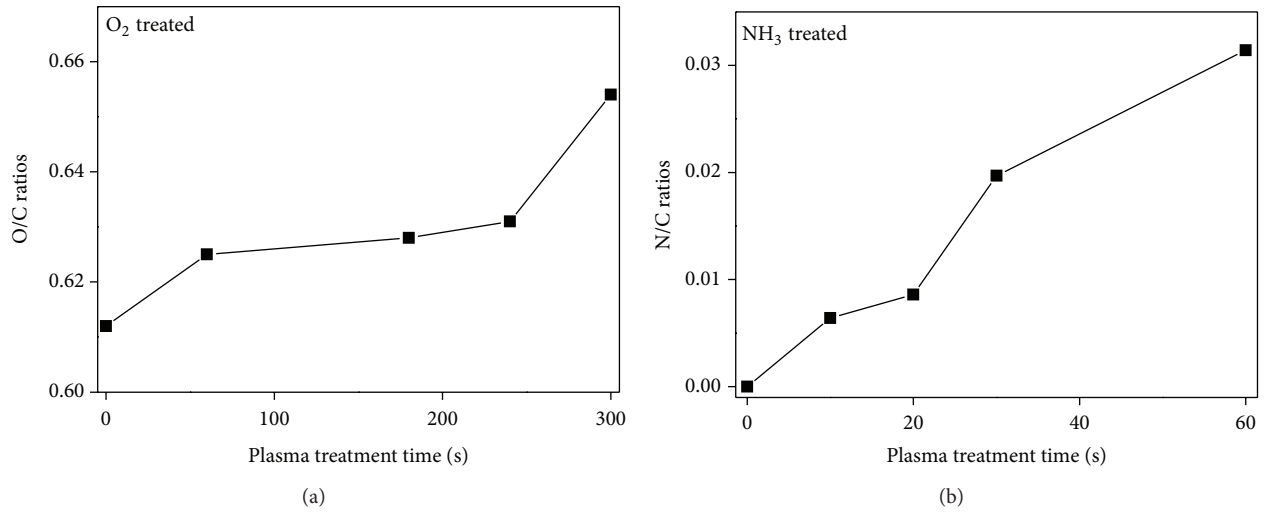


FIGURE 9: Change in chemical compositions of PLA fiber surfaces with plasma treatment time.

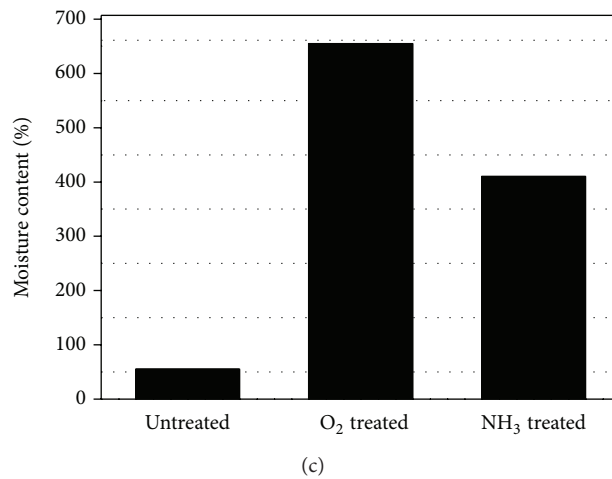
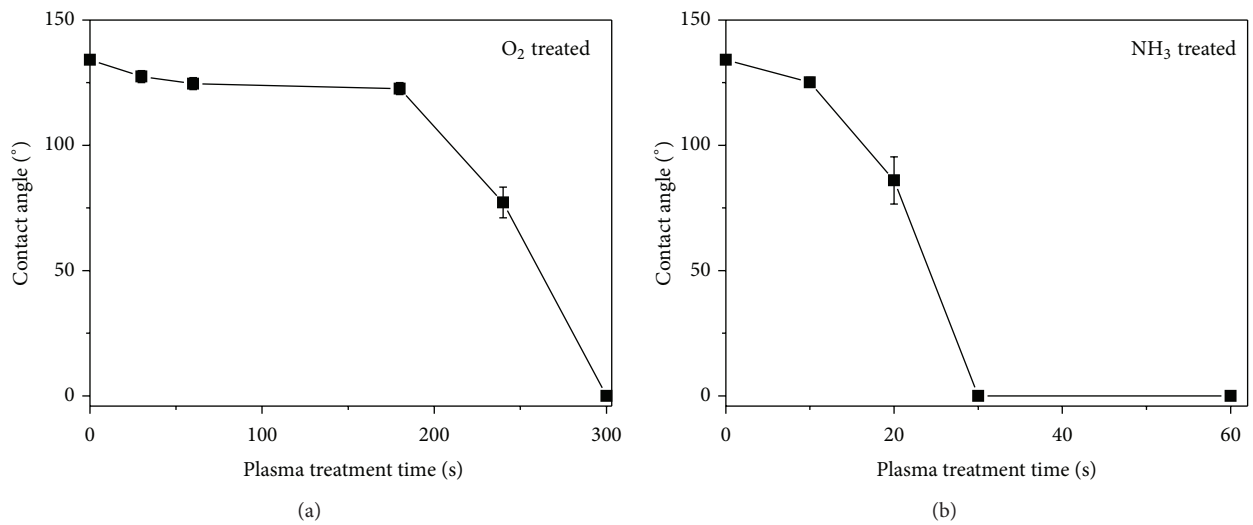


FIGURE 10: Change in (a) water contact angle (WCA) and (b) moisture content (MC) of PLA/PLA composite fibers with plasma treatment time.

(oxygen and ammonia) on the hydrophilicity of fibers. The morphological changes in the plasma-treated PLA fibers were observed by SEM. No significant changes in the morphology of PLA nano- and microfibers were observed. The change in chemical compositions of PLA fiber surfaces before and after plasma treatment was investigated by XPS (Figure 9). The O/C ratio was increased gradually after oxygen plasma treatment for up to 300 sec. This can be attributed to the formation of hydroxyl or peroxy groups on the surface of PLA fibers after oxygen plasma treatment. On the other hand, a new  $N_{1s}$  peak was observed after treatment with ammonia plasma, indicating newly formed N-containing functional groups such as amines (not shown). Interestingly, the surface of the PLA fibers contained an abundance of nitrogen atoms after ammonia plasma treatment, with an N/C ratio of up to 0.03 (Figure 9).

The MC and WCA of plasma-treated PLA/PLA (20/80) composite fibers were also measured to determine changes in the surface hydrophilicity during plasma treatment. Figure 10(a) shows the change in the WCA of PLA/PLA composite fibers with plasma treatment time. The WCA on the nontreated PLA/PLA composite fibers was  $135^\circ$ , indicating that the surface of the nontreated PLA fibers was quite hydrophobic. This value decreased abruptly after oxygen plasma treatment for 240 sec and reached  $0^\circ$  after 300 sec. In the case of ammonia plasma treatment, the WCA value decreased more quickly than the oxygen plasma and reached  $0^\circ$  after 30 sec. The MC of the nontreated PLA fibers was also increased significantly from 55% to 655% and 410% after treatment with oxygen plasma (treatment time = 240 sec) and ammonia plasma (treatment time = 20 sec), respectively. The reduction in WCA and the increase in MC clearly support the increased surface hydrophilicity of the PLA fibers, which might be caused by the introduction of new polar groups on the surface of the PLA fibers. Furthermore, the ammonia gas plasma enhanced the surface hydrophilicity of PLA fibers more effectively than oxygen gas plasma.

#### 4. Conclusion

The effects of plasticizer on the average diameter and morphology of melt electrospun PLA fibers have been examined. The average fiber diameter of the PLA microfibers decreased with increasing PEG plasticizer content due to the lower melt viscosity. Novel composite scaffolds were fabricated to combine the beneficial properties of nanofibers and microfibers. PLA/PLA and SF/PLA nano-/microfiber composite scaffolds were obtained by hybrid electrospinning, in which both the PLA and SF solution and PLA melt produced randomly mixed nanofibers and microfibers. The mechanical properties of the PLA microfibers were improved remarkably by introducing a small amount of nanofibers (20 wt%), even though they had similar pore parameters. The surface hydrophilicity and the content of polar groups on the surface of PLA fibers were increased significantly after plasma treatment in the presence of either oxygen or ammonia gas. This approach to controlling the hydrophilicity and diameters

of PLA composite fibers can be useful in the design and tailoring of novel scaffolds for tissue engineering.

#### Acknowledgment

This study was supported financially by the Biotechnology Development Program (Grant no. 850-20080090) funded by the Ministry of Education, Science, and Technology (MEST) of Korea.

#### References

- [1] A. Karchin, F. I. Simonovsky, B. D. Ratner, and J. E. Sanders, "Melt electrospinning of biodegradable polyurethane scaffolds," *Acta Biomaterialia*, vol. 7, no. 9, pp. 3277–3284, 2011.
- [2] J. Lyons, C. Li, and F. Ko, "Melt-electrospinning part I: processing parameters and geometric properties," *Polymer*, vol. 45, no. 22, pp. 7597–7603, 2004.
- [3] C. S. Kong, K. J. Jo, N. K. Jo, and S. H. Kim, "Effects of the spin line temperature profile and melt index of poly(propylene) on melt-electrospinning," *Polymer Engineering and Science*, vol. 49, no. 2, pp. 391–396, 2009.
- [4] L. Larrondo and R. S. J. Manley, "Electrostatic fiber spinning from polymer melts. 1. Experimental observation on fiber formation and properties," *Journal of Polymer Science*, vol. 19, no. 6, pp. 909–920, 1981.
- [5] L. Larrondo and R. S. J. Manley, "Electrostatic fiber spinning from polymer melts. 2. Examination of the flow field in an electrically driven jet," *Journal of Polymer Science*, vol. 19, no. 6, pp. 921–932, 1981.
- [6] L. Larrondo and R. S. J. Manley, "Electrostatic fiber spinning from polymer melts. 3. Electrostatic deformation of a pendant drop of polymer," *Journal of Polymer Science*, vol. 19, no. 6, pp. 933–940, 1981.
- [7] S. R. Givens, K. H. Gardner, J. F. Rabolt, and D. B. Chase, "High-temperature electrospinning of polyethylene microfibers from solution," *Macromolecules*, vol. 40, no. 3, pp. 608–610, 2007.
- [8] A. Gora, R. Sahay, V. Thavasi, and S. Ramakrishna, "Melt-electrospun fibers for advances in biomedical engineering, clean energy, filtration, and separation," *Polymer Reviews*, vol. 51, no. 3, pp. 265–287, 2011.
- [9] P. D. Dalton, D. Grafahrend, K. Klinkhammer, D. Klee, and M. Moller, "Electrospinning of polymer melts: phenomenological observations," *Polymer*, vol. 48, no. 23, pp. 6823–6833, 2007.
- [10] E. Zhmayev, D. Cho, and Y. L. Joo, "Modeling of melt electrospinning for semi-crystalline polymers," *Polymer*, vol. 51, no. 1, pp. 274–290, 2010.
- [11] E. Zhmayev, D. Cho, and Y. L. Joo, "Nanofibers from gas-assisted polymer melt electrospinning," *Polymer*, vol. 51, no. 18, pp. 4140–4144, 2010.
- [12] E. Zhmayev, H. Zhou, and Y. L. Joo, "Modeling of non-isothermal polymer jets in melt electrospinning," *Journal of Non-Newtonian Fluid Mechanics*, vol. 153, no. 2-3, pp. 95–108, 2008.
- [13] H. Zhou, T. B. Green, and Y. L. Joo, "The thermal effects on electrospinning of polylactic acid melts," *Polymer*, vol. 47, no. 21, pp. 7497–7505, 2006.
- [14] N. Detta, T. D. Brown, F. K. Edin et al., "Melt electrospinning of polycaprolactone and its blends with poly(ethylene glycol)," *Polymer International*, vol. 59, no. 11, pp. 1558–1562, 2010.

- [15] X. Li, H. Liu, J. Wang, and C. Li, "Preparation and characterization of poly( $\epsilon$ -caprolactone) nonwoven mats via melt electrospinning," *Polymer*, vol. 53, no. 1, pp. 248–253, 2012.
- [16] F. Zhao, Y. Liu, H. Yuan, and W. Yang, "Orthogonal design study on factors affecting the degradation of polylactic acid fibers of melt electrospinning," *Journal of Applied Polymer Science*, vol. 125, no. 4, pp. 2652–2658, 2012.
- [17] B. L. Farrugia, T. D. Brown, Z. Upton, D. W. Hutmacher, P. D. Dalton, and T. R. Dargaville, "Dermal fibroblast infiltration of poly( $\epsilon$ -caprolactone) scaffolds fabricated by melt electrospinning in a direct writing mode," *Biofabrication*, vol. 5, no. 2, Article ID 025001, 2013.
- [18] L. D. Harris, B. S. Kim, and D. J. Mooney, "Open pore biodegradable matrices formed with gas foaming," *Journal of Biomedical Materials Research*, vol. 42, no. 3, pp. 396–402, 1998.
- [19] J. Khandare and T. Minko, "Polymer-drug conjugates: progress in polymeric prodrugs," *Progress in Polymer Science*, vol. 31, no. 4, pp. 359–397, 2006.
- [20] Y. Q. Wan, X. Qu, J. Lu et al., "Characterization of surface property of poly(lactide-co-glycolide) after oxygen plasma treatment," *Biomaterials*, vol. 25, no. 19, pp. 4777–4783, 2004.
- [21] B.-M. Min, G. Lee, S. H. Kim, Y. S. Nam, T. S. Lee, and W. H. Park, "Electrospinning of silk fibroin nanofibers and its effect on the adhesion and spreading of normal human keratinocytes and fibroblasts *in vitro*," *Biomaterials*, vol. 25, no. 7-8, pp. 1289–1297, 2004.
- [22] F.-L. Mi, Y.-M. Lin, Y.-B. Wu, S.-S. Shyu, and Y.-H. Tsai, "Chitin/PLGA blend microspheres as a biodegradable drug-delivery system: phase-separation, degradation and release behavior," *Biomaterials*, vol. 23, no. 15, pp. 3257–3267, 2002.
- [23] S. J. Kim, L. Jeong, S. J. Lee, D. Cho, and W. H. Park, "Fabrication and surface modification of melt-electrospun poly(D, L-lactic-co-glycolic acid) microfibers," *Fibers and Polymers*, vol. 14, no. 9, pp. 1491–1496, 2013.
- [24] S. J. Kim, D. H. Jang, W. H. Park, and B.-M. Min, "Fabrication and characterization of 3-dimensional PLGA nanofiber/microfiber composite scaffolds," *Polymer*, vol. 51, no. 6, pp. 1320–1327, 2010.
- [25] H. Bergmeister, C. Schreiber, C. Grasl et al., "Healing characteristics of electrospun polyurethane grafts with various porosities," *Acta Biomaterialia*, vol. 9, no. 4, pp. 6032–6040, 2013.
- [26] M. P. Prabhakaran, J. Venugopal, C. K. Chan, and S. Ramakrishna, "Surface modified electrospun nanofibrous scaffolds for nerve tissue engineering," *Nanotechnology*, vol. 19, no. 45, Article ID 455102, 2008.
- [27] Q. F. Wei, W. D. Gao, D. Y. Hou, and X. Q. Wang, "Surface modification of polymer nanofibres by plasma treatment," *Applied Surface Science*, vol. 245, no. 1–4, pp. 16–20, 2005.